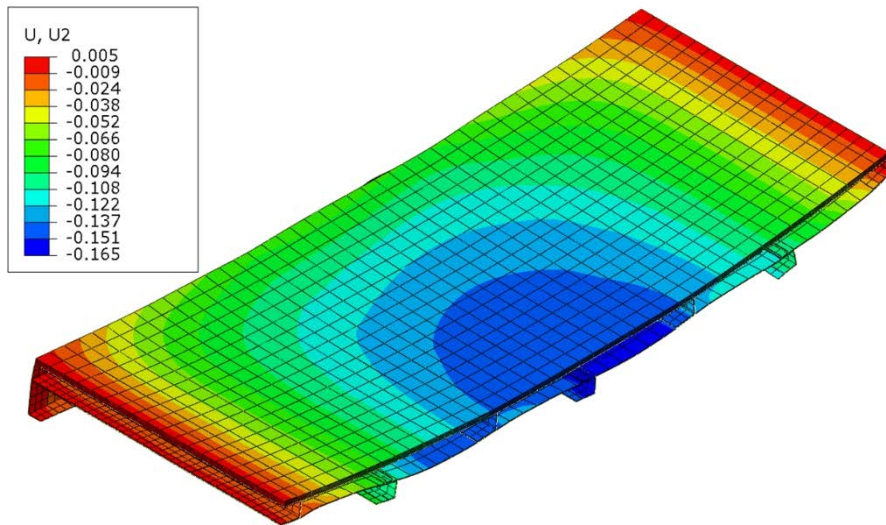U.S. Department of
Transportation
**Federal Railroad
Administration**

Evaluation of Rail Car Floor Fire Resistance and Test Article Scaling

Office of Research,
Development
and Technology
Washington, DC 20590

U, U2
- 0.005
- -0.009
- -0.024
- -0.038
- -0.052
- -0.066
- -0.080
- -0.094
- -0.108
- -0.122
- -0.137
- -0.151
- -0.165

Final Report
December 2018

REPORT DOCUMENTATION PAGE

Form Approved
OMB No. 0704-0188

Public reporting burden for this collection of information is estimated to average 1 hour per response, including the time for reviewing instructions, searching existing data sources, gathering and maintaining the data needed, and completing and reviewing the collection of information. Send comments regarding this burden estimate or any other aspect of this collection of information, including suggestions for reducing this burden, to Washington Headquarters Services, Directorate for Information Operations and Reports, 1215 Jefferson Davis Highway, Suite 1204, Arlington, VA 22202-4302, and to the Office of Management and Budget, Paperwork Reduction Project (0704-0188), Washington, DC 20503.

1. AGENCY USE ONLY (Leave blank)	2. REPORT DATE December 2018	3. REPORT TYPE AND DATES COVERED Technical Report May 2017–September 2018

4. TITLE AND SUBTITLE Evaluation of Rail Car Floor Fire Resistance Exposure and Test Article Scaling	5. FUNDING NUMBERS DTRT57-12-D-30011, Order 0031 DTFR53-15-X-00019
6. AUTHOR(S) Anil Kapahi, Mark McKinnon, Christian Rippe, Matthew DiDomizio, Charles Luo, Soroush Yazdani, Brian Lattimer	

7. PERFORMING ORGANIZATION NAME(S) AND ADDRESS(ES) Jensen Hughes, Inc. 3610 Commerce Drive, Suite 817 Baltimore, MD 21227-7164	8. PERFORMING ORGANIZATION REPORT NUMBER

9. SPONSORING/MONITORING AGENCY NAME(S) AND ADDRESS(ES) U.S. Department of Transportation Federal Railroad Administration Office of Railroad Policy and Development Office of Research, Development and Technology Washington, DC 20590	10. SPONSORING/MONITORING AGENCY REPORT NUMBER DOT/FRA/ORD-18/38

11. SUPPLEMENTARY NOTES
COR: Melissa Shurland

12a. DISTRIBUTION/AVAILABILITY STATEMENT This document is available to the public through the FRA website.	12b. DISTRIBUTION CODE

13. ABSTRACT (Maximum 200 words)
The focus of this research was to determine the appropriate fire resistance exposure severity and duration for passenger rail car floor assemblies, as well as an assessment of the minimum size test article for fire resistance testing. Modeling methodologies were developed to predict the fire, thermal, and structural response of rail car floor assemblies. Using these models, it was determined that the ASTM E119 fire exposure severity adequately represented realistic fire exposures and a duration of at least 30 minutes is required.

Simulations were also used to explore changes in load and boundary conditions leading to a new set of boundary conditions which required rail car floors under fire resistance test to be supported on the longitudinal ends rather than the transverse ends. Based on the simulations of a specific floor geometry, it was shown that the new boundary conditions allowed the test article to be reduced to one-third of the current size while still maintaining a response consistent with the rail car floor assembly in the end-use condition.

14. SUBJECT TERMS Rail car floor, fire resistance test, exposure duration, thermo-structural analysis, standard and realistic fires, floor fire barrier test, floor assembly	15. NUMBER OF PAGES 239
	16. PRICE CODE

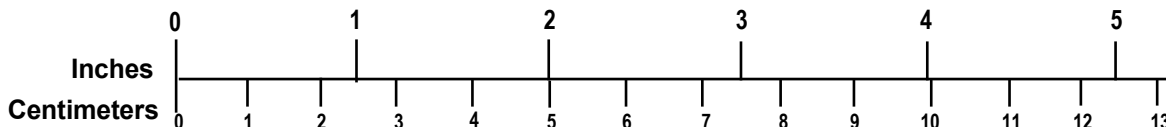| 17. SECURITY CLASSIFICATION OF REPORT Unclassified	18. SECURITY CLASSIFICATION OF THIS PAGE Unclassified	19. SECURITY CLASSIFICATION OF ABSTRACT Unclassified	20. LIMITATION OF ABSTRACT

NSN 7540-01-280-5500

Standard Form 298 (Rev. 2-89)

Prescribed by ANSI Std. 239-18
298-102

METRIC/ENGLISH CONVERSION FACTORS

ENGLISH TO METRIC

LENGTH (APPROXIMATE)

1 inch (in)	=	2.5 centimeters (cm)
1 foot (ft)	=	30 centimeters (cm)
1 yard (yd)	=	0.9 meter (m)
1 mile (mi)	=	1.6 kilometers (km)

AREA (APPROXIMATE)

1 square inch (sq in, in^2)	=	6.5 square centimeters (cm^2)
1 square foot (sq ft, ft^2)	=	0.09 square meter (m^2)
1 square yard (sq yd, yd^2)	=	0.8 square meter (m^2)
1 square mile (sq mi, mi^2)	=	2.6 square kilometers (km^2)
1 acre = 0.4 hectare (he)	=	4,000 square meters (m^2)

MASS - WEIGHT (APPROXIMATE)

1 ounce (oz)	=	28 grams (gm)
1 pound (lb)	=	0.45 kilogram (kg)
1 short ton = 2,000 pounds (lb)	=	0.9 tonne (t)

VOLUME (APPROXIMATE)

1 teaspoon (tsp)	=	5 milliliters (ml)
1 tablespoon (tbsp)	=	15 milliliters (ml)
1 fluid ounce (fl oz)	=	30 milliliters (ml)
1 cup (c)	=	0.24 liter (l)
1 pint (pt)	=	0.47 liter (l)
1 quart (qt)	=	0.96 liter (l)
1 gallon (gal)	=	3.8 liters (l)
1 cubic foot (cu ft, ft^3)	=	0.03 cubic meter (m^3)
1 cubic yard (cu yd, yd^3)	=	0.76 cubic meter (m^3)

TEMPERATURE (EXACT)

[(x-32)(5/9)] °F = y °C

METRIC TO ENGLISH

LENGTH (APPROXIMATE)

1 millimeter (mm)	=	0.04 inch (in)
1 centimeter (cm)	=	0.4 inch (in)
1 meter (m)	=	3.3 feet (ft)
1 meter (m)	=	1.1 yards (yd)
1 kilometer (km)	=	0.6 mile (mi)

AREA (APPROXIMATE)

1 square centimeter (cm^2)	=	0.16 square inch (sq in, in^2)
1 square meter (m^2)	=	1.2 square yards (sq yd, yd^2)
1 square kilometer (km^2)	=	0.4 square mile (sq mi, mi^2)
10,000 square meters (m^2)	=	1 hectare (ha) = 2.5 acres

MASS - WEIGHT (APPROXIMATE)

1 gram (gm)	=	0.036 ounce (oz)
1 kilogram (kg)	=	2.2 pounds (lb)
1 tonne (t)	=	1,000 kilograms (kg)
	=	1.1 short tons

VOLUME (APPROXIMATE)

1 milliliter (ml)	=	0.03 fluid ounce (fl oz)
1 liter (l)	=	2.1 pints (pt)
1 liter (l)	=	1.06 quarts (qt)
1 liter (l)	=	0.26 gallon (gal)
1 cubic meter (m^3)	=	36 cubic feet (cu ft, ft^3)
1 cubic meter (m^3)	=	1.3 cubic yards (cu yd, yd^3)

TEMPERATURE (EXACT)

[(9/5) y + 32] °C = x °F

QUICK INCH - CENTIMETER LENGTH CONVERSION

Inches: 0 1 2 3 4 5

Centimeters: 0 1 2 3 4 5 6 7 8 9 10 11 12 13

QUICK FAHRENHEIT - CELSIUS TEMPERATURE CONVERSION

°F	-40°	-22°	-4°	14°	32°	50°	68°	86°	104°	122°	140°	158°	176°	194°	212°
°C	-40°	-30°	-20°	-10°	0°	10°	20°	30°	40°	50°	60°	70°	80°	90°	100°
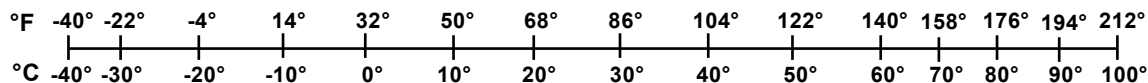
For more exact and or other conversion factors, see NIST Miscellaneous Publication 286, Units of Weights and Measures. Price $2.50 SD Catalog No. C13 10286

Acknowledgements

Contents

Illustrations

Tables

Executive Summary

A research study was conducted to determine the appropriate fire resistance exposure, severity, and duration for passenger rail car floor assemblies, as well as an assessment of the minimum size test article for fire resistance testing. The Federal Railroad Administration (FRA) funded research through the Volpe National Transportation Systems Center for investigation of fire safety of passenger rail equipment. This research effort began on December 2016 and ended on August 2018. The research was conducted by JENSEN HUGHES and partially at their test facilities as well as in test labs. Modeling methodologies were developed to predict the fire, thermal, and structural response of rail car floor assemblies. Using these models, it was determined that the ASTM E119 fire exposure severity adequately represented realistic fire exposures and a duration of at least 30 minutes was required. Simulations were also used to explore changes in load and boundary conditions to assess whether the test article size could be decreased. A new set of boundary conditions were identified which require rail car floors under fire resistance test to be supported on the longitudinal ends rather than the transverse ends. Based on the simulations of a specific floor geometry, it was shown that the new boundary conditions allowed the test article to be reduced to one-third of the current size while still maintaining a response consistent with the rail car floor assembly in the end-use condition.

The suggested boundary conditions and the methodology to use reduced scale-based on the modeling will need to be validated using fire resistance tests. The reduced scale methodology will also be applied to other rail car floors by using computer modeling to ensure the approach is applicable to a wide variety of rail car floors with different structural arrangements.

As specified in National Fire Protection Association (NFPA) 130 "Standard for Fixed Guideway Transit and Passenger Rail Systems" and Title 49 Code of Federal Regulation (CFR) Part 238, Passenger Equipment Safety Standards, rail car floor assemblies are currently required to undergo a scaled furnace test to demonstrate their fire resistance, including structural integrity and limited heat transmission. According to NFPA 130, the current test requirement is to use a floor assembly test article that is 3.6 m (12 ft.) long and as wide as a rail car (approximately 3 m [10 ft.]). The test article is simply supported along the transverse ends and has an applied total distributed load comprising live loads (passenger crush load), dead loads (equipment, other articles), and other relevant design loads. A standard exposure represented by American Society for Testing Materials (ASTM) E119 "Standard Test Methods for Fire Tests of Building Construction and Materials," time-temperature curve is used for 30 minutes in this test. The first purpose of this study was to evaluate if standard exposure such as ASTM E119 adequately represents a real fire scenario such as a gasoline or a diesel spill fire due to an accident which can have temporally and spatially varying exposure. The evaluation also assessed an appropriate exposure duration for a standard exposure which can better represent a real fire scenario. The second purpose of this study was to address the interest of rail car manufacturers in reducing the physical size of the test article used to qualify the fire resistance of a rail car floor assembly to decrease the cost of the compliance process. It was demonstrated that the overall behavior of a full-scale rail car floor is better represented by a test-scale rail car floor when supported at the

transverse ends rather than the longitudinal ends as suggested by the NFPA 130. The new boundary conditions were used to further reduce the size of the rail car floor by evaluating and comparing the response at different scales using the assembly deflection, plastic deformation, and shear stress distribution. It was demonstrated that for the exemplary assembly that a reduced-scale specimen with a one-third length (4 ft.) and width equivalent to that of an actual rail car can represent the behavior of a rail car floor in the end-use application.

1.   Introduction

The Federal Railroad Administration (FRA) has a defined mission to enable the safe, reliable, and efficient movement of people and goods throughout the United States. To this end, FRA has established fire safety regulations for the design and operation of new and existing passenger trains in the U.S., and these regulations have been published in 49 CFR Part 238. In the rule-making process for 49 CFR Part 238 that was issued in 2002, there were technical comments made on the large-scale floor assembly fire resistance testing. In particular, comments were related to whether the fire exposure severity and duration were appropriate as well as the potential of reducing the size of the test article to make the test more cost-effective. The focus of this research was to investigate these two comments. FRA provided funding for the research in collaboration with the Volpe National Transportation Systems Center, while JENSEN HUGHES conducted the research between December 2016 and August 2018.

This work investigated these two critical requirements which should be satisfied for the approval of rail car floor assemblies. The thermal and structural integrity requirements were investigated by developing a methodology to simulate the fire resistance test using a computer model. The developed model simulated the fire resistance test by exposing the rail car floor to passenger loading along with the standard ASTM E119 time-temperature curve for 30 minutes, a typical duration suggested by the National Fire Protection Association (NFPA) Committee 130 for passenger carrying vehicles. The developed methodology was further used to reduce the physical size of the rail car floor assembly.

A summary of the series of tasks performed to address these requirements are as follows:

- The plausible realistic fires that could occur under a rail car were identified through the review of accident reports and standards. The survey of passenger railways included incidents from several international and U.S. sources with an emphasis on incidents that involved exposure of the locomotive or passenger cars to an external fire. Information was obtained from these sources regarding the fuel type and source, duration of fire exposure, quantification of damage to trains, and the time required for full evacuation. The severity of these realistic exposures compared to standard exposures was unclear.

- The relationship between fires that develop on the underside of a rail car and the resulting thermal exposure boundary condition that evolves on the rail car floor were investigated. This was achieved by conducting a series of fire tests using various configurations where temperature and heat flux were measured. The results from this test series provided heat transfer data that were used to validate fire models.

- Fire Dynamics Simulator (FDS) was used to model fire tests conducted above. The effects of different rail car configurations on fire dynamics and severity of fire exposures were studied. FDS was validated by comparing simulation results with experimental data so that FDS could be used to predict other realistic fire exposures that have not been tested.

- A study was conducted to develop modeling methods necessary for predicting the response of rail car floor assemblies to standard fire resistance experiments. This included the investigation and development of relevant thermal and mechanical material property models, section modeling methods, and analysis of an exemplar assembly. Floor assembly materials were investigated in three different groups: structural framing materials, fire insulation materials, and composite floor materials. An exemplar analysis of a rail car floor assembly known to hold a 30-minute resistance rating was conducted using the commercially available finite element (FE) software Abaqus. This model served as a full-scale prediction baseline and showed that the methodology can reasonably capture floor assembly response to furnace exposure.

- A series of simulations were conducted to predict the results of exterior realistic fire scenario incidents identified in a review of fire incidents that involved railroad passenger equipment. The simulations performed in this effort were intended to evaluate the thermal response of the undercar floor assembly when the undercarriage is exposed to realistic fires. The undercar geometries investigated were representative of single-level and bi-level passenger cars from across the United States. Separation between the top of the rail and the rail car floor structure in the geometries that were modeled ranged from 12 inches to 48 inches. The thermal exposures from these simulations were applied to a representative floor assembly section to analyze the heat transmission across the various components of rail car floor. The performance of rail car floors exposed to real exposure was compared with the ASTM E119 exposure to reevaluate the standard exposure duration of 30 minutes.

- Thermal simulations involving the standard fires were performed to determine the difference in the temperature rise of a rail car floor assembly. The standard exposures were simulated using the ASTM E119 and the International Organization for Standardization (ISO) 834 "Fire-resistance tests -- Elements of building construction" time-temperature curves. The two exposures were compared by evaluating the heat transmission through the rail car floor assembly. The evolution of temperature at the exposed and the unexposed surface were simulated to estimate the fire resistance requirements according to NFPA 130 and EN 45545 "Fire protection on railway vehicles." It was noted that the representative loading requirements specified in NFPA 130 can be subject to different interpretation by the test laboratories. Test loading can be representative of loading in practice by either undergoing the same uniform load or by undergoing the same maximum bending moment. These different interpretations can lead to substantially different results in overall structural integrity of the assembly.

- A preliminary study was conducted to determine the minimum size of a reduced-scale assembly such that it represents the behavior of a full-scale assembly and can be used for standard fire resistance experiments. A nomenclature was created to define a representative element which can be used as a building block to construct both full-scale and reduced-scale test articles. A modeling and analysis approach was adopted to ensure loading similarity among different scales by adjusting the uniform load applied to the assembly. Using the same

4

boundary conditions as prescribed in NFPA 130, the final reduced assembly recommended in this work had the full rail car width and a length equal to two-thirds of the full-scale model length.

- A thermo-structural analysis was used to understand the response of a full-scale rail car floor supported at the transverse ends subjected to ASTM E119 exposure and passenger load. The response of the full-scale rail car floor was compared with the response of the test-scale article (as defined by NFPA 130) subjected to the same conditions. The test-scale response was also evaluated using the new boundary conditions. These boundary conditions required supporting the test-scale rail car floor on longitudinal ends rather than the transverse ends as suggested by NFPA 130. It was demonstrated that the overall behavior of full-scale rail car floor is better represented by test-scale rail car floor when supported at the longitudinal ends. The new boundary conditions were used to further reduce the size of the rail car floor by evaluating and comparing the response at different scales using the deflection of assembly, plastic deformation, and shear stress distribution. It was demonstrated that for the exemplary assembly that a reduced-scale specimen with a one-third length (4 ft.) and comprising of the full-width of the rail car floor supported on the longitudinal ends can represent the behavior of a rail car floor in the end-use application.

1.1   Background

Rail car floor assemblies are currently required in NFPA 130 and Title 49 Code of Federal Regulations (CFR) Part 238 to undergo a large-scale furnace test to demonstrate their fire resistance in accordance with ASTM E119, including structural integrity and limited heat transmission. ASTM E119 requires test articles to be exposed to a prescribed time-temperature curve using a furnace. While ASTM E119 provides test article size requirements, these are superseded by requirements provided within NFPA 130 which state that test articles must include the entire width of the rail car and a minimum 3.7 m (12 ft.) of rail car length. In addition, samples must contain one of each type of penetration present in the entire rail car construction. NFPA 130 also specifies fire resistance rating parameters that supersede the requirements of ASTM E119. In particular, NFPA 130 limits the fire rating determination to the following three parameters specified in Section 8.5.1.3.3:

1. Transmission of heat through the assembly shall not be sufficient to raise the temperature on its unexposed surface more than 139 °C (250 °F) average and 181 °C (325 °F) at a single point.

2. The assembly shall not permit the passage of flame or gases hot enough to ignite cotton waste on the unexposed surface of the assembly.

3. The assembly shall support the representative loading.

The required exposure duration is the greater of the following:

- Twice the maximum expected time under normal circumstances for a vehicle to stop completely and safely from its maximum operating speed, plus the time necessary to evacuate a full load of passengers from the vehicle under approved conditions; or

5

- Fifteen minutes for automated guideway transit (AGT) vehicles, 30 minutes for all other passenger-carrying vehicles.

ASTM E119 is a standard test procedure with a prescribed time-temperature exposure curve. However, it does not represent a real fire scenario which can have a temporally and spatially varying exposure. Prior to this study, there were no studies that had assessed how realistic fire exposures that may occur in a rail car operating environment compare with the ASTM E119 fire exposure. In addition, the rationale for the size of the test article and boundary conditions had not been documented previously. The current size test article requires a large-scale test be performed to evaluate a single section of floor. With modern rail car floor assemblies including structural detail that may vary along its length, this may result in testing multiple floor assemblies to demonstrate the adequacy of the floor assembly fire resistance. Reducing the floor size would potentially allow for testing in a smaller furnace or multiple test articles at the same time in a larger furnace.

This effort used computational modeling and analysis to understand the role of various structural members used in a rail car floor assembly and their performance in a typical full-scale floor assembly fire resistance test. This understanding was used to develop a new methodology to reduce the size of a test-scale rail car floor article. The developed methodology demonstrated that the proposed procedure to reduce the size of rail car floor test assembly will successfully capture the overall structural response of the rail car floor assembly in its end-use application.

1.2 Objectives

The main objectives of this work are as follows:

- To determine whether the ASTM E-119 fire exposure severity and duration specified in NFPA 130 represents realistic fire exposures for rail car operating environments.

- To use computational modeling to identify whether the floor assembly test article size can be reduced and still represent the thermal and structural response of the floor assembly inside the rail car.

1.3 Overall Approach

The overall approach of this work was to use computational models to predict the thermal and structural response of rail car floor assemblies when exposed to different fire conditions. These simulations were then used to determine whether the standard fire exposure as explained in Section 1.1 is adequately compared to the current requirement as well as to explore reducing the test article size in fire resistance approval testing.

Computational modeling involved predictions of the fire environment, thermal response of the floor assembly due to the fire, and the structural response due to the elevated temperatures. All simulations to predict the fire dynamics and thermal exposures from realistic fires onto the rail car floor were performed using the computational fluid dynamics (CFD) code FDS. This work also included a series of experiments to validate the use of FDS for simulating realistic fire exposures under rail cars. The thermal response of the rail car floor was simulated using finite element analysis (FEA) with the

commercial software Abaqus [1]. Abaqus was also used to predict the structural response of the floor assembly while being heated by the fire.

These models were first used to assess whether the severity and duration of the ASTM E119 fire exposure was representative of realistic fires. This was done by comparing the thermal response of an exemplar floor assembly exposed to standard and realistic fires. Two different standard exposures were considered: ASTM E119 cellulosic fire curve and UL 1709 hydrocarbon fire curve. Realistic fires were based on fires identified in a review performed in this work of accident data over the last 50 years. The standard scenarios were simulated for 2 hours instead of the typical 30 minutes to identify the appropriate exposure duration which might better represent a real fire scenario. The unexposed side average and peak temperature rise times were used to compare the different exposures.

Reducing the size of the test article for fire resistance approval testing was evaluated using the thermal and structural response of an exemplar floor assembly exposed to a standard ASTM E119 time-temperature curve. Simulations were performed on an entire representative rail car to provide the response benchmark for the furnace test. A series of simulations were then performed to predict the response of various size test articles under different boundary conditions and load levels to assess whether the test article size could be reduced. The through thickness of the test article remained unchanged so that the scaling was only based on the structural response. The different simulations were compared based on the similarities between their deflection profiles, shear stress distributions, and plastic deformations were compared with the result for the full rail car end-use application benchmark.

1.4 Scope

The scope of this effort was mostly limited to a computational study to assess the exposure severity and duration as well as the potential for reducing the size of the test article. The exception was fire testing to validate the FDS model for predicting thermal exposures for fires under rail cars. A single exemplar floor assembly was considered in all the analysis. For the exposure assessment, the use of a single floor assembly is adequate to provide a recommendation on the thermal exposure. The simulations involving reducing the floor assembly test article size were performed to determine if the scaling was feasible. It was beyond the scope of this work to determine a general method for reducing the test article size for floors having different structural details. In addition, it was beyond the scope to validate the scaling identified in this modeling through furnace testing on various floor assemblies.

1.5 Organization of the Report

The report is divided into several sections based on the different aspects of the research. Section 2 provides the review of accident history for the last 50 years involving various rail cars in North America and other international locations. Section 3 contains the experimental test series to provide heat transfer data that was used to validate fire models. Section 4 includes the validation of the FDS thermal exposure predictions by simulating the experiments done in Section 3. Section 5 contains the modeling methodologies to perform the thermal and structural analysis of rail car floors. Section 6 includes a comparison of the standard exposures with realistic fires by

evaluating the heat transmission through a rail car floor. Section 7 compares the ASTM E119 exposure recommended in NFPA 130 with the European standard ISO 834 exposure. Section 8 develops a methodology to reduce the size of rail car floors for fire resistance tests. Section 9 provides the procedure and new boundary conditions required to reduce the size of rail car floor test articles so that the response is similar to that in the full rail car end-use application.

2. Review of Accident Data for Fires Under Rail Cars

The plausible, realistic fires that could occur under a rail car were identified through review of accident reports and standards. The survey of passenger railways included incidents from several international and US sources with an emphasis on incidents that involved exposure of the locomotive or passenger cars to an external fire. Information was obtained from these sources regarding the fuel type and source, duration of fire exposure, quantification of damage to trains, and the time required for full evacuation. It is important to assess if real fires will produce rapid increases in the exposure to the floor assembly, which may be faster and higher than the standard ASTM E119 exposure, resulting in a rapid increase in temperature uncharacteristic of the currently required exposure curve. In this case, these exposures may impart more thermal energy into the rail car structure in the same amount of time as the standard exposure resulting in a more compromised structure than indicated by the standard test.

The identified fire incidents were used as a basis to develop detailed fire scenarios and provide the range of HRRs and burning durations possible with these fires. Detailed fire scenarios will be formulated in the next sections of this work to quantify the heat transfer to the rail car floor and the temperature rise of the floor assembly.

2.1. Summary of Incident Reports

A review of rail car fire incident reports was performed that focused on fires that expose the rail car exterior and undercar. The fire incident review included the U.S., Canada, Europe, and other international sources to ensure that more fire scenarios were captured, and more rail car designs were included. The data from Canada are the most relevant to the U.S. context as the Canadian network is similar in operations. The jurisdiction of FRA extends to all railroads except rapid transit operations in an urban area that are not connected to the general railroad system of transportation (49 CFR Part 209, Appendix A). Rail systems both within and outside of FRA jurisdiction were considered in this survey because the circumstances of the accidents presented here may also be relevant to commuter rail systems in the U.S. The accidents described in this section cover the period from 1966 to 2016.

2.2. U.S. Incidents

A unique feature of the U.S. passenger rail industry is that a majority of locomotives used for inter-city travel are driven by diesel-electric engines. The majority of inter-city trains that operate in Europe and Japan are designed with a continuous connection to the electric grid, making diesel engines unnecessary. A connection to the grid requires infrastructure that was included in the design of passenger-only tracks throughout much of Europe, but are only included in intra-city train systems and in a minority of regional inter-city train networks in the U.S. It is apparent when reviewing rail incident reports from the U.S., that many of the fire incidents are caused by fuel spills, while the major fire incidents in Europe are primarily caused by electrical failures. Incidents that occurred in the United States were identified from the National Transportation Safety Board (NTSB) Rail Accident Reports database, U.S. Fire Administration (USFA) Technical Reports, and directly from various transit agency records. Incidents must involve fatalities or a potential safety issue to be investigated by the NTSB. The

incidents that were identified are presented here based on the train type that was involved in the incident.

2.2.1. Incidents on Inter-City Passenger Trains

The information provided by the various sources on the incidents that occurred on U.S. inter-city passenger trains and locomotives is summarized in Table 2-1. Information from the accident reports was distilled to the pertinent information to characterize the exposure conditions to a passenger car or locomotive. This information included the type of fuel, the size of the fire, duration of the fire, and the location in the train at which the fire impinged or entered the locomotive or passenger cars. Empty cells in Table 2-1 indicate that there was no explicit statement in the report to determine the requisite information to populate the field.

Many of the incidents listed in Table 2-1 involved a collision between two trains or between a train and a highway vehicle at a grade crossing. In the event of a collision between trains, it is apparent that the major fire hazard derives from ruptured locomotive diesel tanks. In the events that involved collisions between trains and other vehicles at grade crossings, the major hazard derived from spilled fuel that was being carried by the struck highway vehicles. In both situations, spilled fuel can readily create a pool fire in the vicinity of the locomotive and passenger cars that impinges on the undercarriage or vehicle exterior.

2.2.2. Incidents on US Passenger Trains

Incidents on U.S. inter-city passenger trains were identified from the FRA incident database, NTSB's Railroad Accident Reports database, as well as directly from information provided by metropolitan transit agencies. The agencies that provided information about incidents directly included the Washington Metropolitan Area Transit Authority (WMATA [MD, VA, DC]), Southeast Pennsylvania Transit Authority (SEPTA [PA, NJ, DE]), New York City Transit Authority (NYCTA [NY]), Massachusetts Bay Transportation Authority (MBTA [MA, RI]), Port Authority Trans-Hudson (PATH) [NY, NJ], and the Bay Area Rapid Transit Authority (BART [CA]).

Incidents that have been identified from the FRA incident database from 2000 to the present are provided in Table 2-2. The set of criteria defined as the threshold for FRA to investigate an incident and generate a report includes deaths or injury to passengers or railroad employees, injury to five or more persons, an incident resulting in evacuation of the train, a minimum dollar amount of damage of $25,000 to a passenger train or $150,000 to railroad and non-railroad property, and incidents that involve a derailment. The majority of the fires that occurred in the commuter rail systems under the jurisdiction of FRA were ignited by electrical arcing or other electrical and mechanical equipment malfunctions. In several cases, damaged and malfunctioning third rail shoes ignited fires that directly affected the train undercarriages. In Table 2-2, the fire locations and common causes are listed in order of frequency.

Table 2-1. Information Determined from Survey of Fire Incidents Involving U.S. Intercity Passenger Trains

Incident Date	Incident Location	Information Source	Fuel/Ignition Source	Fire Size	Duration	Fire/Smoke Enter Train?	Exposed Section/Entry Point	Did Train Derail?	Cost of Damages	Number of Deaths (Injuries)
2/3/2015	Valhalla, NY	NTSB [2]	Gasoline/ automotive			Yes	Cab car	No	$3,700,000	6 (15)
6/24/2011	Miriam, NV	NTSB [3]	Diesel Fuel/ truck-tractor	100 gallons	127 minutes	Yes	Side of passenger car	No		6 (16)
9/12/2008	Chatsworth, CA	NTSB [4]	Diesel Fuel/ locomotive			Yes	Front of Locomotive	Yes	$12,143,000	25 (101)
3/10/2004	Queens, NY	NTSB [5]	Acetylene/ truck			No	Front of Locomotive	No	$83,000	(4)
3/15/1999	Bourbonnais, IL	NTSB [6]	Diesel Fuel/ locomotive		103 minutes	Yes	Rail car Undercarriage	Yes	$14,295,000	11 (122)
5/14/1997	Branson, MO	NTSB [7]				No	Locomotive	Yes	$410,625	0
2/16/1996	Silver Spring, MD	NTSB [8]	Diesel Fuel/ locomotive			Yes	Front of Locomotive	Yes	$7,500,000	11 (26)
9/22/1993	Mobile, AL	NTSB, USFA [9], [10]	Diesel Fuel/ locomotive		>120 minutes	Yes	Locomotive/ Rail car	Yes	$19,818,250	42 (103)
3/17/1993	Ft. Lauderdale, FL	USFA [11]	Gasoline/ Tanker truck	8500 gallons	53 minutes	No		No		6 (19)
12/12/1990	Boston, MA	NTSB [12]	Diesel Fuel/ locomotive		quickly extinguished	No	Locomotive	Yes	$12,675,000	(453)
12/18/1989	Stockton, CA	NTSB, USFA [11], [13]	Diesel Fuel/ locomotive	thousands of gallons	150 minutes	Yes	Locomotive/ Rail car	Yes	$2,435,000	3 (52)
1/4/1987	Chase, MD	USFA [11]	Diesel Fuel/ locomotive			Yes	Locomotive/ Rail car	Yes	$16,561,000	16 (174)

Incident Date	Incident Location	Information Source	Fuel/Ignition Source	Fire Size	Duration	Fire/Smoke Enter Train?	Exposed Section/Entry Point	Did Train Derail?	Cost of Damages	Number of Deaths (Injuries)
3/14/1982	Mineola, NY	NTSB [14]	Gasoline/ automobile			No	Front of Locomotive	No		9 deaths outside of train
1/2/1982	Southampton, PA	NTSB [15]	Gasoline/ Tanker truck	7900 gallons	75 minutes	Yes	Locomotive	No	$452,900	1 (5)
12/28/1966	Everett, MA	NTSB	Fuel Oil/ Tanker truck	7000 gallons		Yes	Locomotive/ Rail car	No		12

Table 2-2. Commuter Rail Incident Information Involving Fire from the FRA Accident Data as Reported by Railroads from 2000 to 2017

Transit Agency	Number of Incidents	Location of Fire	Causes
Alaska Railroad	1	Baggage Car	Unknown
Long Island Railroad	6	Third Rail Shoe Beam Undercarriage Jumper Cables	Electrical Debris Dust Accumulation
MBTA	3	Undercarriage Traction Motor Electrical Cabinet	Electrical Derailment
Metro North	25	Traction Motor Undercarriage Electrical Shoe Mechanism Pantograph Jumper Cable	Electrical Smoothing Reactor Collision with Debris
Metra (Chicago)	2	Top of Coach	Electrical
NJ Transit	18	Main Inductor Traction Motor Undercarriage Top of Coach	Electrical
PATH	4	Undercarriage	Electrical Equipment Malfunction
Caltrain Commuter Railroad	1	Locomotive	Collision
SEPTA	8	Traction Motor Journal Box Undercarriage	Electrical Equipment Malfunction
Trinity Railway Express	1	Traction Motor	Electrical
Utah Transit Authority	1	Trucks	Equipment Malfunction

Table 2-3 displays a summary of the information determined through the survey of fire incidents on intra-city trains. The common causes in Table 2-3 are listed in order of frequency. The incidents summarized in Table 2-3 generally involved ignition of equipment on the train undercarriage or debris on the tracks through electrical arcing. Train equipment that was ignited included contact shoe insulation, cable insulation, and various other external components. Debris on tracks encompassed a wide range of materials including newspapers, rope, track tie debris, construction refuse, and various other trash items. We could not get detailed information about the fire impinging or penetrating the cars from the studied data.

Table 2-3. Information Gathered from Survey of Fire Incidents Involving U.S. Intra-City Passenger Trains

Transit Agency	Location of Fire	Number of Incidents	Common Causes
WMATA	Tracks	1	Debris from train ignited when run over
	Undercarriage	0	
SEPTA	Tracks	91	Electrical, Debris, Grease, Equipment Failure
	Undercarriage	1	Electrical transformer malfunction
NYCTA	Tracks	5	Electrical, Debris, Collision
	Undercarriage	0	
MBTA	Tracks	1	Broken overhead power line
	Undercarriage	0	
PATH	Tracks	36	Electrical, Debris, Equipment Failure, Grease
	Undercarriage	18	Debris, Equipment Failure, Grease
BART [16]	Tracks	10	Debris, Electrical, Grease
	Undercarriage	1	Electrical Arcing

2.2.3. Incidents on Freight Trains that Share Right-of-Way

The majority of U.S. intercity trains share the right-of-way with freight trains due to the infrastructure in place for a large U.S. rail freight shipping industry. By sharing the right-of-way with freight trains, the potential fire exposures to locomotives and passenger cars due to collisions between trains or derailments of tank cars are more severe than the fire scenarios that are possible in incidents involving only passenger trains. Several incident reports from the NTSB database were identified as having occurred on tracks where the right-of-way is shared between freight and passenger trains. The information presented in Table 2-4 includes only data on freight train fires where reports indicated that the freight trains shared the right-of-way with passenger trains. As this type of incident was not the main focus of this survey, only fire events that occurred after the year 2000 are listed here.

Freight trains generally have several locomotives to haul trains that are longer and heavier than typical passenger trains, which increases the number of diesel fuel tanks and the amount of diesel fuel carried by the trains. In three of the cases presented in Table 2-5, the fire incidents resulted from ruptured fuel tanks, which held a maximum of 5,000 gallons of diesel fuel. A more severe possible fire hazard is presented by ruptured tank cars that hold flammable or combustible liquids. Three cases presented in Table 2-4 involved derailment and rupture of tank cars that each held in excess of 10,000 gallons of a flammable liquid that, in some cases, endangered nearby homes. The fires that resulted from these spills burned for many hours and were generally beyond the firefighting capabilities of local fire departments. In regions of the U.S. where it is

common for freight trains and passenger trains to share the right-of-way, the possibility of a large-scale flammable liquid spill must be considered as a possible fire exposure scenario to the undercarriage of passenger trains.

Table 2-4. Information Determine from Survey of Fire Incidents Involving U.S. Freight Trains that Occurred on Tracks that Share the Right-of-Way with Passenger Trains

Incident Date	Incident Location	Information Source	Type of Fuel/Ignition Source	Size of Fire	Duration	Did Train Derail?	Cost of Damages	Number of Deaths (injuries)
4/7/2011	Red Oak, IA	NTSB [17]	Diesel Fuel/ locomotive	< 5,000 gallons	140 minutes	Yes	$8,726,151	2 (2)
3/12/2007	Oneida, NY	NTSB [18]	• Liquid propane gas • Toluene • Tank cars	• 1 full propane tanker car • 500 gallons of toluene		Yes	$6,730,000	0
1/16/2007	Shepherdsville, KY	NTSB [19]	• Cyclohexane • Methyl ethyl ketone • Butadiene • Tank cars	35,000 square feet		Yes	$22,400,000	(52)
10/20/2006	New Brighton, PA	NTSB [20]	Ethanol/ Tank cars	485,278 gallons	48 hours	Yes	$5,800,000	0
7/10/2005	Anding, MS	NTSB [21]	Diesel Fuel/ locomotives	15,000 gallons	15 hours	Yes	$10,281,800	4
5/19/2004	Gunter, TX	NTSB [22]	Diesel Fuel/ locomotives	3,000 gallons		Yes	$2,161,458	1 (3)
11/15/2003	Kelso, WA	NTSB [23]	Diesel Fuel/ locomotives	<2,800 gallons		Yes	$2,700,000	(2)

2.3. Canada Incidents

Incidents that occurred in Canada were identified from the Transportation Safety Board of Canada and directly from transit agency records.

2.3.1. Incidents on Intercity Passenger Trains

The rail network and infrastructure in Canada is similar to the infrastructure in the United States and because of this, the locomotives on intercity passenger trains are generally the diesel-electric type that are also common in the U.S. Two incidents were identified as having involved intercity passenger trains in Canada and the information on these incidents is presented in Incidents on Intercity Passenger Trains in Table 2-5. The Brighton, ON, incident in Table 5 involved ignition of diesel fuel from the locomotive fuel tanks. The fire incident that occurred in 1994 involved a ruptured fuel tank that resulted in a pool fire under several of the passenger cars that lasted for a duration of approximately 150 minutes.

Table 2-5. Information Determined from Survey of Fire Incidents Involving Canadian Intercity Passenger Trains

Incident Date	Incident Location	Information Source	Fuel	Duration	Fire/Smoke Enter Train?	Exposed Section/ Entry Point	Did Train Derail?	Number of Deaths (injuries)
8/16/2009	Richmond, ON	Canada TSB [24]	Diesel Fuel/locomotives	15 minutes	No	Locomotive	No	0
11/20/1994	Brighton, ON	Canada TSB [25]	Diesel Fuel/locomotive	150 minutes	Yes	Undercarriage	Yes	(46)

Table 2-6. Information Determined from Survey of Fire Incidents Involving Canadian Intra-City Passenger Trains

Transit Agency	Location of Fire	Number of Incidents	Causes
TTC	Tracks	0	
	Undercarriage	1	Electrical arcing ignited rubber pads
STM	Tracks	3	Electrical, Collision, Debris
	Undercarriage	1	Electrical Arcing ignited flat tire

2.3.2. Incidents on Intra-City Passenger Trains

Fire incident data were also collected from the Toronto Transit Commission (TTC) and the Montreal Transit Corporation (STM). The trains on the TTC system run on a 600 V DC electrical feed from a third rail and the trains on the Montreal Metro roll on rubber tires and run on a 750 V DC electrical feed from a third rail. The incident data provided

by the TTC and STM were sparse and included few incidents that occurred on tracks and train undercarriages. It is evident from the data in Table 2-6 provided by these agencies that the most common cause of fires in these systems outside of train stations is electrical arcing, which results in ignition of trash or debris that has fallen from trains onto tracks or ignition of components of the trains.

2.4.   European Incidents

Fire incidents that occurred on European railways were identified from European Railway Accident Information Links (ERAIL), UK Health and Safety Executive (HSE) [UK], and Railway Accident Investigation Unit (RAIU), as well as directly from the transit agencies on which fire accidents occurred. The results of this survey are provided in Table 2-7 and Table 2-8. Information related to the three fires from France were obtained from the transportation investigation bureau (the "Bureau d'Enquêtes sur les Accidents de Transport Terrestre" [BEATT]), which investigates larger or more concerning fires that occur in transit systems in France. Fire incident information was provided by individual transit agencies which included the London Underground (LUL) [UK], U-Bahn [DE], British Railway [UK], Moscow Metro [RU], and Paris Metro [FR]. Though information concerning the specific details of the fire incidents were not available from the transit agencies, frequencies of incidents and basic cause were provided, as shown in Table 2-7. Typical of electrified trains, the fires on railways from the European transit agencies that provided information were generally ignited by electrical faults.

Table 2-7. Information Determined from Survey of Fire Incidents Involving European Passenger Trains Obtained from Transit Agencies

Transit Agency	Location of Fire	Number of Incidents	Causes
LUL	Tracks	501	Electrical, Debris, Arson, Grease
	Undercarriage	26	Electrical, Equipment Failure, Debris, Grease
U-Bahn	Tracks	0	
	Train	4	Electrical, Arson
	Tracks	0	
British Airways	Tracks	0	
	Train	2	Derailment, HVAC
Moscow Metro	Tracks	0	
	Train	2	Electrical, Arson
Paris Metro	Tracks	1	Electrical Short Circuit
	Train	4	Electrical, Collision, Arson

The data collected from European incident reporting groups are provided in Table 2-8. The typical causes for fires on railways in Europe were ignition of trash on the tracks or damage to the train undercarriage caused by electrical arcing. Only three of the fire incidents identified in the survey and presented in Table 2-8 were caused by ignition of a petroleum product and these fires were isolated to the locomotive.

Table 2-8. Information Determined from Survey of Fire Incidents Involving European Passenger Trains Obtained from ERAIL and RAIU

Incident Date	Incident Location	Information Source	Fuel/Ignition Source	Duration	Fire/Smoke Enter Train?	Exposed Section/Entry Point
9/14/2016	Bulgaria	ERAIL [26]	Transformer oil	240 minutes	No	Locomotive
7/8/2016	Bulgaria	ERAIL [27]	Electrical Arcing	300 minutes	No	Locomotive
6/16/2016	Bulgaria	ERAIL [28]	Oils	120 minutes	No	Locomotive
4/13/2016	Bulgaria	ERAIL [29]		180 minutes	No	Locomotive
10/13/2015	Bulgaria	ERAIL [30]	Electrical Arcing		No	Locomotive
1/30/2015	UK	ERAIL [31]	Electrical Arcing	60 minutes	Yes	Floor
11/7/2013	Ireland	RAIU [32]	Electrical Arcing		No	
1/8/2013	UK	ERAIL [33]	Electrical Arcing		No	
12/19/2012	Bulgaria	ERAIL [34]	Short circuit		No	Locomotive
8/2/2012	Romania	ERAIL [35]	Short circuit		No	Locomotive
7/20/2011	Bulgaria	ERAIL [36]		120 minutes	Yes	
5/11/2011	Romania	ERAIL [37]	Short circuit	300 minutes	No	Locomotive
11/2/2010	Romania	ERAIL [38]	Short circuit		No	Locomotive
8/23/2010	Romania	ERAIL [39]	Diesel Fuel/ Locomotive		No	Locomotive
2/7/2010	Romania	ERAIL [40]				
12/26/2009	France	BEATT [41]	Inter-car diaphragm	30 minutes	Yes	Inter-car diaphragm
11/30/2009	Bulgaria	ERAIL [42]	Electrical components			
7/30/2008	Czech Republic	ERAIL [43]	Electrical Arcing		Yes	
6/24/2008	France	BEATT [44]	Electrical components	95 minutes	Yes	Undercarriage
8/6/2005	France	BEATT [45]	Tires	85 minutes	Yes	Windows
10/5/1999	UK	HSE [46]	Diesel/ Locomotive		Yes	Undercarriage
9/8/1995	UK	HSE [47]	Diesel/ Locomotive		Yes	Undercarriage

2.5.   Other Incidents

Incidents that occurred in countries outside of Europe and North America are not well-documented. The data provided in Table 2-9 were collected from literature sources that provided limited information about the incidents.

Table 2-9. Information from Incidents that Occurred Outside the Americas and Europe

Incident Date	Incident Location	Information Source	Type of Fuel	Duration	Fire Enter Train?	Exposed Section/Entry Point
1/5/2004	Hong Kong	Chow [48]	Gasoline, newspaper	3 minutes	Yes	Arson
2/18/2003	South Korea	Roh et al. [49]	Gasoline	180 minutes	Yes	Arson
1/24/2002	Japan	Hasemi [50]	Electrical			Undercarriage
11/13/1997	Japan	Hasemi [50]	Electrical			Undercarriage
4/14/1995	Japan	Hasemi [50]	Electrical			Undercarriage
3/22/1994	Japan	Hasemi [50]	Electrical			Undercarriage
8/27/1993	Japan	Hasemi [50]	Electrical			Undercarriage
8/29/1992	Japan	Hasemi [50]	Electrical			Undercarriage
10/22/1985	Japan	Hasemi [50]	Motor caught fire			Undercarriage
9/26/1985	Japan	Hasemi [50]	Mechanical components			Undercarriage
2/6/1983	Japan	Hasemi [50]	Generator			Undercarriage
2/25/1982	Japan	Hasemi [50]	Generator			Undercarriage

2.6. Incident Analysis

Several of the incidents for which information was presented in Section 2 were well-documented and all pertinent information required to determine the fire size, location of fire exposure, duration of the exposure, and damage to the locomotive and/or rail car is provided in various accounts and reports. An analysis of these incidents provides the basis for the recommendations made in this work. The pertinent information from these incidents is provided in the following sections, covering the period of time between 1979 and 2016.

2.7. Fire Exposures

The incident that occurred in the UK on January 30, 2015, involved electrical arcing under a train that resulted in a small explosion under one of the passenger cars, followed by 22 seconds of severe electrical arcing [31]. Shortly after the explosion, the floor of the car was penetrated by fire and smoke rapidly filled the car. The report indicated that the metal in contact with the floor adjacent to the burned areas was

estimated to have reached a temperature of 1,200 °C (2,192 °F) during and immediately after the arcing. A photograph from inside the car that shows the damage to the floor where the fire penetrated the undercarriage is provided as Figure 2-1.

Figure 2-1. Photograph of Damage to Floor Inside Tram Rail Car from UK Incident on January 30, 2015

The incident that occurred on December 26, 2009, in France involved a tramway on rubber tires [41]. One brake failed in the locked position and set fire to a mudguard and the inter-car diaphragm. The estimated fuel burned was 1,850 kg (4,079 lbs.) (made of 50% polymer) and the peak mass loss is estimated at 1 kg/s when the inside of the car was burning over a length of 25 m (82 ft.).

The incident that happened in France on June 24, 2008, involved a small regional train powered by a diesel engine [44]. The fire started due to an electric fault and spread through a wire penetration in the floor. The engine car (including a space for passengers) was destroyed. The primary fuels were the components available in the electrical cabinet and spread later to the whole rail car.

The fire involving two subway trains on August 6, 2005, in France was due to a slipping tire that caught fire when a train was stopped at a station [45]. It then spread to another car that was stopped on an adjacent track. Two cars were seriously damaged. The floor did not lose its integrity even where exposed to the burning tires and other components. The windows of the two contiguous cars exploded and the fire entered through the openings.

The incident that occurred in the UK on October 5, 1999, involved a head-on collision between two passenger trains [46]. The collision resulted in significant mechanical damage to both trains and ruptured both of the fuel tanks on the locomotives of each train. The ruptured tanks released diesel fuel under pressure which resulted in approximately 182 gallons (688 L) of finely dispersed airborne diesel fuel in the vicinity of the collision. Immediately after the collision the finely dispersed diesel fuel ignited which resulted in a fireball that covered a horizontal distance of approximately 230 ft. (70 m). In addition to the finely dispersed fuel, some portion of 1,091 gallons (4,130 L) of diesel fuel was also released from the ruptured fuel tanks. It was noted that fire entered one of the damaged passenger cars through the floor in the toilet. Pictures

taken shortly after the collision and after development of the fire are provided in Figure 2-2.

Figure 2-2. Photographs from Incident in UK on October 5, 1999, Showing Size of Fire

The incident in Bourbonnais, IL, that occurred on March 15, 1999, consisted of an Amtrak train with 207 passengers that struck and destroyed the trailer of a tractor-trailer loaded with ¾-inch-diameter rebar at a grade crossing [6]. Both locomotives of the Amtrak train as well as 11 of the 14 passenger cars derailed, and these derailed cars struck 2 of 10 freight cars on an adjacent siding, which resulted in several cars being overturned. The collision resulted in a fire in the lead locomotive of the Amtrak train and it was noted that the fire was seen travelling toward the back of the locomotive and under a sleeper car directly behind the locomotive. The fire was described as petroleum-based and burned in the vicinity of the locomotive and sleeper car for approximately 2 hours, when a large foam suppression tanker arrived at the scene and quickly extinguished the flames. The collision resulted in significant mechanical damage to the locomotive and the sleeper car including breaches of the walls and floor of the car. Fire damage to the interior materials was noted as consistent with long exposure to high temperatures. A photograph of the scene of the incident is provided in Figure 2-3.

Figure 2-3. Aerial Photograph of Incident Scene from Bourbonnais, IL, on March 15, 1999, Showing the Extent of Collision and Fire Damage

The incident that occurred in the UK on September 8, 1995, involved a high speed train with approximately 500 passengers [47]. A fastener attaching the fuel tank to the lead locomotive failed, causing the fuel tank to drop and drag along the tracks. The tank ruptured and friction between the tank and tracks generated sparks that facilitated the ignition of leaking diesel fuel. The resulting fire engulfed the outside of the three leading passenger cars and damaged many components on the undercarriage of the passenger cars. Fire penetrated the cars from underneath through service ducts adjacent to the toilets.

The incident that occurred in Brighton, ON, on November 20, 1994, consisted of a VIA Rail train that struck a piece of rail that had been intentionally placed on the tracks [25]. The rail punctured the diesel fuel tank and severed electrical power cables which resulted in a fire that trailed behind the locomotive and underneath the two passenger cars directly behind the locomotive. The fire continued to burn for approximately two-and-a-half hours and it was noted during the investigation that there was sufficient heat exposure to deform the primary supporting structure of the passenger car directly behind the locomotive such that there was a pronounced sag in the frame between the front and rear trucks. It was noted by passengers that windows began to melt and shatter from the heat, which may have contributed to penetration of the fire into the rail car. A photograph of the damage to the cars is provided in Figure 2-4.

Figure 2-4. Photograph from Incident in Brighton, ON, Showing Fire Damage to Rail Cars

The incident in Boston, MA, on December 12, 1990, consisted of a derailment of an Amtrak train that resulted in a collision with a commuter train [12]. A fuel tank on the Amtrak train broke away from the locomotive and resulted in a diesel fire. Firefighters that arrived shortly after the incident quickly extinguished the majority of the fire, although residual diesel fires were noted near the locomotives over the next 2 hours.

The incident in Stockton, CA, that occurred on December 18, 1989, consisted of an Amtrak train that struck a tractor-trailer at a grade crossing [11] [13]. The locomotive and one passenger car overturned and came to rest on their sides. A fire resulted from leaking diesel fuel tanks on the locomotive and it was noted that several thousands of gallons leaked out and pooled in a depression under the locomotive. It required approximately 2 ½ hours of attention from the fire department to completely extinguish the fire, although the damage to the train and locomotive were not well documented.

The incident that occurred in Chase, MD, on January 4, 1987, consisted of a collision between an Amtrak passenger train and a string of Conrail freight train locomotives [11]. A large diesel pool fire fed by leaking locomotive fuel tanks had formed by the time first responders arrived on the scene and a second, smaller pool fire was discovered underneath derailed passenger cars. It was noted that the large pool fire endangered two passenger cars as well as nearby homes.

An incident that occurred in the Transbay Tube of the BART system in San Francisco, CA, on January 17, 1979, resulted from electrical arcing from the 1,000 V DC propulsion current supplied by the electrified third rail to various broken and malfunctioning components of the cars and undercarriages [16]. During the analysis of the incident, it was noted that the 1,000 V DC current can generate temperatures of approximately 3,000 °F (1,650 °C) and the materials in the vicinity of the electrical fault included polymers, rubber, aluminum, and stainless steel, each of which has an ignition temperature lower that 3,000 °F. It was also noted that fire entered the cars from below due to melting of aluminum and steel seal plates. The train departed in good order from a train station 6 minutes prior to the first signs of fire and smoke.

During the incident that occurred in Valhalla, NY, on February 3, 2015, a locomotive struck an automobile at a highway grade crossing. A small fire ensued, but the majority

of the damage and the fatalities on the train were attributed to approximately 480 feet of electrified third rail penetrating the undercarriage and wall of the train. This incident details the importance of designing the undercarriage not only to resist penetration of fire, but also to resist puncture. However, the design and evaluation or the resistance to puncture is outside of the scope of this work.

There are accounts of many fires that burned trash located on the track or debris from train components that were ignited in some cases by electrical arcing from the electrified rail designed to supply power to trains. Another common ignition source was heat from friction caused by malfunctioning brakes and other mechanical equipment. Details of the resulting fires and potential damage to rail cars and locomotives are not well-documented, so it is difficult to assess the intensity of the exposures that resulted from these incidents. The materials that fueled fires that ignited underneath the rail cars and locomotives included paper trash, electrical cables, contact shoe insulation, rubber tires, and other polymer-based transit system components. In several instances, it was noted that grease on mechanical components or grease-covered trash and debris ignited. It is a safe assumption that the intensity of fires that burn debris or trash on the tracks or on the undercarriage of the locomotive and passenger cars is less severe than the intensity of hydrocarbon fuel fires that result from ruptured fuel tanks and tanker cars.

The rail car cables that were identified from the survey as being involved in fires on undercarriages have heat release rate per unit area (HRRPUA) in the range of approximately 98 to 1,071 kW/m^2 (8.63–94.4 Btu/s-ft^2) [51]. It has been shown in experiments that paper trash typical of Amtrak trains has an approximate HRRPUA within the range for electrical cables [51]. The fire properties of grease may be approximated by transformer oil, which has an approximate HRRPUA of 1,800 kW/m^2 (158.6 Btu/s-ft^2) [52] [51]. The diesel pool fires have a HRRPUA of approximately 1,400 kW/m^2 (123.3 Btu/s-ft^2) and can be expected to encompass a much larger burning surface area when spilled from a ruptured fuel tank than the trash and components that have been known to ignite due to electrical arcing [51] [53]. There is currently a lack of information on the duration and intensity of fires typical in intra-city train systems. The information on fire size and damage to rail cars learned from the survey are provided in Table 2-10.

Table 2-10. Summary of Pertinent Information Obtained for Size of Fires and Damage to Trains

Incident Date	Incident Location	Information Source	Fuel/Ignition Source	Fire Size	Fire Enter Train?	Exposed Section/Entry Point
1/30/2015	UK	ERAIL	Electrical Arcing		Yes	Floor
12/26/2009	France	BEATT	Inter-car diaphragm	1,850 kg (4,079 lbs.)	Yes	Inter-car diaphragm
6/24/2008	France	BEATT	Electrical components		Yes	Undercarriage
8/6/2005	France	BEATT	Tires	4 tires	Yes	Windows
10/5/1999	UK	HSE	Diesel Fuel/Locomotive		Yes	Undercarriage
3/15/1999	Bourbonnais, IL	NTSB	Diesel Fuel/Locomotive		Yes	Undercarriage
9/8/1995	UK	HSE	Diesel Fuel/Locomotive	>182 gallons	Yes	Undercarriage
11/20/1994	Brighton, ON	Canada TSB	Diesel Fuel/Locomotive		Yes	Undercarriage
12/12/1990	Boston, MA	NTSB	Diesel Fuel/Locomotive		No	Locomotive
12/18/1989	Stockton, CA	NTSB, USFA	Diesel Fuel/Locomotive	thousands of gallons		
1/4/1987	Chase, MD	USFA	Diesel Fuel/Locomotive			
1/17/1979	San Francisco, CA	NTSB	Electrical Arcing		Yes	Undercarriage

2.8. Duration of Exposures and Passenger Evacuation

The duration of fire exposures determined in the survey covers a wide range of times due, in part, to the range of fuel volumes and types and sizes of trash and components that fueled the fires in these incidents. Long duration fires were those that resulted from incidents involving freight trains that share the right-of-way with passenger trains in the United States. The longest reported fire from these cases lasted longer than 2 days and firefighters and emergency personnel decided to passively contain the fires due to the risk involved with attempting to extinguish them. However, freight trains are not relevant to this study. A more pertinent definition of the fire duration in cases with spilled

combustible liquids is the time required to remove all passengers from the trains that are endangered by the spilled fuel fire. Several of the incidents identified in the survey provide information relevant to the egress and extrication of passengers and this information is summarized in the following paragraphs. It should be noted that in the accidents described below, the egress duration corresponds to the time to get the passengers out of the train unless specified otherwise.

An incident that occurred in the UK on January 8, 2015, involved electrical arcing under a train that resulted in a small fire [31]. Smoke entered a passenger car from underneath 28 seconds after detection of the fire. Evacuation of all passengers on the train was completed approximately 10 minutes after initial detection of the fire.

An incident in Richmond, ON, occurred on August 16, 2009, when diesel fuel injectors malfunctioned and a small fire erupted in the locomotive of a passenger train [24]. The fire was contained to the locomotive and no one was injured. All passengers from five passenger cars had safely detrained 8 minutes after the fire was identified.

During the incident that occurred in Bourbonnais, IL, on March 15, 1999, egress and extrication of passengers began shortly after the collision and was mainly attended to by employees of a nearby steel plant [6]. These efforts continued for approximately 45 minutes at which point the fire was too intense for them to continue. Several passengers were unaccounted for in the sleeper car that was subjected to the most severe fire exposure.

The incident that occurred in Silver Spring, MD, on February 16, 1996, involved a head-on collision between a Maryland Area Regional Commuter (MARC) train and an Amtrak train [8]. Atomized fuel from the Amtrak train immediately entered the commuter train on collision and ignited a fireball. Surviving passengers claimed that the passenger cars had been filled with smoke and fire and that difficulties in exiting the rail car resulted from faulty emergency exit release latches. Amount of time required for egress ranged from 5 to 10 minutes for the car which was on fire.

During the incident that occurred in Brighton, ON, on November 20, 1994, passengers in the cars that were affected by smoke and fire met with trouble exiting the cars [25]. A panic ensued and several passengers broke windows and exited via the windows.

During a train derailment in Intercession City, FL, on November 30, 1993, a fire did not occur, but evacuation and extrication of passengers required 52 minutes [11].

After a derailment in the subway in New York, NY, on August 28, 1991, evacuation and extrication of 216 passengers took 183 minutes [11]. There were 5 fatalities and 121 passengers were transported to hospitals following evacuation.

During the incident that occurred in Chase, MD, on January 4, 1987, it was noted that as the fire was extinguished, trapped passengers were located and it became apparent that the rescue effort for the remaining trapped passengers would be long and resource-intensive [11].

During the incident in San Francisco, CA, on January 17, 1979, all passengers were clear of the train 53 minutes after the first observation of fire [16].

Egress and extrication of passengers can cover a wide range of durations after an incident occurs or a fire ignites based on the damage to the train and severity of injuries

suffered by the passengers and employees. Based on information from the incidents that occurred in the UK on January 8, 2015, Richmond, ON, and Silver Spring, MD, egress can take place safely over a time period on the order of 10 minutes when a fire on an above-ground train is not accompanied by catastrophic mechanical damage. This survey shows that when a collision or other severe mechanical damage occurs during the incident, search and rescue and extrication of injured or trapped passengers requires on the order of 1 hour. These reports have also shown that the severity of the fire may increase the time required for extrication because attempts to extinguish the fire generally come before attempts at extrication of injured passengers.

A study sponsored by FRA to determine egress rates under ideal circumstances concluded that mean egress rates depend on the location to where evacuation is taking place, the number of doors available for egress, and the locations of those doors [54]. The mean egress rates determined in this study included 52 people per minute (ppm), 41 ppm, and 20 ppm. Although the egress time for bi-level cars was not investigated in this FRA study, they are expected to be higher than for single level cars.

When incidents occur in subways and tunnels, the time for complete evacuation from the tunnel is always longer than for incidents that occur on ground-level and may be in excess of 3 hours due to logistical complexities. The fires that involve subway trains are less severe than fires on trains that require diesel-electric locomotives, and it is likely that the duration of fires that involve trash and debris ignited by electrical arcing are considerably less than the 3 hours required for complete extrication of passengers from mechanically damaged subway trains. The information on fire duration and time to evacuation based on the survey are provided in Table 2-11.

Table 2-11. Summary of Pertinent Information Obtained on Duration of Fire Exposures and Egress Times

Incident Date	Incident Location	Information Source	Duration	Time to Evacuation
9/14/2016	Bulgaria	ERAIL	240 minutes	
8/7/2016	Bulgaria	ERAIL	300 minutes	
6/16/2016	Bulgaria	ERAIL	120 minutes	
4/13/2016	Bulgaria	ERAIL	180 minutes	
1/30/2015	UK	ERAIL	60 minutes	
1/8/2015	UK	ERAIL		10 minutes
7/20/2011	Bulgaria	ERAIL	120 minutes	
5/11/2011	Romania	ERAIL	300 minutes	
12/26/2009	France	BEATT	30 minutes	No passengers
8/16/2009	Richmond, ON	Canada TSB	15 minutes	8 minutes
6/24/2008	France	BEATT	95 minutes	3-5 minutes
8/6/2005	France	BEATT	85 minutes	17 minutes
3/15/1999	Bourbonnais, IL	NTSB	103 minutes	>45 minutes
2/16/1996	Silver Spring, MD	NTSB		10 minutes
11/20/1994	Brighton, ON	Canada TSB	150 minutes	
11/30/1993	Intercession City, FL	USFA [11]	N/A	52 minutes
3/17/1993	Ft. Lauderdale, FL	USFA	53 minutes	
8/28/1991	New York, NY	USFA [11]	N/A	183 minutes
12/18/1989	Stockton, CA	NTSB, USFA	150 minutes	
1/17/1979	San Francisco, CA	NTSB		53 minutes

2.9. Design Exposures

From the information available in incident reports, it appears that a typical fire exposure scenario consists of a pool fire fed by diesel fuel spilled from ruptured fuel tanks. The typical fuel tank capacity for passenger train locomotives used by Amtrak and manufactured by Electro-Motive Diesel is in excess of 1,800 gallons [55]. The length of the most common passenger car operated by Amtrak, the Amfleet I, produced by the (now defunct) Budd Company, is approximately 85 ft. (26 m) [56]. The most severe scenario assumes that a pool of diesel fuel is confined to the volume between the rails and bounded by the front and rear edge of the rail car. The standard rail gauge in the U.S. is 1.44 m (4.72 ft.), and the resulting surface area of the pool fire would be approximately 37.4 m^2 (402.6 ft^2). Assuming a volume of 1,800 gallons (6.81 m^3) of diesel fuel spills and fills the entire area under the passenger car, the depth of the pool is calculated as 18.2 cm (0.597 ft.) according to Equation 2-1:

$$\delta = \frac{V}{A} \qquad \text{(2-1)}$$

where V is the spill volume and A is the spill surface area. The steady-state burning rate for diesel fuel pool fires has been reported as 0.035 kg/m^2-s (0.00748 lb/ft^2-s), and with an assumed density of 1,000 kg/m^3 (62.4 lb/ft^3), the duration of burning for this theoretical pool fire would be approximately 87 minutes (5,200 seconds) according to Equation 2-2 [51]:

$$t = \frac{V \cdot \rho}{\dot{m}'' A}$$
(2-2)

where V is the spill volume, A is the spill surface area, ρ is the fuel density, and $\dot{m}''$ is the mass loss rate per unit surface area. The HRRPUA for steady burning of diesel pool fires has been reported as approximately 1,400 kW/m^2 (123.3 Btu/s-ft^2). After the fuel has spread the length of the rail car and the burning has reached a steady-state, the maximum HRR expected from this fire is approximately 52 MW (49,670 Btu/s) according to Equation 2-3:

$$q = q'' A$$
(2-3)

where A is the fuel surface area and q'' is the HRRPUA. This is conservative due to the assumption that all the fuel has been spilled and flowed along the length of the rail car. Hurley et al. (2016) caution against the assumption that the maximum burning rate is immediately achieved, and have shown that when transient flame spread is taken into consideration, the experimentally measured duration may be as much as six times longer than the predicted duration and the maximum HRR may be approximately 40 percent lower [51]. Therefore, it is reasonable that the maximum HRR to be expected from this theoretical scenario is approximately 21 MW (19,905 Btu/s) and the duration may be as long as 9 hours without firefighter intervention. Both the total HRR and the reduced HRR values are very high, but they likely represent the worst possible scenario. An additional possible scenario with leaking diesel fuel includes a continuously-fed pool fire. In this case, the contents of the diesel fuel tank are constantly feeding an existing fire and the differences in maximum HRR and duration between the static pool fire and the continuously-fed fire are difficult to predict.

For many of the train systems in operation in the U.S., diesel and other fuels are not necessary and so there is no possibility of a hydrocarbon pool fire exposure. However, trains on the intercity and commuter rail routes are mostly diesel and it is required to study fires involving diesel spill. In some of the identified incidents, the train electrification infrastructure faulted or shorted and resulted in electrical arcing or electrical overload of a circuit. These electrical faults and arcing generate enough energy to act as ignition sources for combustible materials, but may also generate enough energy and a high-temperature environment that is adequate to melt or cause combustion of metals. Cases provided in this report in which these phenomena were observed include the incident that occurred on January 30, 2015, in the UK and the incident that occurred on January 17, 1979, in San Francisco, CA. The duration of arcing that led to catastrophic damage and failure of the undercarriage in both cases ranged from 22 seconds in the UK incident to no more than 6 minutes in the San Francisco incident. It is difficult to assign an estimated HRR or time-temperature curve to electrical arcing, but it has been estimated that an electrical arc that passes through air can reach temperatures up to 19,427 °C (35,000 °F), which is 4 times the temperature of the surface of the sun [57].

A common cause of fires for electrified trains is ignition of trash, components on the rail car, or debris that has fallen from the rail car or locomotive. These fuels are often ignited through electrical arcing from the electrification system for the train or from overheating mechanical components and they can range significantly in size and duration of burning. The most severe incidents related to the ignition of train components or trash involved electrical arcing to ignite rubber tires that are common to the transit vehicles in automated people mover systems. Rubber tired vehicles do not connect to the general rail system, which makes rubber tires as a fuel for a fire outside the scope of this work.

Additional severe scenarios involving fires from trash and debris include grease used to lubricate mechanical components. Deposition of grease onto trash or train system components mounted to the undercarriage is probable and this deposition effectively increases the fuel load for a potential fire that impinges on the undercarriage. Table 2-12 provides some typical HRR ranges expected for various fire scenarios and fuel sources to provide a reference for the HRRs cited in this section.

Table 2-12. Typical HRR for Various Fire Scenarios

Fuel Source	Typical Maximum HRR [kW(Btu/s)]
Suitcase filled with Clothing	20–120 (19–114)
Twin-Size Mattress	38–200 (36–190)
Standard Amtrak trash bag	150–250 (142–237)
Waste basket	5–350 (4.7–332)
Two Truck Tires [58]	878–964 (832–914)
Diesel Pool Fire (1 m^2)	1,400 (1,327)
Stack of Wood Pallets (1.2 m high)	3,700 (3,507)
King-Size Mattress	3,000–5,200 (2,843–4,929)
Magazine Rack loaded with Newspapers (15–90 kg)	3,000–8,000 (2,843–7,582)
Automobile	1,200–8,200 (1,138–7,772)
Electrical Cable Trays	3,200–10,800 (3,033–10,236)

2.10. Section Summary

The review of accident data revealed that there are a limited number of rail accidents involving fires. As a result, the accident review included U.S. as well as other international accident incidents. The incident survey and subsequent analysis of the collected data and details about the incidents revealed that typical severe fires to which passenger rail cars and locomotives were subjected in incidents that occurred in the U.S. and internationally involved ruptured fuel tanks, pool fires, trash and debris, and grease build-up on rail car components. These fires (particularly the fuel fires) will produce rapid increases in the exposure to the floor assembly, which may be faster and higher than the standard ASTM E119 exposure.

The duration of fire exposures determined through the incident survey for spilled fuel fires are consistent with the range of durations calculated and presented in Section 2.9, although many were extinguished by emergency personnel. A fire exposure duration

that is consistent with the current NFPA 130 requirements is the time required for full evacuation of all passengers from the train. From data in Table 2-11, the incident survey has shown that when no collision occurs prior to the fire, the time required for complete evacuation of above-ground trains is on the order of 10 minutes. The survey also showed that when a fire occurred simultaneously with a derailment or a collision for above-ground trains, or when a fire occurred in a subway tunnel, the time required to evacuate all personnel increased to be on the order of 60 minutes or even more if many passengers had to be extricated from the trains.

Based on the accident data review, the operating environment of the rail car will have an impact on both the severity and duration of the fire exposure. For example, rail cars that operate over vehicle grade crossings or with diesel powered locomotives will have potential for fuel spill fires that may last for long periods (possibly several hundred minutes as shown in Table 2-11). Currently in NFPA 130, the floor barrier exposure type and duration do not take the operating environment into consideration. Future work should develop an approach for determining the floor barrier exposure type and duration that considers the operating environment. Methods for predicting egress times from passenger rail cars should also be considering carry-on items (luggage, bikes, strollers, etc.), which may block or reduce the size of the egress paths. An engineering methodology for assessing the exposure and egress times would provide a consistent approach for determining the floor barrier requirements.

It is possible that the situations identified in this work (fuel spill fires) would result in a more rapid increase in exposure compared with the currently required ASTM E119 exposure curve. These exposures may impart more thermal energy into the rail car structure in the same amount of time as the standard exposure and result in a more compromised structure than the standard test indicates. It is also possible that a large source fire in a realistic fire scenario could result in ventilation-limited combustion due to the small clearance between the undercarriage and bottom of the rail car common for bi-level commuter trains, resulting in an increase in temperature that is less severe than the current standard exposure. This would essentially indicate that the current standard and test duration is adequate for these perceived severe situations. It is important to test these possibilities in large-scale experiments to determine the expected exposure temperatures for the exterior of rail cars to ensure people and property is adequately protected. The next tasks in this research will quantify the exposure to the undercar from plausible, realistic fires and compare these to furnace exposures in ASTM E119 and other fire resistance standards.

The exposure fires identified in this accident review may vary from a 100 kW (94.8 Btu/s) to over 50 MW (47,390 Btu/s). Both modeling and testing will be conducted in future work to quantify the exposures from plausible, realistic fire exposures. The number of laboratories that are capable of conducting a test with a HRR above 20 MW is very low and such an experiment would be very expensive and deriving meaningful data from such an experiment would be difficult. It is recommended that experiments be conducted with several scaled-down fires, the sizes of which may be determined from the capacity of the laboratory (typically 3 to 5 MW [2,843–4,739 Btu/s]) while keeping in mind the ranges of HRRPUA for the fuel sources provided in Section 2.9. It is expected that the gas temperatures in the fire plume that impinges on the undercarriage will be unaffected by scaling down the fire sources in these experiments. These recommended

scenarios are provided in Table 2-13. It is recommended that a single, representative rail car mockup be fabricated for these experiments with a minimum of a floor and two vertical walls to simulate impingement of flame to the undercarriage. Fire tests should be designed to last for 15–30 minutes and include the growth, steady-state, and decay stages of the fire. Details of the fire including physical size and HRR will be determined in the testing and modeling activities. The data from the testing is expected to provide the input data necessary for future modeling efforts. Data collected in these experiments will validate a modeling approach that will be used to simulate various larger fire scenarios and various rail car designs that cannot be tested experimentally.

Table 2-13. Fire Scenario Tests Recommended by JENSEN HUGHES

Scenario	Scenario Description
1	Trash typical of rail car distributed under car (paper- and polymer-based)
2	Trash typical of rail car distributed under car with cables attached to the floor
3	Trash typical of rail car distributed under car with cables attached to the floor and grease coating on the floor
4	Diesel fuel pool fire under car
5	Gasoline fuel pool fire under car

3. Fire Testing to Quantify the Undercar Exposure onto a Rail Car Floor

It has been suggested that the furnace exposure of the ASTM E119 fire test may not be an accurate representation of exposures typical of rail car fires (Section 2). Severe fire incidents which involve ruptured fuel tanks and a resulting pool fire will produce exposures of greater intensity and grow more rapidly than the ASTM E119 exposure in the initial 15 to 30 minutes. While fuel fires represent a significant hazard scenario, many fire incidents of lesser severity, involving trash and debris, cables, and grease covering rail car components, were found to have occurred (Section 2).

In addition to the fuels involved, the configuration of the fire relative to the rail car is an important factor in the overall exposure. Field surveys of passenger rail cars identified that the separation distance between a rail car floor and the tracks could vary from 45.7 cm (18 in.) to 121.9 cm (48 in.). Furthermore, some rail cars contained equipment boxes along the sides of the cars, forming a channel along the center. It is expected that the different configurations will have a direct impact on the thermal exposures produced by a fire.

It is desired to understand the impact of plausible, realistic undercar fires on a rail car floor. The first step in this endeavor is to understand the spatial characteristics and intensity of the heat flux boundary condition that may evolve on the underside of a rail car due to localized fires. This was achieved in the present work by conducting a series of fire tests in which a rail car floor mockup was subjected to a specified fire, in various configurations. In studying this phenomenon experimentally, a valuable set of data was generated, which was used for validation of fire models for this scenario. The present work outlines the requirements, design, and methodology used for this test series. Experimental results are presented, including observations and other details pertinent to the fire dynamics and exposure condition.

3.1. Objectives

The main objective of the work presented in this section was to investigate the relationship between fires that develop on the underside of a rail car and the resulting thermal exposure boundary condition that evolves on the rail car floor. This was achieved by conducting a series of fire tests using various configurations where temperature and heat flux were measured. The results from this test series provide heat transfer data that can be used to validate fire models.

3.2. Methodology

The apparatus used for this test series consisted of a rail car floor mockup exposed to a fire from below that included instrumentation for the measurement of gas temperatures and heat flux to the mockup. The test space was comprised of a 3.05 m (10 ft.) by 3.05 m (10 ft.) area located below an extraction hood located 2.44 m (8 ft.) above the ground. Given the size of the test space, the overall length of the apparatus was constrained to 3.05 m (10 ft.). Due to the propane gas supply system design, the fire HRR could be no greater than 300 kW. Given these physical and fire size constraints, the following section details the design of the experiment and its relationship to fires under actual rail cars.

3.2.1. Design of Experiment

Two test series were conducted in the present work including tests with the cement board and tests with a steel plate. The following sections describe the apparatus along with details of diesel and trash fires used for designing these experiments.

3.2.1.1. Apparatus

The apparatus shown in Figure 3-1 consisted of a 1.22 m (4 ft.) by 3.05 m (10 ft.) mockup of a rail car floor with baffles along the longitudinal sides to represent the sides of the rail car (preventing flames from wrapping around to the top side of the mockup). The mockup was constructed of 22 gauge (ga) (0.79 mm, 0.03125 in.) stainless steel with both sides coated in high-temperature, high emissivity paint (TREMCLAD® Rust-Oleum high heat matte black spray paint). The reflective properties of this surface have been characterized by emissivity in previous work as $\varepsilon = 0.95 \pm 0.01$ which also demonstrated the use of an infrared (IR) camera and heat transfer model to quantify the heat flux to the surface from a fire exposure [59]. The steel was purchased in a sheet size of 1.22 m (4 ft.) by 1.83 m (6 ft.), and the paint applied in four even coats, changing the direction of application by 90 degrees between coats.

A frame was constructed using 16 ga (1.59 mm, 0.0625 in.) steel studs, from which the steel sheet was suspended using 12 screws, and separated by 1.91 cm (0.75 in.) strips of ceramic fiber insulation. Since the test space could accommodate a total apparatus length of 10 ft. (3.05 m), the mockup was extended by 0.61 m (2 ft.) on both ends using 1.59 cm (0.625 in.) USG Sheetrock® Firecode® gypsum board. The side baffles were also constructed using 1.59 cm (0.625 in.) Firecode® gypsum board and were 0.61 m (2 ft) tall.

A propane sand burner was positioned below the mockup and aligned in the center as seen in Figure 3-1. Rationale for the burner size and fire HRR are provided in the following section. A floor was constructed around the sand burner such that the top of the burner was flush with the floor surface located 20.3 cm (8 in.) above the ground. As noted in Figure 3-1, the mockup was positioned above the floor at the heights dictated by the configuration of interest. Temperature of the steel sheet was measured using an IR camera, and gas temperatures below the sheet were measured at several locations using thermocouples. Instrumentation details are provided in Appendix A.

A second panel was constructed in which 1.59 cm (0.625 in.) USG Durock® cement board was used in place of the steel sheet, and water-cooled Schmidt-Boelter heat flux gauges were installed in three locations [60]. Tests were conducted first using the cement board mockup to establish the procedure and obtain a preliminary measure of heat flux. Subsequently, tests were conducted with the steel mockup to determine the two-dimensional exposure to the mockup.
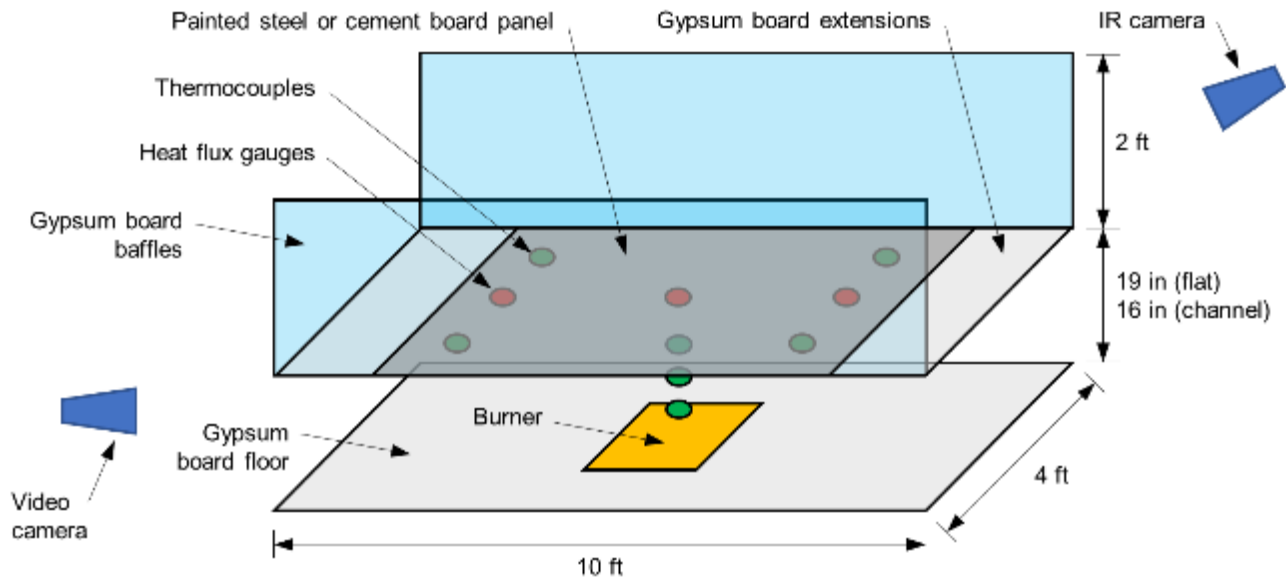
Figure 3-1. Schematic of the Test Apparatus

The mockup depicted in Figure 3-1 represents a scaled-down rail car. A full-scale rail car has a width of 3.10 m (10.17 ft.); reducing this dimension to 1.22 m (4 ft.) represents a 39.3% reduction in length scale. This dimensional scaling factor was applied to other geometric features of the rail car mockup.

A survey of incidents and site visits to two railyard facilities identified two configurations of interest. The first configuration was, representative of bi-level and single level passenger cars that had a flat bottom located 1.22 m (48 in.) above the ground, typical of equipment operated in passenger service on the northeast corridor. For this configuration, denoted "flat" in the present work, the test panel was positioned 48.3 cm (19 in.) above the floor based on the 39.3% scale reduction.

The second configuration identified in site visits featured a channel along the longitudinal dimension of the rail car created by undercarriage components which was common to most single level rail cars. The bottom of the rail car was found to be 1.02 m (40 in.) above the ground in this channel configuration, with the bottom of the undercarriage components being 45.7 cm (18 in.) above the ground. The width of the channel was 81.3 cm (32 in.), and a gap measuring 10.2 cm (4 in.) was present between the bottom of the rail car and the top of the undercarriage components. In the present work, this "channel" configuration was formed by placing rectangular obstructions constructed of 1.59 cm (0.625 in.) Firecode® gypsum board along the longitudinal direction of the apparatus. Based on the 39.3% scale reduction, the test panel was positioned 40.6 cm (16 in.) above the floor, the channel width was 31.8 cm (12.5 in.), and the tops of the obstructions were located 3.8 cm (1.5 in.) below the bottom of the test panel.

Figure 3-2 (side view) and Figure 3-3 (end view) depict the geometry of the test apparatus. In the figures, the channel configuration is shown; the flat configuration was identical except that the obstructions were not present, and the test panel was located 7.6 cm (3 in) higher.
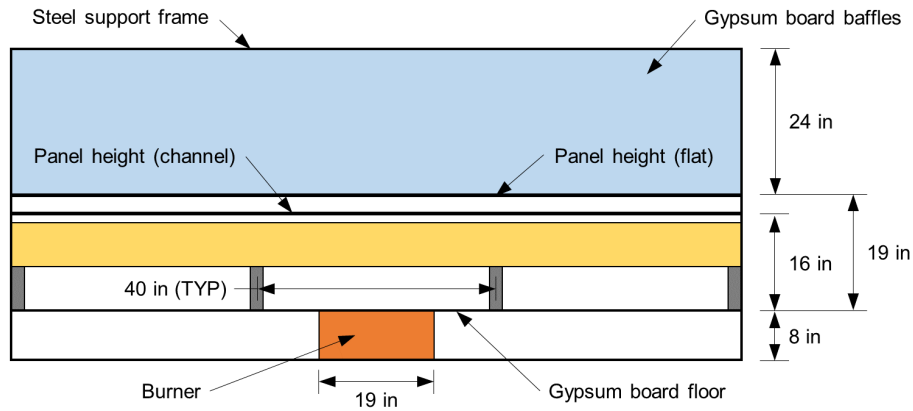
Figure 3-2. Schematic of the Test Apparatus—Side View
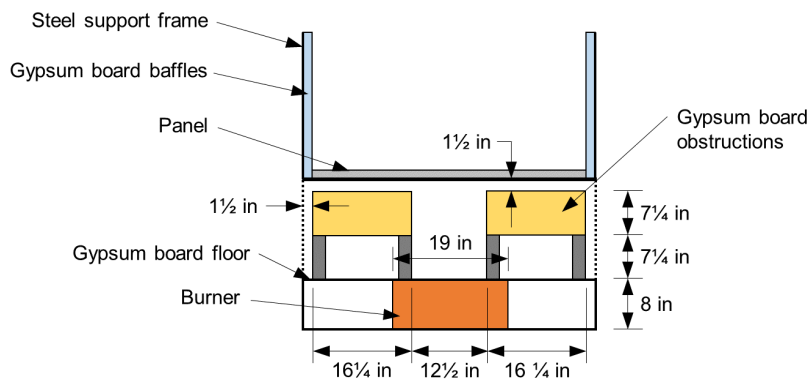
Figure 3-3. Schematic of the Test Apparatus—End View (Channel Configuration)

3.2.1.2. Fires

Two fires were conducted in this test series, being representative of a diesel pool and a pile of trash. The pool fire might be expected to evolve as a result of a fuel spill, while the trash fire might occur due to a buildup of trash on the rail tracks. A gas burner measuring 48.3 cm (19 in.) by 48.3 cm (19 in.) was used in the present work to reproduce HRRs which would be representative of such fires. The test detail design process is outlined below.

Considering the length scale of the apparatus, the burner represents a full-scale fire area of 1.23 m (48.3 in.) by 1.23 m (48.3 in.) or an effective fire diameter of 1.38 m (54.5 in.). Given this information and the type of fuel involved, the theoretical HRR of the pool fire was calculated using a pool fire model [61]:

$$\dot{Q} = \Delta h_c \dot{m}''_\infty \left(1 - e^{-k\beta D}\right) A \qquad (3\text{-}1)$$

where A is the area, D is the diameter, and the other design parameters are provided in Table 3-1 for each of the three fuels considered.

Table 3-1: Full-Scale Design Parameters for Fire Size Calculations

Fire Type	Diesel [61]	Gasoline [61]	Trash
Density, ρ (kg·m^{-3})	970	740	44.2
Effective heat of combustion, Δh_c (MJ·kg^{-1})	39.7	43.7	23.1
Asymptotic mass burning rate, $\dot{m}''_\infty$ (g·m^{-2}·s^{-1})	35	55	14
Empirical constant, $k\beta$ (m^{-1})	1.7	2.1	1.0
Theoretical heat release rate, $\dot{Q}$ (MW)	1.89	3.42	0.37

A pool fire model was also adopted for the trash fire, which may be suitably approximated if the design parameters are selected with scrutiny. As shown by Lee, the HRR of a trash fire can be expected to increase with the effective diameter and decrease with tighter packing densities [61]; a relationship is given in Figure 3-4. Packing density was calculated based on the assumption that the trash composition will be well represented by a combination of newsprint (miscellaneous paper products), polyethylene (plastic drink bottles), and expanded polystyrene (food containers). This design consideration was based on previous work by Nagy et al., in which representative piles of mixed materials in a recycling facility were assembled using a combination of newsprint, corrugated cardboard, polyethylene, and expanded polystyrene [62]. In the present work, the composition of the trash pile was taken to be 70 percent newsprint, 15 percent polyethylene, and 15 percent polystyrene by volume. The average density of the pile was calculated to be 49.1 kg·m^{-3} (3.1 lb·ft^{-3}) based on composition:

- Single sheets of newsprint weighing 29 g (1.02 oz.) crumpled into balls of 10.2 cm (4 in.) diameter, resulting in a density of 55.5 kg·m^3 (3.5 lb·ft^{-3})

- Polyethylene soda bottles of 500 mL (30.5 in^3) capacity, weighing 26 g (0.92 oz.) with lids removed, resulting in a density of 52.0 kg·m^{-3} (3.2 lb·ft^{-3})

- Pieces of expanded polystyrene with nominal density of 16.0 kg·m^{-3} (1.0 lb·ft^{-3})

Assuming that conservatively 10 percent of the pile will be air, the loose-packed density of the trash pile will be 44.2 kg·m^{-3} (2.76 lb·ft^{-3}). Based on this packing density and the effective fire diameter, the maximum theoretical HRR is calculated to be 0.37 MW. This number is consistent with the peak HRRs reported by the National Institute of Standards and Technology (NIST) from fire tests of "standard" Amtrak trash bags filled with crumpled newspapers (0.20 MW), as well as from fire tests of 114 L (30 gal) plastic trash containers filled with various construction materials (0.45 MW) [61]. Notably, the polymer materials contribute significantly to the HRR calculated here.

In the present work, the fire size is intended to be constant, therefore, additional design parameters are not required for the trash fire beyond the maximum theoretical HRR. However, future work may necessitate the calculation of time-varying HRRs; therefore, the remaining design parameters were also calculated. Effective heat of combustion of the trash pile was calculated to be 23.1 MJ·kg^{-1} based on composition:

- Newsprint is approximated to be equivalent to cellulose (17.5 MJ·kg^{-1}) [63]

- Polystyrene and polyethylene are the base polymers (43.7 MJ·kg^{-1} and 44.6 MJ·kg^{-1}) [64]

Taking the asymptotic mass burning rate $\dot{m}''_\infty$ to be 14 g·m^{-2}·s^{-1}, and considering the maximum theoretical HRR $\dot{Q}$ calculated above, the empirical constant $k\beta$ was calculated to be 1.0 [63].
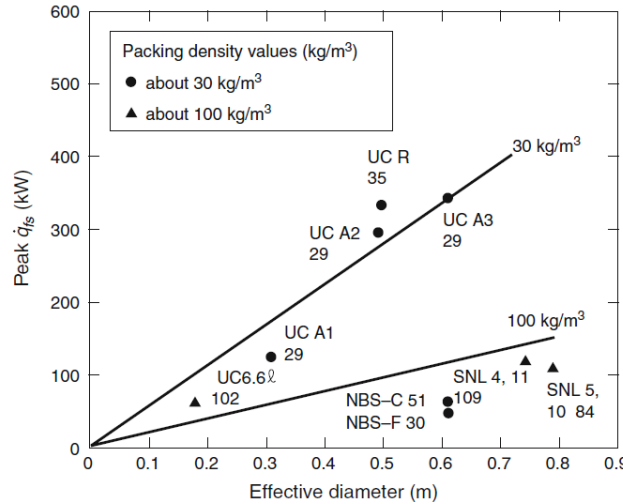
Figure 3-4: Peak Heat Release Rates of Trash Bag Fires (Image Reproduced from the SFPE Handbook of Fire Protection Engineering [61])

With the full-scale maximum theoretical HRRs of the design fires calculated, the next step was to calculate the HRRs of the design fires at the mockup scale used in the testing. This was achieved using the following scaling correlation, based on Froude scaling [65]:

$$\frac{\dot{Q}_1}{\dot{Q}_2} = \left(\frac{L_1}{L_2}\right)^{\frac{5}{2}}$$

(3-2)

where $\dot{Q}$ is the HRR, L is the length dimension, subscript 2 refers to full-scale parameters, and subscript 1 refers to reduced-scale parameters. Given that L_1/L_2 is 39.3 percent, the reduced-scale HRR is calculated to be 9.7 percent of the full-scale HRR. Thus, the reduced-scale diesel, gasoline, and trash fire HRRs are 184 kW, 332 kW, and 35 kW, respectively. Given the design constraint that the fire size must be less than 300 kW, it was decided that the gasoline fire would be omitted in the present work. Therefore, fires representing diesel and trash fires were used in this test series by prescribing a mass flow rate of propane to the sand burner such that fire sizes of 184 kW and 35 kW were achieved.

The impact of the fire on the mockup can be visualized by considering the theoretical flame height of these fires, and in the event that the fire plume is predicted to impinge upon the underside of the panel, the flame extensions. The following correlation based on Froude scaling was used to calculate the theoretical flame heights (L) based on diameter of fire (D) and HRR ($\dot{Q}$) of the fire plumes [66]:

$$L = -1.02D + 0.235\dot{Q}$$

(3-3)

The flame height for the trash fire was predicted to be 16.7 in., which results in a fire that just barely impinges upon the rail car floor in the channel configuration and does not reach the floor in the flat configuration. For the diesel fire, the flame height was predicted to be 52.6 in., resulting in flame extensions of approximately 32 in. from the fire centerline (refer to Drysdale for details of flame extension approximation [63]). Given that the distance from the fire centerline to the side of the rail car mockup was 24 in, it was predicted that flames would extend beyond the sides of the mockup and upwards along the vertical baffles.

3.2.2. Measurements and Instrumentation

For the test with steel as the floor material, temperature of the unexposed side of the steel panel was measured using a FLIR T440 IR camera [67]. The camera was positioned 180 in. from the center of the panel, at an angle sufficient to see the entire steel surface which represented the rail car floor in the mockup. Note that due to the presence of the steel frame on the unexposed side of the steel, the effective viewable portion of the panel was reduced to an area 69 in. long by 45 in. wide. The emissivity of the panel was taken to be 0.95 and ambient conditions at the time of the test were input to the camera software. This is necessary to ensure that the camera uses an appropriate value for atmospheric absorption. Post-test analysis of the temperature measurements utilized an inverse heat transfer model to calculate gauge heat flux to the exposed side of the steel panel, as described in Section 3.2.3 below.

For the cement board tests, gauge heat flux to the exposed side of the panel was measured at three locations using water-cooled Schmidt-Boelter heat flux gauges; water at 40 °C (104 °F) was used to inhibit soot collection on the gauge surfaces. Holes were drilled into the cement board and the gauges were tightly fit into the holes from the unexposed side, such that the exposed surface of the gauges were flush with the exposed side of the cement board panel. These measurements of heat flux were used to establish a baseline characterization of the exposure condition to which the steel panel results can be compared.

For tests with both the steel plate and cement board, gas temperatures were measured in order to provide a means of validation for computer models of this scenario. Thermocouples were positioned on the underside of the panel, approximately 1 in. below the exposed side, at various locations. These thermocouples were 22 ga (0.645 mm, 0.0254 in) Omega K-type with glass fiber sheathing and bead-welded exposed hot junctions [68]. The manufacturer reports the response time[1] of these thermocouples to be 2 seconds [69]. In addition, three thermocouples were positioned over the burner to measure the temperature of the fire plume. Since temperatures approaching 1,000 °C were expected in this region, more robust thermocouples were used (3.18 mm (0.125 in.) K-type Inconel-sheathed). While these instruments are better suited to the high temperature region above the burner, the trade-off is a longer response time of 10 seconds [69]. Due to the steady-state nature of these fire tests, the longer response was sufficient to measure the thermal environment. Additional details, including the exact locations for each sensor, are provided in Appendix A. For reference, the

---

[1] Response time is defined as the time required for the sensor output to reach 63.2% of a step-change input.

orientation of the apparatus relative to the IR and video cameras is depicted in Figure 3-5.
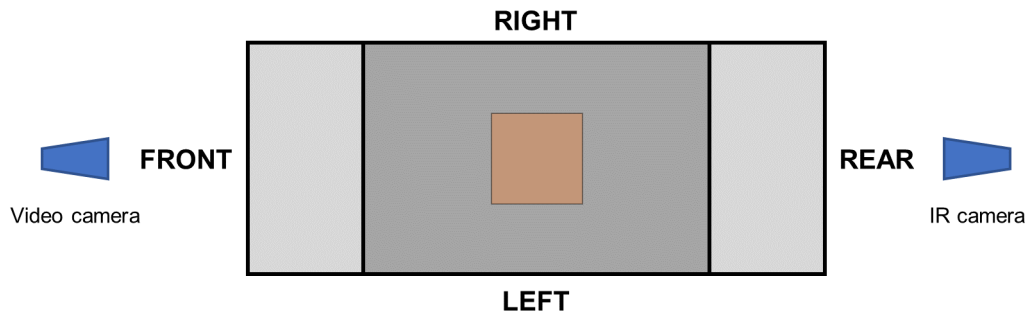
Figure 3-5. Schematic of the Test Apparatus—Top View, Orientation Reference

3.2.3. Heat Flux Calculation

Heat flux to the steel panel was calculated from IR camera measurements of the temperature of the steel panel using an inverse heat transfer model. This model has been used previously for this type of analysis, and details of the model formulation and application are provided by Rippe et al. [59].

An example of a practical application of the model is provided here. Figure 3-6 shows an IR camera image taken from a sample fire exposure of the apparatus in the flat configuration at a particular time. Prior to running the heat transfer model, the four corners of the steel panel were identified to transform the image such that the size of the region of interest was equal to the actual size of the panel (45 in. wide by 69 in. tall). A representation of this transformation is depicted in Figure 3-7.
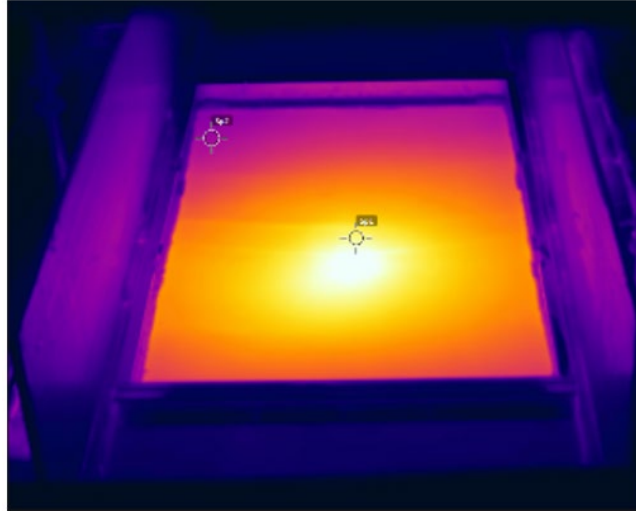
Figure 3-6: Original IR Camera Image
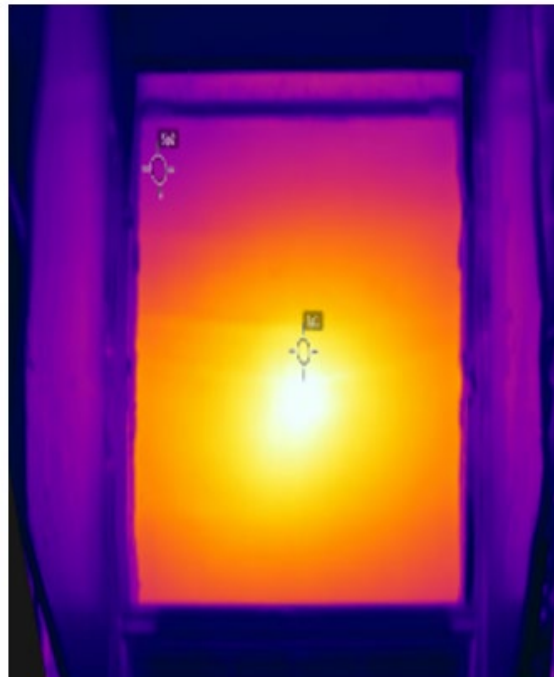
Figure 3-7: Transformed IR Camera Image

Once transformed, the heat transfer model calculated the gauge heat flux to the exposed side of the panel using a global energy balance, as follows:

$$\dot{q}_g'' = \frac{\dot{q}_{rad}''}{\varepsilon} + \dot{q}_{conv}'' + \sigma\left(T^4 - T_g^4\right) + h_c\left(T - T_g\right) \tag{3-4}$$

where $\dot{q}_{rad}''$ is the net radiative heat flux to the surface, $\dot{q}_{conv}''$ is the convective heat flux to the surface, ε is the emissivity of the surface, σ is the Stefan-Boltzmann constant, h_c is the convective heat transfer coefficient on the exposed surface, T is the temperature of the surface, and T_g is the temperature of the gauge. Gauge heat flux calculated in this

manner is representative of the heat flux that would be measured by a water-cooled heat flux gauge that is maintained at temperature T_g.

Using the field measurements of temperature, gauge heat flux was calculated by the model over the two-dimensional area of the steel panel. For the example presented here, Figure 3-8 contains the transformed temperature gradient over the steel panel, and Figure 3-9 includes the derived gauge heat flux. Contour plots were created with the "contour" function in MATLAB® R2016b, with 15 contour levels. This quantified heat flux characterizes the two-dimensional exposure gradient from the fire to the rail car floor mockup. In the present work, this heat transfer analysis was conducted for each of the steel tests, using a time series of IR images as input, and calculating the exposure gradient over time.
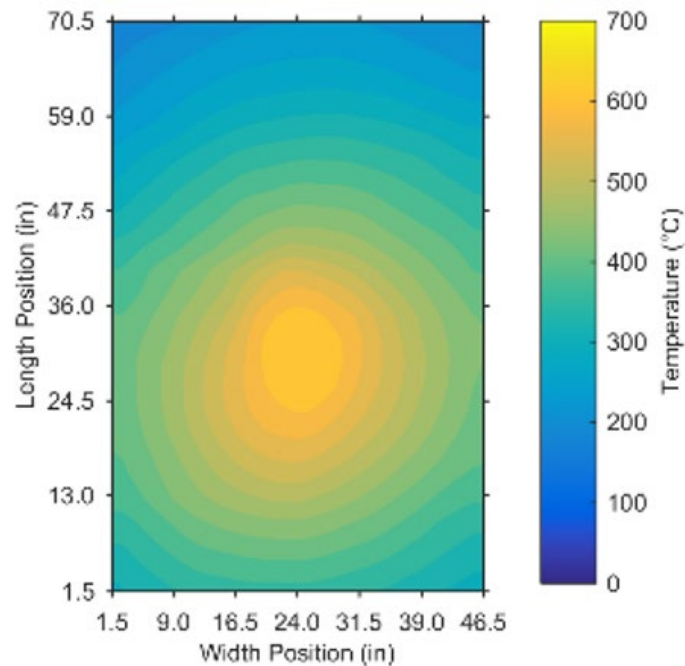
Figure 3-8: Temperature of the Steel Panel Corresponding to the Sample IR Image
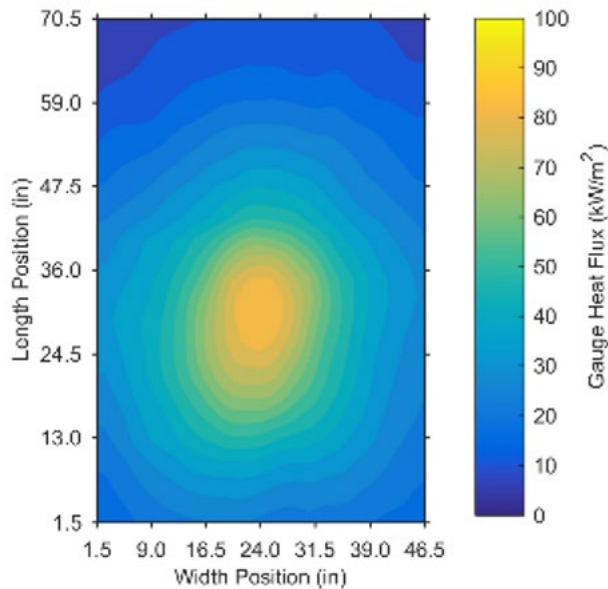
Figure 3-9: Gauge Heat Flux to the Steel Panel Corresponding to the Sample IR Image

3.2.4. Test Methodology

For each series, a total of four tests were conducted using two configurations (flat and channel) and the two fire HRRs (representing diesel and trash fires). For both test series, a video camera was located at the front of the mockup to observe the fire development and impingement on the underside of the panel. For the steel series, an IR camera was located above the rear of the mockup, capturing the unexposed side of the steel panel in frame. All other transducers were connected to a National Instruments data acquisition system and their signals were recorded in real time at 1 Hz [70]. Tests were conducted in the following manner:

- The extraction fan was turned on and set to 30 Hz (2,265 L·s^{-1}, 4,800 ft^3·min^{-1}) for the trash fire tests, and 60 Hz (4,436 L·s^{-1}, 9,400 ft^3·min^{-1}) for the diesel fire tests

- The data acquisition system, video camera, and IR camera were started in sequence

- The propane burner mass flow controller was set to achieve the target HRR

- The fire was ignited by placing a pilot flame over the burner and starting the flow of fuel

- The fire burned for a minimum of 10 minutes, after which time the gas burner was shut off

- Data were recorded for a minimum of 20 minutes following burner shut-off

The following section presents the results from this test series and characterization of the two-dimensional exposure gradient due to the undercar fires.

3.3. Results

For each configuration and fire type, the time series of transducer measurements and two-dimensional contour plots of temperature and gauge heat flux at a time of interest are provided in Appendix B through Appendix E. Additionally, a set of results is presented and discussed in the subsequent sections.

Figure 3-10 depicts the steel test for the channel/trash configuration. The overhead door is visible at the rear of the apparatus, as well as a piece of gypsum board located 1.83 m (6 ft.) behind the rear of the apparatus, which provided a flat background for the video camera (which was positioned at the front of the apparatus).

Figure 3-10: Steel Test Series, Trash Fire, Channel Configuration.

Figure 3-11 shows the steel test for the channel/diesel configuration. Flame extensions are visible on the left side of the apparatus (right in the image below), which is consistent with the prediction of flame extensions calculated in Section 3.2.1.2. The side baffles prevented flames from wrapping around to the unexposed side of the panel, and flames did not extend to the ends of the panel in the longitudinal direction. Combustion products were drawn up from the sides of the panel and into the overhead exhaust fan.

Figure 3-11: Steel Test Series, Diesel Fire, Channel Configuration.

3.3.1. Results – Flat Configuration/Diesel Fire

For the flat/diesel configuration, Figure 3-12 contains a plot of gas temperatures where it is seen that temperatures reached approximately 600 °C (1,112 °F) above the fire plume in both the cement board and steel tests during the first 6 minutes. The temperature of the steel panel directly above the fire plume was consistent with the gas temperature.

For the cement board test, at approximately 6 minutes after ignition an overhead door was opened to vent accumulating gases from the test space. This caused a shift in the fire dynamics, resulting in an apparent increase in plume temperature to approximately 800 °C (1,472 °F); it is noted that this shift may simply be an artifact of the position of the fire plume relative to the point-source sensor location. This is a high gradient area so small shifts in the flame location can result in significant differences in the measurements. The overhead door was left open for all subsequent tests, so the phenomenon was not reproduced.

Gauge heat flux at the center of the panel was computed to be approximately 75 kW·m^{-2} in the steel test, and measured to be approximately 80 kW·m^{-2} in the cement board test in the first 6 minutes as seen in Figure 3-12. The heat flux in the cement board tests should be slightly greater than that in the steel tests due to the cement board being more insulating. However, for this experimental setup the gases readily exhaust around the sides of the panel, and the centerline heat flux was consistent for both the steel and cement board test series.

At a position 61.0 cm (2 ft.) away from the center of the panel in the length dimension, heat flux was computed to be approximately 30 kW·m^{-2} in the steel test, and measured to be approximately 20 kW·m^{-2} in the cement board test (in the first 6 minutes). This is a clear indication that the exposure condition was significantly nonuniform over the floor mockup, as can be verified in the derived contours (Appendix B).

47
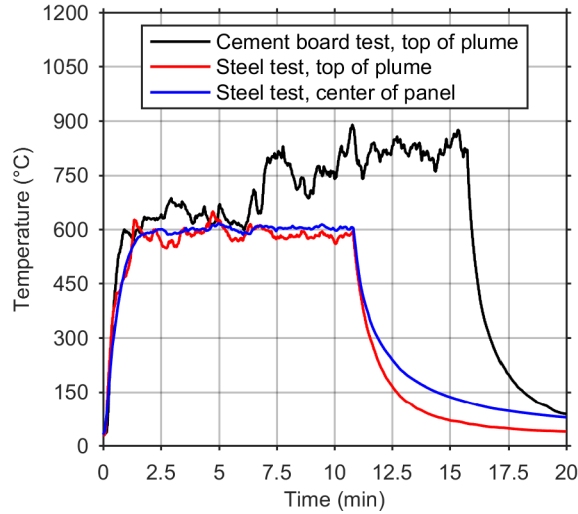
Figure 3-12: Temperature Over Time (Flat/Diesel Configuration)
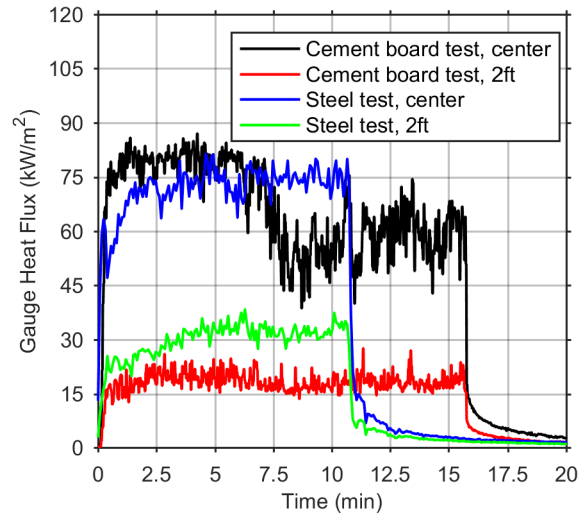
Figure 3-13: Gauge Heat Flux Over Time (Flat/Diesel Configuration)

3.3.2. Results – Channel Configuration/Diesel Fire

For the channel/diesel configuration, gas temperatures reached as high as 1,000 °C (1,832 °F) in the fire plume for both the steel test and the cement board test, as shown in Figure 3-14. There was a significant discrepancy of approximately 300 °C (572 °F) between the plume temperature and the temperature of the steel panel above the plume. It is hypothesized that the channel configuration sufficiently impacted the flow dynamics so as to draw a significant portion of the hot gases away from the fire along the channel. This is consistent with gas temperature measurements between the top of the obstructions and the steel panel, which also reached maximum values of approximately 650 °C (1,202 °F). The temperature gradients, in this case, further support this hypothesis (see Appendix C).

48

Heat flux to the center of the panel reached peak values of approximately 130 kW·m^{-2} in the cement board test, and was approximately 100 kW·m^{-2} in the steel test, as shown in Figure 3-15. Heat flux was greater at the 61.0 cm (2 ft) location in the steel tests than in the cement board tests, by approximately 20 kW·m^{-2}. The difference in the heat flux in these two tests was likely due to the fire dynamics established in the test and shows the potential variability that may exist in this configuration.
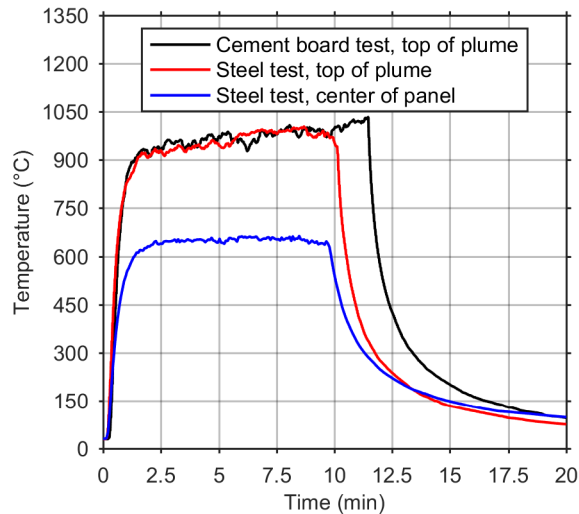
Figure 3-14: Temperature Over Time (Channel/Diesel Configuration)
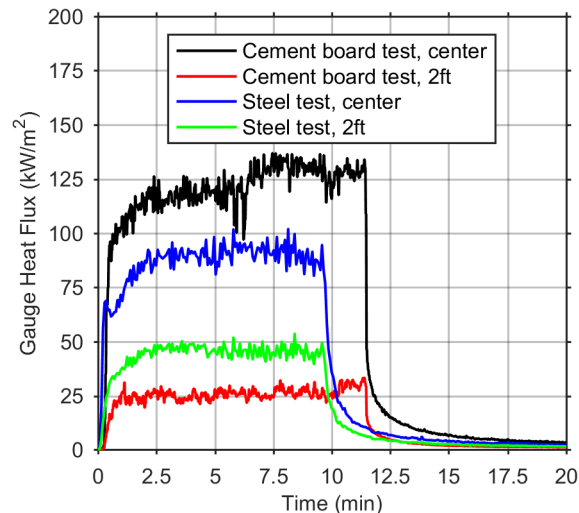
Figure 3-15: Gauge Heat Flux Over Time (Channel/Diesel Configuration)

3.3.3. Results – Flat Configuration/Trash Fire

For the flat/trash configuration, gas temperatures reached a moderate temperature of approximately 200 °C (392 °F) above the fire plume, as shown in Figure 3-16. Temperatures were measured to be approximately 50 °C (122 °F) less in the cement board test than in the steel test. It is possible that this could be explained by under-controlled ventilation conditions, as was the case for the flat configuration diesel fire.

49

Since thermocouples provide a point-source measurement, if ventilation caused the fire shape to alter (e.g., leaning slightly away from center), then the resulting temperature measurement would be impacted. It is reasoned that this discrepancy could be identified (and minimized) by repeat testing.

Contours (see Appendix D) show that the temperature of the steel panel and gauge heat flux were at a maximum in the approximate center of the panel in the trash fire test, while the maximum was located at the rear end of the panel in the diesel test. This is attributed to changing the exhaust fan conditions between the two tests.

Heat flux to the center of the steel panel was measured to be approximately 15 kW·m^{-2} in the cement board test and determined to be the same in the steel test, as shown in Figure 3-16. This is an indication that the steel and cement board tests were quite similar for the flat/trash fires. At the 61.0 cm (2 ft.) location, heat flux was similar (within 1 kW·m^{-2}) when comparing the steel test results to those with the cement board.
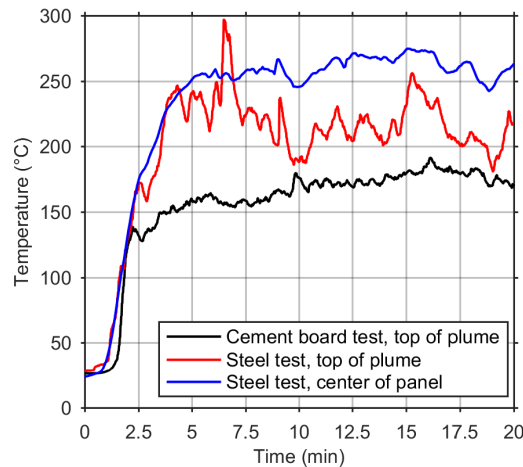
Figure 3-16: Temperature Over Time (Flat/Trash Configuration)
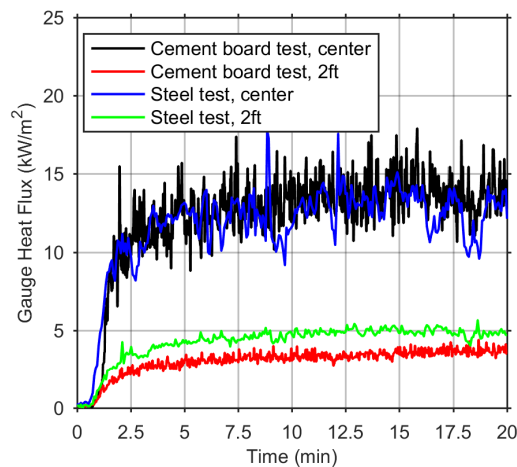
Figure 3-17: Gauge Heat Flux Over Time (Flat/Trash Configuration)

3.3.4. Results – Channel Configuration/Trash Fire

For the channel/trash configuration, gas temperatures were consistent between the steel and cement board tests, reaching a maximum of approximately 400 °C (752 °F) after 15 minutes of exposure, as shown in Figure 3-18. The temperatures did not level out, as was the case in the flat configuration tests. It is hypothesized that the obstructions slowly absorbed heat from the fire gases and panel re-radiation occurred. The obstructions were constructed of gypsum board which has a very low thermal diffusivity, meaning that the rate of heat transfer through the material was relatively slow. As time progressed, the obstructions absorbed more thermal energy, the temperature of obstruction surfaces increased, and radiation to the panel increased. The consequence of this was a gradual increase in gas temperature and heat flux to the panel.

Figure 3-19 shows that heat flux reached a maximum of 25 kW·m^{-2} in the center of the panel in the steel test, and approximately 18 kW·m^{-2} in the cement board test. In addition, heat flux at the 61.0 cm (2 ft.) location was greater in the steel test than in the cement board test. These differences are attributed to the location of measurements being in a region in which very steep thermal gradients were present.
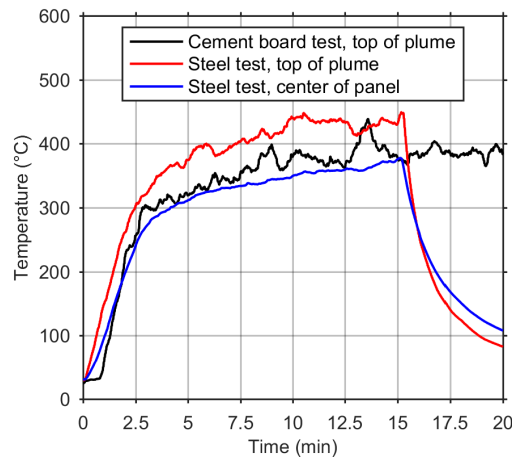
Figure 3-18: Temperature Over Time (Channel/Trash Configuration)

51
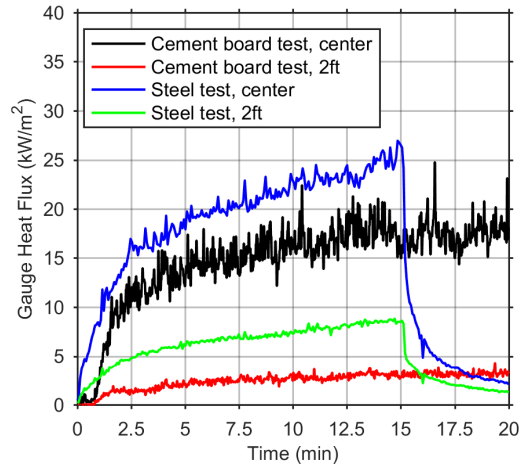
Figure 3-19: Gauge Heat Flux Over Time (Channel/Trash Configuration)

3.4. Section Summary

A series of tests were conducted in which a rail car floor mockup was exposed to realistic undercar fires. A methodology was established for estimation of the sizes of the fires, which were then implemented using a propane gas sand burner. Instrumentation was included in the experiments to obtain data for validating fire models, including gas temperatures, point heat flux measurements, and two-dimensional heat flux distributions. Comparing the data, tests without obstructions were more reproducible than the tests with obstructions. The tests with the obstructions resulted in higher heat flux due to channeling the flames between the obstructions, resulting in longer flame extensions and thicker flames. The two-dimensional heat flux maps provided additional data that will be useful for validating models for these scenarios where there are larger gradients in the heat flux due to complex flows that develop with the impinging fire and obstructions.

It was found that the exposure to rail car floor was predominantly nonuniform in nature, as should be expected in any realistic fire exposure. This type of exposure is distinct from that of a furnace test, and future work will assess the impact of this difference on the floor fire resistance. A robust set of data was collected, which will be used for validation of models of this fire scenario.

4. Simulating Undercar Fire Exposure Tests Using Fire Dynamics Simulator

The review of accident data demonstrated that a wide range of fire incidents from trash fires to large fuel spill fires are possible exposure fires underneath a rail car. In addition, surveys of rail cars across the United States highlighted the differences in the undercar geometries and distances between the floor assembly and the track. All these factors result in a wide range of possible exposures, and it is difficult to determine which exposures and rail car geometries result in the worst exposures. As a result, CFD fire modeling is a cost effective way to quantify these fire exposures and demonstrate which scenarios would result in the most severe exposures. They would also provide the temporal and spatial varying data required to predict the thermal response of floor assemblies when exposed to realistic fires.

FDS, Version 6.5.2 was selected for predicting the thermal exposures from external fires located beneath the rail car onto the floor assembly [71]. Though FDS has an extensive verification and validation data suite, it had not been validated for predicting thermal exposures for fires impinging on the underside of horizontal surfaces. Specifically, no validation had been performed on the flame behavior and heat transfer for a fire impinging onto a horizontal surface at the offset distances that would be representative for this application. As a result, FDS was used to predict the fire dynamics and thermal exposures measured in the testing described in Section 3. Following this validation, the FDS model could be used to predict the thermal exposure for larger realistic fire exposures for other aspects of this research.

4.1. Background

Current standards for addressing the fire resistance of rail car floor systems are published in 49 CFR Part 238 and the National Fire Protection Association (NFPA) 130, *Fixed Guideway Transit and Passenger Rail Systems* for the U.S., as well as EN 45545-3:2013 for Europe [72]. In the U.S., assemblies are generally tested according to NFPA 130 using ASTM E119 while in Europe, EN 45545-3 requires assemblies to be tested according to EN 1364-2 (which references EN 1363-1 [75]) [73] [74]. For all standards, the fire resistance test is conducted to ensure that, if there is a fire in the undercar region, the floor maintains structural integrity and does not allow passage of flames for a period sufficient for passengers to egress the rail car. In NFPA 130, this is evaluated based on an ASTM E119 fire resistance test with a duration of twice the time for the train to stop and egress passengers, or 30 minutes for non-AGT vehicles, whichever is greater. The ASTM E119 time-temperature exposure furnace curve is provided in Figure 4-1.
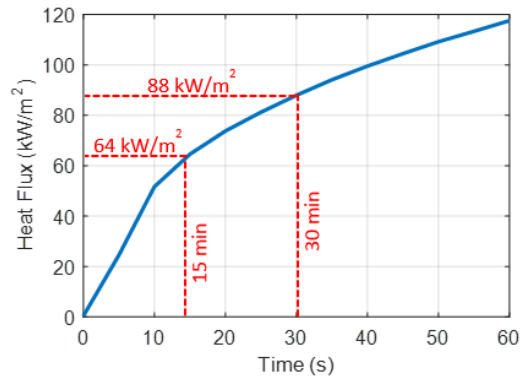
Figure 4-1. Blackbody Heat Flux for Furnace Time-Temperature Curve Specified in 49 CFR Part 238 (Reference ASTM E119)

It has been suggested in Section 2 that the furnace exposure of the ASTM E119 fire test may not be a good representation of exposures typical of rail car fires. Severe fire incidents, which involve ruptured fuel tanks and a resulting pool fire, may produce exposures of greater intensity and grow more rapidly than the ASTM E119 exposure in the initial 30 minutes. Many fire incidents of lesser severity, involving trash and debris, cables, and grease covering rail car components, were found to have occurred as well. The slow initial growth of this prescriptive fire curve can be non-conservative compared to other real fire scenarios with flames in direct contact with the surface. Due to the limited distance between the track and rail car, common fire scenarios for this region would involve a fire on the track impinging onto the underside of the flooring system.

4.2. Undercar Exposure Testing

To investigate the relationship between fires that develop on the underside of a rail car and the thermal exposure boundary conditions that evolve on the rail car, a series of tests were conducted at the JENSEN HUGHES fire laboratory. The fire tests involved two different rail car mockup configurations and two representative fires.

4.2.1. Testing Apparatus

In the tests, a mockup was designed to represent a scaled-down rail car. A schematic of the test apparatus is shown in Figure 4-2 and Figure 3-2. It consisted of a 4 ft. by 10 ft. mockup of a rail car floor, with baffles located along the 10 ft. sides to represent the sides of the rail car which also prevent flames from wrapping around to the top side of the mockup. A full-scale rail car has a width dimension of 10 ft. 2 inches. Using the width of the rail car as a dimensional scaling parameter, this represents a 39.3 percent reduction in length scale from 10 ft. 2 in. to 4 feet. The height of the panel above the floor was scaled accordingly.

The mockup was constructed of 22 ga (0.03125 in. thick) stainless steel, with both sides coated (Section 3). The mockup was extended by 2 ft. on both ends using 5/8 in. Firecode® gypsum board. The side baffles of the gypsum board are 2 ft. tall. A propane sand burner was positioned below the mockup, aligned in the center. The mockup was positioned above the floor, at a height dictated by the configuration of interest, as detailed in Figure 4-2 and Figure 3-2.

Steel support frame   Gypsum board baffles

Panel height (channel)   Panel height (flat)

24 in

Gypsum board obstructions

16 in   19 in

Burner   Gypsum board floor

8 in

19 in

(a)

Steel support frame

Gypsum board baffles

Panel

1½ in

Gypsum board
obstructions

1½ in   7¼ in

7¼ in

Gypsum board floor   19 in   8 in

Burner

16¼ in   12½ in   16 ¼ in
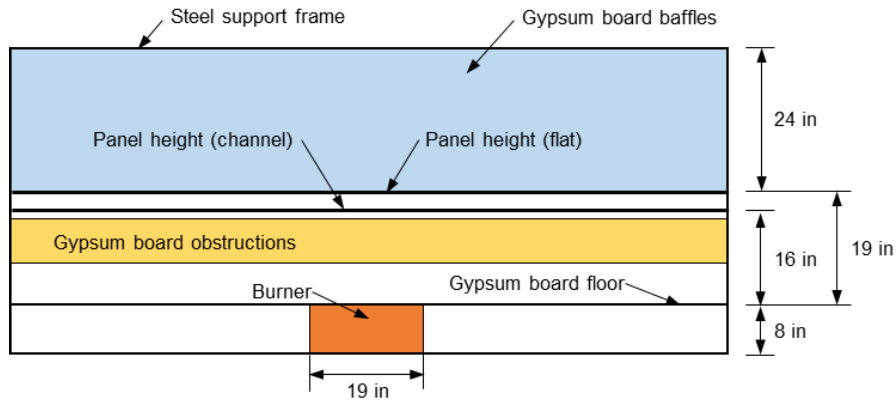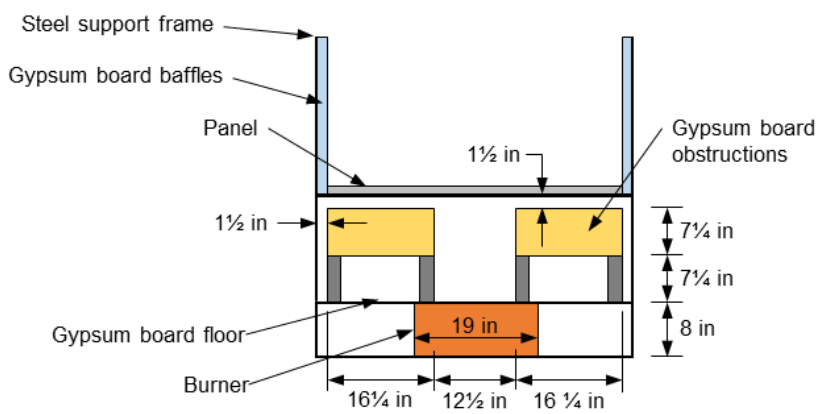
(b)

Figure 4-2. Schematic of the Test Apparatus—(a) Side View and (b) End View

There were two configurations used in testing (Section 3), as depicted in Figure 4-2, to represent rail cars with and without undercar equipment. The first configuration, denoted by "flat," represents a separation distance of 48 in. between the rail car floor and the ground at the full-scale. To represent this case in the test, the panel was positioned 19 in. above the gypsum board floor in the mockup. In the second obstruction configuration, shown in Figure 4-2, the height of the rail car floor is 40 in. above the ground at the full-scale with obstructions along the sides of the setup representing equipment boxes. In the testing, the panel was 16 in. above the gypsum board floor and obstructions were appropriately scaled and offset from the panel to represent the size and mounting used in an actual rail car. These obstructions (only present in the "obstructed" configuration) effectively created a channel along the center of the mockup that redirects flames along the center of the mockup.

A graphical overview of each sensor location is provided in Figure 4-3. Gas temperatures below the steel sheet were measured at several locations using thermocouples. Thermocouples at S1 to S10 were 1 in. below the steel panel, while those at S11 to S13 were all on the centerline and 2.5 in. apart vertically. The surface temperature of the steel sheet was measured using an IR camera, which can be post-processed to calculate the heat flux to the steel panel using an inversed heat transfer model [59].

55
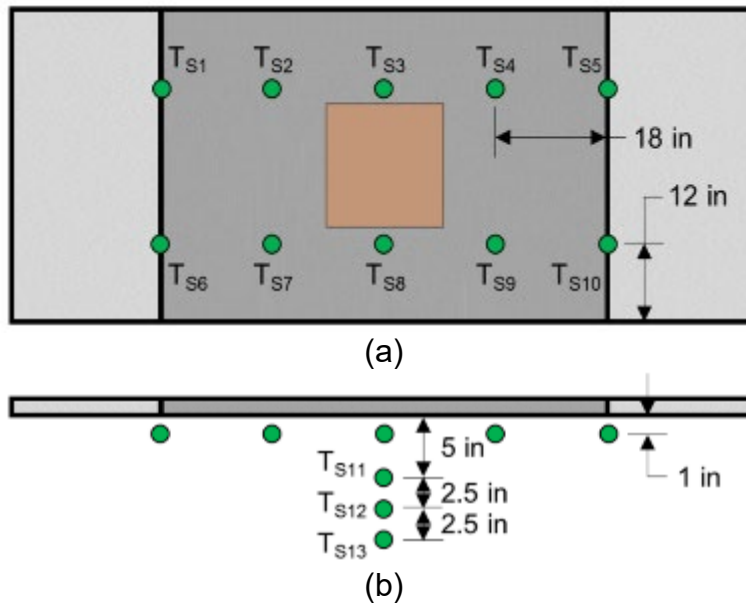
Figure 4-3. Sensor Locations for the Steel Tests—(a) Overhead View and (b) Side View

4.2.2. Scaling of Fires

A propane sand burner measuring 19 in. by 19 in., as shown in Figure 4-2, was used in the tests to reproduce HRRs which would be representative of rail car undercar fires. Two different fires, representative of a diesel pool and a pile of trash, were considered in the tests. The diesel pool fires might be expected from a diesel fuel spill, while the trash fires might occur due to a buildup of trash left on the rail tracks. The fires were scaled down based on the Froude scaling correlation [51]:

$$\frac{\dot{Q}_1}{\dot{Q}_2} = \left(\frac{L_1}{L_2}\right)^{5/2} \tag{4-1}$$

Given that L_1/L_2 is 39.3 percent from real scale rail car to the mockup, the reduced-scale HRR was calculated to be 9.7 percent of the full-scale HRR. The HRRs of the full-scale diesel and trash fires were 1.89 MW and 0.37 MW, respectively (see Section 3). Thus, HRRs used in the fire tests representing the diesel and trash fires were 184 kW and 35 kW, respectively. The diesel and trash fires were produced in the test by prescribing mass flow rates of propane to the sand burner such that the desired fire HRRs were achieved.

4.3. Modeling of Undercar Fire Exposure Using FDS

In this section, FDS Version 6.5.2 is used to simulate the fire tests. Fire models were validated using the data from the undercar fire exposure tests described in Section 3. Both testing configurations, flat and obstructed as introduced in Section 4.2, were modeled as shown in Figure 4-4. For each configuration, two different fires of 184 kW and 35 kW were considered representing diesel and trash fires, respectively.
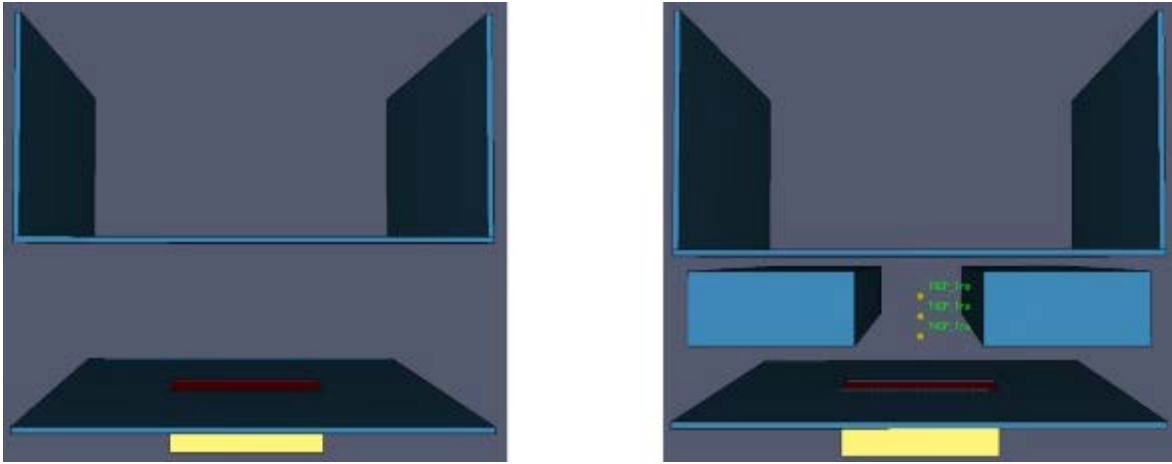
Figure 4-4. FDS Models of Flat (Left) and Obstructed (Right) Configurations

For both configurations, a computational domain of the same sizes and boundary conditions were used. Figure 4-5 demonstrates the FDS model used for the obstructed configuration. The computational domain was 14 ft. (4.3 m) long, 10 ft. (3 m) wide and 8 ft. (2.4 m) high, which gives 2 ft. (0.6 m) and 3 ft. (0.9 m) additional space on each side in the longitudinal and transverse directions, respectively. This was done to ensure that the flames were within the computational domain so the fire dynamics could be captured. An exhaust fan, which was operating during testing, was simulated directly above the floor mockup (8 ft. from the floor) operating during all tests. The fan inlet had a dimension of 10 ft. by 10 ft. (3 m by 3 m). Open boundary conditions were applied to the four sides and the top boundary areas of the domain except the exhaust fan. The domain was divided into lower half and upper half regions. A fine mesh of 1.73 in. x 1.73 in. x 0.91 ft. (0.044 m x 0.044 m x 0.023 m) was used in the lower region for dynamic gas flows under the testing panels, and a moderate mesh of 1.73 in. x 1.73 in. x 1.7 in. (0.044 m x 0.044 m x 0.043 m) was used for upper domain as shown in Figure 4-5.
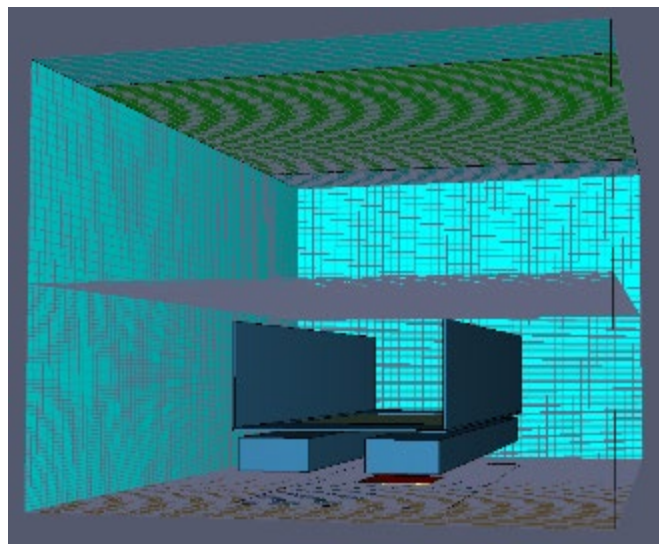
Figure 4-5. FDS Model of Obstructed Configuration

4.4. Trash Fire with Flat Configuration

The trash fire with flat configuration is first considered. Figure 4-6 presents the time history of gas temperature above the center of fire plume. The locations of vertically aligned thermocouples (S11, S12 and S13) are shown in Figure 4-3. In the FDS simulation, the gas temperature above the sand burner was predicted to reach approximately 250 °C in 2 minutes and then stayed around 225 °C until the test was terminated. The gas temperature prediction was on average 25 °C higher than the experimental data. The flame height for the trash fire, with a HRR of 35 kW, was calculated to be 16.7 in. using a Froude scaling based correlation [51]. The flame tip should be of similar height as the thermocouple at S11, which was 14 in. above the top surface of the burner. This can be verified by the video image, as shown in Figure 4-7 (left). There was not a significant difference in gas temperature at the three locations, as these thermocouples were all close to the flame tip. The flame simulated by FDS, which used a heat release rate per unit volume (HRRPUV) of 200 kW/m^3, has a similar height to the actual fire flame observed in the test, as demonstrated in Figure 4-7.
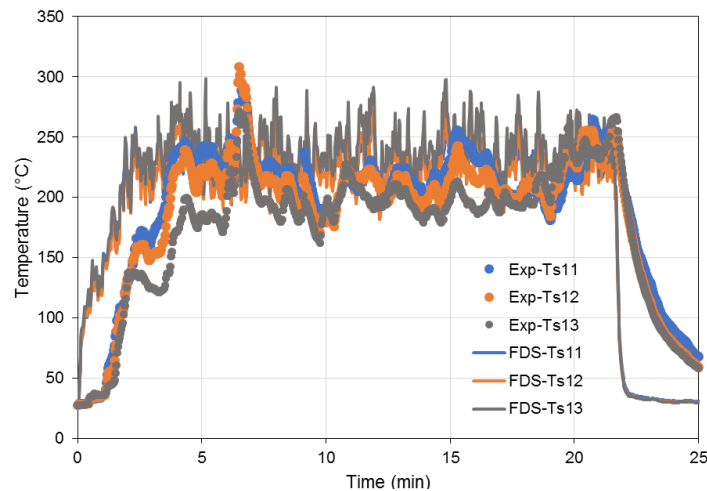
Figure 4-6. Time History of Gas Temperature Above Fire Plume for Flat Configuration/Trash Fire
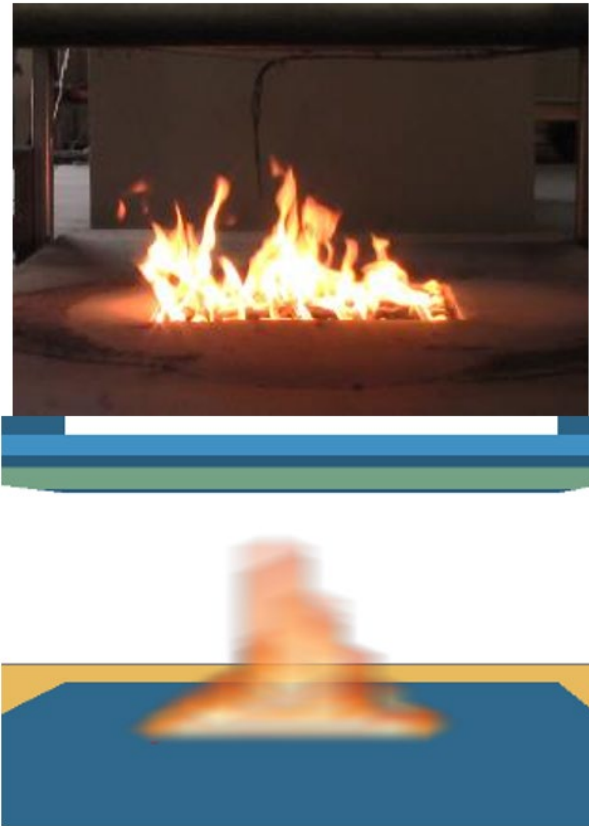
Figure 4-7. Fire Flame of Testing (Top) and FDS Simulation (Bottom) at the Time of 10 Minutes for Flat Configuration/Trash Fire

The time history of gas temperature at locations S3 and S5, which were 1 in. below the steel panel, is shown in Figure 4-8. Thermocouple S3 was at the transverse centerline and 12 in. from the center of the panel, while S5 was at the edge of the panel (Figure 4-3). The gas temperature at S3 reached steady state after 2 minutes and stayed around 250 °C, which was about 25 °C higher than the temperature reported by vertically aligned thermocouples (S11–S13). This was because S3 was 1 in. below the steel panel (location shown in Figure 4-3), but still relatively close to the fire source. The gas temperature at the S5 location reached about 125 °C after 2 minutes due to its greater distance from the fire source and was about 25 °C lower than the measured data.
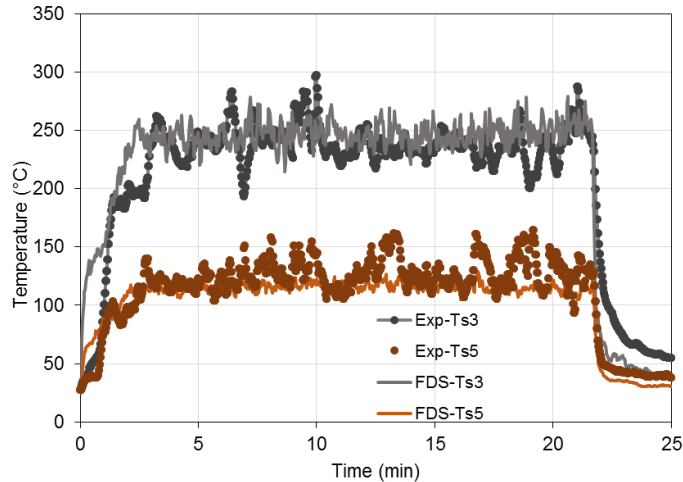
Figure 4-8. Time History of Gas Temperature Below Steel Panel for Flat Configuration/Trash Fire

The time history of heat flux to the steel panel from the trash fire with the flat configuration is shown in Figure 4-9. The predicted heat flux to the center of the steel panel was close to 15 kW/m^2, which is 2 kW/m^2 greater than the experimental data. The experimental estimate of heat flux was calculated from an inversed heat transfer model using the temperature data from the IR camera [59].

Figure 4-10 shows the comparison of heat flux distribution between the experimental data (left) and the simulation results (right) for the trash fire with the flat configuration, both plotted using the same scale. Note that the experimental estimate of heat flux was based on an inversed analysis of the IR camera temperatures that were taken at a single snapshot when the surface temperature of the steel panel reached a steady state. For all scenarios, it was found that the two-dimensional distribution of surface heat flux reached a steady state within 3 minutes. The snapshot at 8 minutes was found to be representative of the fire exposures. This can also be verified by the time history of gas temperature and heat flux in Figure 4-6 and Figure 4-8. In this report, therefore, the snapshot at 8 minutes will be used for comparison for all the scenarios. In the FDS simulation, the surface heat flux from fires was obtained at discrete locations. The two-dimensional contour plot of the FDS prediction for heat flux was not as smooth as that of the experimental data which had more data points from the IR camera measurement.

The trash fire imposed a nonuniform heat flux to the steel panel with a maximum of around 14 kW/m^2 at the center, as shown in Figure 4-10 (left). The heat flux to the edge areas of the panel was not as significant as that in the center. This is especially true near the corners, where the heat flux was only 2 to 3 kW/m^2. The minimum of 2 kW/m^2 heat flux was at the top left corner in Figure 4-10 (left). Due to unexpected ventilation changes when a door was opened during the test, the flame was slightly tilted. It can be seen in Figure 4-10 (left), the heat flux to the top and bottom left corners was found to be lower than the other two corners. This effect of ventilation was not accounted for in the simulation, so the prediction of heat flux was similar at all four corners as shown in Figure 4-10 (right). The predicted heat flux was about 1-2 kW/m^2 higher than the experimental data at the center and 1-2 kW/m^2 lower in the ceiling jet region (the region outside of the plume impingement).
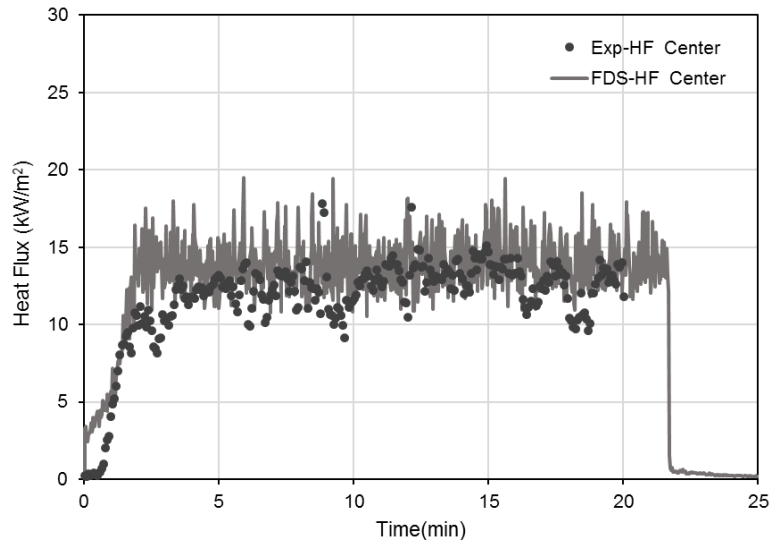
Figure 4-9. Time History of Heat Flux to Steel Panel from Flat Configuration/Trash Fire
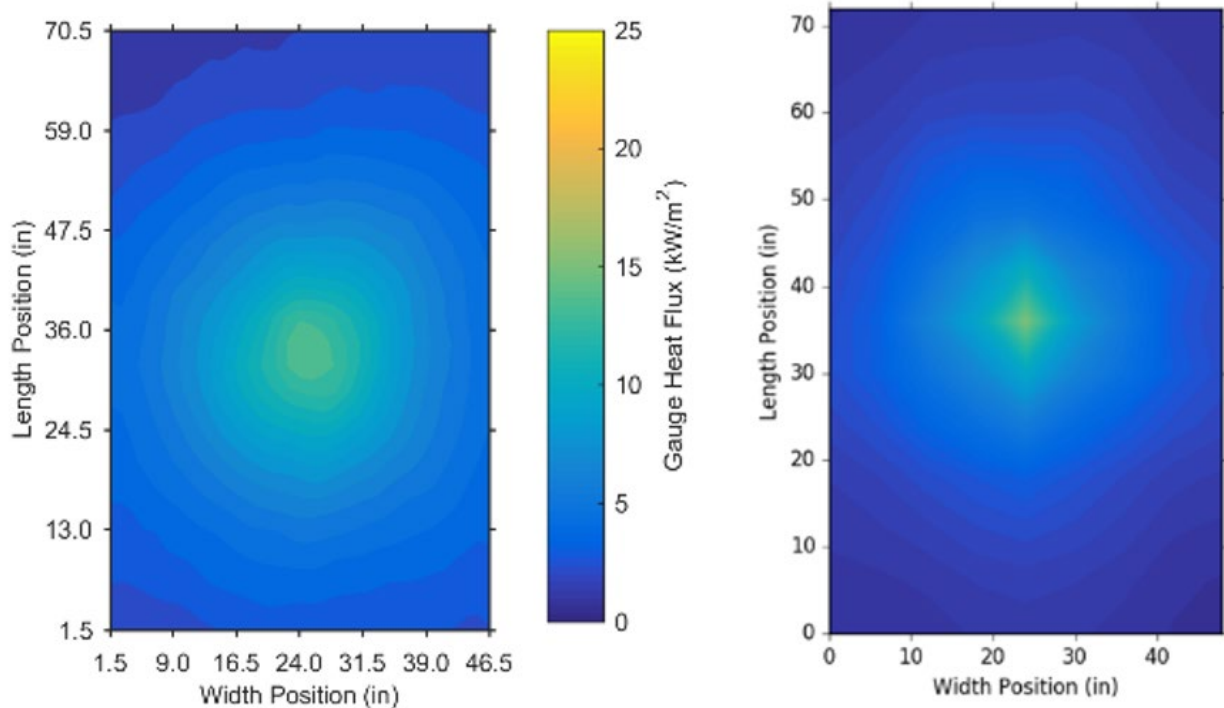
Figure 4-10. Heat Flux to Steel Panel from Flat Configuration/Trash Fire, (Left) Experimental Data and (Right) FDS Prediction at the Time of 8 Minutes

For the trash fire with the flat configuration, the steel panel was heated nonuniformly. The FDS prediction in gas temperature at various locations was not more than 25 °C higher than the experimental data. The hot gases reached the steel panel and were redirected outward away from the fire. As expected, the maximum heat flux to the exposed surface was at the center where the fire impinged on the panel. The prediction of heat flux to the panel was within 1 kW/m^2 to 2 kW/m^2 greater than the experimental data at the center and within 1 kW/m^2 to 2 kW/m^2 lower in the ceiling jet region outside of plume.

4.5.   Diesel Fire with Flat Configuration

The second scenario was a diesel fire under a flat configuration. For a HRR of 184 kW, the flame height was calculated, using a Froude scaling based correlation, to be 52.6 in. with flame extensions of approximately 32 in from the fire centerline (refer to Drysdale for details of flame extension approximation [63]) [51]. The fire flame would impinge on the steel panel and spread in all directions horizontally. Given that the distance from the fire centerline to the side of the rail car mockup was only 24 in., flames were observed to extend beyond the sides of the mockup as shown in Figure 4-11 (left). In the FDS simulation, the fire dynamics were captured showing that the fire extended beyond the steel panel, as demonstrated in Figure 4-11 (right), consistent with experimental observations.
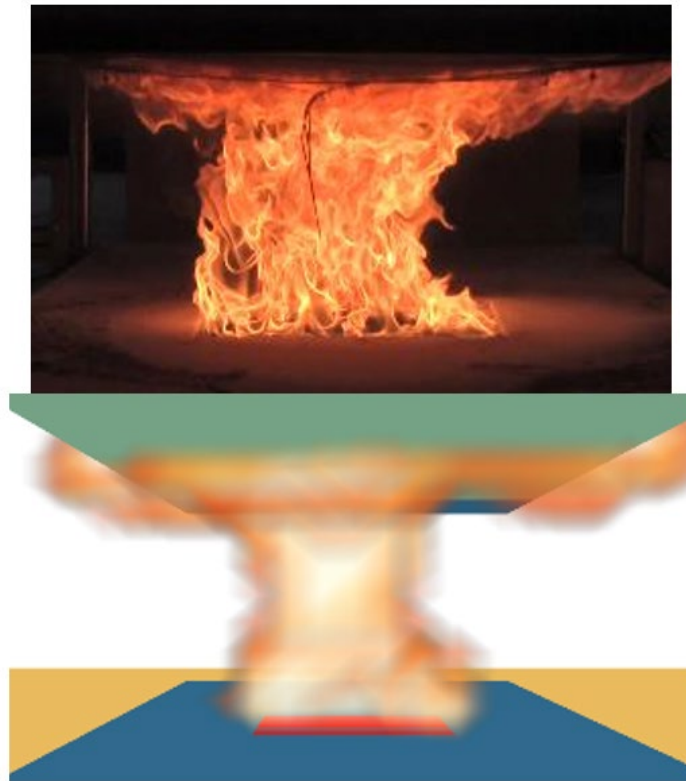
Figure 4-11. Fire Flame of Testing (Top) and FDS Simulation (Bottom) at Time of 10 Minutes for Flat Configuration/Diesel Fire

Since a higher HRR was applied in this case, a higher gas temperature and greater heat flux to the panel were expected. Figure 4-12 presents the time history of gas temperature at three locations (S11, S12 and S13) above the sand burner. From the FDS prediction, the gas temperature reached over 800 °C and stayed around 700 °C after 1.5 minutes. The gas temperature was the highest at the S11 location and the lowest at the location of S13 (see Figure 4-3), which is consistent with the experimental data. With an expected flame height of 52.6 in., the fire would impinge on the steel panel. Therefore, the gas temperature would be higher at locations closer to the steel panel. Overall, the predicted gas temperature was 100–200 °C higher than the experimental measurements. This may be attributed to air currents in the test area causing the flame to tilt slightly in one direction and reducing the gas temperatures directly above the fire source.
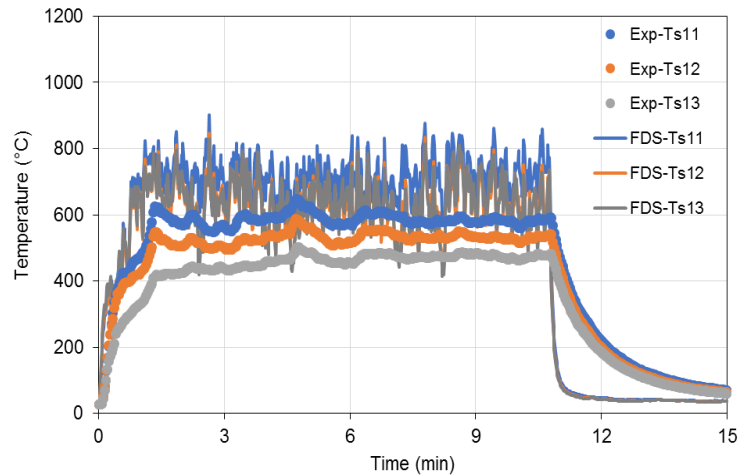
Figure 4-12. Time History of Gas Temperature Above the Fire Plume for Flat Configuration/Diesel Fire

Figure 4-13 presents the comparison of gas temperature 1 in. below the steel panel. The predicted gas temperature at S3 (see Figure 4-3) was about the same as the experimental data, and was about 75 °C higher than the experimental data at S5. The gas temperature at S3 location reached over 800 °C and stayed around 750 °C after 1.5 minutes, which was about 50 °C higher than the gas temperature at S11. Similar to the flat/trash case, this was because S3 was on the path of hot gases going around the panel edges after reaching the center of the steel panel. The predicted gas temperature at the S5 location was about 375 °C, which was within 75 °C higher than the experimental data.
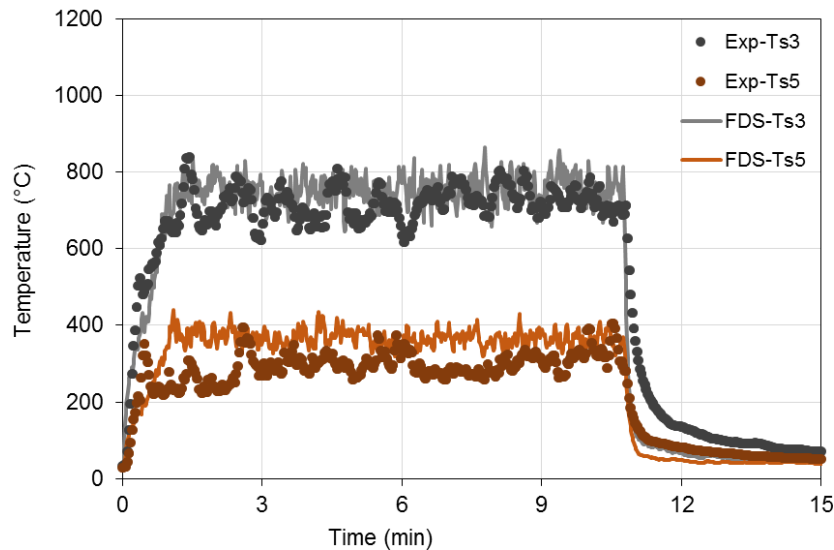
Figure 4-13. Time History of Gas Temperature Below Steel Panel for Flat/Diesel Fire

The heat flux to the center of steel panel is presented in Figure 4-14. The heat flux to the panel center was predicted to be about 75 kW/m², which is five times greater than that in flat configuration with a trash fire. The heat flux measured at the center was also approximately 75 kW/m².

64
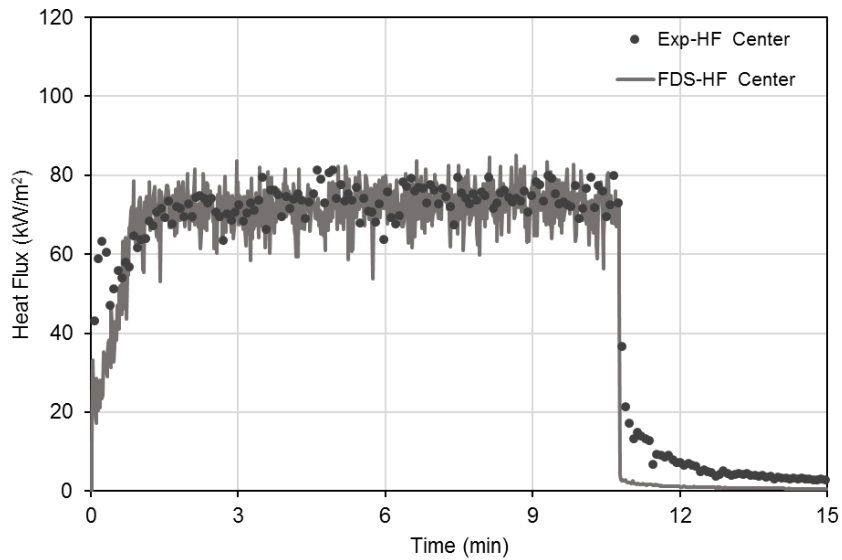
Figure 4-14. Time History of Heat Flux to Center Panel from Flat Configuration/Diesel Fire

Figure 4-15 presents the comparison of heat flux distribution between the experimental data (left) and the simulation results (right) for the diesel fire with the flat configuration. The diesel fire imposed a higher heat flux to the steel panel than the trash fire. The maximum heat flux was 85 kW/m2, approximately 6 in. away from the center, which was about 10 percent higher than the predicted maximum heat flux at the center. Due to air currents in the laboratory space, the flame was tilted away from center position. Even though the predicted heat flux at the center coincided with experimental data (Figure 4-14), it can be seen from Figure 4-15 that the predicted heat flux was in some locations 10 kW/m^2 lower than experimental data. In the ceiling jet area, outside of the plume, the predicted heat flux was within 5 kW/m^2 of the experimental data. The predicted heat flux to the corners of the panel was about 4 kW/m^2, 2 kW/m^2 lower than the experimental data at the top corners in Figure 4-15.
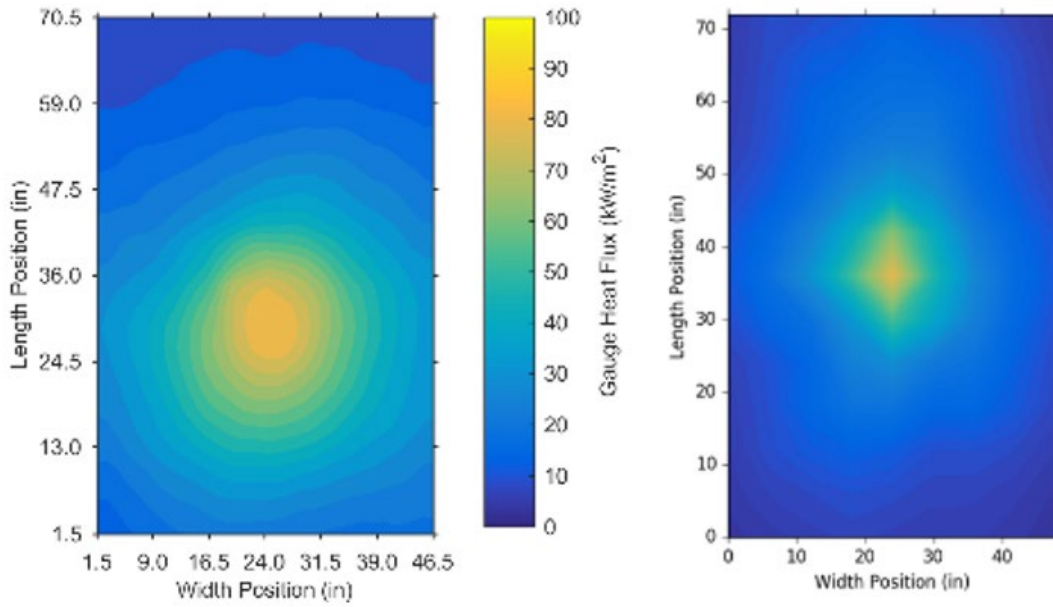
Figure 4-15. Heat Flux to Steel Panel from Flat Configuration/Diesel Fire, (Left) Experimental Data and (Right) FDS Prediction at Time of 8 Minutes

For the diesel fire with the flat configuration, the FDS prediction in gas temperature at the centerline was about 100–200 °C higher than the experimental data because the flame was tilted 6 in. away from the center. The gas temperature was found to be higher closer to the steel panel, because the diesel fire flame impinged upon the steel panel. The maximum heat flux was underestimated about 10 kW/m^2 by the FDS simulation and within 10 kW/m^2 in the ceiling jet region outside of the plume region.

4.6.   Trash Fire with Obstructed Configuration

The third scenario considered the trash fire with the obstructed configuration, as illustrated in Figure 4-4 (right) in Section 4.2.1. Figure 4-16 contains the time history of the gas temperature above the fire plume (S11, S12 and S13 shown in Figure 4-6). The gas temperature above the sand burner was predicted to reach approximately 325 °C, which was 50 °C higher than that with the flat configuration. This was caused by the obstructed configuration, which caused the flames to flow more along the length of the space between the obstructions. In the testing, the gas temperature was measured to reach a maximum of over 400 °C after 5 minutes, which was approximately 100 °C higher than the simulation results. Figure 4-17 (right) shows the flame simulation after 10 minutes. The flames appear to have a similar shape and height as in the actual testing.
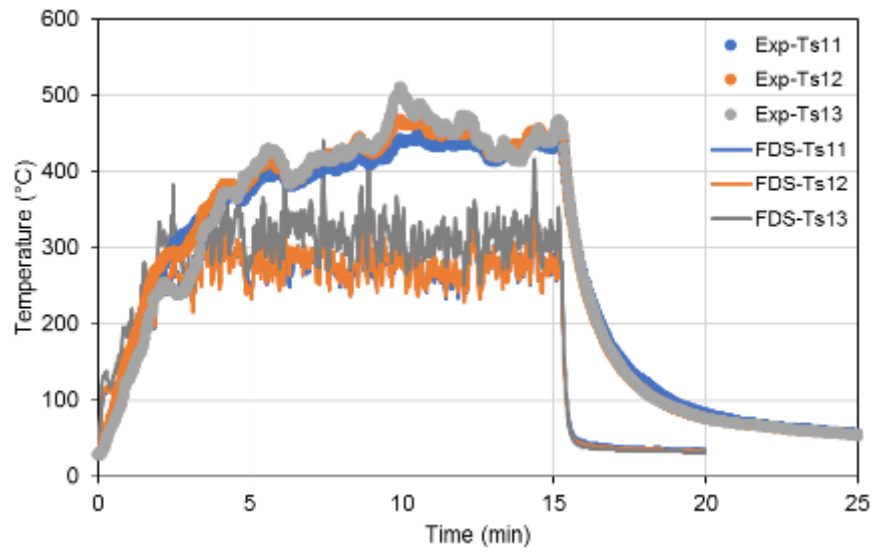
Figure 4-16. Time History of Gas Temperature for Obstructed Configuration/Trash Fire

Figure 4-17. Fire Flame of Testing (Top) and FDS Simulation (Bottom) at the Time of 10 Minutes for Obstructed Configuration/Trash Fire

The gas temperature of 1 in. below the steel panel is shown in Figure 4-18. Thermocouple S3 was at the transverse centerline and 12 in. from the center of the panel and S4 was 12 in. further down the length of the panel (see Figure 4-3). Thermocouple S6 was at the edge of the panel (shown in Figure 4-3). The predicted gas temperature at the S3 location reached and remained at 275–300 °C after 2 minutes, which was 25 °C lower than the temperature reported by the vertically aligned thermocouples (S11, S12 and S13). This is because the hot gases were cooled down after going into the gap between the steel panel and obstructions. The predicted gas temperature at the S6 location reached 75–100 °C, much lower than the gas temperature in the middle region. Due to the air currents moving the flame and some deformation of the steel plate, the highest temperatures occurred at a location between Thermocouple S3 and S4. There was an error in the Thermocouple S3 measurement near the beginning of the test, but the predicted value was between the measured S3 and S4 temperatures. Overall, the predicted gas temperatures were within 50 °C of the measured temperatures.
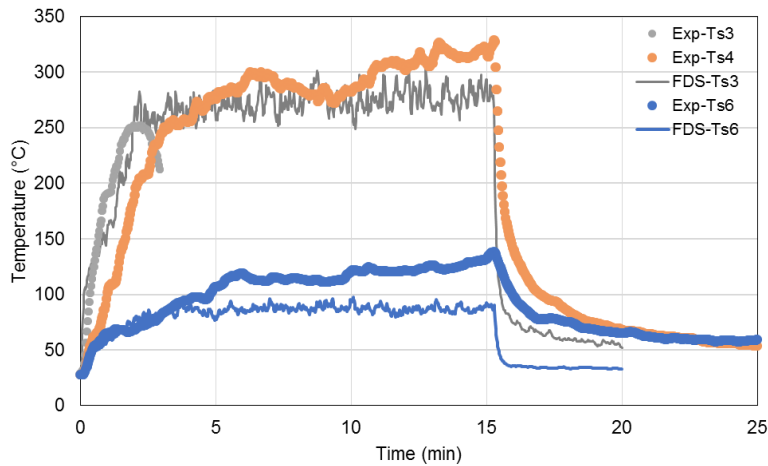
Figure 4-18. Time History of Gas Temperature Below Steel Panel for Obstructed Configuration/Trash Fire

Figure 4-19 shows the heat flux to the steel panel from the trash fire with the obstructed configuration. The heat flux to the center of the steel panel was predicted to have an average value of 20 kW/m^2 (varying between 15 kW/m^2 and 25 kW/m^2), which was 5 kW/m^2 or 30 percent higher than that in the flat configuration. The calculated heat flux from the IR camera measurements shows that it was slowly increasing and reached a maximum of 25 kW/m^2 at end of the test. It is reasoned that since the obstructions constitute a large thermal mass within the vicinity of the fire, they tend to absorb heat from the fire. Given a longer test duration or larger fire size, it is hypothesized that the heat flux would reach steady values in the time periods considered here, as predicted by the FDS model.
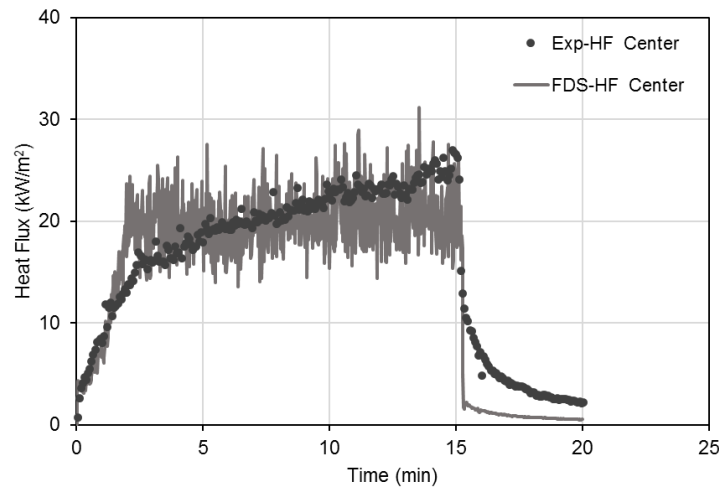
Figure 4-19. Time History of Heat Flux to the Center Panel from Obstructed Configuration/Trash Fire

Figure 4-20 contains the comparison of heat flux distribution between experimental data (left) and simulation results (right) for the trash fire in the obstructed configuration. Because of the obstructions, the fire was restricted within the channel between the obstructions so the center region of the steel panel along the longitudinal direction was exposed to a higher heat flux. Both sides in the transverse direction were predicted to

69

be exposed to a heat flux higher than the corners, because of the hot gases going through the gap between the steel panel and obstructions. The heat flux levels between the obstructions were higher in the experiments compared with the predictions. This may be in part due to the steel frames at both sides changing the gas flow path, as shown in Figure 4-21 (left). The effect of the vertical steel frames on the gas flow path and heat flux distribution was not considered in the simulation. As shown in Figure 4-20, the maximum heat flux from the experiment was about 21 kW/m^2, which was similar to the predicted heat flux. At the four corners, the prediction underestimated the heat flux by 4 to 5 kW/m^2. It is reasoned that the gas flow path was changed by the steel frames at both sides. Along the length of the panel at the center, the predicted heat fluxes were within 5-10 kW/m^2 of the measured quantities with the largest deviations in the ceiling jet region outside of the plume. Overall, all heat flux measurements were within 5 kW/m^2 to 10 kW/m^2 of the predicted values.
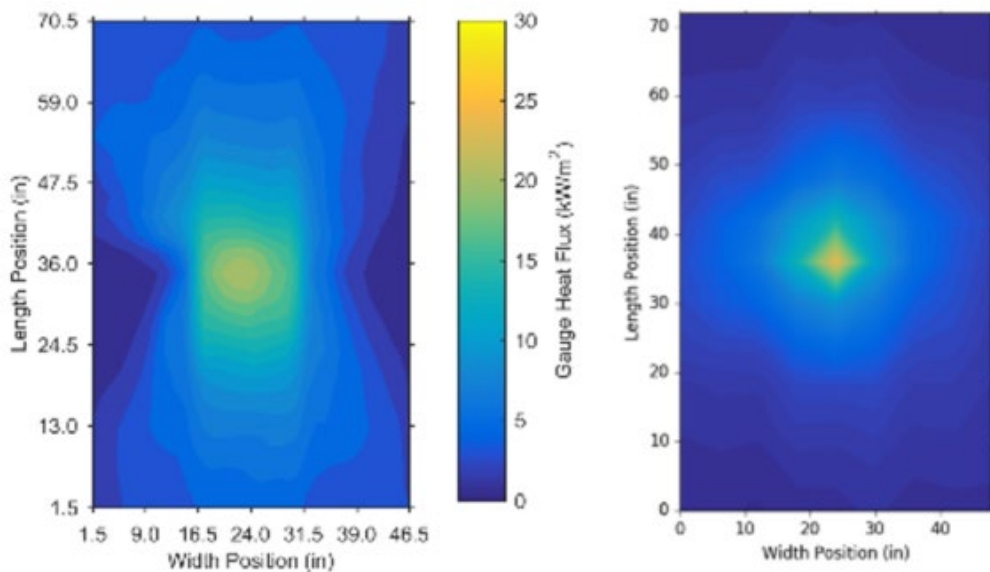
Figure 4-20. Heat Flux to Steel Panel from Obstructed Configuration/Trash Fire, (Left) Experimental Data and (Right) FDS Prediction at Time of 8 Minutes

For the trash fire with the obstructed configuration, FDS predicted gas temperatures in the centerline are approximately 100 °C lower than experimental data. The predicted heat flux was within 5 kW/m^2 to 10 kW/m^2 of the measured values at all locations. Differences were in part attributed to air currents in the laboratory and some deformation of the steel plate during the test resulting in some nonuniform flows.

4.7.   Diesel Fire with Obstructed Configuration

The last scenario was the diesel fire with obstructed configuration, as shown in Figure 4-21 (top). Figure 4-21 (bottom) presents the flames from FDS simulation, which was created using a HRRPUV of 200 kW/m^3. The flame came out of the gap and went up around the vertical baffle boards, consistent with the actual testing observations as in Figure 4-21 (top) indicating the general fire dynamics were captured in the FDS simulation.
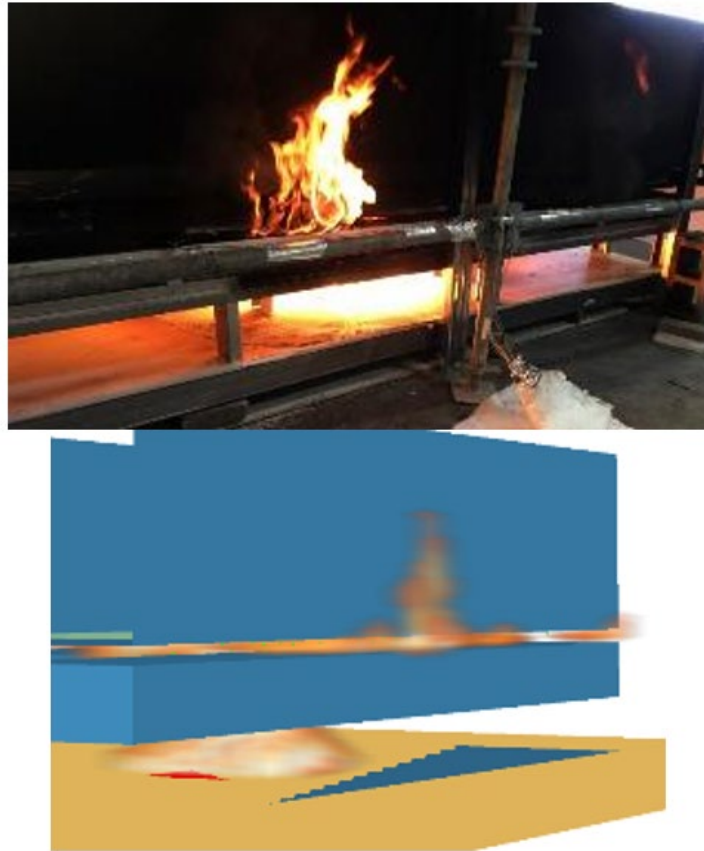
Figure 4-21. Fire Flame of Testing (Top) and FDS Simulation (Bottom) at the Time of 10 Minutes for Obstructed Configuration/Diesel Fire

Figure 4-22 provides the time history of gas temperature at three locations (S11, S12 and S13) on the centerline. From the FDS prediction, the gas temperature reached over 900 °C after 1 minute, with an instantaneous peak value above 1,000 °C after 8 minutes. This is the highest among all scenarios, as the flames were contained between the obstructions. The measured gas temperature reached as high as 1,000 °C at S11 and was around 850 °C at S13. Overall, the predictions of gas temperature were within 125 °C of the experimental data.
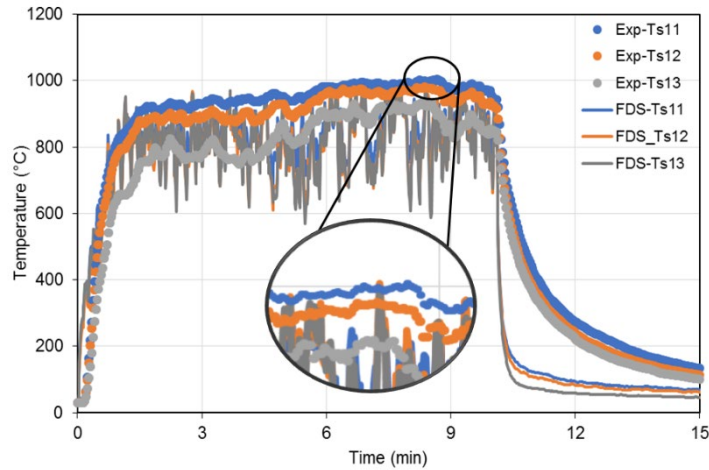
Figure 4-22. Time History of Gas Temperature for Obstructed Configuration/Diesel Fire

Figure 4-23 presents the gas temperature 1 in. below the steel panel. Thermocouple S8 was at the transverse centerline and 12 in. from the center of the panel, while S10 was at the edge of the panel (shown in Figure 4-3). The predicted gas temperature reached over 800 °C at S8 and over 600 °C at S10. The predicted temperature at S8 was about 75–100 °C higher than the experimental data at S9, which had the maximum measured temperature. There was an error in the thermocouple S8 measurement near the beginning of the test, but the predicted value was between the measured S8 and S9 temperatures. The prediction of gas temperature at S10 was on average 50 °C higher than the experimental data. There were some sudden fluctuations in experimental data, which may be due to the time variation in the fire dynamics.
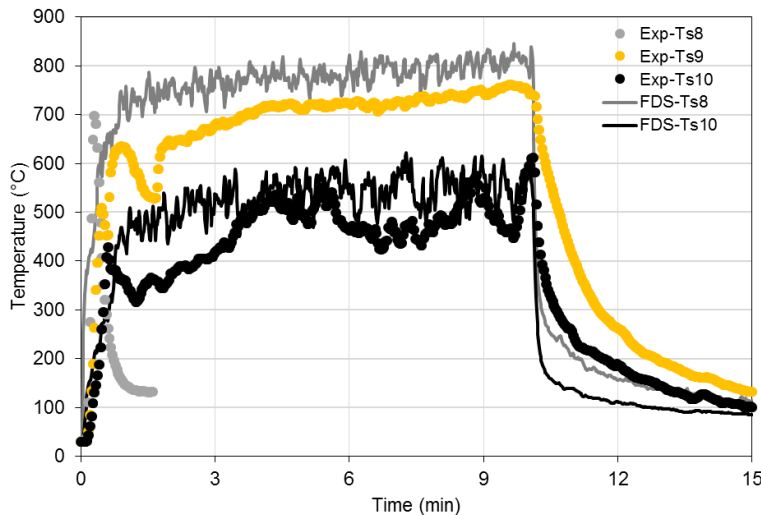
Figure 4-23. Time History of Gas Temperature Below Steel Panel for Obstructed Configuration/Diesel Fire

Figure 4-24 presents the heat flux to the center of the steel panel. The predicted heat flux to the center of the steel panel had an average value of 85 kW/m^2, which is about 20 percent higher than that in the flat configuration. The measured heat flux inferred

72

from IR camera data reached a maximum over 100 kW/m^2 with an average of 95 kW/m^2. The prediction of heat flux was on average 10 kW/m^2 lower than the experimental data.
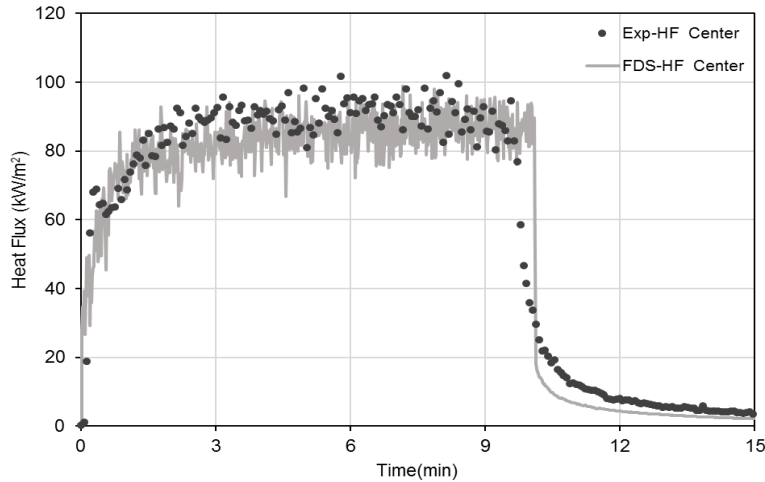
Figure 4-24. Time History of Heat Flux to Center Panel from Obstructed Configuration/Diesel Fire

Figure 4-25 presents the comparison of heat flux distribution between experimental data (left) and simulation results (right) for the diesel fire with the obstructed configuration. The fire was restricted within the channel area between obstructions so the center region of the steel panel along longitudinal direction was apparently exposed to a higher heat flux. Similar to the trash fire in the obstructed configuration, the steel frames on both sides changed the gas flow during the test. Another factor to lead to the unsymmetrical heat flux distribution shown in Figure 4-25 (left) might be the slight warping of the steel panel, which caused a non-uniform gap between the steel panel and the obstructions. As a result, the heat flux at the top right and bottom left corners (as shown in Figure 4-25) reached 20 kW/m^2 but was only 10 kW/m^2 at the other two corners. Without considering the effect of warping and the presence of the steel frames, the predicted heat flux at all four corners was around 10–15 kW/m^2. The maximum heat flux was predicted to be 85 kW/m^2 at the center of the panel, approximately 5 kW/m^2 to 10 kW/m^2 lower than the experimental data. The largest deviations were along the length of the panel and at the mid-width in the ceiling jet region beyond the fire plume, where predicted levels were 10 kW/m^2 to 20 kW/m^2 lower than the measured quantities.
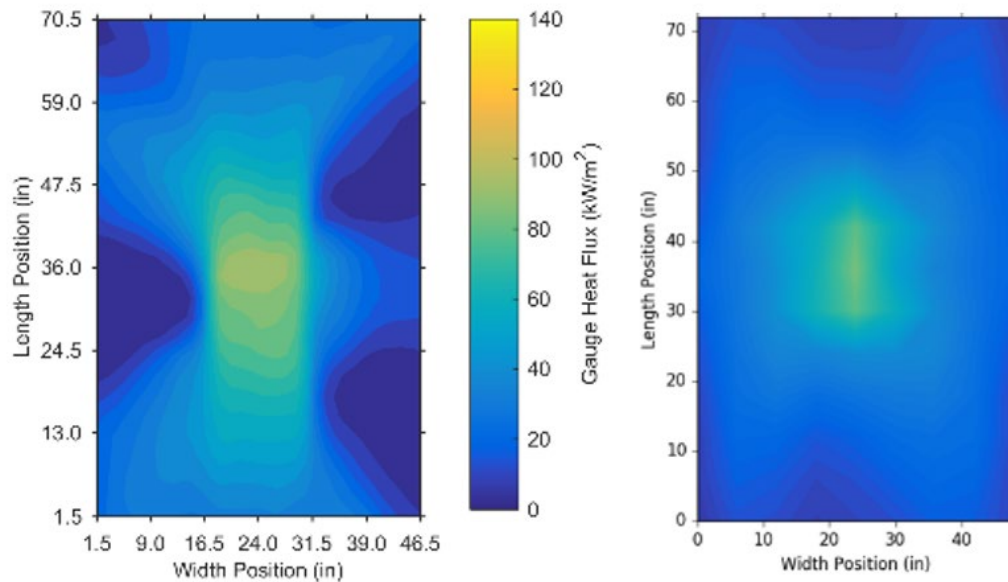
Figure 4-25. Heat Flux to Steel Panel from Obstructed Configuration/Diesel Fire, (Left) Experimental Data and (Right) FDS Prediction at the Time of 8 Minutes

For the diesel fire with the obstructed configuration, the FDS prediction in gas temperature was 50 °C to 125 °C lower than the experimental data at various locations. The center region of the steel panel along the longitudinal direction was predicted to be exposed to a greater heat flux. Although the effects of the steel frames and warping of the panel on the gas flow path were not modeled, the heat flux at locations further from the fire were predicted to be around 10 kW/m^2 which is consistent with the experimental data. In general, the difference in predicted and measured heat fluxes was less than 10 kW/m^2 to 20 kW/m^2.

4.8. Validation Summary

A summary of the comparison between the data and the model predictions is provided in Table 4-1 for both gas temperatures and heat flux. The comparison is divided between quantities in the fire plume region (directly above the fire source) and the ceiling jet region (region outside of the fire plume impingement). In the fire plume region, the heat fluxes were predicted to be within 11 to 20 percent of the experimental data while gas temperatures were predicted within 11–28 percent. For the ceiling jet region, the heat fluxes were predicted within 17 to 33 percent of the data and gas temperatures within 3 to 15 percent of the data. This level of agreement is similar to that achieved in the FDS validation guide (NIST Special Publication 1018-3, sixth edition, Chapter 6 – Fire Plumes and Chapter 12 – Heat Flux) for heat transfer in more simple geometries [71]. As a result, the model is considered validated for use in the configurations considered in this study.

Table 4-1. Comparison of Model and Measured Quantities for the Different Configurations

Configuration	Heat Flux - Fire Plume Region			Heat Flux - Ceiling Jet		
	Model Prediction kW/m²	Measurement kW/m²	%-Diff %	Model Prediction kW/m²	Measurement kW/m²	%-Diff %
Flat Trash	16	14	14%	10	12	-17%
Flat Diesel	75	85	-12%	35	45	-22%
Obstructed Trash	20	25	-20%	10	15	-33%
Obstructed Diesel	85	95	-11%	40	60	-33%
Configuration	Temperature - Fire Plume Region			Temperature - Ceiling Jet		
	Model Prediction °C	Measurement °C	%-Diff %	Model Prediction °C	Measurement °C	%-Diff %
Flat Trash	250	225	11%	250	230	9%
Flat Diesel	700	550	27%	750	725	3%
Obstructed Trash	325	450	-28%	275	325	-15%
Obstructed Diesel	800	900	-11%	800	725	10%

4.9. Section Summary

FDS, Version 6.5.2, was used to simulate a series of tests of a rail car floor mockup exposed to realistic undercar fires. Four scenarios were considered in this study. Two fires with 35 kW and 184 kW HRRs were used to represent trash and diesel fuel fires, located below the center of the rail car floor mockup. For each fire, both flat and obstructed configurations were simulated representing actual rail car geometries.

The floor mockup (a steel panel in the tests) was exposed to nonuniform heating from the fires. In the fire plume region, the heat fluxes were predicted to be within 2 to 10 kW/m² (11 to 20 percent) of the experimental data while gas temperatures were predicted within 25 to 150 °C (11 to 28 percent) of the experimental data. For the ceiling jet region, the heat fluxes were predicted within 2 to 20 kW/m² (17 –33 percent) of the experimental data and gas temperatures within 20 to 75 °C (3–15 percent) of the experimental data. Some of these differences in results may be due to the air currents inside of the laboratory during testing, slight warping of the steel panel, and the presence of the vertical steel frames on both sides of the mock-up.

The fire dynamics were well predicted by FDS models for all scenarios. The flame heights of trash fires were found to be consistent with experimental observations. For diesel fires, the flames were predicted to impinge the floor mockup, extend beyond the edges in the transverse direction (through the gap in the obstructed configuration) and go up along the vertical baffle boards, similar to that observed in the testing.

The study has demonstrated that the FDS model is capable of simulating realistic undercar fires. Predictions were within 3–33 percent of measurements. This level of agreement is similar to that achieved in the FDS validation guide (NIST Special

Publication 1018-3, Sixth Edition, Chapter 6 – Fire Plumes and Chapter 12 – Heat Flux) for heat transfer in simpler geometries. As a result, the model is considered validated for use in this configuration. For future tasks, additional undercar fire exposure conditions which have not been tested can be simulated using FDS. This includes the use of FDS to investigate the effects of larger, realistic fire exposures as well as different rail car geometries and different materials of construction.

5. Modeling Method for Rail Car Floor Assemblies Exposed to ASTM E-119 Fire Resistance Tests

Rail car manufacturers' interest in reducing the physical size of the large-scale rail car floor assembly test article can result in a decrease in the cost of the floor assembly approval process. Computational modeling can be used initially to determine the feasibility reducing the size and potential small-scale test article boundary conditions that would represent the larger scale floor assembly response. The focus of this aspect of the research effort was to develop and demonstrate a modeling methodology that can be used to predict the thermo-mechanical response of a rail car floor assembly during a fire resistance test. This section discusses the development of the methodology based on using a commercially available FEA software tool. Input data required for the simulation were collected from data in the literature for use in computational studies of reduced-scale floor assemblies.

Modeling furnace exposure experiments of structural assemblies has become common using FEA software packages such as Abaqus and ANSYS [1] [76]. Such analyses consist of two parts: a thermal model to predict the temperature response and a structural model to predict the displacement response. These two models are generally sequentially, or loosely, coupled together such that any effect of the displacement response on the thermal exposure is neglected. This is generally true for furnace exposures that are nominally uniform.

Typical rail car floor assembly construction includes structural framing members, a composite floor, and insulation as seen in Figure 5-1. For both the thermal and structural analyses, appropriate material and section models for each of these components must be selected or developed to accurately capture the behavior of the assembly. To accurately predict the response of a floor assembly, accurate material models of each of the materials within the assembly is required. Assembly materials typically consist of a structural frame material such as stainless steel, a thermal insulation such as spun glass or mineral fiber, and a composite floor consisting of metals, polymers, and wood. This report discusses the selection or development of material and section models for typical constructions followed by an exemplar analysis of a full-scale fire resistance test of an exemplar floor assembly. This exemplar analysis provides a pass/fail validation of the method for this particular assembly as well as a results database to be used in subsequent modeling of reduced scale feasibility.
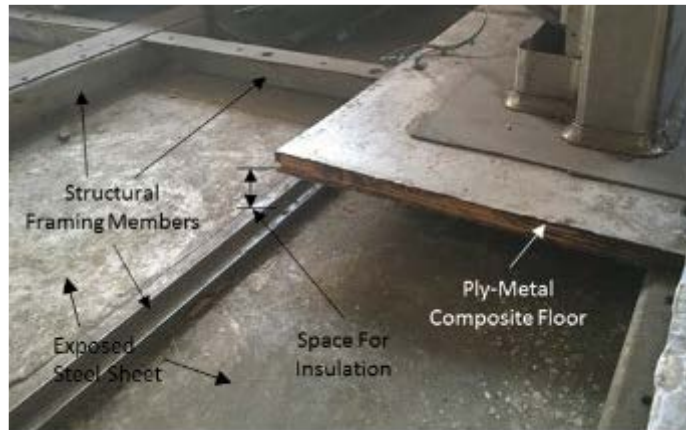
Figure 5-1. Typical Rail Car Floor Assembly Construction Including Structural Frame, Composite Floor, and Gap for Insulation

5.1. Material Modeling Methods

This section describes the material models used for various components of the frame assembly.

5.1.1. Frame Materials

Structural frames of rail car floor assemblies are fabricated almost exclusively of metals such as high strength steel, stainless steel, and aluminum. Stainless steel's high strength coupled with its resistance to environmental effects such as corrosion make it a suitable material for rail car structure. The lower density of aluminum can reduce floor weight, but its low melting temperature results in poor fire performance. The behavior of common stainless-steel alloys has been well documented. Several building codes from around the world have recommended thermal and structural property data for use in advanced structural calculation methods such as finite element analyses. For example, recommended thermal and mechanical property values up to 1200 °C from the Eurocode (EN 1993-1-2) for stainless steel grade 304 (SS304) are provided in Appendix F.1. More detailed and complex material models designed for particular applications can also be found within the engineering literature [77] [78].

Aluminum alloys are another common rail car floor framing material due to their low density compared to steel. In particular, 5xxx and 6xxx series alloys are preferred due to their resistance to environmental effects. Like stainless steels, the material behavior of many aluminum alloys is well documented and available in either building codes such as Eurocodes or the engineering literature [79]

5.1.2. Insulation Materials

Insulation within a rail car floor assembly can span an array of commercially available materials. Typically, spun fiber blankets of fiberglass, mineral wool, or ceramic fiber is used. Temperature dependent material properties (particularly thermal conductivity) is generally available from commercial manufacturers or distributors of the insulation products. Material property data for these products are typically provided up to the specified material operating temperature, which can be below temperatures seen in fire

78

resistance tests. For example, typical fiberglass maximum operating temperature is 538 °C (1,000 °F) while temperatures during a 30-minute fire resistance test can exceed 800 °C. Additional property testing could be required to obtain properties above the insulation's typical operating temperature. Unlike mineral wool or ceramic fiber insulations, fiberglass insulation may also melt during fire tests which will result in the loss of its insulating effectiveness. This must be accounted for in the modeling. Specified properties of insulation materials can also vary depending on the manufacturer as no universally recognized property values exist. While reported values are generally similar, some discrepancy can exist. As example, thermal conductivity data of ceramic fiber blanket insulation as reported from multiple manufacturers is provided in Figure 5-2. While trends between the sources match, the standard deviation at any temperature is typically 10 to15 percent of the average value.
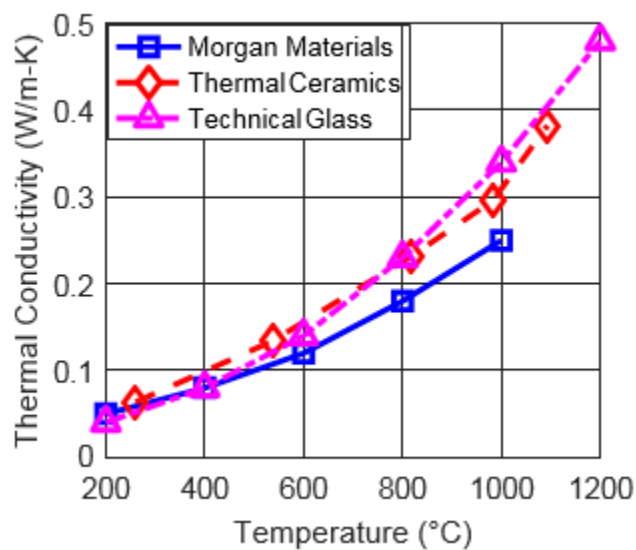
Figure 5-2. Published Thermal Conductivity of 128 kg/m^3 (8 lbm/ft^3 Ceramic Fiber Blanket from Multiple Manufacturers

5.1.3. Composite Materials

The thermal and mechanical modeling of materials typically used in composite fabrication is generally more complex than framing and insulation material because of the use of organic materials. Materials such as wood and polymers are typical in sandwich composite construction and undergo decomposition reactions at temperatures as low as 200 °C for woods while property degradation of polymers may occur as low as 50 °C [80] [81] [82]. These reactions affect both the thermal and mechanical response of the material. While the engineering literature contains many models for representing these reactions for particular materials, the available literature only represents a fraction of materials currently used in sandwich composite construction. Additionally, data are rarely reported at the high temperatures typical of a fire exposure.

Even when the necessary material data are available, the complex nature of many kinetic reaction models makes them unattractive for use in FE simulations. Therefore, the ability to develop simplified models is desirable. For example, Fateh et al. developed

79

a complex kinetic reaction model for fire retardant plywood that might be used in a ply-metal sandwich composite structure [83]. The model considered six phases of kinetic evolution that occur between 200 °C and 570 °C as seen in Table 5-1. The model developed by Fateh considered the conservation of condensed and gas phase mass, species, and energy as well as the evolution of pressure in a 1 dimensional kinetic model. Phase property data developed by Fateh seen in Table 5-2 were used in conjunction with the temperature ranges of each kinetic reaction to develop effective temperature dependent material properties for plywood. This formed a simplified material model for the thermal properties of plywood provided in Appendix F.2.

Table 5-1. Kinetic Reaction Temperature Ranges of Fire Retardant Plywood [83]

Reaction	Temperature (°C)	Reactant	Product
Pyrolysis	200–290	Plywood	α Plywood
Pyrolysis	290–380	α Plywood	β Plywood
Pyrolysis	380–450	β Plywood	o Plywood
Oxidation	450–570	o Plywood	θ Plywood
Oxidation	>570	θ Plywood	λ Plywood

Table 5-2. Effective Thermal Properties of Plywood Phases According to Fateh et al. [83]

Phase	k (W/m-K)	ρ (kg/m3)	Cp (J/kg-K)
Plywood	0.17	480	1790
α Plywood	0.18	365	1220
β Plywood	0.09	253	1450
o Plywood	0.13	143	1470
θ Plywood	0.1	49	1670
λ Plywood	0.1	47	1680

The accuracy of this simplified material model for thermal properties was benchmarked using constant exposure experiments performed by Fateh. In these experiments, 18 mm (0.7 in) thick fire retardant plywood was exposed to a constant exposure using a cone calorimeter. Thermocouples were used to measure the temperature of the exposed and unexposed surfaces of the sample. A simple 1 dimensional FE simulation of the exposure was created using 20 quadratic elements (DC3D20) through the sample thickness. Figure 5-3 contains the predicted temperature response using the simplified material property model compared to experimental data and the kinetic driven model developed by Fateh. The simple material model captures the exposed surface temperature for both exposure levels and conservatively over-predicts the unexposed surface temperature. However, the accuracy of the simplified material model is similar to the kinetic driven model.
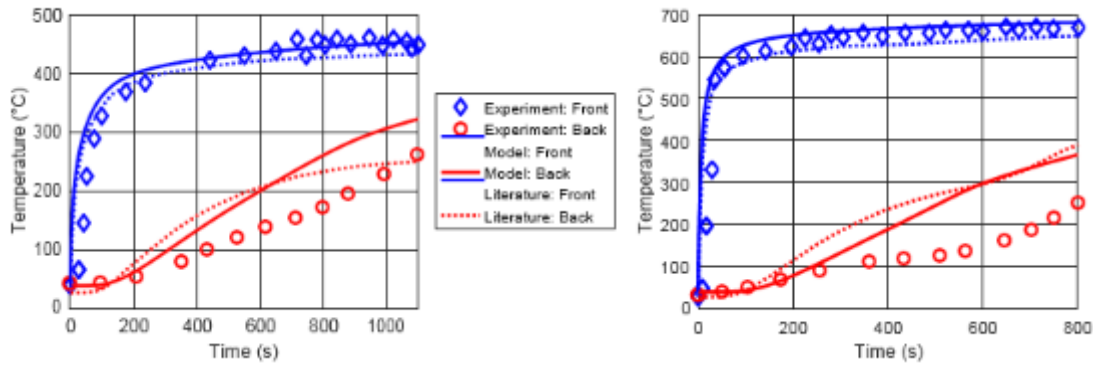
Figure 5-3. Temperature Response of Plywood Exposed to (Left) 20 kW/m2 and (Right) 50 kW/m2 Heat Flux from a Cone Calorimeter. Experimental and Literature Data from Fateh et al. [83]

Accurate mechanical properties of these organic materials are more scarce than thermal properties. Ultimately, the kinetic reactions that effect the thermal properties also effect the mechanical properties. As these reactions are highly dependent on the temperature and heating rates of a sample, it can be difficult or impossible to obtain accurate mechanical property data for many of these materials.

Due to this, at times, conservative property values such as those listed in design standards (such as EN 1995-1-2) must be utilized. In the analysis conducted as part of this preliminary research, room temperature material property data were obtained from the Wood Handbook with temperature based reductions taken from the Eurocodes [84].

5.2. Composite Section Modeling Methods

Structural modeling of a sandwich composite section like that present on many typical rail car floor assembly constructions requires more than consideration of the individual components. Sandwich composites obtain their strength through the interaction of the facesheets and core. Thus, the failure of either component or the interaction can result in significant reduction in composite capacity. The governing failure mechanism depends on the geometry of the composite, the relative material properties of the core and facesheets, as well as heating [85]. During this preliminary study, two exemplar failure modes have been identified for inclusion in modeling efforts: shear failure of the core and pull-off failure of the interface. Both composite failure modes discussed in the subsequent sections were implemented into the commercial FEA program, Abaqus, with user defined field variables and a corresponding user subroutine.

5.2.1. Core Shear Failure

Core shear failure is a common failure mode of sandwich composites which are relatively short and thick when subjected to bending loads [85]. A typical core shear failure is seen in Figure 5-4 (left). Core shear failure is ultimately governed by the shear behavior of the core. This can be relatively simple for cores constructed of isotropic foams. However, the non-isotropic behavior of typical wood materials used in sandwich composites (such as plywood or balsa) can make implementation of this failure mode within an FE model more complex. In particular, input parameters necessary to

81

characterize capture the behavior and failure of the material are not available for most composite material configurations.
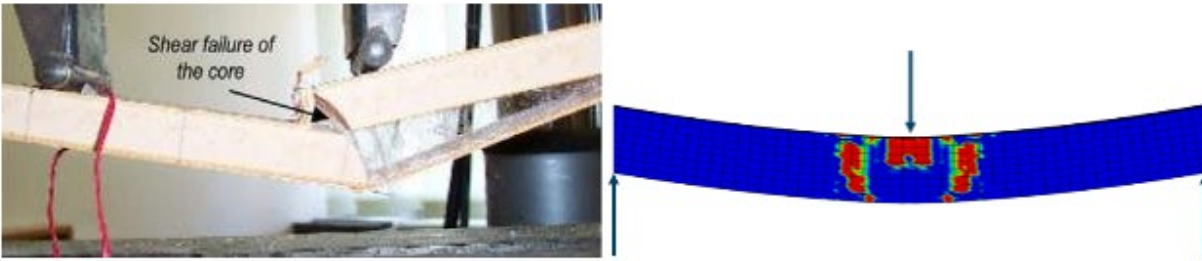
Figure 5-4. (Left) Typical Core Shear Failure of a Wood Core Sandwich Composite Subjected to Bending (Right) Example of Predicted Core Shear Failure Using Developed Routines on a 3 Point Bending Test [86]

A core shear failure model was implemented into Abaqus for isotropic and orthotropic materials. The isotropic shear failure model calculated the maximum principle shear as

$$\tau_{max} = \frac{\sigma_1 + \sigma_3}{2}$$

(5-1)

and compared this to a temperature dependent maximum shear stress threshold obtained from engineering literature or material testing. The orthotropic shear failure model considered failure of each orthotropic direction independently. An example of a predicted failure due to core shear from three-point bending is seen in Figure 5-4 (right).

The orthotropic material properties of plywood were identified within the engineering literature and developed for use within Abaqus. The layered construction of plywood results in significantly less strength in the plane of the plies [84]. This is offset by the reduced shear stresses in this plane compared to the cross-ply stresses. Due to this, the direction of the initial shear failure will be unknown. Thus, shear failure was checked independently in the ply plane and across the ply plane. Core shear failure was initiated using a temperature dependent shear stress threshold. While material property data for developing the core shear failure model for plywood were available, a suitable validation data suite was not so the core shear failure model could not be explicitly validated at this time.

5.2.2. Interface Failure

Interface failure of a sandwich composite (also called debonding) is a failure of the connection between the composite core and the facesheets. When this occurs, the debonded facesheet is no longer braced by the core and is susceptible to buckling under relatively small compression loading. Characterization of an interface failure is experimentally conducted using a facesheet push off test as seen in Figure 5-5 (left).

Failure initiation and debond propagation are often characterized using a temperature dependent effective strain energy release rate [87]. This release rate is dependent on the material of the facesheet and core, the adhesive (if any) as well as the fabrication

method of the sandwich composite. Due to this, characterization of only a select combination of materials and fabrications is available in the engineering literature.

Failure tracking of the interface within Abaqus was conducted using the strain energy at the inner surface of the facesheet. The total strain energy present at this interface was calculated as

$$E = \epsilon 1 * \sigma 1 \tag{5-2}$$

Model input parameters were identified, but values are not available within the engineering literature for most constructions typical of rail car floor assemblies. Model input parameters were identified in Couchman and Mouritz [87] for glass fiber reinforced polymer facesheets with balsa wood cores. A sample interface failure result using these materials is seen in Figure 5-5 (right).
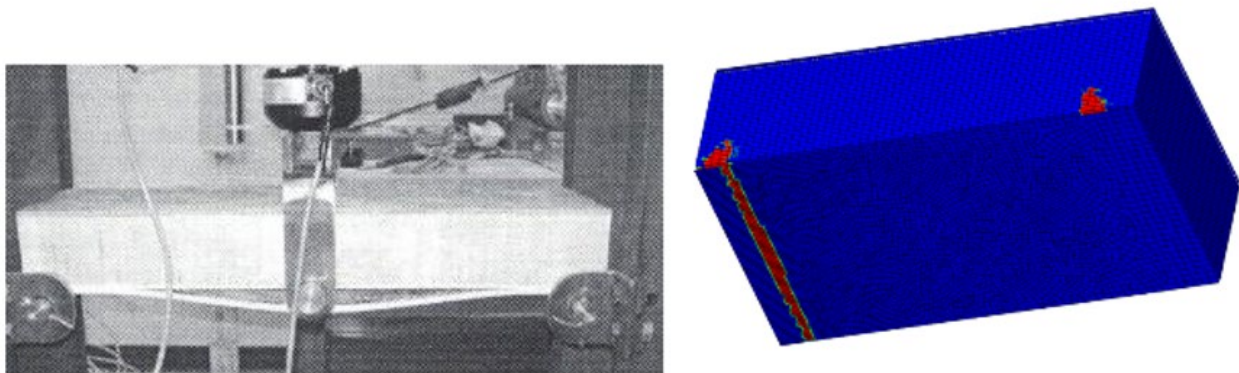
Figure 5-5. Typical Interface Failure from a Push-Off Test of a Sandwich Composite Made of Glass Fiber Reinforced Polymer Facesheet with Balsa Wood Core (Left) [87]. Example Failure Initiation Prediction for Interface Failure Model Developed Within Abaqus (Right)

5.3.   Example Analysis

An example analysis of an exemplar rail car floor assembly was conducted using the methods described in the previous section. Thermal and mechanical models of the rail car floor assembly were developed and sequentially coupled. The modeled section is representative of a typical construction. The assembly was analyzed using the commercial FE software package Abaqus. The modeled section was 3.4 m (11.2 ft.) long with structural repetitions every 1.1 m (3.6 ft.). The modeled section width was 2.7 m (9 ft.) representing the entire rail car width. The section consisted of a stainless steel 304 (SS304) structural frame below a SS304 and plywood (ply-metal) composite floor protected by spun fiberglass blanket insulation.

The SS304 frame was built primarily of intersecting 76x101x3 mm (3x4x1/8 in) channels attached to a 3 mm (1/8 in) plate. Above this, the ply-metal floor consisted of a pair of 3 mm (1/8 in) SS304 face sheets with a 19 mm (3/4 in) plywood core. The frame was surrounded with fiberglass blanket providing 76 mm (3 in.) thickness insulation below the ply-metal floor. Lastly, a pair of 229 mm x 64 mm x 3 mm (9 in x 2½ in. x1/8 in.) angles ran longitudinally along the exterior edges of the assembly. The modeled section is seen in Figure 5-6. The section did not include any penetrations. The floor assembly

was modeled using solid continuum elements. While many of the elements of the structural frame are thin, the use of shell elements creates inconsistencies at the interface of adjoining members and solid modeled insulation geometries.

5.4. Thermal Model

To simulate the ASTM E119 furnace exposure, convection and radiation boundary conditions were used on the exposed and unexposed surfaces. On the exposed surface, the ASTM E119 temperature exposure was used with a convection heat transfer coefficient of 25 W/m^{2}K and an emissivity of 0.7 [88]. An ambient temperature of 25 °C was applied to the unexposed side boundary conditions with a convection heat transfer coefficient of 9 W/m^{2}K and an emissivity of 0.7 [88]. This methodology has previously been successfully implemented for fire resistance modeling of composite steel and concrete bridge sections [89]. Temperature dependent thermal conductivity and specific heat capacity were used for all materials in the assembly (Appendix F).
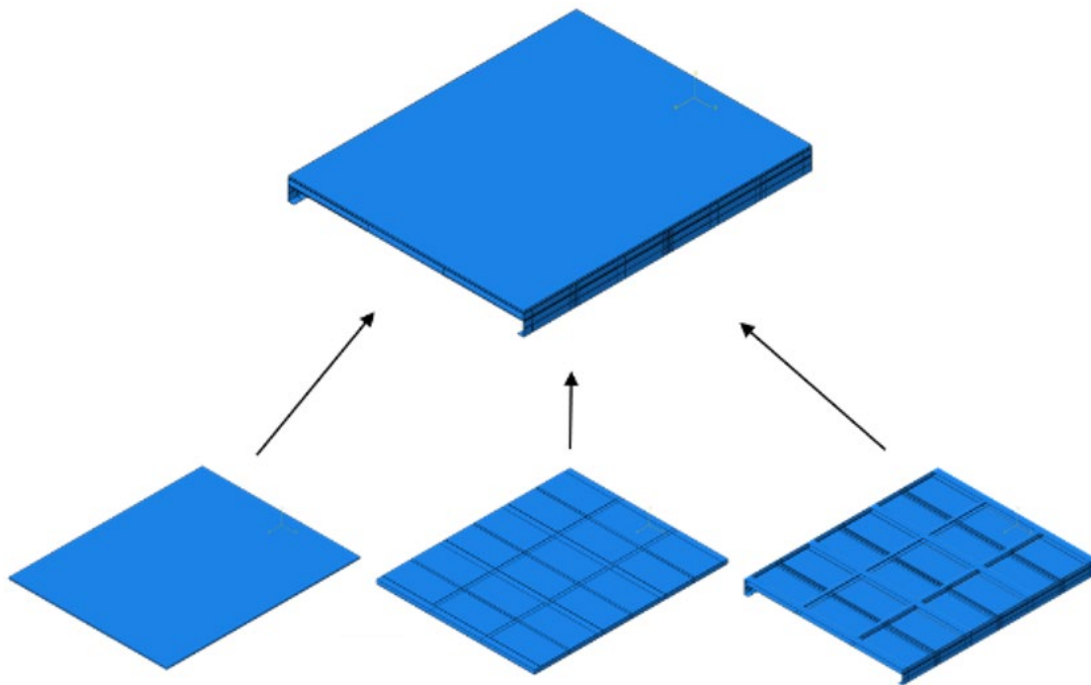
Figure 5-6. Model Geometry Included in Preliminary Analysis of Representative Floor Assembly Exposed to ASTM E119 Furnace Conditions

One difficulty in working with fiberglass insulation is that it breaks down between 500 °C and 600 °C. The exposed surface of the insulation is typically near the furnace temperature which is 843 °C for the ASTM E119 fire curve at 30 minutes. This means that a typical fire resistance test would result in the degradation and loss of fiberglass insulation. Once the insulation has degraded, cavity radiation within the insulation space would replace conduction as the dominant form of heat transfer. In order to model the thermal response of a fiberglass insulated panel, this change in heat transfer mechanism needs to be considered. In this model, the fiberglass insulation was removed when the exposed surface reached 538 °C (typical maximum operating temperature) and radiation exchange between the interior surfaces of the insulation cavity was initiated [88]. While the actual process of insulation degradation and change

of heat transfer mechanism is much more complex, this allows for a simplistic methodology to represent the change in the heat transfer mechanism. This method was also deemed to be conservative as more energy could be transferred via radiation and this method would under-predict the time of the insulation degradation and loss.

The thermal mesh of the floor assembly needed to be fine enough to capture the spatial thermal gradients through each of the materials. The SS304 frame was meshed with a 25 mm (1 in.) seed over the entire assembly. This provided three elements along the height of the 76 mm (3 in.) channel elements of the frame. The composite floor facesheets and core were meshed in the plane with a 34 mm (1-1/3 in.) seed. A single layer of elements was used through the thickness of the facesheets and four elements were used through the thickness of the core. The fiberglass insulation was also modeled with 34 mm in plane seed but had 11 elements through the thickness. The entire assembly was meshed using solid linear heat transfer elements (DC3D8) providing a total of 232,000 degrees of freedom. A section of the meshed geometry is seen in Figure 5-7. Mesh convergence was confirmed using general mesh seeds with 25 percent increased density.
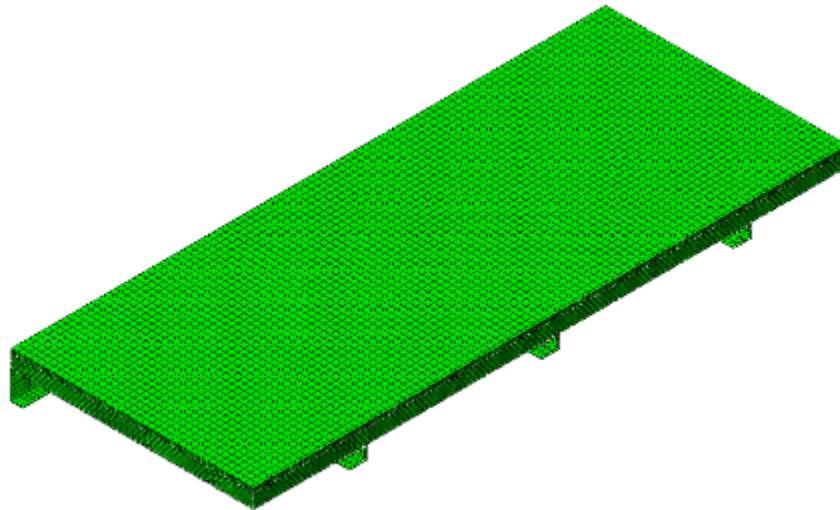
Figure 5-7. Thermal Finite Element Mesh for Section of Representative Floor Assembly.

5.5.   Structural Model

The predicted temperature response of the floor assembly was input into a sequentially coupled structural model to predict the displacement behavior during the ASTM E119 furnace exposure. The structural model consisted of identical geometry as the thermal model, except the fiberglass insulation was not included. This means the weight of the insulation (less than 1 percent of applied live load) was neglected. A live load of 3.6 kN/m^2 (75 lb/ft^2) corresponding to a typical passenger crush density of 0.2 m^2/person (2.2 ft^2/person) was applied on the entire top surface of the model resulting in a total load of 33 kN (7,560 lbs.) [90]. Additionally, the weight of the structural frame and composite floor were included in the analysis.

The modeled assembly was vertically restrained at the transverse ends and allowed to expand in the longitudinal and lateral directions according to NFPA 130 [73]. Temperature dependent material elasticity, plasticity, and thermal expansion properties were included in the model. A user subroutine (computer algorithm) was included in the structural model to track failure initiation of the composite floor due to core shear failure. The user subroutine developed to track failure initiation due to debonding was not included in this model as viable input parameters for a debonding ply-metal composite system are not in the engineering literature.

The mesh of the structural model needed to be fine enough to capture the displacement and stress behavior of the assembly during the exposure. The entire structural model was meshed using solid quadratic elements with reduced integration points (C3D20R). Quadratic elements were used because of their inherent ability to capture linear stress gradients present in bending-dominated loading configurations. The steel support frame was meshed using 38 mm (1.5 in.) seeds in the plane of the members and two elements through any member thickness. The composite floor was meshed with a 76 mm (3 in.) in plane seed and four elements through the core thickness. This provided a total of 228,000 degrees of freedom. A section of the structural mesh is provided in Figure 5-8. Mesh convergence was confirmed using general mesh seeds with 50 percent increased density over the first 200 seconds of exposure.
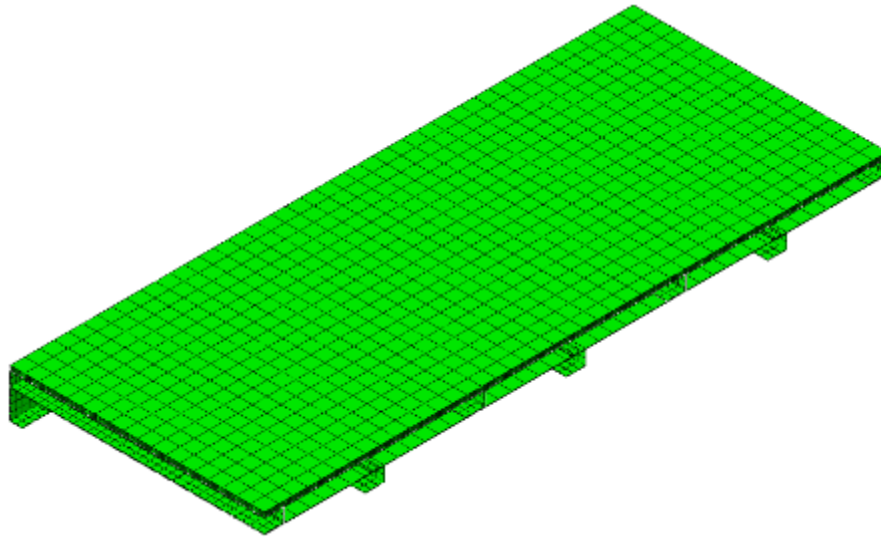
Figure 5-8. Structural Finite Element Mesh of Representative Floor Assembly

5.6.   Model Results

This section describes the results for both thermal and structural analysis.

5.6.1. Thermal Model

The thermal response of the floor assembly at several locations through the thickness of the sample is provided in Figure 5-9. Before the removal of the fiberglass insulation, the exposed surface temperature response is similar to the furnace temperature and the temperature at the bottom of the composite section remains unchanged. When the exposed surface of the insulation reaches 538 °C and is removed from the model, the

radiation exchange within the section is allowed. With the exposed hot surface at 538 °C and the opposing cold surface at 25 °C, this provided an initial ~13 kW/m2 thermal flux exchange between the two surfaces. This energy loss from the hot surface and gain at the cold surface caused the sudden heating of the composite bottom and cooling of the exposed surface after 526 seconds of exposure.
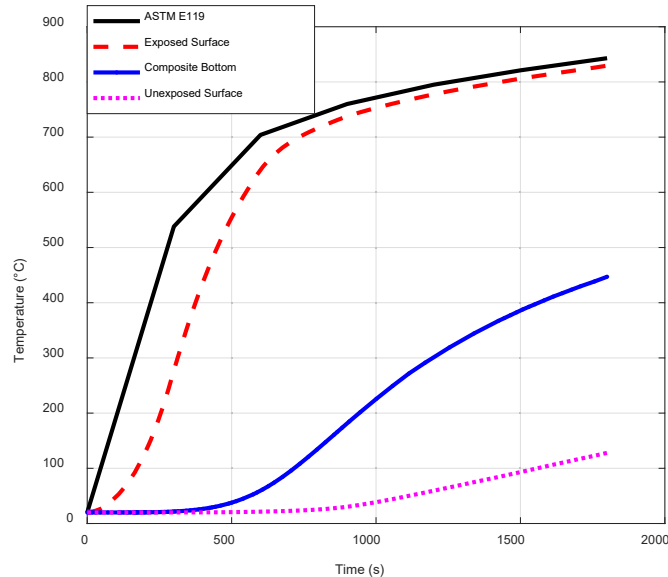
Figure 5-9. Temperature Response at Several Through Thickness Locations of the Floor Assembly

The temperature response of the unexposed surface is provided in Figure 5-10 and Figure 5-11. Figure 5-10 contains the point temperature responses obtained at locations according to ASTM E119. The hottest location temperature was 138 °C above ambient (181 °C allowed by NFPA 130 Section 8.5.1.3.3). The thermocouple mean was taken as the average of 9-point temperature measurements obtained from a 3x3 grid uniformly distributed over the location with the maximum temperature on the unexposed surface. The average measured temperature was 118 °C above ambient (139 °C allowed by NFPA 130 Section 8.5.1.3.3). Both the hottest location on the unexposed surface and the measured average temperature remained below the NFPA 130 limits for a 30-minute exposure. The hottest locations on the unexposed surface were between the structural frame elements as seen in Figure 5-11. While metallic structural frame elements generally provide a thermal short resulting in localized heating, the removal of the insulation and activation of radiative heat transfer through the sample provided a more efficient thermal path. Due to this, the structural stiffeners provided cooler locations on the unexposed surface. For insulation materials that can withstand furnace temperatures (such as mineral wool), the expected hottest locations in the spatial temperature profile would occur at the structural frame elements.
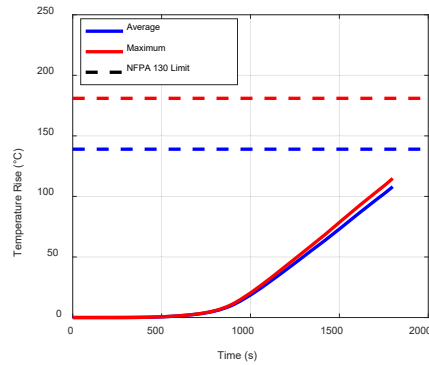
Figure 5-10. Unexposed Surface Temperature Response as Measured According to ASTM E119
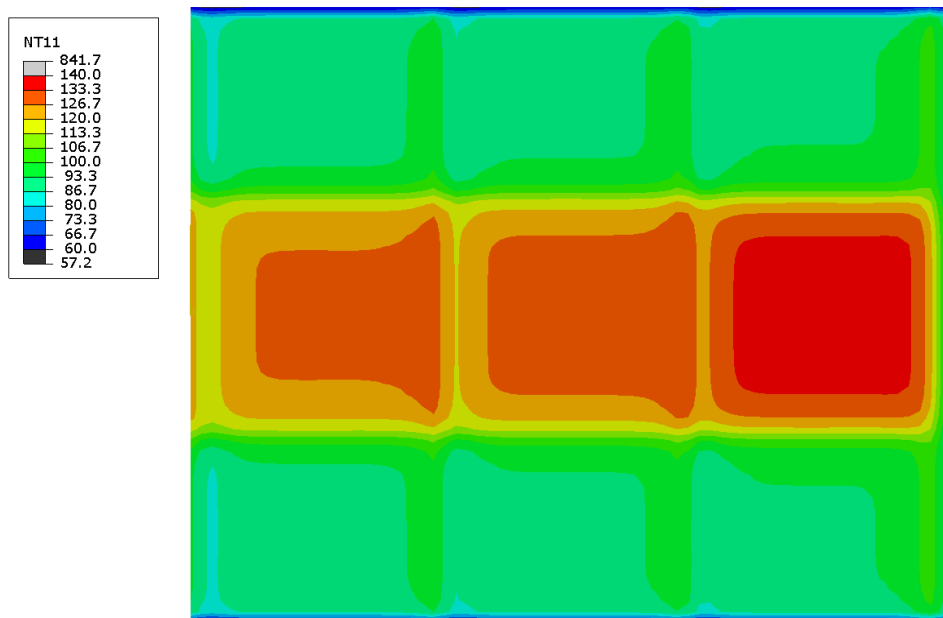
Figure 5-11. Unexposed Surface Temperature Profile at 1,800 Seconds of Exposure to ASTM E119 Furnace

5.6.2. Structural Model

The predicted vertical displacement at the center of the panel is provided in Figure 5-12. The initial panel deflection due to the applied load and assembly weight was 1.8 mm. Deflection increased to 86 mm during the first 500 seconds of exposure as the material softened and thermal gradients through the assembly thickness generated positive bending moments. When the fiberglass insulation was assumed to be lost, the deflection of the panel decreases because temperature gradients through the assembly thickness decrease by approximately 200 °C, and the bending moments are reduced. As panel heating continues, softening and strength reductions cause increased deflections.

The panel was able to sustain the applied load through the 1,800 seconds duration of the exposure meeting the structural criteria in Section 8.5.1.3.3 of NFPA 130. The

maximum vertical displacement during the exposure was 160 mm (6.3 in.). This is less than the acceptance criteria stated in ASTM E119 Section 8.8.5.1 where

$$\delta_{max} = \frac{L_c^2}{400d} = \frac{(3400 \text{ mm})^2}{400 * 177.8 \text{ mm}} = 163 \text{ mm}$$

(5-3)

where L_c is the longitudinal span of the sample and d is the total depth of the structure. A section view of the final deformed shape following 1,800 seconds of exposure is provided in Figure 5-13. The maximum deflection at the center of the assembly can be seen. Additionally, the local buckling of the lower steel sheet caused by thermal expansion and confinement by the cooler structure can be seen.
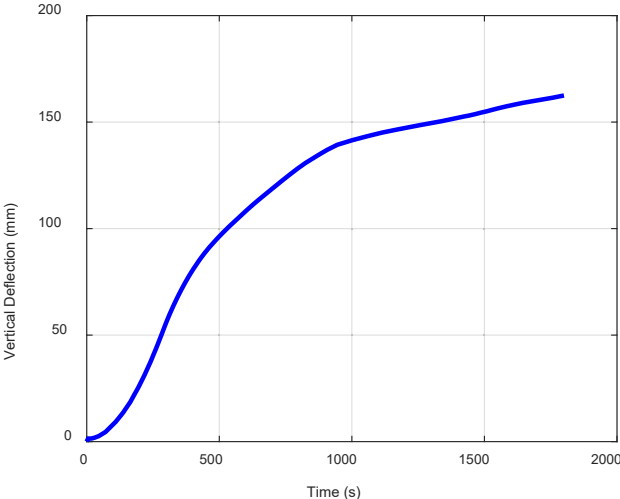
Figure 5-12. Vertical Displacement Response at the Center of the Representative Floor Assembly
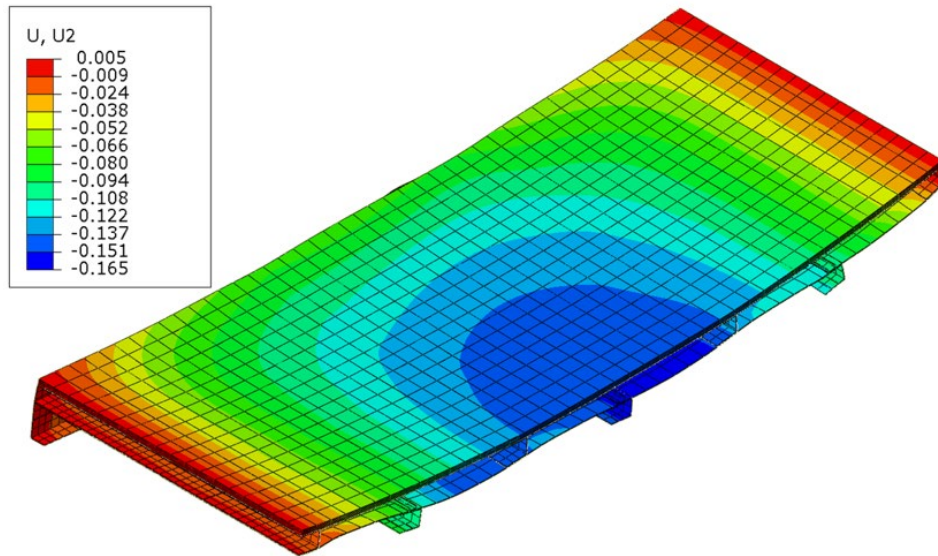
Figure 5-13. Out-of-Plane Displacement Contour on Deformed Geometry Following 1800 Seconds of ASTM E119 Furnace Exposure

5.7. Section Summary

A study was conducted to develop modeling methods necessary for predicting the response of rail car floor assemblies to standard fire resistance experiments. This included the investigation and development of relevant thermal and mechanical material property models, section modeling methods, and analysis of an exemplar assembly. Floor assembly materials were investigated in three different groups: structural framing materials, fire insulation materials, and composite floor materials. Material and section models for structural framing are generally well established within the engineering literature and present within building codes around the world, particularly the Eurocodes. Insulation material properties are less standardized and reported values vary between manufacturers of the material. Additionally, locating property data at temperatures typical in fire resistance testing can be difficult if the insulation material is not rated to such temperatures. Composite section material properties are not as well understood and documented because they are often more complex than framing and insulation materials. Organic composite materials such as wood and polymers undergo decomposition and pyrolysis. For these simulations where the wood is on the unexposed side, the decomposition is expected to be limited and the simplified material models that are viable for FE analyses are adequate for predicting thermal response of assemblies. Such a material model was developed here for commercially available fire retardant plywood.

An exemplar thermo-structural analysis of a rail car floor assembly was conducted using the commercially available FE code Abaqus. The underside of the assembly was exposed to an ASTM E119 furnace exposure with natural convection on the unexposed surfaces. The assembly weight and an applied crush load of 3.6 kN/m^2 (75 lb/ft^2) was applied to the top surface. The predicted average and maximum unexposed surface temperatures following a 30 minute ASTM E119 furnace exposure were 118 °C and 138

°C, respectively. This is below the limits of 139 °C for the average temperature and 181 °C for the maximum temperature. The assembly was also predicted to be able to carry the applied structural load for 30 minutes with a peak deflection on the unexposed surface of 160 mm (6.3 in.). Ultimately, the model predicted a 30-minute resistance rating with reasonable thermal and mechanical behavior predictions. Comparison of the model results with test data on an actual rail car floor assembly would further demonstrate the ability of the model performance. This model will serve as a full scale prediction baseline and has shown that the methodology can be used to capture floor assembly response to furnace exposure making it suitable for a numerical investigation into the feasibility of reducing the physical scale of experiments.

6. Evaluation of Real Fire Exposures on Thermal Response of Rail Car Floor Assembly

Current standards such as NFPA 130 require rail car floor assemblies to achieve a fire resistance rating according to ASTM E119 by exposing the assemblies to a prescribed 30-minute duration time-temperature curve using a furnace [91] [74]. Though the ASTM E119 is a standard test procedure, it does not represent a real fire scenario which can have temporally and spatially varying exposure. This work developed a computational framework to evaluate and compare standard fire exposures such as ASTM E119 to realistic fire exposures by determining the difference in the temperature rise of a rail car floor assembly.

A series of simulations were conducted to predict the results of exterior realistic fire scenario incidents identified in Section 2 that involved railroad passenger equipment. The simulations performed in this effort were intended to evaluate the thermal response of the undercar floor assembly when the undercarriage is exposed to realistic fires. The undercar geometries investigated were representative of single-level and bi-level passenger cars from across the United States. Separation between the top of the rail and the rail car floor structure in the geometries that were modeled ranged from 12 inches to 48 inches. The thermal exposures from these simulations were applied to a representative floor assembly section to analyze the heat transmission across the various components of rail car floor. The performance of rail car floors exposed to real exposure was compared with the ASTM E119 exposure to reevaluate the standard exposure duration of 30 minutes.

6.1. Modeling Methodology

JENSEN HUGHES conducted the simulations on rail car models that replicated actual rail cars as closely as possible to the dimensions identified in site surveys. Two rail car undercarriage configurations were modeled in these simulations: one which contained undercar equipment that formed a channel along the length of the car and corresponded to a single-level intercity rail car, and one which had no undercar components and corresponded to bi-level intercity rail cars. Three fire scenarios that were identified in a review of train accidents (Section 2) were simulated to quantify the thermal exposure to the undercar floor assembly of the rail car when exposed to these realistic fires. All simulations to predict the fire dynamics and the resulting thermal exposure onto the rail car were performed using the CFD code FDS [71]. The thermal exposure at the underside of the rail car assembly was extracted using the heat transfer coefficient and the adiabatic surface temperature (AST) provided by FDS. These spatial-temporal exposures were coupled with a detailed rail car floor assembly FE model in Abaqus to analyze the thermal behavior of the assembly [1]. The thermal model in Abaqus provided the evolution of temperature in different components of a floor assembly consisting of a structural frame, an insulation layer, and a composite floor. The standard scenario (ASTM E119) was simulated for 2 hours instead of the typical 30 minutes to identify the appropriate exposure duration which might better represent a real fire scenario.

6.1.1. FDS Model

FDS is a CFD code developed by NIST for buoyancy-driven fluid flow that is capable of representing smoke and heat transfer due to fires [71]. FDS numerically solves a form of the Navier-Stokes equations for low Mach number flows. FDS uses a predictor-corrector solution algorithm, which is second-order accurate in space and time. Turbulence is modeled according to the Large Eddy Simulation (LES) approach. Convective heat transfer to surfaces is calculated according to a combination of natural and forced convection empirical correlations. A radiation transport equation for gray gas is solved in the model using the Finite Volume Method with approximately 100 discrete angles. In this work, complex stoichiometry was defined for several individual combustion reactions in each simulation with the mixing-controlled combustion model, which means the reaction rate was infinite and only limited by species concentrations. This combustion model is a simplification of the actual physics present in fires and is generally a conservative approach to fire modeling. Details of the physics represented and solution approach for FDS are available in the technical literature [92].

Geometry is represented in FDS using a rectilinear grid, and all geometric elements must conform to the underlying grid. Heat and mass transfer conditions at the interface between the gas and solid phases are handled with empirical correlations as a default in FDS. The solid phase in FDS is defined essentially as a boundary condition to the gas phase using surface definitions. Surfaces with associated thermo-physical properties may be defined and assigned to each geometry defined in a FDS model. Heat transfer in the solid is represented as one-dimensional and may account for temperature-dependent thermal properties and heat release or absorption due to reactions. Multiple computational meshes may be defined in a FDS model, which facilitates parallel processing to expedite simulations. This feature was utilized for all the models constructed in this work. By utilizing parallel computing with multiple meshes, the average runtime for full rail car simulations was approximately 7 days to simulate a 1 hour fire.

FDS has been under development by NIST for the past few decades and the first public release was made available in 2000. Development is ongoing, but in the ensuing 17 years, the physics represented in FDS were extensively verified and the modeling methodology was validated for use in a wide range of building, transportation vehicle, and outdoor applications. In validation cases where heat fluxes and ASTs were measured at various elevations and radial distances from open flames, FDS predictions were within 10 percent of experimental data when the HRRPUA was within the range used in this work [93]. The FDS development team and beta testers include several JENSEN HUGHES engineers. All simulations presented here were conducted with FDS Version 6.5.2.

The multi-physics CFD calculations conducted as part of these FDS simulations are complicated and there are several possible sources of error that may contribute to uncertainty in the final results. Geometry, combustion chemistry, and heat transfer parameter definitions have an effect on the results presented in the following sections. Due to the purpose of these simulations to understand realistic fire exposures that occur underneath passenger rail cars and to pass these data to a more detailed three-dimensional thermal and structural model, it is most important that the geometry

represented in the heat transfer model is identical to the geometry represented in the detailed thermo-structural model. There is some uncertainty in the geometry represented in both models as compared to the real flooring assemblies, but this uncertainty is unlikely to affect the exposures from the undercar fires and the geometry represented here was intended to provide a conservative representation of typical rail car structures.

The combustion chemistry presented in the following section was defined to represent a stoichiometric, balanced equation for the combustion reaction for each presented fuel. This idealization typically results in approximately the highest possible temperatures produced from a combustion event and also means that if the requisite amount of oxygen is not available in a given computational cell, combustion will not occur. In fact, combustion may be possible at a small range of lower oxygen concentrations, but the chemical species produced and energy released in such reactions are not well-studied for these fuels and it is known that the flame temperatures are lower in such a situation. Ultimately, the combustion chemistries defined in these simulations have been determined as conservative representations of the fuels that have been studied here.

The heat transfer properties in FDS may also be a source of uncertainty because empirical convective heat transfer coefficients based on natural and forced convection are used that are typically lower than the expected convection coefficients for locations of fire impingement. There is also uncertainty in the surface radiation properties of the solid objects that are modeled in FDS. To account for these issues, the emissivity of all surfaces was defined conservatively and the AST is the metric that has been most fully investigated in this work and is used in coupling between the fire model and the detailed heat transfer model. The AST is capable of capturing the total amount of energy transferred to the surface, and with knowledge of the convection coefficient, the total heat flux to a surface may be calculated in a more detailed thermal model. The potential uncertainties were taken into consideration when constructing FDS models in this work and the resultant models are realistically conservative.

6.1.2. Abaqus Model

A coupled thermal analysis (Section 5) was performed for an exemplar rail car floor assembly using the commercially available FE code Abaqus. The thermal exposure was extracted from the FDS simulation for a whole rail car and applied to a Abaqus modeled section which was 3.4 m (11.2 ft.) long with structural repetitions every 1.1 m (3.6 ft.). The modeled section width was 2.7 m (9 ft.) representing the entire rail car width. The section consisted of a stainless steel 304 (SS304) structural frame below a SS304 and plywood (ply-metal) composite floor protected by spun fiberglass blanket insulation as shown in Figure 6-1. The frame was surrounded with fiberglass blanket providing 76 mm (3 inch) insulation thickness below the ply-metal floor. The detailed investigation and development of relevant thermal and mechanical material property models, section modeling methods, and analysis was addressed in Section 5.
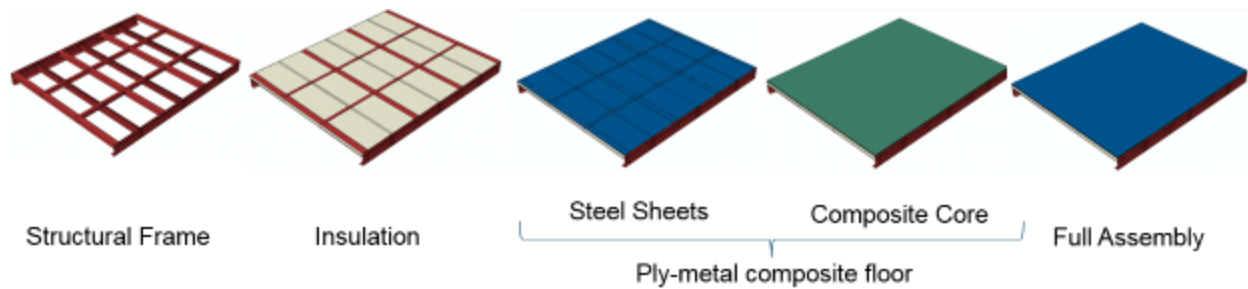
Figure 6-1. Various Components and Abaqus Model Geometry Used for the Standard and the Realistic Exposures

These models undergoing standard and realistic fire exposures were evaluated against the following requirements according to NFPA 130 2017 8.5.1.3.3:

1. Transmission of heat through the assembly shall not be sufficient to raise the temperature on its unexposed surface more than 139 °C (282 °F) average and 181 °C (357 °F) at a single point.

2. The thermocouple average is taken as the average of 9-point temperature measurements obtained from a 3x3 grid (10 ft. X 8 ft.) uniformly distributed over the unexposed surface. The highest and mean temperatures on the unexposed surface are used to evaluate both real and standard fire scenarios in this work.

6.1.3. Insulation Model

The thermal properties of the insulation model used in this work and available in the literature are provided for temperatures up to ~550 °C (1,022 °F), see Appendix F.3. This temperature is the maximum operating temperature as stated by the manufacturers. However, the exposed surface of the insulation in fire resistance tests is close to the furnace temperature which is ~850 °C (1,562 °F) for ASTM E119. This means that a typical fire resistance test would result in the degradation of fiberglass insulation. Once the insulation has degraded, cavity radiation within the degraded insulation space would be a mode of heat transfer in addition to conduction. Convection in the cavity was not included. To model the thermal response of a fiberglass insulated panel, the inclusion of radiative heat transfer mechanism is needed.
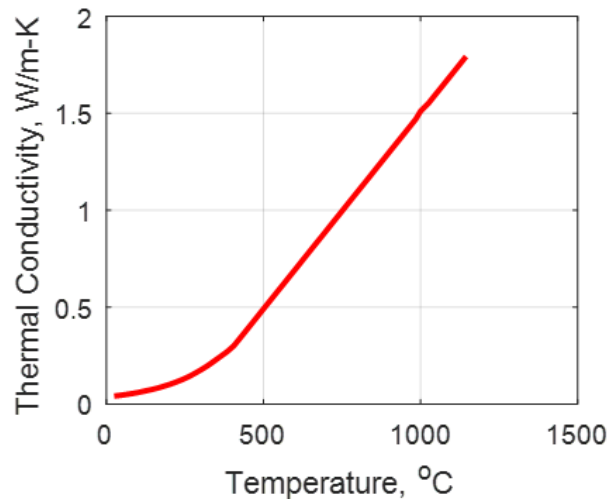
Figure 6-2. Extrapolated Thermal Conductivity at Higher Temperatures for the Insulation Model

A few approaches were identified to better represent the insulation model. An insulation thickness of 76 mm (3 in.) is considered for all the approaches. In the first approach, the thermal analysis was conducted with the insulation present until it reaches its maximum operational temperature, then the insulation is removed from the model and the analysis allowed to continue. The removal of insulation as soon as the operating temperature is reached can result in the underprediction of insulation efficiency due to a sudden loss of insulation. While the actual process is more complex, this approach represented the change in the heat transfer mechanics in a simple manner. In the second approach, the thermal properties of the insulation were extrapolated to a higher temperature (Figure 6-2) and the insulation was retained throughout the analysis. In this approach, the heat transfer across the insulation increases with temperature because the thermal properties were extrapolated to elevated temperatures. Although this approach involved retaining the insulation, it overpredicted the efficiency of the insulation as its degradation above 550 °C (1,022 °F) was not considered. Moreover, the increase in the heat transfer due to the addition of cavity radiation was substituted by increasing the thermal conductivity of the insulation.

The temperatures recorded at several through thickness locations for both approaches are shown in Figure 6-3. In the first approach, when the insulation is removed, the rate of increase of temperature (solid blue line) at the exposed surface is decreased. The exposed surface, which is nearly adiabatic, suddenly exhibits cavity radiation when the insulation is removed. In the second approach, in which the insulation is retained throughout the analysis, the temperature at the exposed surface follows the prescribed temperature, behaving as an adiabatic surface throughout the simulation. This happens due to less loss of heat as the insulation remains present throughout the analysis. The highest and mean temperatures at the unexposed surface as measured according to ASTM E119 are shown in Figure 6-4 for both models. Figure 6-4(a) shows the underprediction of the insulation efficiency for the model in which the insulation is removed after the operating temperature has been reached. This resulted in higher temperatures at the unexposed surface and the model failed to satisfy the ASTM criteria

96

at 1,800 seconds (30 minutes) which is a standard test duration specified in NFPA 130. However, Figure 6-4 (b) shows the overprediction of the insulation efficiency for the model which retained the insulation throughout resulting in satisfaction of the ASTM limit for a duration significantly longer than the test duration.

Though these approaches helped to understand the insulation behavior, they did not represent the degradation of insulation leading to shrinkage seen in the post-test pictures shown in Figure 6-5. In addition, Figure 6-5 also shows that the insulation is sagged/shrunk but is still present after the test.
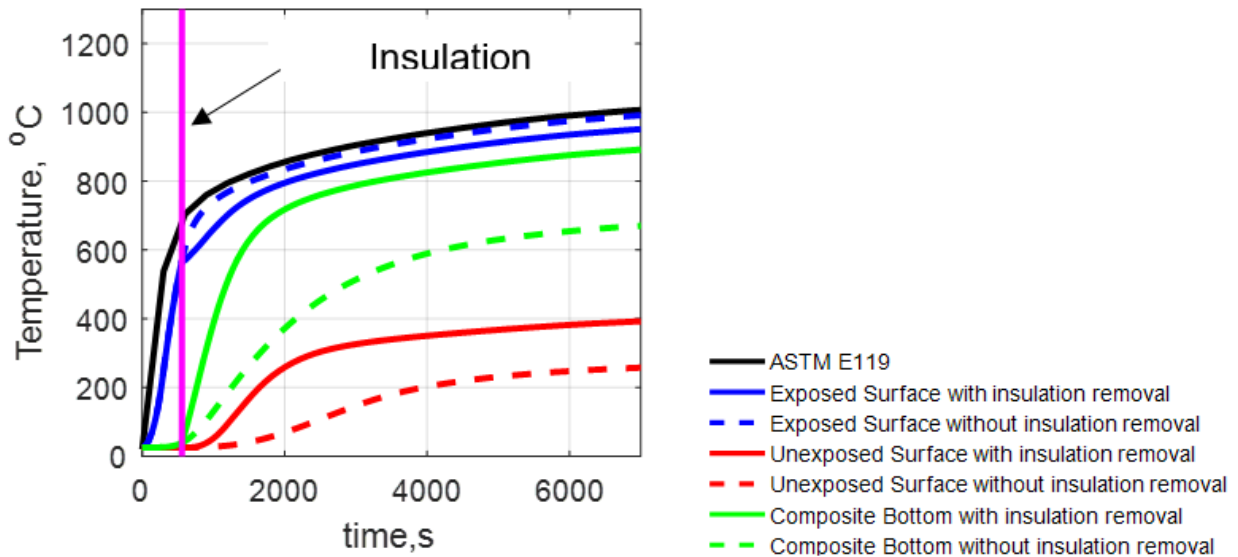
Figure 6-3. Variation of Temperature with Time for Several Through Thickness Locations for ASTM E119 Exposure to a Rail Car Floor Assembly
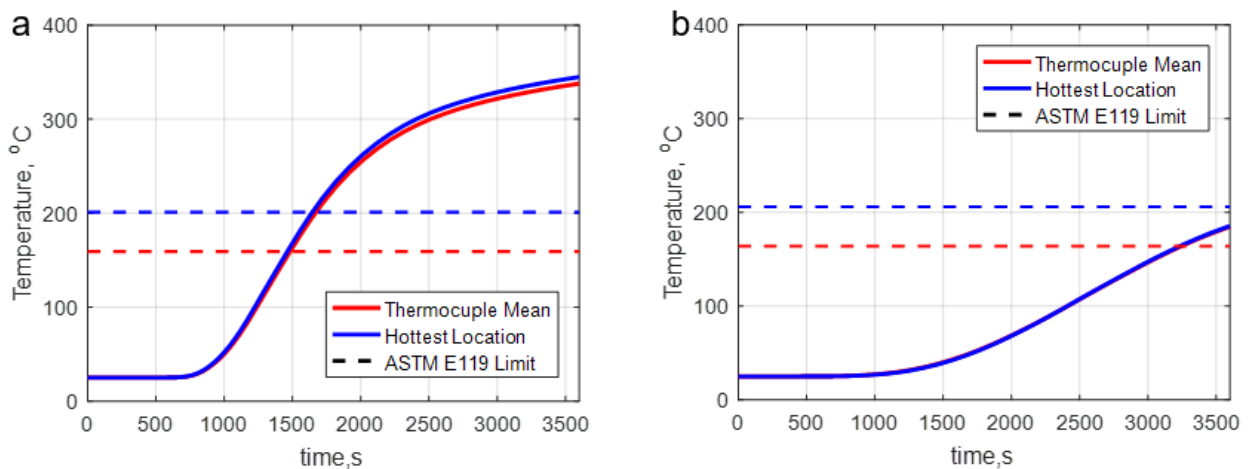
Figure 6-4. Temporal Variation of the Mean and the Highest Temperature on Unexposed Surface During ASTM E119 Exposure (a) Model with the Removal of Insulation (b) Model Without the Removal of Insulation. The Blue and Red Dashed Lines Represent the ASTM E119 Limit for Hottest and Mean Temperature

Figure 6-5. Post-Test Pictures of the Unexposed Surface of a Rail Car Floor Showing Shrunken/Degraded Insulation

A final approach used a thermal contraction model to represent the shrinkage of insulation. This model assumed that the insulation starts shrinking at 500 °C (932 °F) and melts completely at 1,500 °C (2,732 °F) which is the melting point of glass [94]. The thermal contraction factor is assumed to be orthotropic with shrinkage taking place only in the direction perpendicular to the exposed surface. This results in only α_{33} having a non-zero value which is the component of thermal contraction in the direction perpendicular to the exposed surface and its values are provided in Table 6-1. In addition, this model required the use of the coupled thermo-structural analysis in Abaqus without any external loads. This was done to capture the displacement degrees of freedom associated with the insulation model.

Table 6-1. Thermal Expansion Coefficients for the Insulation Model in Different Directions. α_{ii} Represents the Value of Thermal Expansion Coefficient in the ith Direction

α_{11} (°C⁻¹)	α_{22} (°C⁻¹)	α_{33} (°C⁻¹)	Temperature (°C)
0	0	0	0–500
0	0	-0.001	500–1,500

Finally, this model allowed representation of the two heat transfer modes (i.e., conduction and radiation) simultaneously. The heat is transferred by conduction mode from the exposed surface to the lower surface of insulation and by the radiation mode from the top surface triggered by exposing the top surface as the temperature is increased. Note that none of the approaches considered convective heat transfer in the cavity. The shape of insulation before and after the ASTM E119 exposure for 2 hours is shown in Figure 6-6.
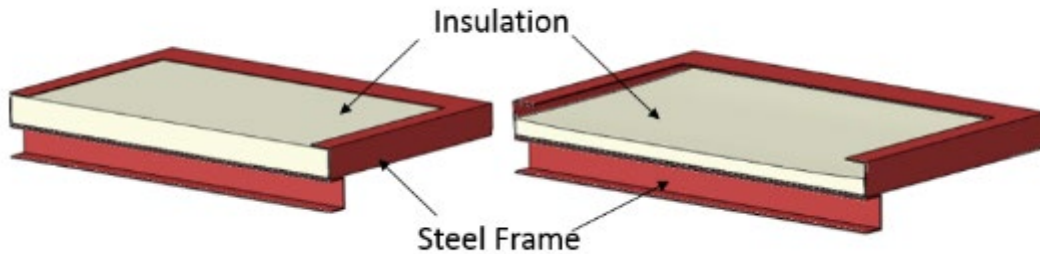
Figure 6-6. Abaqus Insulation Geometry Showing the Initial (Left) and the Final (Right) Insulation Shapes Enclosed in the Stainless Steel Frame After an ASTM E119 Exposure for 2 Hours

The vertical displacement of the insulation with time as the temperature is increased is shown in Figure 6-7. This model intuitively captures the shrinkage of insulation as the temperature is increased and needs to be validated. It is recommended that small-scale thermal experiments be performed to create test data for the validation of this model.
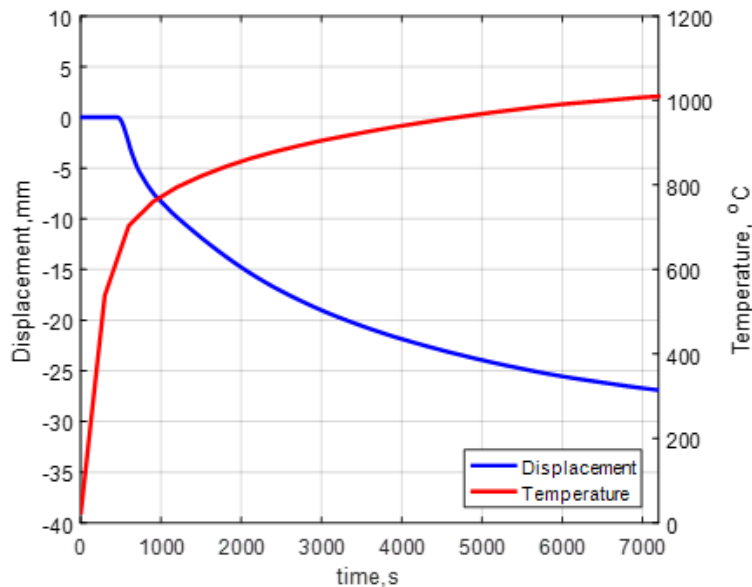
Figure 6-7. Vertical Displacement at the Center of the Insulation Model Along with the ASTM E119 Time-Temperature Curve

The temperature recorded at several through thickness locations using the new insulation model is shown in Figure 6-8 (a). Figure 6-8 (b) shows the comparison of the unexposed surface temperature for all three models. The temperature rise for the new model is approximately an average of the temperature values calculated from the previous two models. This is because the new model represents the combination of both heat transfer modes. The developed insulation shrinkage model is believed to be able to capture the behavior of these floor assemblies beyond the 1,800 seconds (30 minutes) time period, which is required to evaluate standard fire exposures with realistic fires.

99
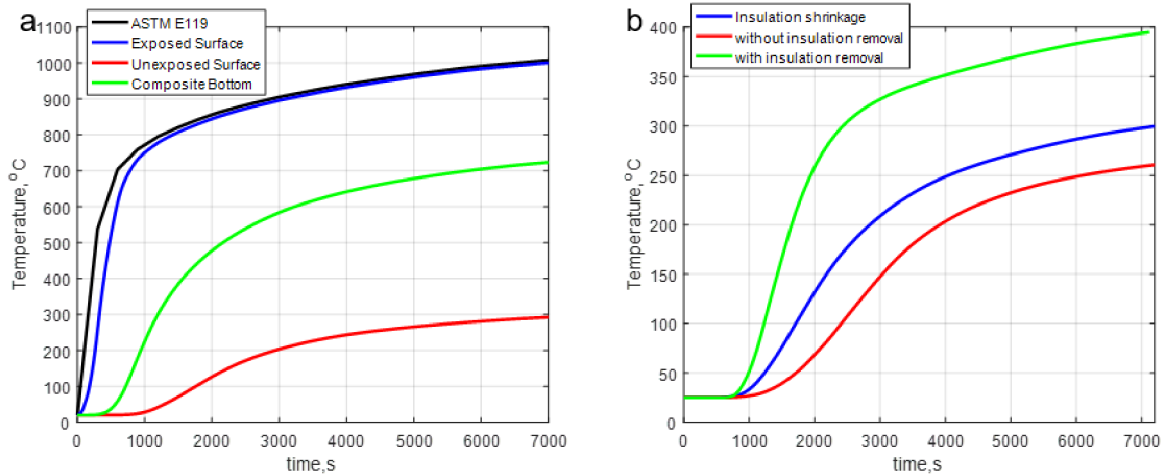
Figure 6-8. ASTM E119 Exposure (a) Through Thickness Temperature at Several Locations for Insulation Shrinkage Model (b) Unexposed Surface Temperature Comparison for All Insulation Models

6.2. Standard Exposures

Standard furnace exposures provided by ASTM E119 and UL 1709 were used for 2 hours to identify the appropriate exposure duration representative of a realistic fire [74] [95]. While NFPA 130 requires the rail car floor assembly to achieve a fire resistance rating according to ASTM E119, UL 1709 is generally used to establish the fire resistance rating for structural steel when exposed to hydrocarbon pool fires [96]. The time-temperature curves for these standards are compared in Figure 6-9. On the exposed surface, the ASTM E119 temperature exposure was used with both convection and radiative heat transfer. An ambient temperature of 25 °C (77 °F) was applied to the unexposed side boundary conditions with both convection and radiative heat transfer.
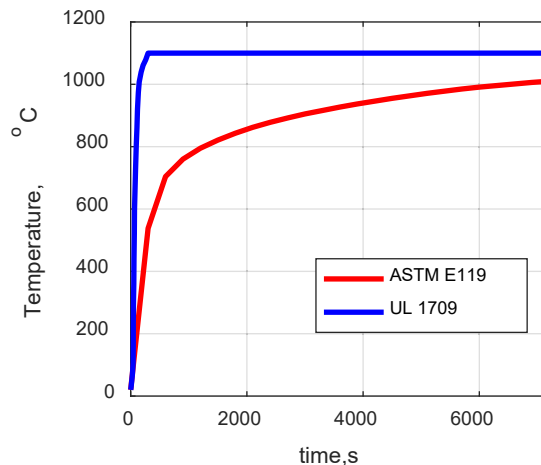
Figure 6-9. Time-Temperature Curves for Standard Exposures

The temperature contours at the exposed surface and the unexposed surface for the ASTM E119 exposure are provided in Figure 6-10. The temperature recorded at various through thickness locations is provided in Figure 6-11 (a).
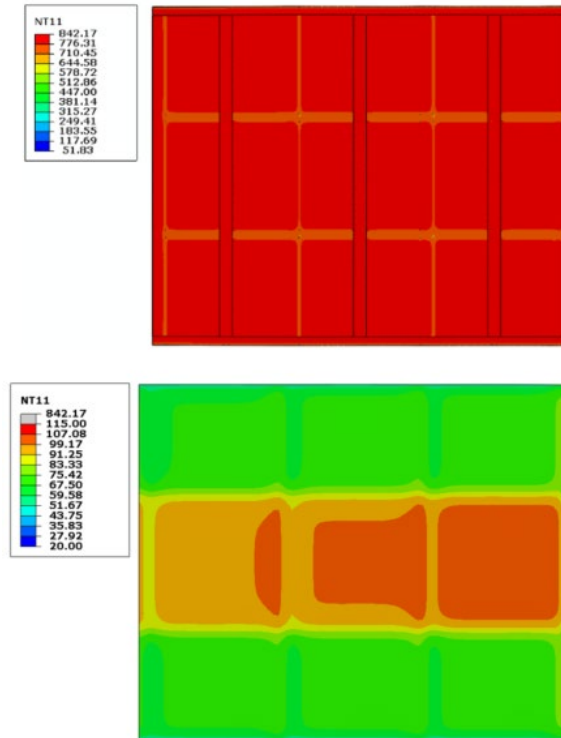
Figure 6-10. ASTM E119 Exposure (a) Exposed Surface Temperature at 1,800 Seconds (b) Unexposed Surface Temperature at 1,800 Seconds
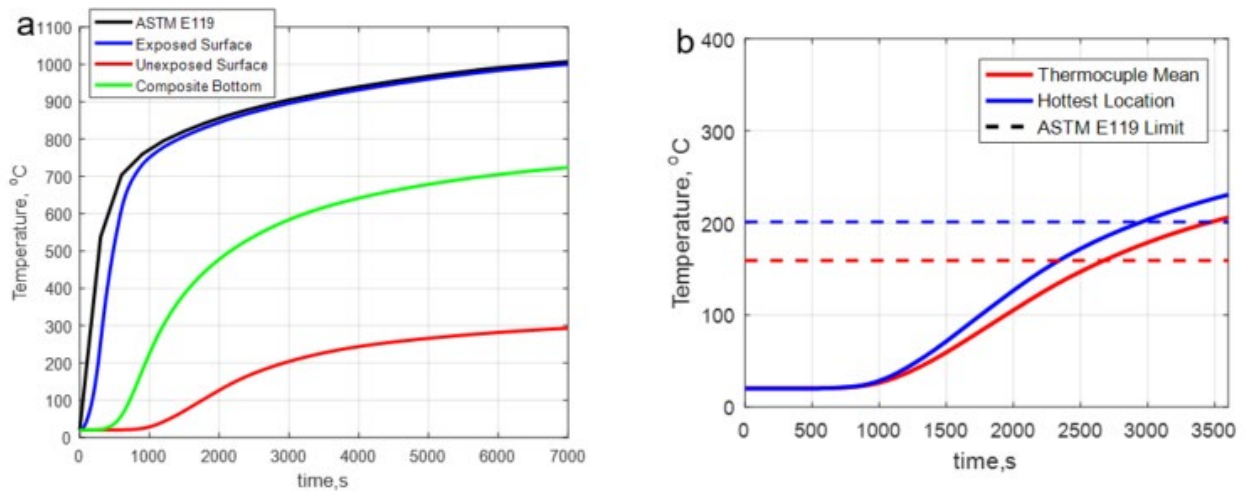
Figure 6-11. ASTM E119 Exposure (a) Through Thickness Temperature at Several Locations (b) Unexposed Surface Temperature as Measured According to ASTM E119. The Blue and Red Dashed Lines Represent the ASTM E119 Limit for Hottest and Mean Temperature

Figure 6-11 (b) shows the temperature response obtained at locations according to ASTM E119. At 30 minutes (1,800 seconds), the temperature of the hottest location was 86 °C (187 °F) above ambient (181 °C (358 °F) is allowed by NFPA 130 Section 8.5.1.3.3) and the average measured temperature was 68 °C (154 °F) above ambient 139 °C (282 °F) is allowed by NFPA 130 Section 8.5.1.3.3). Both the hottest location on

101

the exposed surface and the measured average temperature remained below the NFPA 130 limits for a 30-minute exposure. The figure also shows that the ASTM E119 limit is exceeded for both the average and maximum temperature at approximately 50 minutes (3,000 s). An identical analysis was performed with the UL 1709 time-temperature curve resulting in significantly higher temperatures compared to the ASTM E119 exposure. The temperature recorded at several through thickness locations is provided in Figure 6-12 (a). The average and the maximum temperature recorded according to NFPA 130 is shown in Figure 6-12 (b). The figure shows that both the maximum and the average temperature limits are exceeded at approximately 1,200 s (20 minutes) into the test.
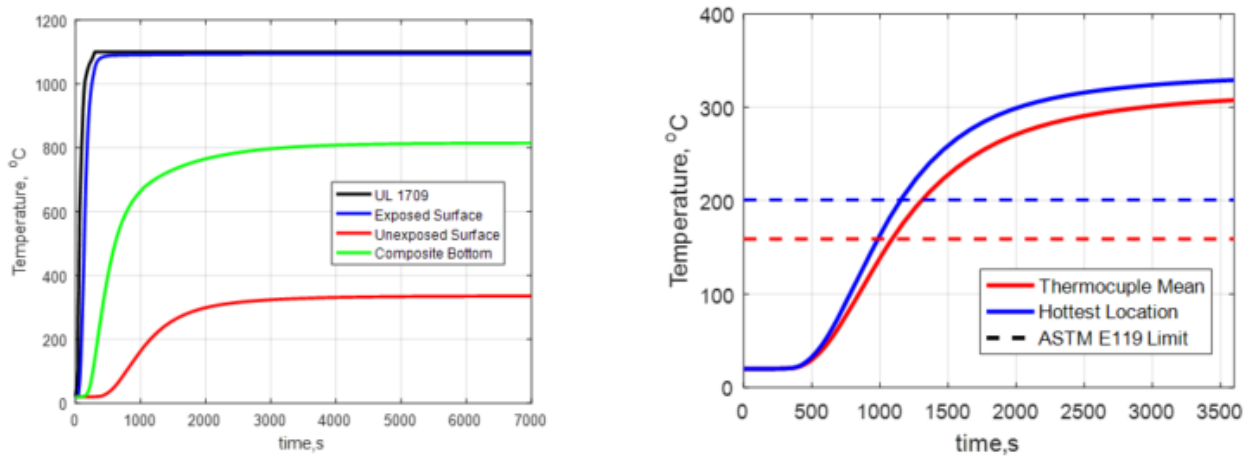
Figure 6-12. UL 1709 exposure (a) Through Thickness Temperature at Several Locations (b) Unexposed Surface Temperature as Measured According to ASTM E119. The Blue and Red Dashed Lines Represent the ASTM E119 Limit for Hottest and Mean Temperature

6.3.   Real Exposures

Six individual models were constructed in FDS that included three common undercarriage configurations and three fire scenarios.

Due to the complexity of the chemical compounds present in the fuel sources, it was necessary to define complex stoichiometry for each primary fuel source as well as for soot combustion. The following sections describe the parameters used to simulate the exposure conditions, the rail car geometry, and the reaction stoichiometry.

6.3.1. Exposure Conditions

The most common fire exposures that affect the undercarriages of passenger trains were identified in a survey of rail incidents. The fuel sources included a diesel fuel spill, a diesel fuel spill with some pooling, and a gasoline spill. All models also included cables located at the center of the rail car and extending along its length. Table 6-2 shows the chemical formula, soot yield, and carbon monoxide (CO) yield for each fuel source used in this work. The chemical reactions were balanced and the resulting reactant and product yields were defined in FDS.

Table 6-2. Fuel Chemical Formulas with Soot and CO Yields

Fuel Source	Chemical Formula	Soot Yield	CO Yield
Diesel	$C_{15}H_{28}$	1.2%	4.2%
Gasoline	C_8H_{18}	1.1%	3.8%
Cables	$0.5C_2H_3Cl$ $+ 0.5C_2H_4$	11.4%	5.0%
Soot	$C_{0.9}H_{0.1}$	-	-

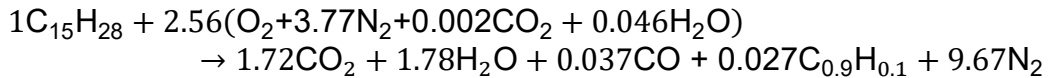### 6.3.1.1. Diesel Spill Over Flat Surface

This model represents a diesel fuel spill scenario that includes a puncture hole in the diesel fuel tank of the locomotive. The scenario was constructed assuming the train is at rest in a location with ballastless tracks and the spilled fuel is confined between the rails. It is assumed that the liquid fuel spill is ignited over a flat surface between the rails along the entire length of the modeled rail car. Due to the relatively high flash point of diesel fuel, it is assumed that flame propagates along the liquid fuel at a rate controlled by the liquid temperature. The literature shows that this rate is on the order of 0.33 ft/s (0.1 m/s) [51].

The burning rate of a diesel fuel spill was assumed to have a steady burning rate that is 20 percent of the steady burning rate for a diesel fuel pool fire based on a review of the literature [51]. The burning rate defined in the diesel fuel spill simulations was 0.015 gal/ft²min (0.0076 kg/m²s), which is consistent with fuel spill burning rates over completely flat surfaces without pooling and limited heat feedback to accelerate burning. It is assumed that the size of the puncture hole in the fuel tank causes the fuel to spill from the tank at the same rate that the liquid fuel beneath the rail car is consumed in the ensuing fire such that the fire does not spread beyond the far end of the rail car. The rate at which the fuel under the rail car is consumed is 6.1 gal/min (0.28 kg/s), which corresponds to a puncture area size of 0.305 in². To provide a reference point, a fuel tank filled with 1000 gallons of diesel fuel with a puncture orifice area of 0.305 in² results in a duration of spilling of 3.1 hour (11,070 seconds). It was determined during the review of rail car incidents (Section 2) that it is common for prompt firefighter intervention and extinguishment of large-scale diesel spill fires and that the upper limit for the duration of the fires was more typically on the order of 1 hour (3,600 seconds). As a result, the burning duration of the fire used in these simulations was set to 1 hour (3,600 seconds).

A diesel spill with dimensions of 4 ft. - 8.5 in. (1.44 m) wide (width between the tracks) and 85 ft. (25.9 m) long (length of the rail car), for a total surface area of approximately 400 ft² (37.2 m²), was simulated as part of this work. The spill fire was modeled as several surface vents with a burning rate per unit area equal to the steady burning rate for a diesel fuel spill determined from the literature [51]. Each vent had a dimension along the length of the train equal to 0.66 ft. (0.2 m). With a flame propagation rate of 0.33 ft/s (0.1 m/s) along the surface of the spill, each adjacent vent was activated sequentially every 2 seconds.

As diesel fuel is a mixture of chemicals, a representative chemical formula was defined such that complex stoichiometry could be invoked within FDS. The balanced chemical equation is displayed below. The resulting heat of combustion for this balanced equation is 39,700 kJ/kg (17068 Btu/pound).

$$1C_{15}H_{28} + 2.56(O_2 + 3.77N_2 + 0.002CO_2 + 0.046H_2O)$$
$$\rightarrow 1.72CO_2 + 1.78H_2O + 0.037CO + 0.027C_{0.9}H_{0.1} + 9.67N_2$$

6.3.1.2. Diesel Spill with Pooling

A second diesel fuel spill was considered to provide an upper bound on the severity for a fuel fire scenario. In this scenario, diesel fuel was spilled between the tracks and allowed to pool. With this pooling, the burning rate of the fuel is increased. The steady burning rate of diesel in this scenario is 0.075 gal/ft^{2}min (0.038 kg/m^{2}s), which is the value for a diesel pool fire. In addition, this could represent the scenario where there is limited pooling between the tracks but there is significant radiation heat feedback to the fuel surface from the rail car. This scenario followed the same liquid-controlled flame spread rate and combustion model as the diesel fuel spill scenario described in Section 6.3.1.1.

6.3.1.3. Automobile Gasoline Fuel Spill

A common cause of incidents identified in the review is a collision with an automobile at a highway-railroad crossing. It was determined that the most likely fuel source in a fire resulting from this type of incident is gasoline draining from the automobile fuel tank. To simulate leakage of gasoline from an automobile fuel tank, a nozzle was defined in the model that injected fuel droplets modeled as Lagrangian particles into the domain. The rate of the spill was calculated as 6.7 gal/min (0.00042 m^3/s) based on a 22-gallon capacity fuel tank emptying through a 4 in. x 4 in. puncture hole over approximately 200 seconds. The spill spread rate across the ground between the rails was defined as 0.33 ft/s (0.1 m/s). The stoichiometric chemical equation defined for combustion of the gasoline is represented below.

$$C_8H_{18} + 12.07(O_2 + 3.76N_2) \rightarrow 7.56CO_2 + 8.98H_2O + 0.44C_{0.9}H_{0.1} + 0.04CO + 45.38N_2$$
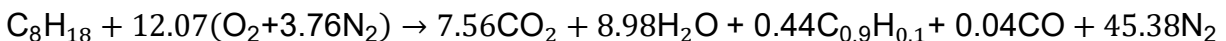
FDS accounts for the rate of evaporation of liquid fuel droplets by calculating the liquid equilibrium vapor fraction using the Clausius-Clapeyron equation. Combustion of vaporized fuel is also explicitly accounted for in FDS, which results in a feedback loop that adjusts the rate of evaporation based on the heat generated from combustion. Additional technical details of the droplet evaporation model are available in the FDS Technical Reference Guide [97].

6.3.1.4. Cables

Cables were defined under the rail car for all simulations unless otherwise noted. The cable jacket and insulation were assumed to be composed entirely of cross-linked polyethylene [98]. Visits to rail car maintenance centers revealed that cables for the rail cars represented in these simulations were not housed in conduit beneath the cars with higher clearance and were typically grouped together with approximately 1–2 diameters of separation between the cables. Cables were modeled as solid obstructions in close proximity to the underside of the rail car with a surface area equal to 2 ft^2/ft. (0.6 m^2/m),

which is consistent with eight 1 in. diameter cables. The cables were assigned the thermo-physical properties typical of polymers. The balanced chemical equation for combustion of polyethylene is provided below:

$$C_2H_4 + 2.70(O_2+3.76N_2) \rightarrow 1.68CO_2 + 1.99H_2O + 0.005CO + 0.30C_{0.9}H_{0.1} + 10.16N_2$$
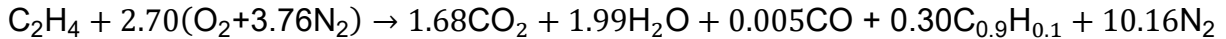
The resulting heat of combustion for this balanced equation is 40,900 kJ/kg (17068 Btu/pound). The HRRPUA of typical cross-linked polyethylene cables has been measured by researchers at NIST [99]. The time-dependent HRR of the cables defined in this work is displayed in Figure 6-13. The maximum HRRPUA of the defined fire is approximately 215 kW/m^2. The ignition temperature of the cable jacket was defined as 804 °F (429 °C), according to a critical heat flux for ignition equal to 16 kW/m^2 [51].
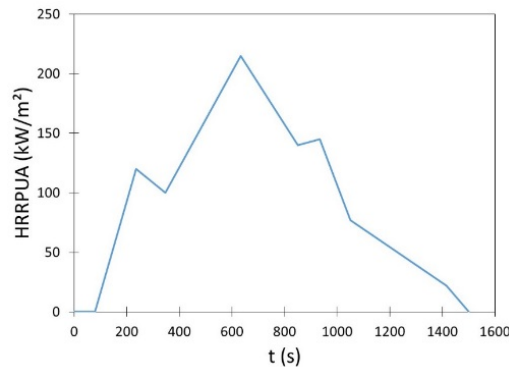
Figure 6-13. HRRPUA Defined for Cable Fire

6.3.1.5.   Soot

Soot oxidation is a topic that is consistently being researched to improve understanding of the chemical and kinetic parameters that best describe the reactions. The default chemical definition of soot in FDS is $C_{0.9}H_{0.1}$. The balanced chemical equation for soot oxidation is provided below. This reaction was defined in all simulations to account for the contribution of heat release due to oxidation of soot.
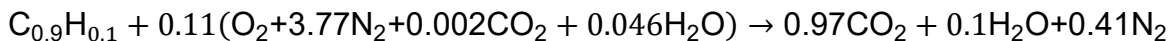
$$C_{0.9}H_{0.1} + 0.11(O_2+3.77N_2+0.002CO_2 + 0.046H_2O) \rightarrow 0.97CO_2 + 0.1H_2O+0.41N_2$$

6.3.2. Geometries

The survey of incidents and site visits to several railyard facilities on the East and West Coasts of the U.S. revealed a wide range of undercar configurations. The scope of these simulations was developed to provide a range of floor clearance levels above the track based on rail car field measurements to assess the impact of this on fire exposure onto the floor. A previous report revealed that the most severe exposure to the undercarriage of single-level passenger rail cars that were found on the East Coast occurred with a configuration that included a clearance of approximately 40 inches (1.0 m) between the top of the rail and the lowest undercar structural elements, approximately 48 inches (1.2 m) between the top of the rail and the flat-bottom floor, and included undercarriage components that created a channel along the center of the length of the car.

Visits to several railyard facilities on the West Coast of the U.S. revealed typical bi-level rail cars that have flat-bottom undercarriages with a clearance between the top of the

rail and the flat-bottom floor that range between approximately 12 inches (0.3 m) and approximately 22 inches (0.55 m). These rail car geometries were modeled with the same structural undercarriage frame as was presented in the previous report to provide a direct comparison between the exposures for each undercarriage configuration.

6.3.3. Thermo-Physical Properties of Materials

The thermal properties of all the materials included in these simulations are provided in Table 6-3, where c denotes specific heat capacity, k denotes thermal conductivity, and ρ denotes density. The absorption coefficient and emissivity of all the materials presented in Table 6-3 were defined according to the default values for FDS (absorption coefficient = 5E+5 1/m and emissivity = 0.95).

Table 6-3. Thermal Properties of Materials Defined in FDS Models

	c (kJ/kg-K)		k (W/m²-K)		p (kg/m³)
Steel [100]	20 °C	0.440	20 °C	53.3	7,850
	100 °C	0.488	100 °C	50.7	
	200 °C	0.530	200 °C	47.3	
	300 °C	0.565	300 °C	44.0	
	400 °C	0.606	400 °C	40.7	
	500 °C	0.667	500 °C	37.4	
	600 °C	0.760	600 °C	34.0	
	700 °C	1.01	700 °C	30.7	
	730 °C	2.29	800 °C	27.3	
	735 °C	5.00	900 °C	27.3	
	800 °C	0.803	1,000 °C	27.3	
	900 °C	0.650	1,100 °C	27.3	
	1,000 °C	0.650	1,200 °C	27.3	
	1,100 °C	0.650			
	1,200 °C	0.650			
Polymer (Cables) [101]	1.50	0.2			2,535

6.3.4. Individual FDS Models

FDS models were constructed to simulate the effect of various fire sources ignited beneath a full rail car that simulate common intercity and commuter trains regulated by FRA. The review of train incidents informed the worst possible realistic fire exposures. A summary of the models that are presented in this work is provided in Table 6-4. Models 1–3 involved the rail car that simulated single-level car with undercar components. Models 4–6 involved the rail car that simulated West Coast bi-level cars with a clearance between the top of the rail and the flat-bottom floor of 12 inches (0.3 m). Models 7–9 involved the rail car that simulated West Coast bi-level cars with a clearance between the top of the rail and the flat-bottom floor of 22 inches (0.55 m). The fire source for Models 1, 4, and 7 was the diesel fuel spill fire, the source for Models 2, 5, and 8 was the diesel spill fire with pooling described in Section 6.3.1.2, and the fire source for Models 3, 6, and 9 was the gasoline spill described in Section 6.3.1.3. All models also included the cables as a target fire source as described in Section 6.3.1.5.

Table 6-4. Summary of Models Constructed in this Work

| Model	Description
1	48 in. Clearance Undercarriage with undercar components with Diesel Spill Fire
2	48 in. Clearance Undercarriage with undercar components with Diesel Spill Fire with Pooling
3	48 in. Clearance Undercarriage with undercar components with Gasoline Spill Fire
4	12 in. Clearance Undercarriage with Diesel Spill Fire
5	12 in. Clearance Undercarriage with Diesel Spill with Pooling Fire
6	12 in. Clearance Undercarriage with Gasoline Spill Fire
7	22 in. Clearance Undercarriage with Diesel Spill Fire
8	22 in. Clearance Undercarriage with Diesel Spill with Pooling Fire
9	22 in. Clearance Undercarriage with Gasoline Spill Fire

6.4. Model Descriptions

This section describes the different FDS geometric models used for this work.
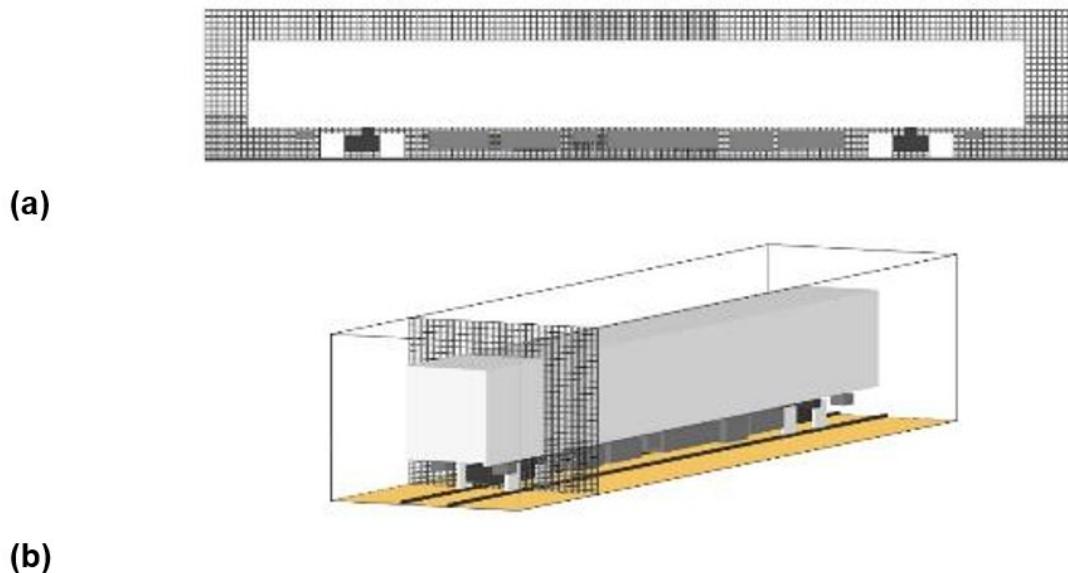
6.4.1. FDS Models

The rail cars modeled for the 48-in. clearance in this work have slightly different geometries in the region near the trucks compared to the models with 12 in. and 22 in. clearance. These differences in geometry are minimal and generally have no effect on the conclusions drawn from these analyses. Furthermore, the boundary data that were used for coupling with the detailed heat transfer model were taken from the center of the span between the trucks, which was unchanged for each simulation, with the exception of its clearance from the top of the rail.

6.4.1.1. Models 1–3

The geometry modeled in FDS Models 1–3 is displayed in Figure 6-14. Images of the grid used to mesh the rail car geometry are provided in Figure 6-15. The extents of the computational domain for FDS Models 1–3 were defined with overall dimensions of length = 94.5 ft. x width = 20.7 ft. x height = 16.4 ft. (28.8 m x 6.3 m x 5.0 m). With the exception of the solid ground, all extents of the computational domain were defined as open boundaries to allow the escape of smoke and the inflow of entrained air. An identical computational grid in six meshes was defined in each model for a total of 353,430 elements. The smallest mesh elements were located beneath the geometric center of the rail car and had dimensions of 4 in x 4 in x 4 in (0.1 m x 0.1 m x 0.1 m).

(a)

(b)
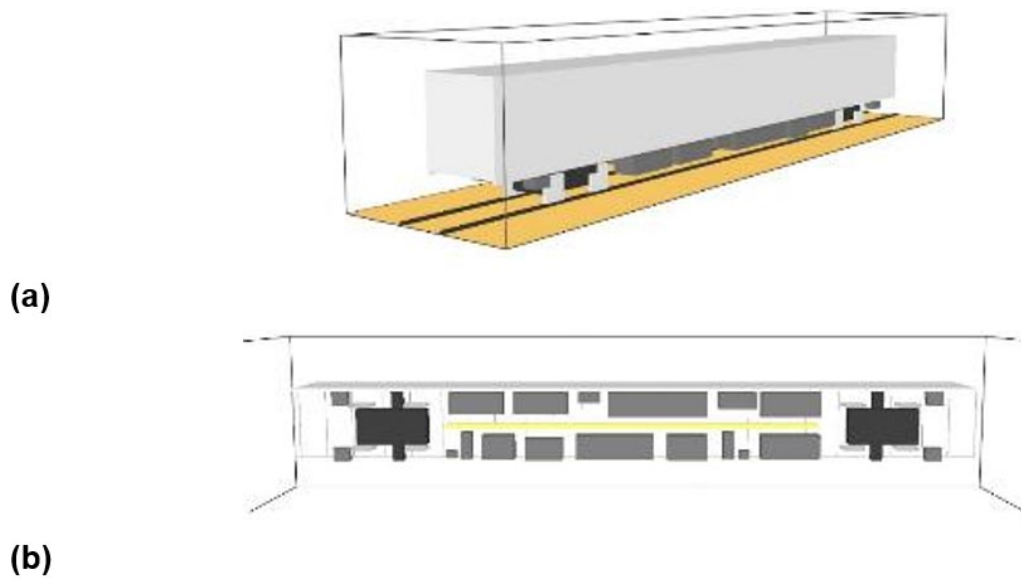
Figure 6-14. Images of Modeled Geometry for Models 1–3. (a) Perspective View (b) Bottom View

(a)

(b)

Figure 6-15. Images of Mesh Used in FDS Models 1–3 (a) Profile View (b) Perspective View

6.4.1.2. Models 4–6

The geometry modeled in FDS Models 4–6 is displayed in Figure 6-16. The modeled geometry consisted of a rail car designed to simulate West Coast bi-level rail cars with a 12 in. (0.3 m) clearance between the top of the rail and the undercarriage. Two in. (0.05 m) deep transverse beams were included along the length of the undercarriage typically spaced 44 in. (1.1 m) on center. A 4-in. deep (0.1 m) lip was also included at the outer edges of the undercarriage. The computational mesh for these models is shown in

Figure 6-17. The extents of the computational domain for FDS Models 4–6 were defined with overall dimensions of length = 94.5 ft. x width = 20.7 ft. x height = 16.4 ft. (28.8 m x 6.3 m x 5.0 m). With the exception of the solid ground, all extents of the computational domain were defined as open boundaries to allow the escape of smoke and the inflow of entrained air. An identical computational grid in six meshes was defined in each model for a total of 364,140 elements. The smallest mesh elements were located beneath the geometric center of the rail car and had dimensions of length of 4 in., width of 4 in., height of 2 in. (0.1 m x 0.1 m x 0.05 m).

(a)

(b)

Figure 6-16. Images of Modeled Geometry for Models 4–6 (a) Perspective View (b) Bottom View
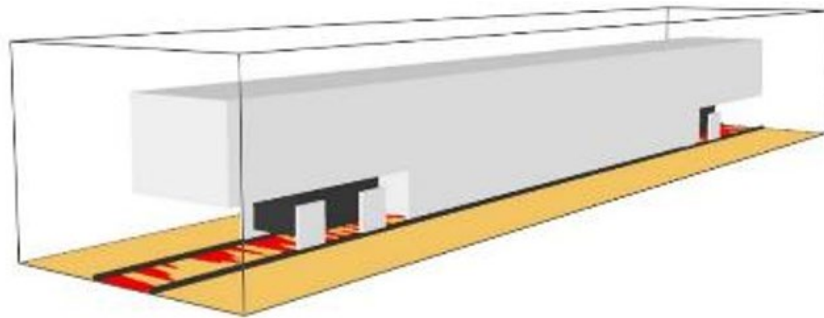
(a)

(b)

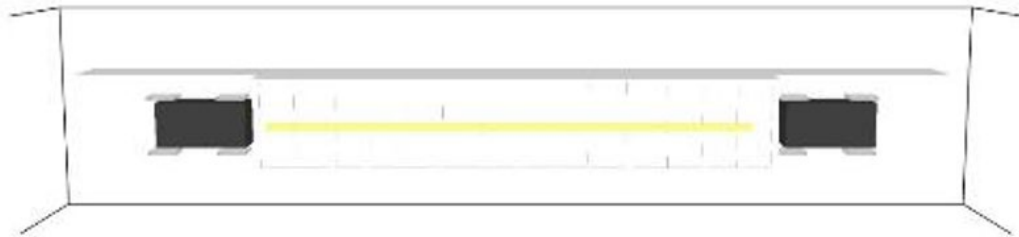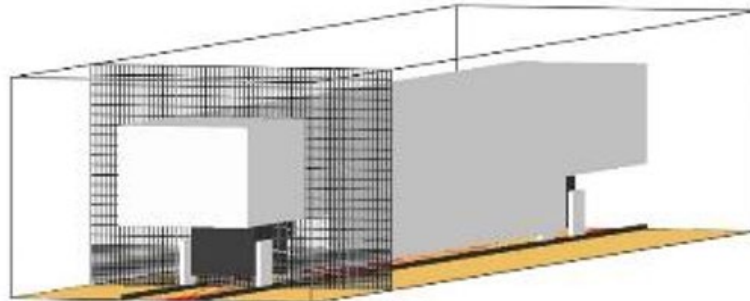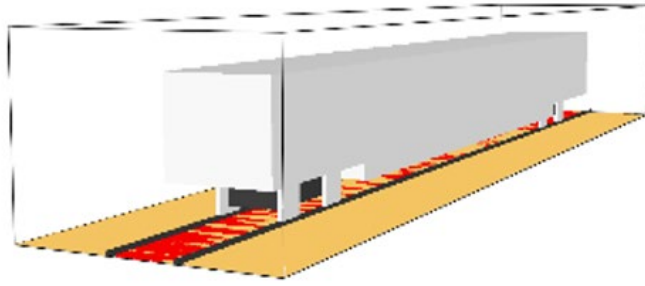**Figure 6-17. Images of Mesh Used in FDS Models 4–6 (a) Profile View (b) Perspective View**

6.4.1.3. Models 7–9

The geometry modeled in FDS Models 7–9 is displayed in Figure 6-18. The modeled geometry consisted of a rail car designed to simulate the West Coast bi-level rail cars with a clearance of 22 inches (0.55 m) above the top of the rail. Two in. (0.05 m) deep transverse beams were included along the length of the undercarriage typically spaced 44 in. (1.1 m) on center. A 4-in. deep (0.1 m) lip was also included at the outer edges of the undercarriage. The computational mesh for these models is shown in Figure 6-17. The extents of the computational domain for FDS Models 4–6 were defined with overall dimensions of length of 94.5 ft. width of 20.7 ft. height of 16.4 ft. (28.8 m x 6.3 m x 5.0 m). With the exception of the solid ground, all extents of the computational domain were defined as open boundaries to allow the escape of smoke and the inflow of entrained air. An identical computational grid in six meshes was defined in each model for a total of 364,140 elements. The smallest mesh elements were located beneath the geometric center of the rail car and had dimensions of 4 in. x 4 in. x 2 in. (0.1 m x 0.1 m x 0.05 m).
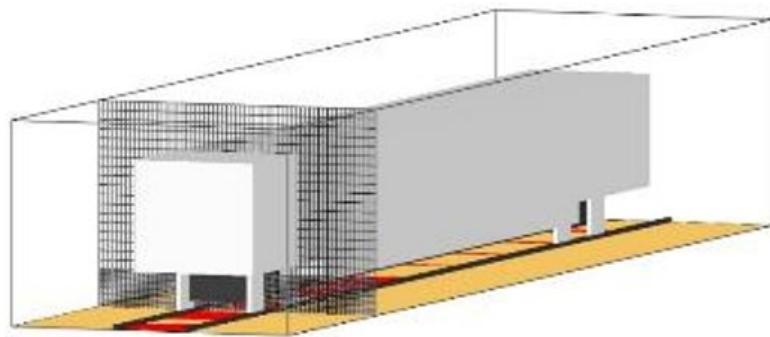
(a)

(b)

Figure 6-18. Images of Modeled Geometry for Models 7–9 (a) Perspective View (b) Bottom View

(a)

(b)

Figure 6-19. Images of Mesh Used in FDS Models 7–9 (a) Profile View (b) Perspective View

6.5. FDS Simulation Results

Data and images extracted from the FDS simulations are provided in the following sections. For each simulation the total HRR, the adiabatic surface temperature (AST), and the gas temperature at the geometric center of the rail car are displayed. Images are also provided to show the expected fire plume and smoke generation at the time the maximum HRR is achieved.

The AST is the theoretical temperature of a surface with a specified emissivity and convection coefficient that is calculated under the assumption that the surface transfers no heat away from the surface (i.e., perfectly insulated). The AST is the maximum possible temperature of the surface given the exposure conditions and can be used to calculate the incident heat flux to the surface.

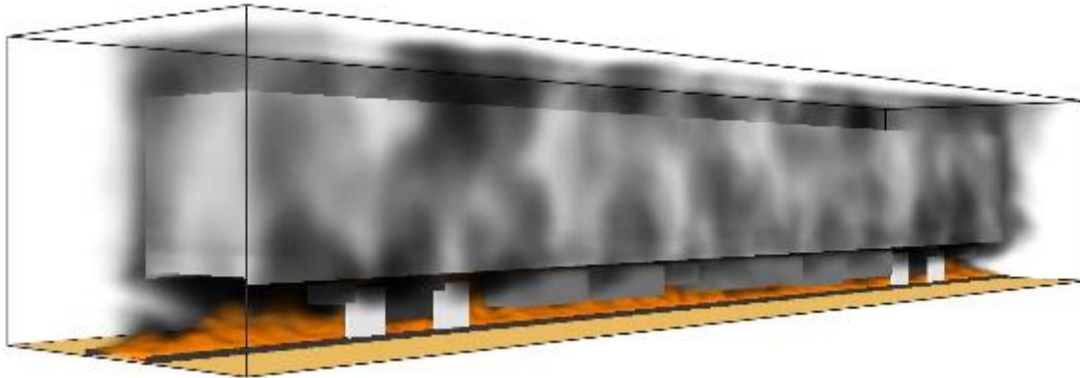### 6.5.1. Model 1 – 48 in. Clearance Undercarriage with Undercar Components and Diesel Spill Fire

The total HRR from the simulation of Model 1 is provided in Figure 6-20. This scenario involves a diesel spill rate and burning rate of approximately 6.1 gal/min. The total steady HRR for the diesel spill fire is approximately 13 MW. This is the expected total HRR for this fire source and this indicates that all the fuel vapors burn in the domain. Figure 6-21 shows the HRRPUV at 3,600 seconds (1 hour) in the simulation, which is manifested as the orange fire plume. Also shown in Figure 6-21 is typical smoke generation, shown as dark airborne soot. Figure 6-22 shows the typical gas temperature contours in the plane at the geometric center of the rail car along its length and width. These gas temperatures are in excess of 1,832 °F (1,000 °C).

Contours of the steady AST on the underside of the rail car with and without the undercar components shown are provided in Figure 6-23. The maximum AST on the undercar frame is approximately 1,472 °F (800 °C) although the mean AST is in the range of 1,022–1,202 °F (550–650 °C). The highest heat exposure is in the center of the rail car between the undercar components. The mean convection heat transfer coefficient calculated at the bottom surface of the undercar frame is approximately 10 W/m^{2}K. The maximum heat flux to the undercar frame calculated with the AST, heat transfer coefficient, and emissivity is approximately 80 kW/m^2 and the typical heat flux is in the range of 30 to 35 kW/m^2. The exposure was sufficient to ignite the cables and contribute a maximum of approximately 1.15 MW to the fire.
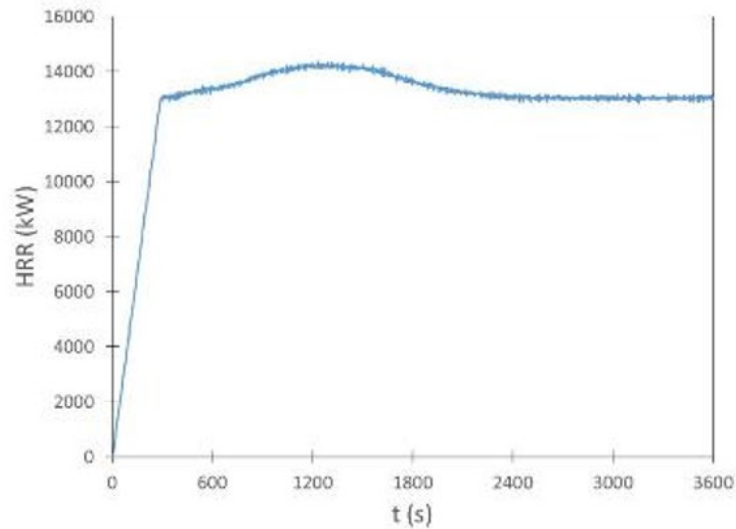
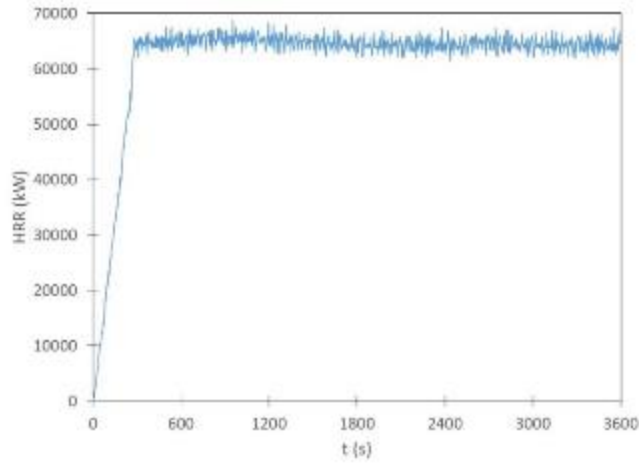**Figure 6-20. Total HRR in Model 1 (Diesel Spill Fire) Simulation**

Figure 6-21. Visualization of HRRPUV and Soot Production for Model 1 (Diesel Spill Fire) Simulation

6.5.2. Model 2 - 48 in. Clearance Undercarriage with Undercar Components and Diesel Spill Fire with Pooling

The total HRR from the simulation of Model 2 is provided in Figure 6-24. This scenario involves a significant portion of diesel fuel spilled prior to ignition and a burning rate of approximately 30.5 gal/min. The total steady HRR for the diesel pool fire is approximately 65 MW. Figure 6-25 shows the HRRPUV at 3,600 seconds (1 hour) in the simulation as well as typical smoke generation, shown as dark airborne soot. Figure 6-26 shows the typical gas temperature contours at the plane at the geometric center of the rail car along its length and width. These gas temperatures are in excess of 1,832 °F (1,000 °C). Contours of the steady AST on the underside of the rail car with and without the undercar components shown are provided in Figure 6-27. The maximum AST on the undercar frame is approximately 1,832 °F (1,000 °C) although the mean AST is in the range of 1,472–1,652 °F (800–900 °C). The mean convection heat transfer coefficient calculated at the bottom surface of the undercar frame is approximately 10 W/m²K. The maximum heat flux to the undercar frame calculated with the AST, heat transfer

114

coefficient, and emissivity is approximately 150 kW/m^2 and the typical heat flux is in the range of 80 to 110 kW/m^2. The exposure was sufficient to ignite the cables and contribute a maximum of approximately 1.3 MW to the fire.

Figure 6-22. Total HRR in Model 2 (Diesel Spill Fire with Pooling) Simulation

Figure 6-23. Visualization of HRRPUV and Soot Production for Model 2 (Diesel Spill Fire with Pooling) Simulation
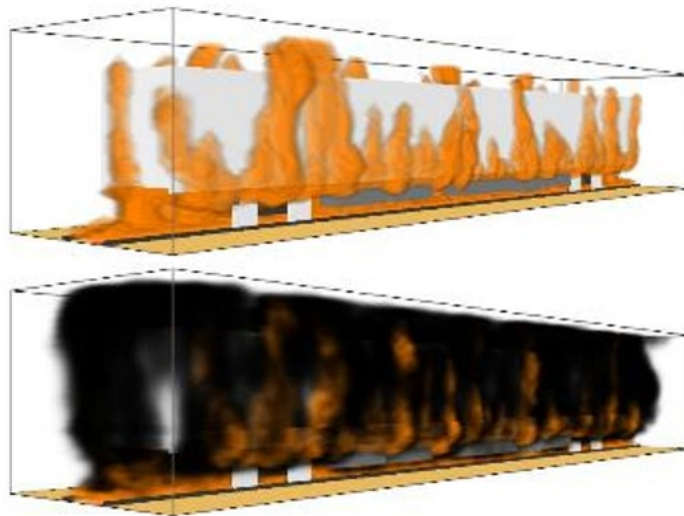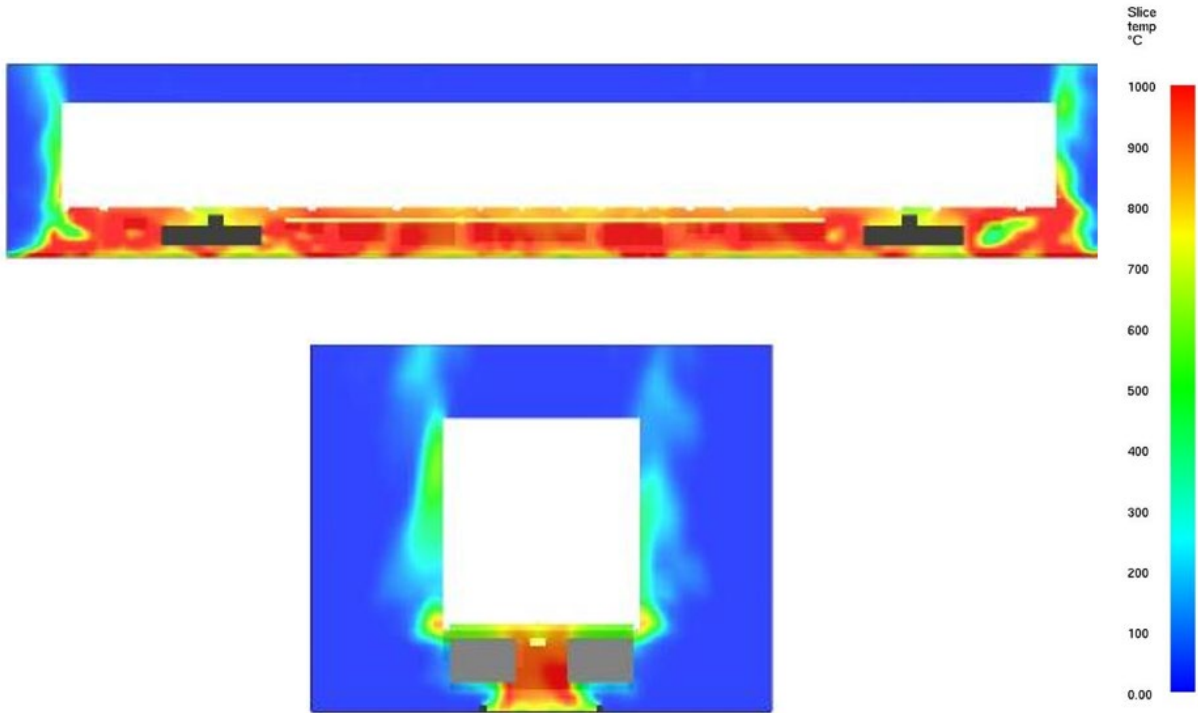
Figure 6-24. Typical Gas Temperature Contours at Center Plane of Rail Car in Transverse and Lateral Directions for the Model 2 (Diesel Spill Fire with Pooling) Simulation
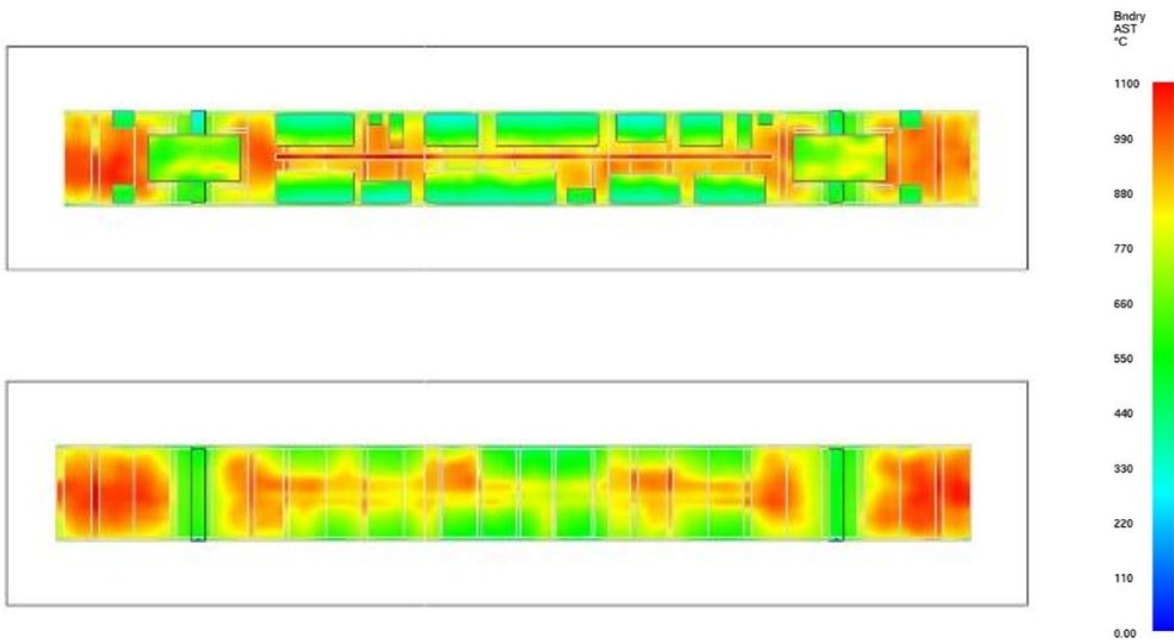
Figure 6-25. Steady State Adiabatic Surface Temperature of Bottom Surface of Undercarriage Frame in Model 2 with (Top) and Without (Bottom) Undercar Components for (Diesel Spill Fire with Pooling) Simulation

6.5.3. Model 3 - 48 in. Clearance Undercarriage with Undercar Components and Gasoline Spill Fire

The total HRR from the simulation of Model 3 with the gasoline spill fire is provided in Figure 6-28. The maximum total HRR for the gasoline is approximately 2.6 MW, which corresponds to a burning rate of 1.27 gal/min (0.058 kg/s), and occurs at approximately 200 seconds. Figure 6-29 shows the HRRPUV at 200 seconds in the simulation as well as typical smoke generation, shown as dark airborne soot. Figure 6-30 shows the typical gas temperature contours at the plane at the geometric center of the rail car along its length and width. These gas temperatures are in excess of 1,472 °F (800 °C). Contours of the AST at approximately 200 seconds into the simulation on the underside of the rail car with and without the undercar components shown are provided in Figure 6-31. The maximum AST on the undercar frame is approximately 1,832 °F (1,000 °C) in the center of the rail car that is directly affected by the gasoline spill. The mean convection heat transfer coefficient calculated at the bottom surface of the undercar frame is approximately 12 W/m²K. The maximum heat flux to the undercar frame calculated with the AST, heat transfer coefficient, and emissivity is approximately 150 kW/m² although the duration of this exposure is limited by the duration of the fuel spill. The exposure was sufficient to ignite the cables, which continued to burn at approximately 200 kW after the gasoline fire burned out.
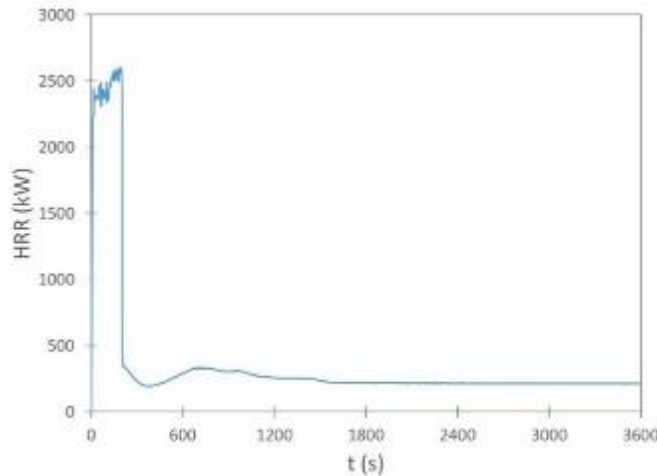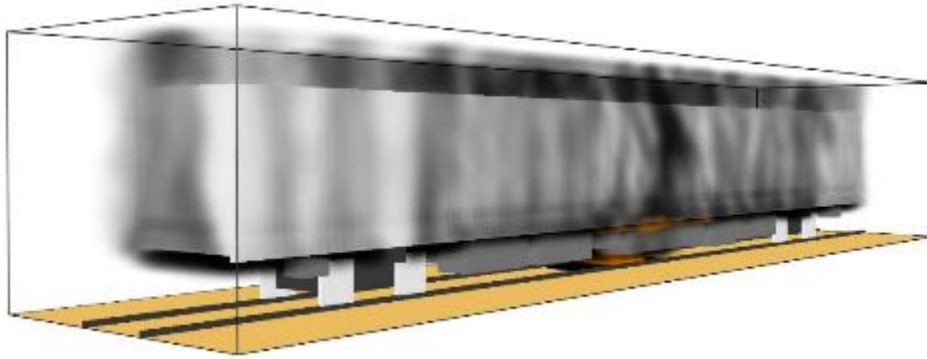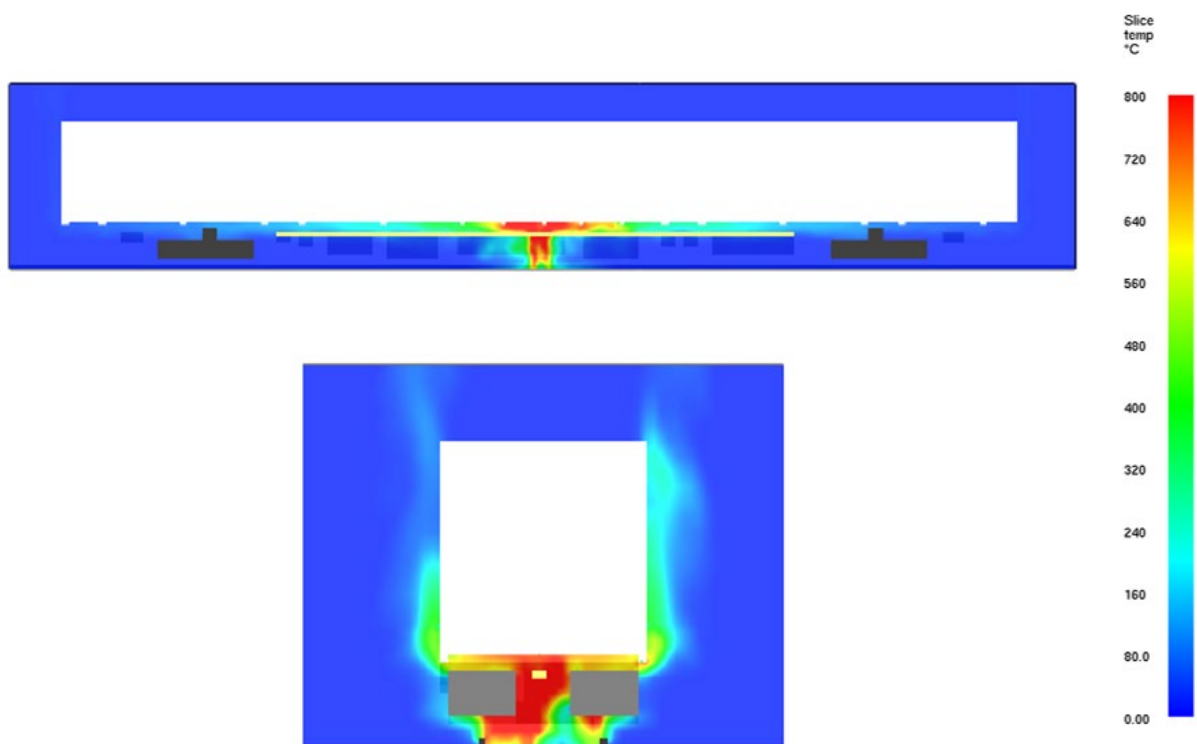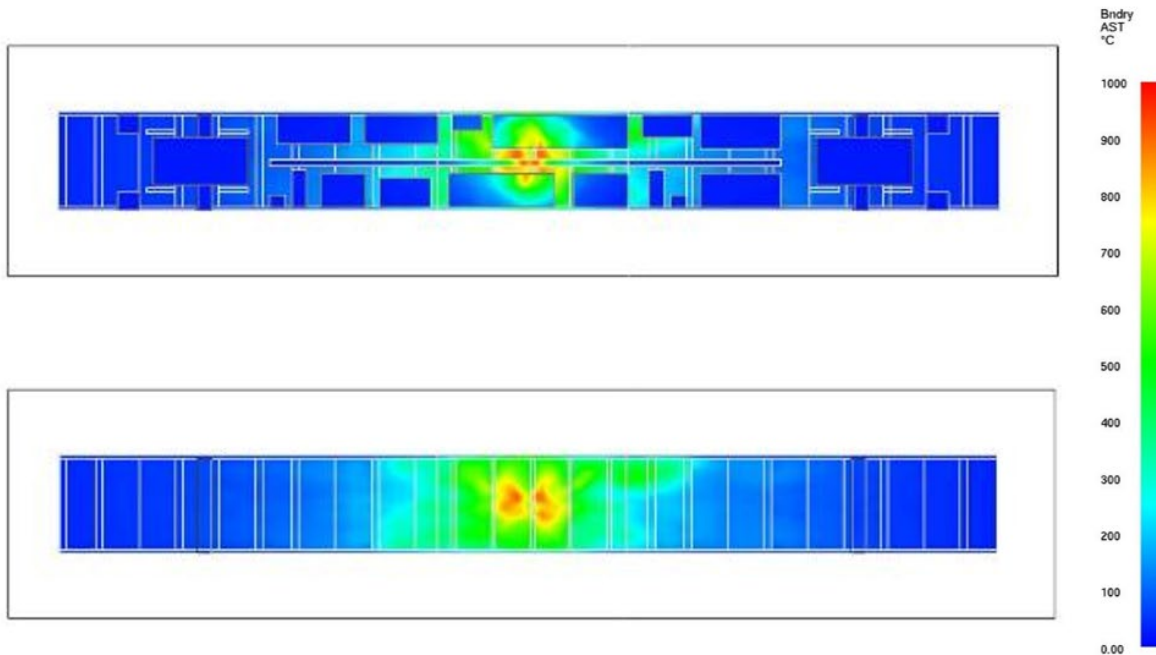

Figure 6-26. Total HRR in Model 3 (Gasoline Spill Fire) Simulation

117

Figure 6-27. Visualization of HRRPUV and Soot Production for Model 3 (Gasoline Spill Fire) Simulation

Figure 6-28. Gas temperature Contours at Center Plane of Rail Car in Transverse and Lateral Directions at Approximately 200 Seconds in the Model 3 (Gasoline Spill Fire) Simulation

Figure 6-29. Adiabatic Surface Temperature of Bottom Surface of Undercarriage Frame in Model 3 Simulation at Approximately 200 Seconds with (Top) and Without (Bottom) Undercar Components in the Model 3 (Gasoline Spill Fire) Simulation

6.5.4. Model 4 - 12 in. Clearance Undercarriage with Diesel Spill Fire

The total HRR from the simulation of Model 4 is provided in Figure 6-32. This scenario involves a diesel spill rate and burning rate of approximately 6.1 gal/min. The maximum total HRR for the diesel spill fire is approximately 13 MW. Figure 6-33 shows the HRRPUV at 3,600 seconds in the simulation as well as typical smoke generation at steady state. Figure 6-34 shows the typical gas temperature contours at the plane at the geometric center of the rail car along its length and width at steady state. The maximum gas temperatures are typically approximately 932 °F (500 °C). Contours of the steady AST on the underside of the rail car are provided in Figure 6-35. The AST on the undercar frame above the fire source is in the range of 662–842 °F (350–450 °C). The pattern of the contours on the exposed surface of the undercarriage indicates that the fire is ventilation-limited, which causes the flame sheet to migrate toward the outer edge of the rail car. The mean convection heat transfer coefficient at the bottom surface of the undercar frame is approximately 10 W/m^{2}K. The maximum heat flux to the undercar frame calculated with the AST, heat transfer coefficient, and emissivity is approximately 38 kW/m^2. With higher heat fluxes toward the sides of the rail car, the cables that ran along the center of the rail car were not predicted to ignite and contribute to the fire in this exposure.

Figure 6-30. Total HRR in Model 4 (Diesel Spill Fire) Simulation

Figure 6-31. Visualization of HRRPUV and Soot Production for Model 4 (Diesel Spill Fire) Simulation
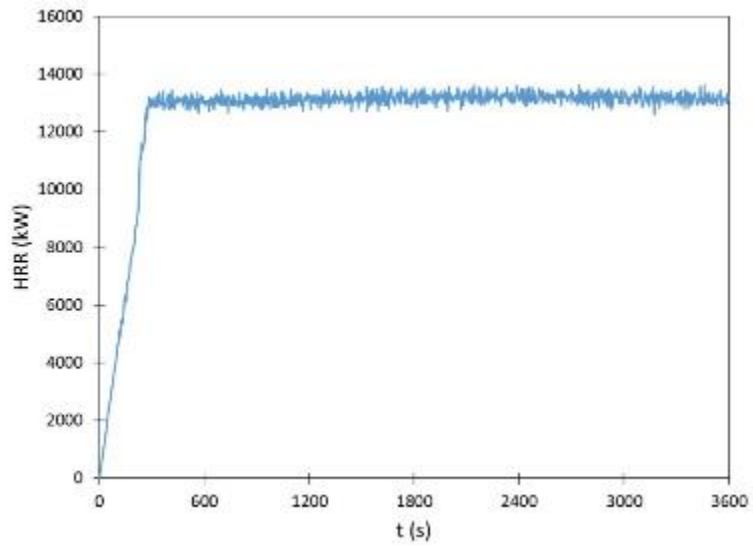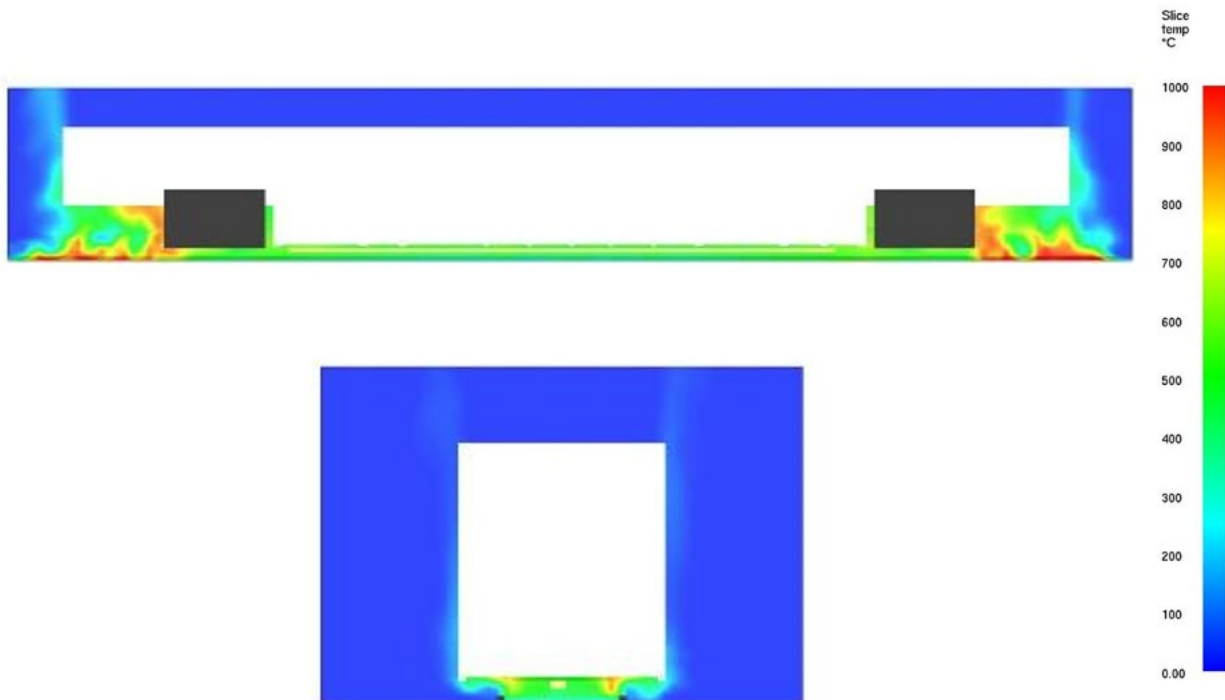
Figure 6-32. Gas Temperature Contours at Center Plane of Rail Car in Transverse and Lateral Directions at Approximately 3,600 Seconds in the Model 4 (Diesel Spill Fire) Simulation
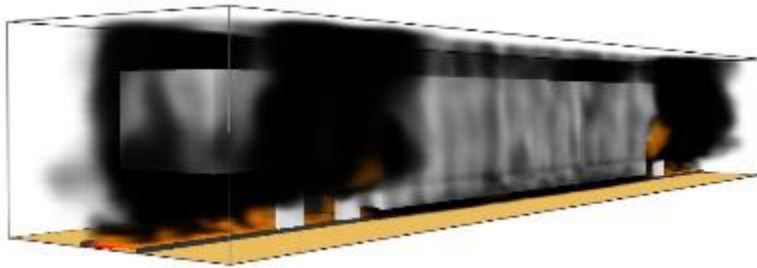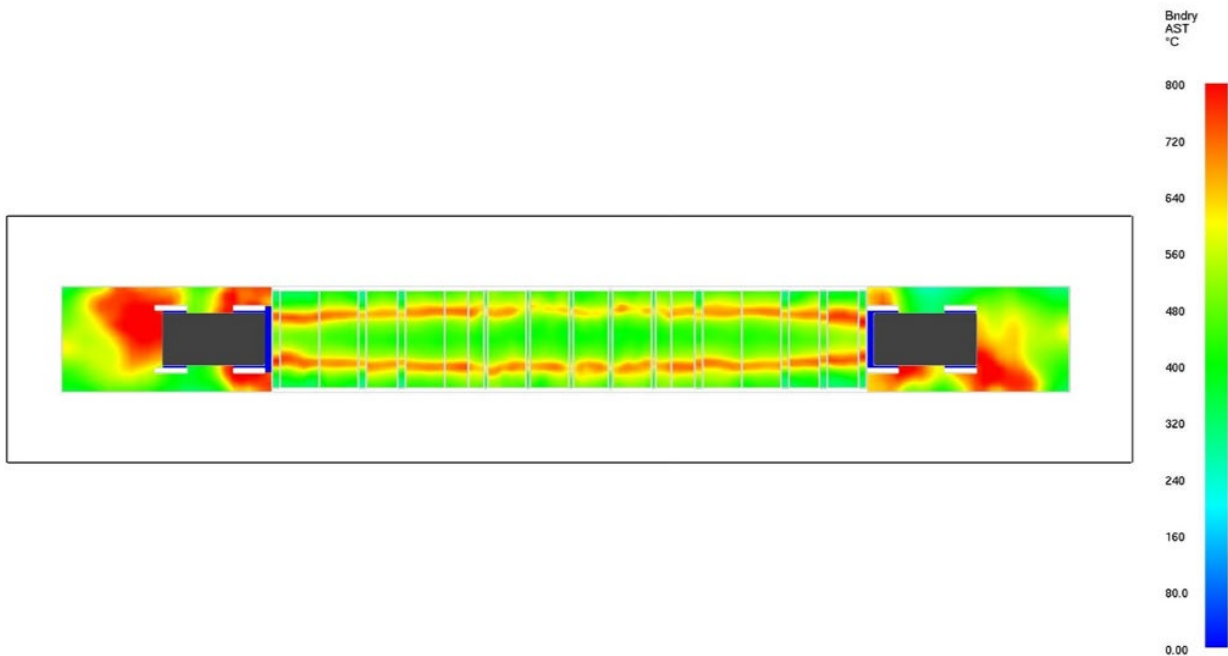

Figure 6-33. Adiabatic Surface Temperature of Bottom Surface of Undercarriage Frame in Model 4 (Diesel Spill Fire) Simulation at Approximately 3,600 Seconds

6.5.5. Model 5 - 12 in. Clearance Undercarriage with Diesel Spill Fire with Pooling

The total HRR from the simulation of Model 5 is provided in Figure 6-36. This scenario involves a significant portion of diesel fuel spilled prior to ignition and a burning rate of approximately 30.5 gal/min. The total steady HRR for the diesel spill is approximately 56 MW, Figure 6-37 shows the HRRPUV at 3,600 seconds in the simulation. Figure 6-38 shows the typical gas temperature contours at the plane at the geometric center of the rail car along its length and width. These gas temperatures are typically in the range of 932 °F (500 °C) in the vicinity of the undercar frame. Contours of the steady AST on the underside of the rail car are provided in Figure 6-39. The mean AST on the undercar frame is approximately in the range of 842–1,022 °F (450–550 °C). The mean convection heat transfer coefficient at the bottom surface of the undercar frame is approximately 10 W/m^{2}K. The mean heat flux to the undercar frame calculated with the AST, heat transfer coefficient, and emissivity is approximately 45 kW/m^2. With higher heat fluxes toward the sides of the rail car, the cables that ran along the center of the rail car were not predicted to ignite in the simulations.

Figure 6-34. Total HRR in Model 5 (Diesel Spill Fire with Pooling) Simulation
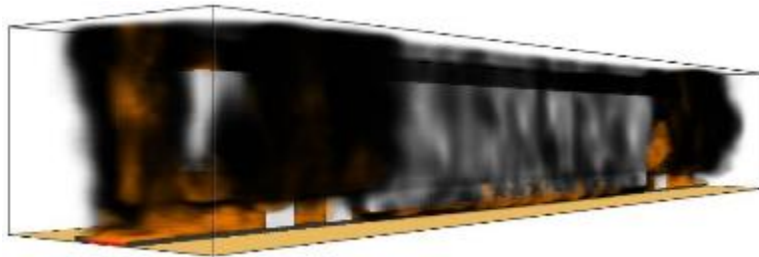
Figure 6-35. Visualization of HRRPUV and Soot Production for Model 5 (Diesel Spill Fire with Pooling) Simulation

122

Figure 6-36. Typical Gas Temperature Contours at Center Plane of Rail Car in Transverse and Lateral Directions for the Model 5 (Diesel Spill Fire with Pooling) Simulation

Figure 6-37. Steady State Adiabatic Surface Temperature of Bottom Surface of Undercarriage Frame in Model 5 (Diesel Spill Fire with Pooling) Simulation

6.5.6. Model 6 - 12 in. Clearance Undercarriage with Gasoline Spill Fire

The total HRR from the simulation of Model 6 with the gasoline spill fire is provided in Figure 6-40. The maximum total HRR for the gasoline is approximately 800 kW, which corresponds to a burning rate of 0.4 gal/min (0.018 kg/s), and occurs at approximately 200 seconds. Figure 6-41 shows the HRRPUV at 200 seconds in the simulation as well as typical smoke generation. Figure 6-42 shows the typical gas temperature contours at the plane at the geometric center of the rail car along its length and width. The maximum gas temperatures are in excess of 1,472 °F (800 °C), but these temperatures are more typically in the range of approximately 932 °F (500 °C). Contours of the AST at 200 seconds on the underside of the rail car are provided in Figure 6-43. The maximum AST on the undercar frame is approximately 1,832 °F (1,000 °C) in the center of the rail car that is directly affected by the gasoline spill. The mean convection heat transfer coefficient at the bottom surface of the undercar frame is approximately 12 W/m^{2}K. The maximum heat flux to the undercar frame calculated with the AST, heat transfer coefficient, and emissivity is approximately 58 kW/m^2 although the duration of this exposure is limited by the duration of the fuel spill. The fire was sufficient to ignite the cables, resulting in steady burning of a fire of approximately 220 kW after the gasoline burned out.

Figure 6-38. Total HRR in Model 6 (Gasoline Spill Fire) Simulation


Figure 6-39. Visualization of HRRPUV and Soot Production for Model 6 (Gasoline Spill Fire) Simulation

124
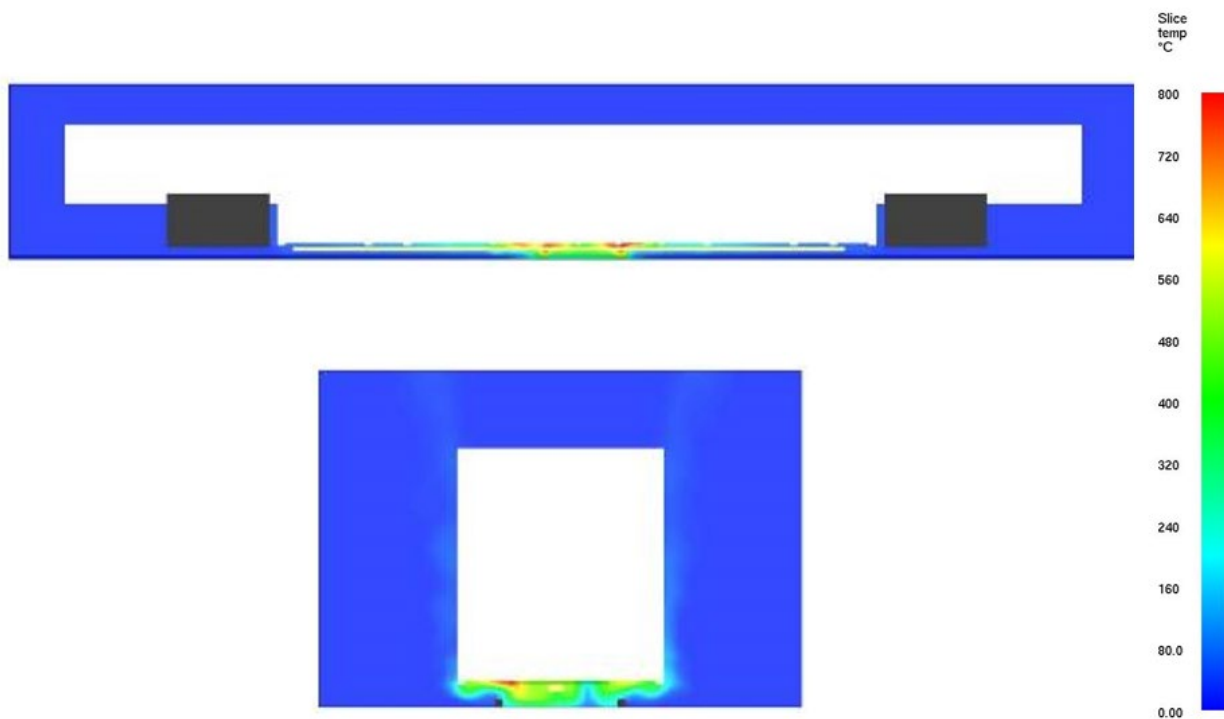
Figure 6-40. Gas Temperature Contours at Center Plane of Rail Car in Transverse and Lateral Directions at Approximately 200 Seconds in the Model 6 (Gasoline Spill Fire) Simulation
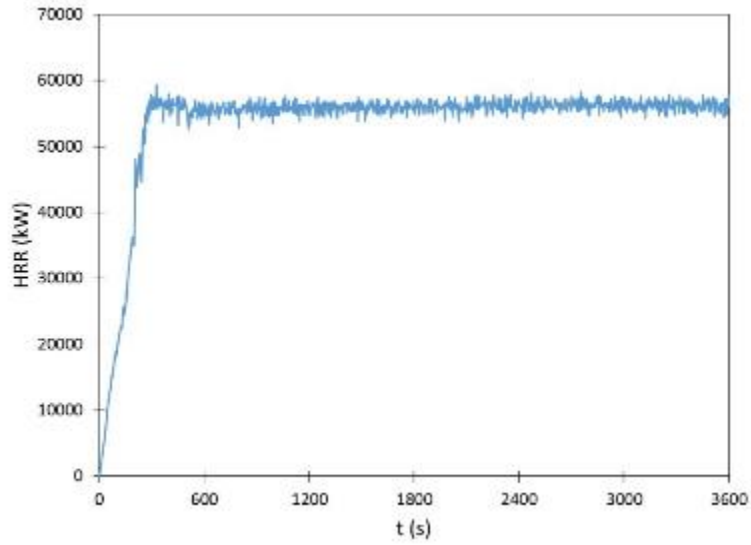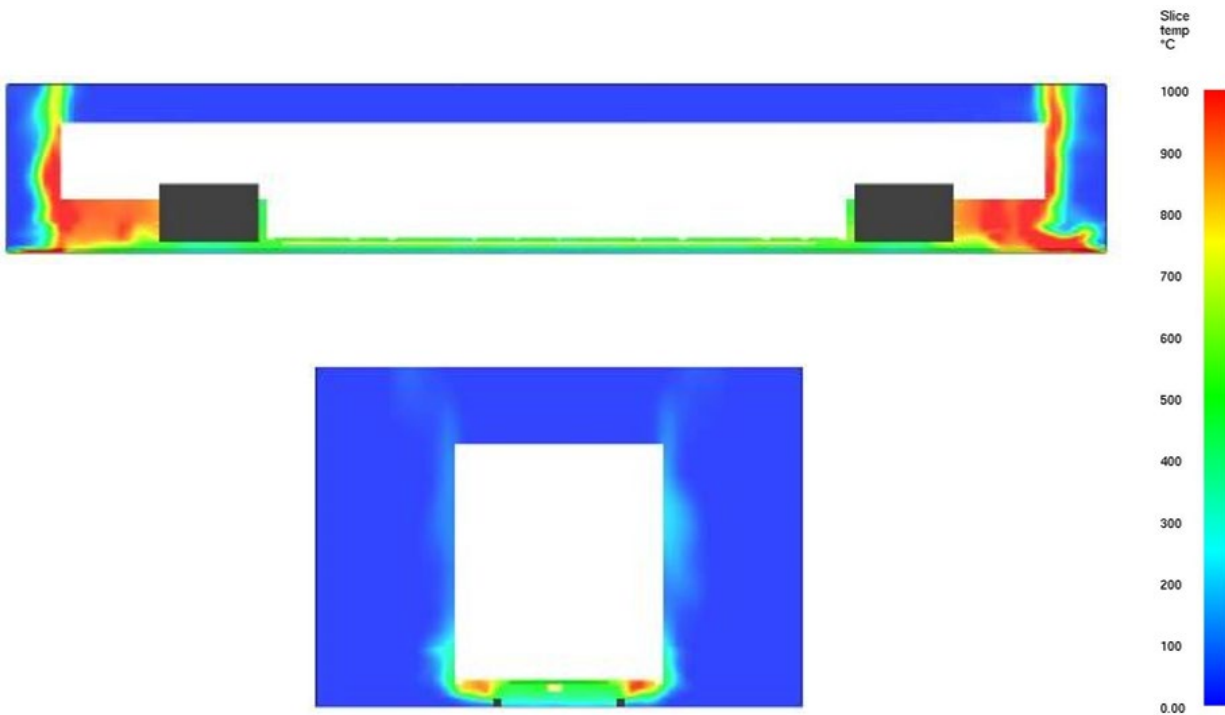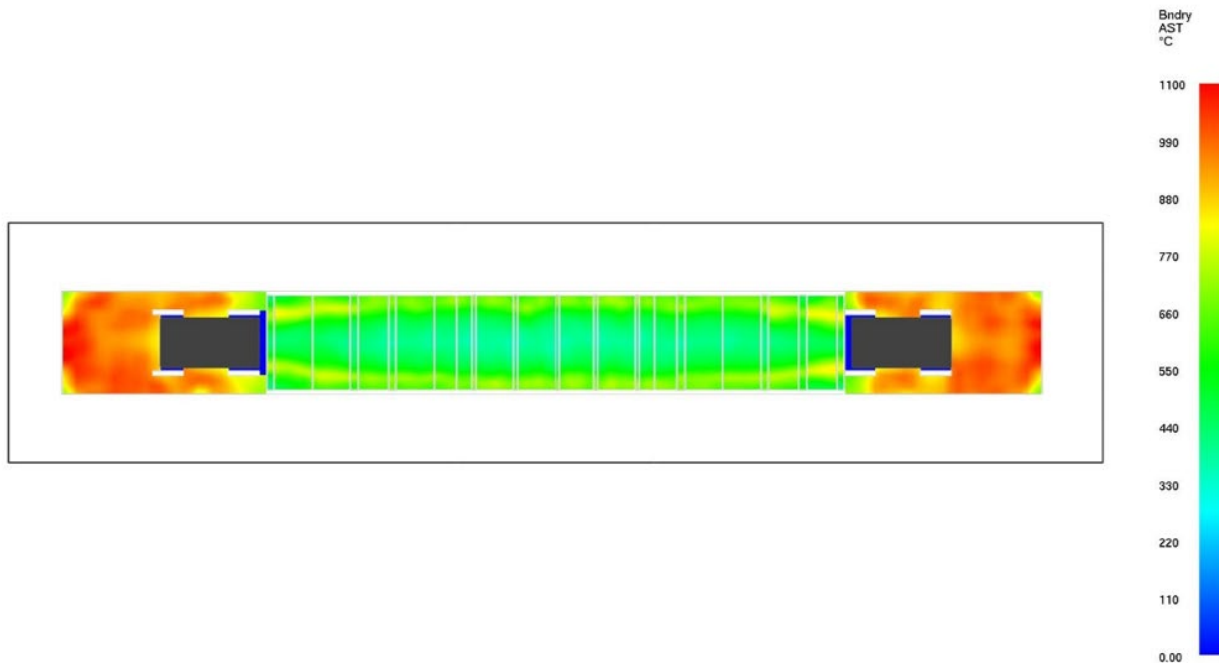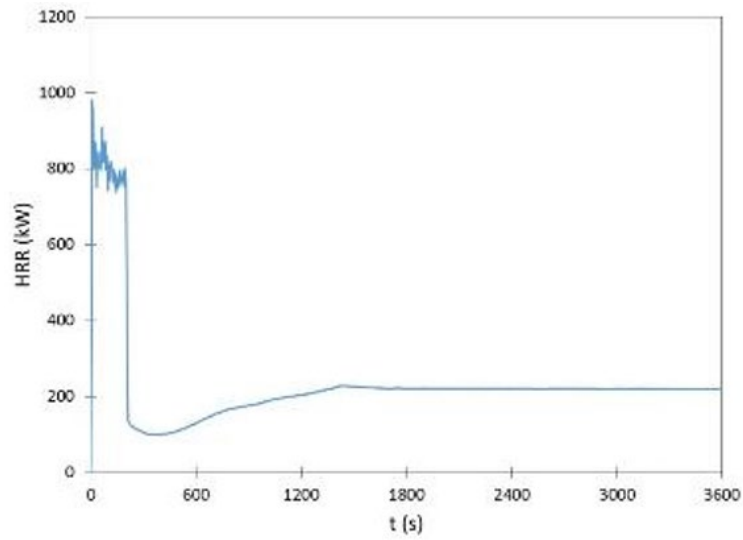

Figure 6-41. Adiabatic Surface Temperature of Bottom Surface of Undercarriage Frame in Model 6 (Gasoline Spill Fire) Simulation at Approximately 200 Seconds

6.5.7. Model 7 - 22 in. Clearance Undercarriage with Diesel Spill Fire

The total HRR from the simulation of Model 7 with the diesel spill fire is provided in Figure 6-44. This scenario involves a diesel spill rate and burning rate of approximately 6.1 gal/min. The maximum total HRR for the diesel spill fire is approximately 14.6 MW. Figure 6-45 shows the HRRPUV at 850 seconds in the simulation as well as typical smoke generation. Figure 6-46 shows the typical gas temperature contours at the plane at the geometric center of the rail car along its length and width. The maximum gas temperatures are typically in the range of approximately 900–1,000 °C. Contours of the steady AST on the underside of the rail car are provided in Figure 6-47. The AST on the undercar frame above the fire source is in the range of 1,202–1,472 °F (650–800 °C). The mean calculated convection heat transfer coefficient at the bottom surface of the undercar frame is approximately 11 W/m^{2}K. The maximum heat flux to the undercar frame calculated with the AST, heat transfer coefficient, and emissivity is approximately 60 kW/m^2. With higher heat fluxes along the center of the rail car, this exposure was sufficient to ignite the undercar cables and contribute approximately 1.4 MW to the fire.
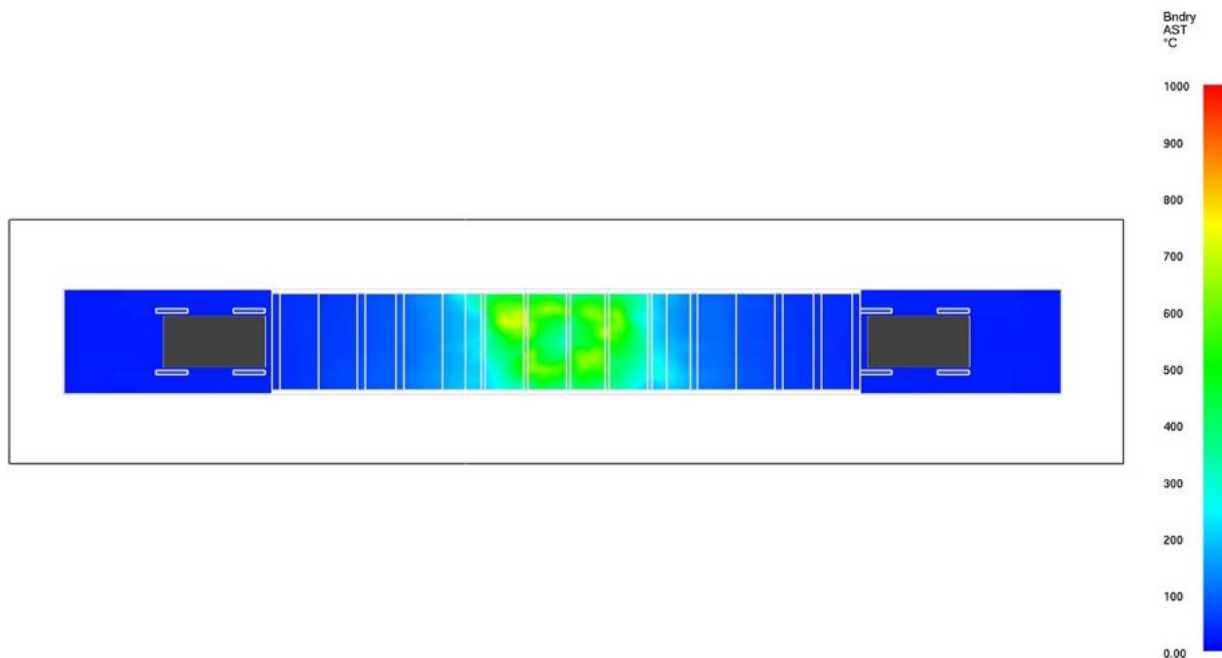
Figure 6-42. Total HRR in Model 7 (Diesel Spill Fire) Simulation

Figure 6-43. Visualization of HRRPUV and Soot Production for Model 7 (Diesel Spill Fire) Simulation
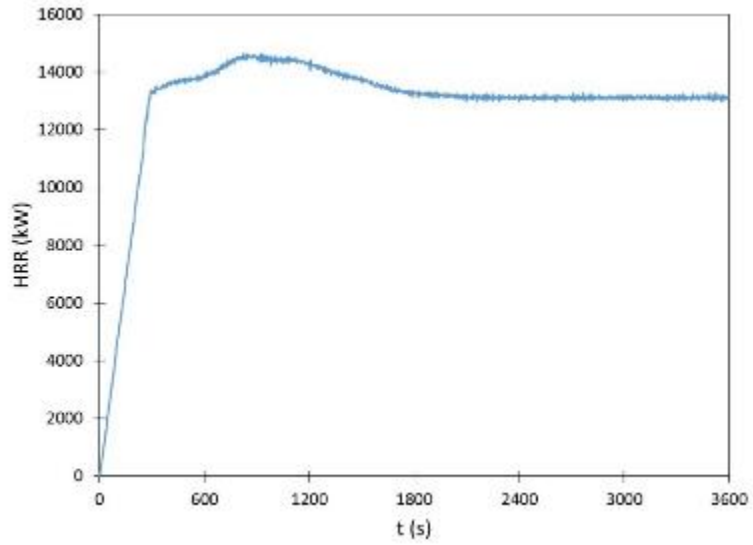
Figure 6-44. Gas Temperature Contours at Center Plane of Rail Car in Transverse and Lateral Directions at Approximately 850 Seconds in the Model 7 (Diesel Spill Fire) Simulation
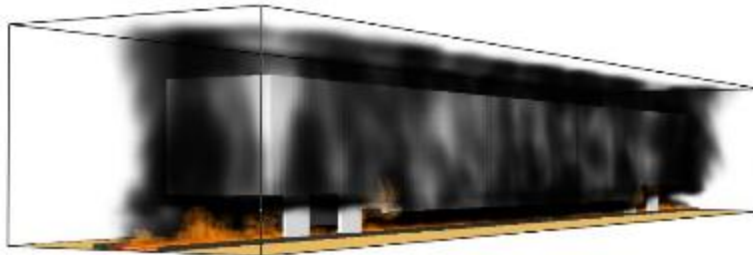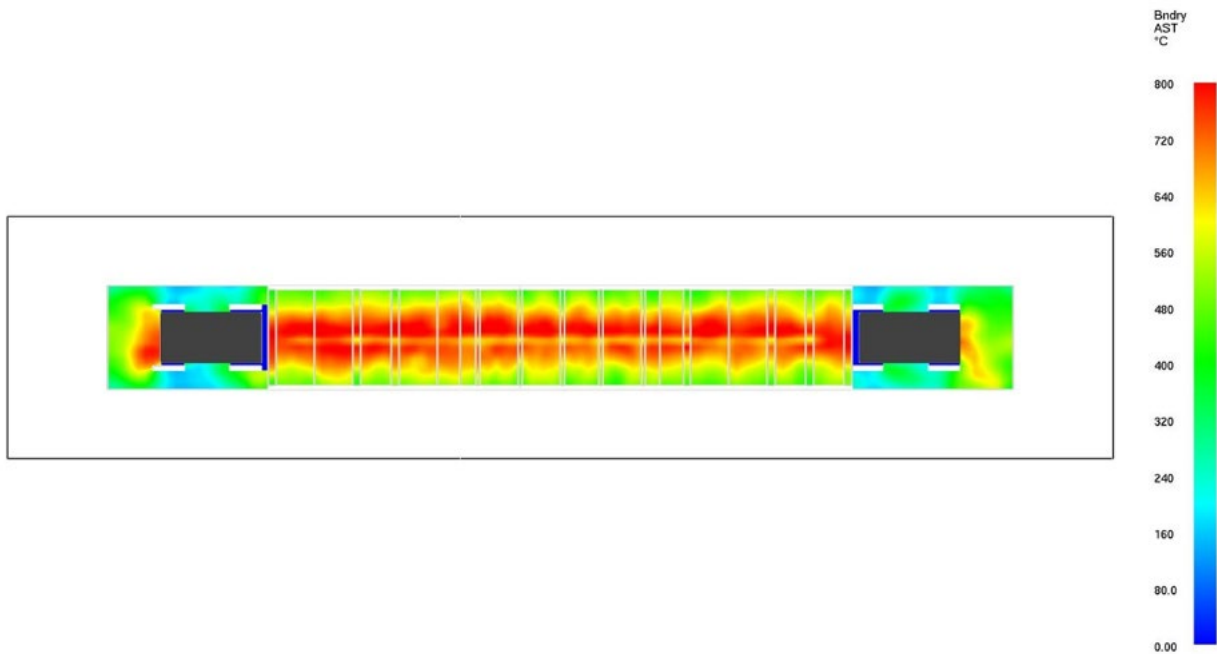

Figure 6-45. Adiabatic Surface Temperature of Bottom Surface of Undercarriage Frame in Model 7 (Diesel Spill Fire) Simulation at Approximately 850 Seconds

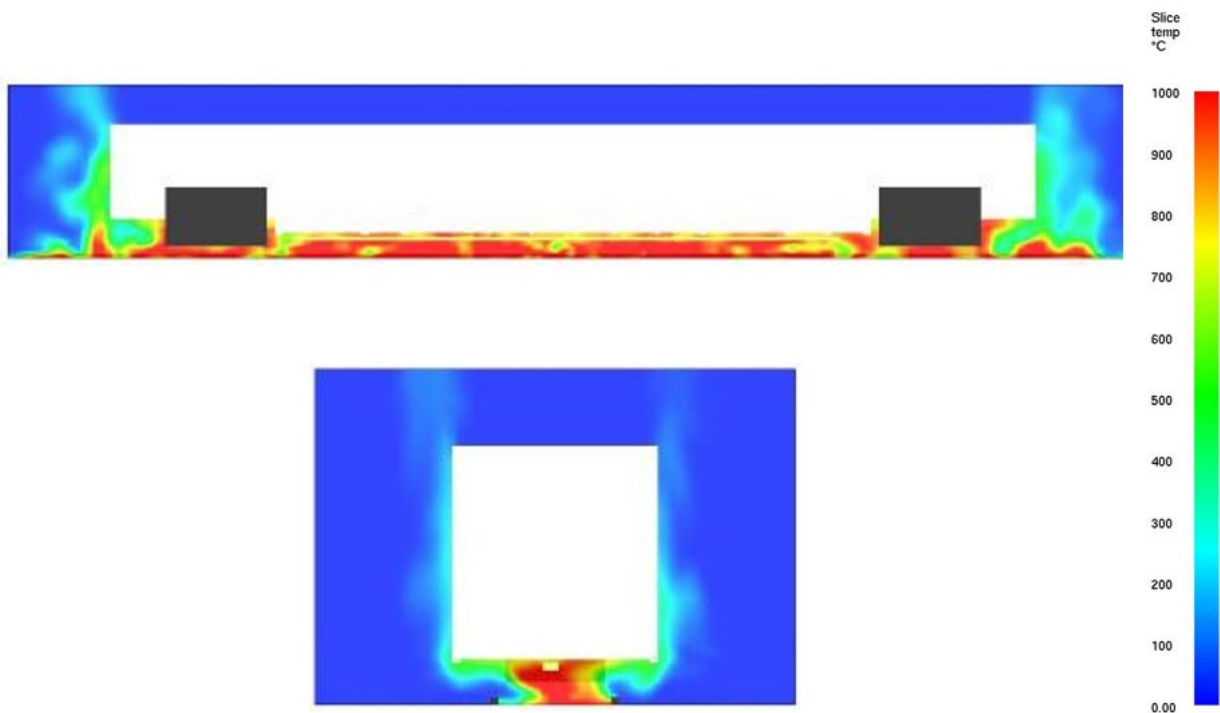### 6.5.8. Model 8 - 22 in. Clearance Undercarriage with Diesel Spill Fire with Pooling

The total HRR from the simulation of Model 8 with the diesel spill fire with pooling is provided in Figure 6-48. This scenario involves a significant portion of diesel fuel spilled prior to ignition and a burning rate of approximately 30.5 gal/min. The maximum total HRR for the diesel spill fire with pooling is approximately 49 MW. Figure 6-49 shows the HRRPUV at 3,600 seconds in the simulation as well as typical smoke generation. Figure 6-50 shows the typical gas temperature contours at the plane at the geometric center of the rail car along its length and width. The maximum gas temperatures are in excess of 1,832 °F (1,000 °C) and the mean gas temperature at the undercar frame is in the range of approximately 1,112–1292 °F (600–700 °C). Contours of the steady AST on the underside of the rail car are provided in Figure 6-51. The AST on the undercar frame above the fire source is in the range of 1,112–1,292 °F (600–700 °C) at a steady state. The relatively high burning rate of the source fire results in a ventilation-limited condition where the flame sheet migrates toward the outer edges of the rail car undercarriage. The mean calculated convection heat transfer coefficient at the bottom surface of the undercar frame is approximately 10 W/m^{2}K. The maximum heat flux to the undercar frame calculated with the AST, heat transfer coefficient, and emissivity is approximately 82 kW/m^2. Due to the higher heat fluxes being close to the sides, the cables were not predicted to ignite for this scenario.

**Figure 6-46. Total HRR in Model 8 (Diesel Spill Fire with Pooling) Simulation**

Figure 6-47. Visualization of HRRPUV and Soot Production for Model 8 (Diesel Spill Fire with Pooling) Simulation
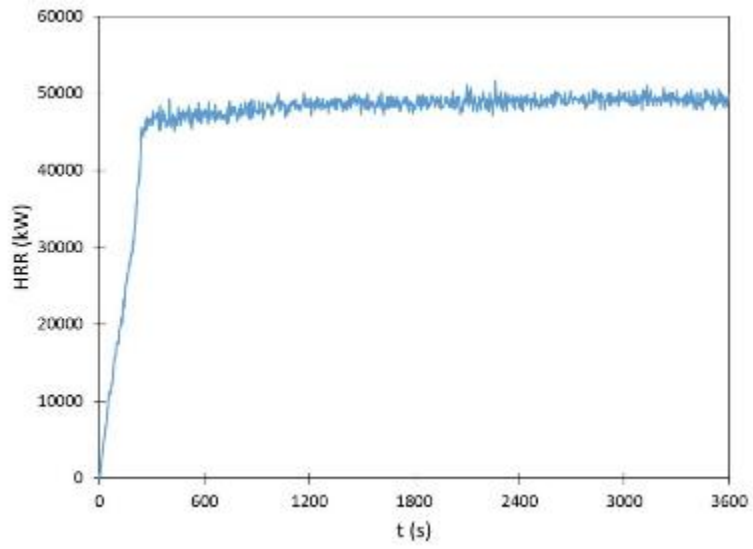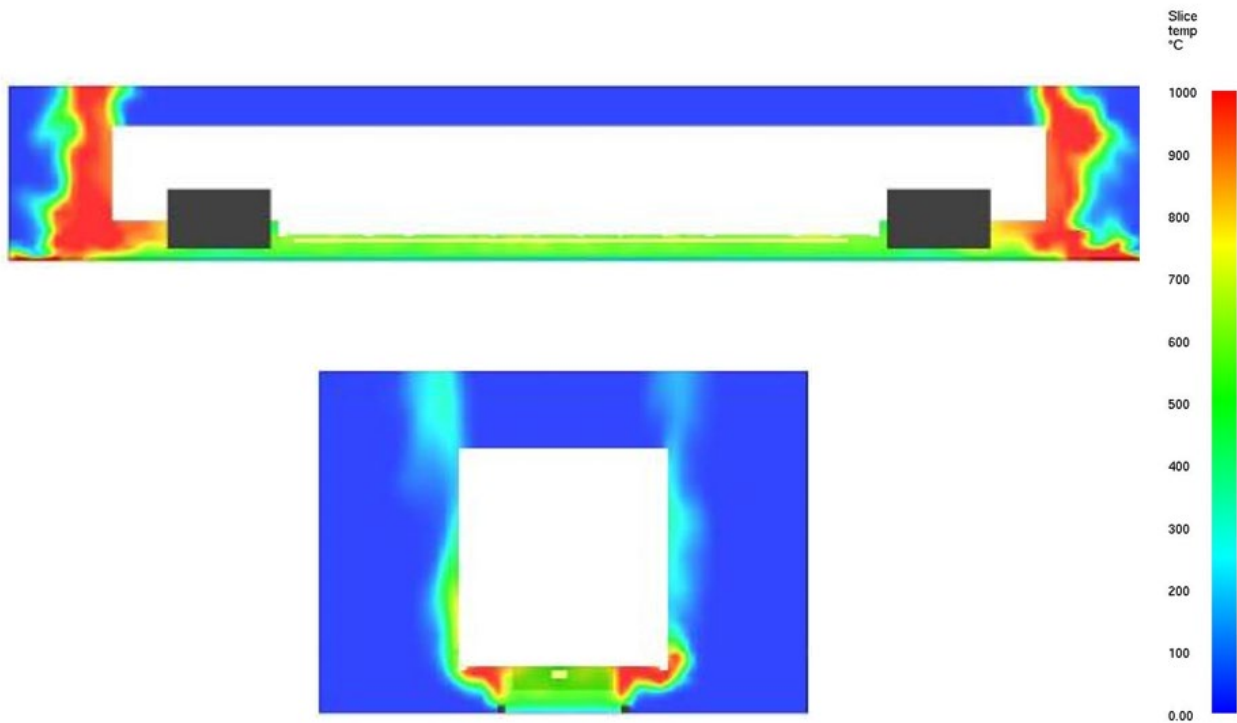

Figure 6-48. Gas Temperature Contours at Center Plane of Rail Car in Transverse and Lateral Directions at Approximately 3,600 Seconds in the Model 8 (Diesel Spill Fire with Pooling) Simulation
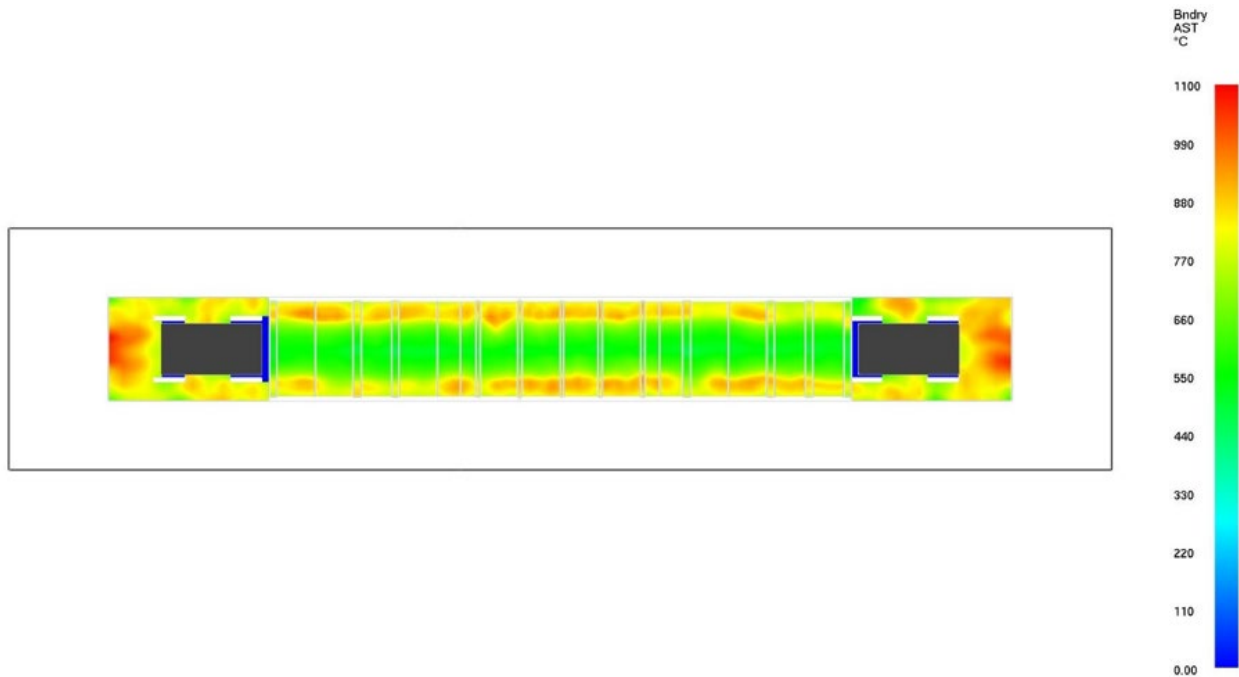
Figure 6-49. Adiabatic Surface Temperature of Bottom Surface of Undercarriage Frame in Model 8 (Diesel Spill Fire with Pooling) Simulation at Approximately 3,600 Seconds

6.5.9. Model 9 - 22 in. Clearance Undercarriage with Gasoline Spill Fire

The total HRR from the simulation of Model 9 with the gasoline spill fire is provided in Figure 6-52. The maximum total HRR for the gasoline spill fire is approximately 3.0 MW, which corresponds to a burning rate of 1.52 gal/min (0.069 kg/s), and occurs at approximately 200 seconds. Figure 6-53 shows the HRRPUV at 200 seconds in the simulation as well as typical smoke generation. Figure 6-54 shows the typical gas temperature contours at the plane at the geometric center of the rail car along its length and width. The maximum gas temperatures are in excess of 1,472 °F (800 °C). Contours of the steady AST on the underside of the rail car with and without the undercar components and trucks shown are provided in Figure 6-55. The maximum AST on the undercar frame above the fire source is approximately 1,832 °F (1,000 °C). The mean calculated convection heat transfer coefficient at the bottom surface of the undercar frame above the fire source is approximately 13 W/m^{2}K. The maximum heat flux to the undercar frame calculated with the AST, heat transfer coefficient, and emissivity is approximately 74 kW/m^2. The fire was predicted to ignite the cables, which contributed approximately 210 kW to the fire after the gasoline burned out.
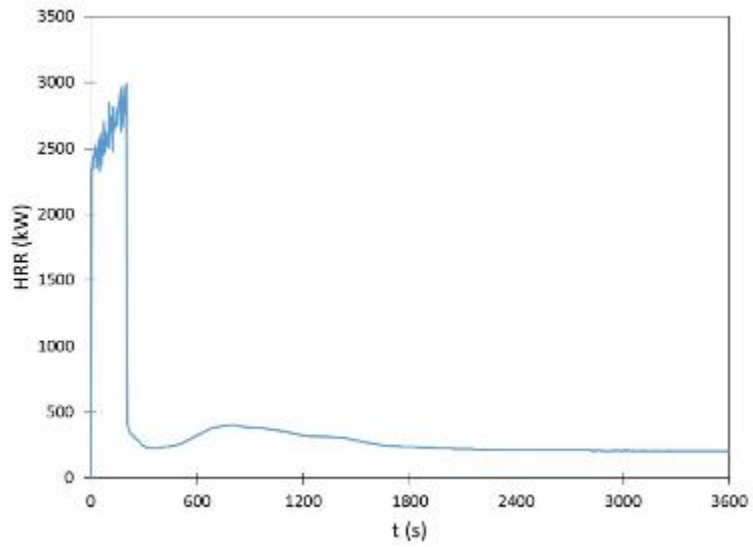
Figure 6-50. Total HRR in Model 9 (Gasoline Spill Fire) Simulation
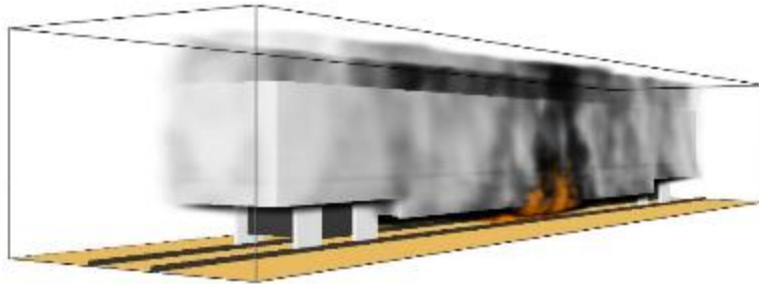
Figure 6-51. Visualization of HRRPUV and Soot Production for Model 9 (Gasoline Spill Fire) Simulation
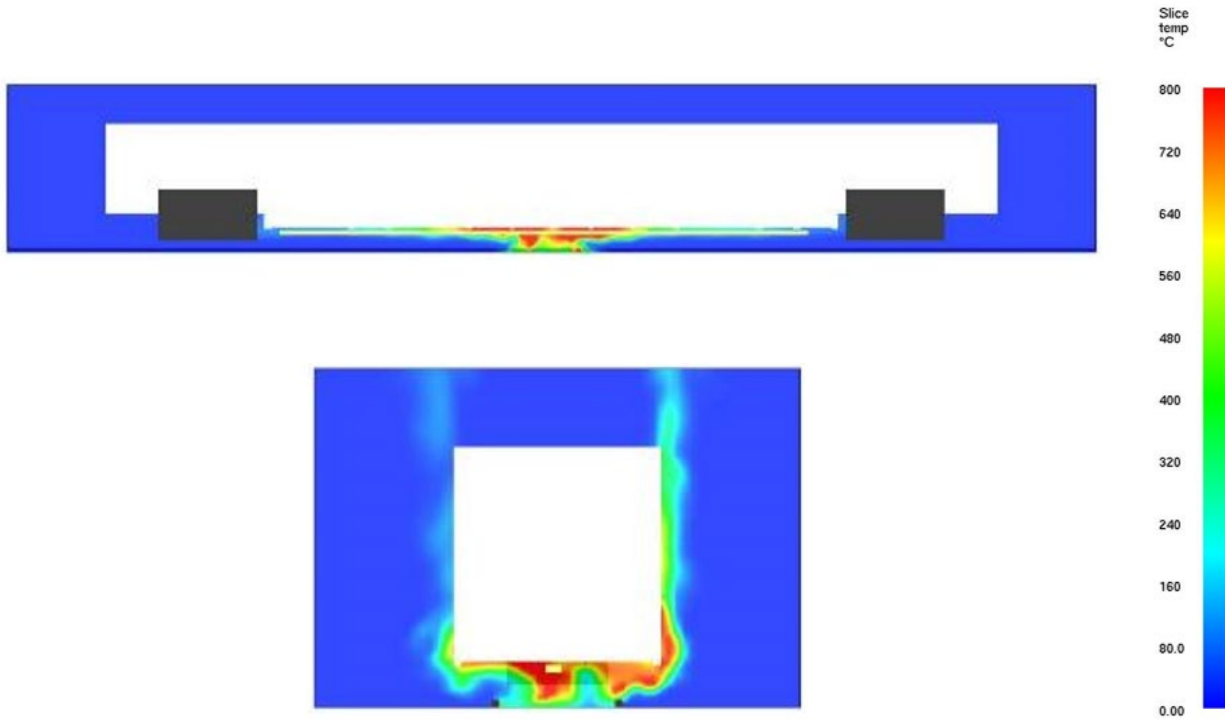
Figure 6-52. Gas Temperature Contours at Center Plane of Rail Car in Transverse and Lateral Directions at Approximately 200 Seconds in the Model 9 (Gasoline Spill Fire) Simulation
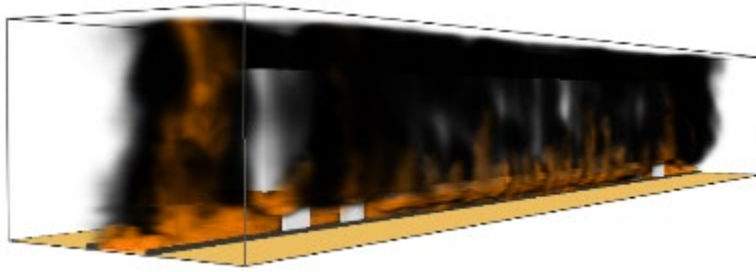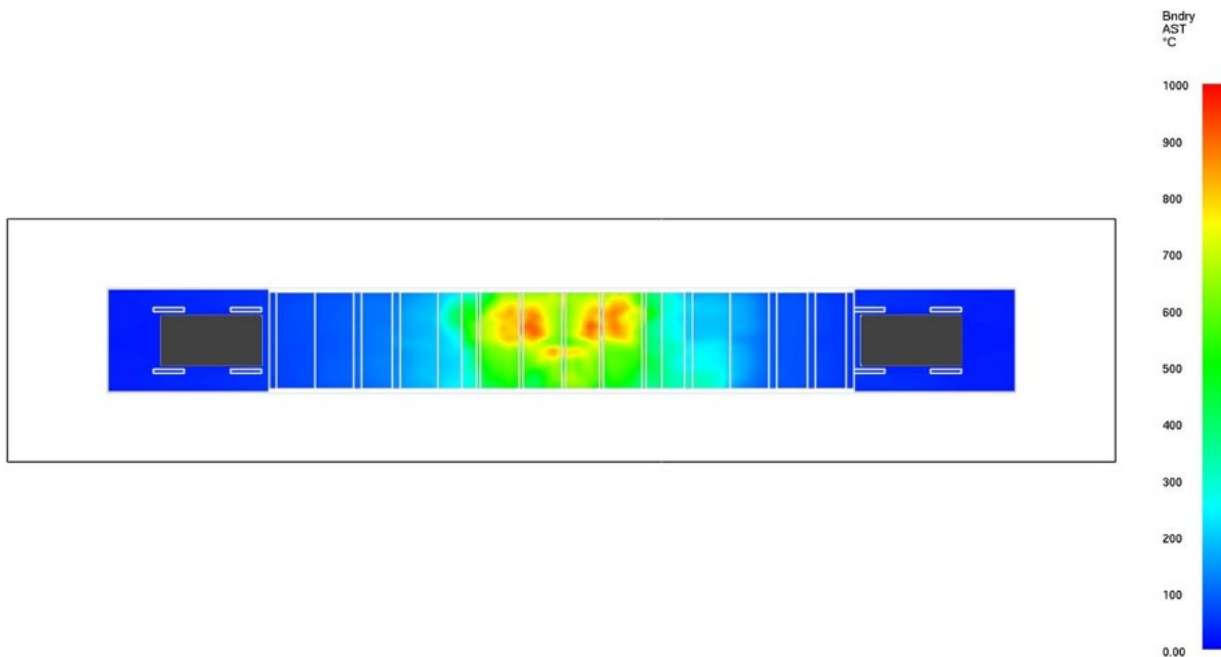

Figure 6-53. Adiabatic Surface Temperature of Bottom Surface of Undercarriage Frame in Model 9 (Gasoline Spill Fire) Simulation at Approximately 200 Seconds

6.6.   FDS-Abaqus Coupling

The thermal response of the floor assembly to these realistic fires was simulated using a coupling algorithm between Abaqus and FDS. This coupling algorithm extracted the AST from FDS and used it to define the thermal boundary condition in the Abaqus model as shown in Figure 6-56.
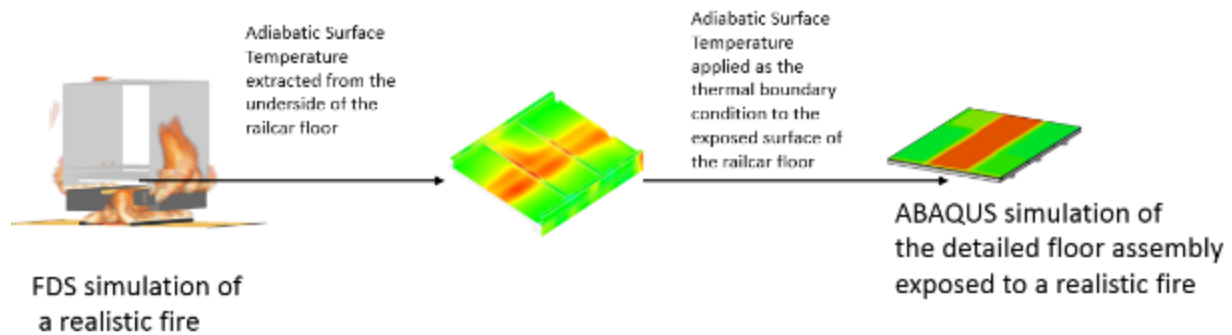
Figure 6-54. Coupling Procedure Used to Extract Data from FDS to Apply Thermal Boundary Condition in the Abaqus Model

This coupling procedure provided realistic time-temperature profiles to estimate the thermal response of the rail car floor assembly. Figure 6-57 shows representation of AST simulation contours of the exposed underside of the rail car floor for a diesel fire at a time instant. These contours when supplied to Abaqus are used to define the thermal boundary conditions at the exposed surface and are displayed in Figure 6-57.
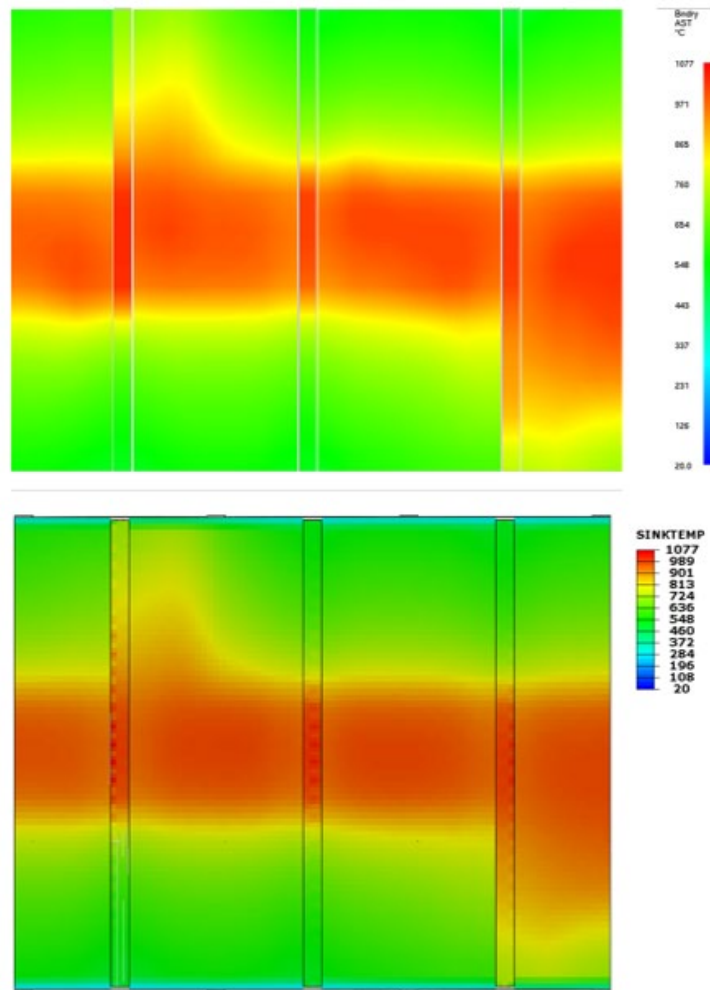
Figure 6-55. Adiabatic Surface Temperature Extracted from FDS at the Underside of the Rail Car Floor (Top).

6.6.1. Diesel Spill

The diesel fuel spill on a flat surface scenario that has been simulated in this work results from a puncture hole in the locomotive diesel fuel tank. The scenario is constructed assuming the train is at rest in a location with ballastless tracks and the spilled fuel is confined between the rails. The FDS models corresponding to these spill cases are Model 1, Model 4, and Model 7. The fire was simulated for 1 hour and spatially and temporally varying ASTs were extracted at the underside of the rail car floor. In addition to ASTs, heat transfer coefficients from FDS were extracted to accurately predict the response of a rail car floor assembly to a diesel fuel fire. The temperature distribution at the exposed surface for all three models at 1 hour is shown in Figure 6-58. The maximum temperature at the exposed surface is highest for the floor with 22-inch clearance from the rail. The maximum temperature was observed at this clearance height because the undercarriage was far enough away from the fire source that fire was not oxygen-limited, and close enough to the fire source that the flames impinged directly on the undercar frame. The temperature at the unexposed surface for all the models at 3,600 seconds (1 hour) is shown in Figure 6-59.

134

12 inch clearance **22 inch clearance** **48 inch clearance**
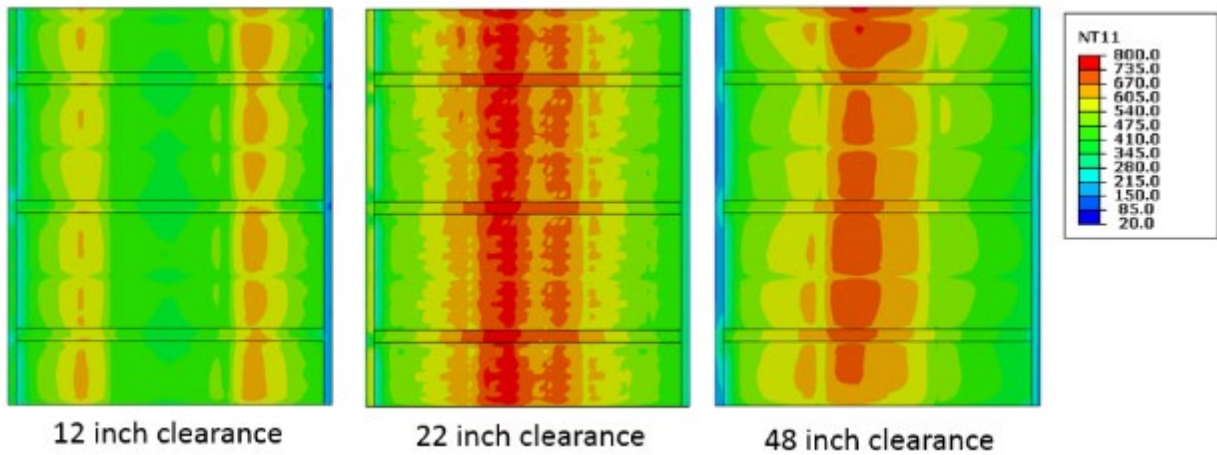
Figure 6-56. Exposed Surface Temperature for Diesel Fire at 1 hour for All Three Floor Configurations Representing Distance Between Rail and the Rail Car Floor

12 inch clearance **22 inch clearance** **48 inch clearance**
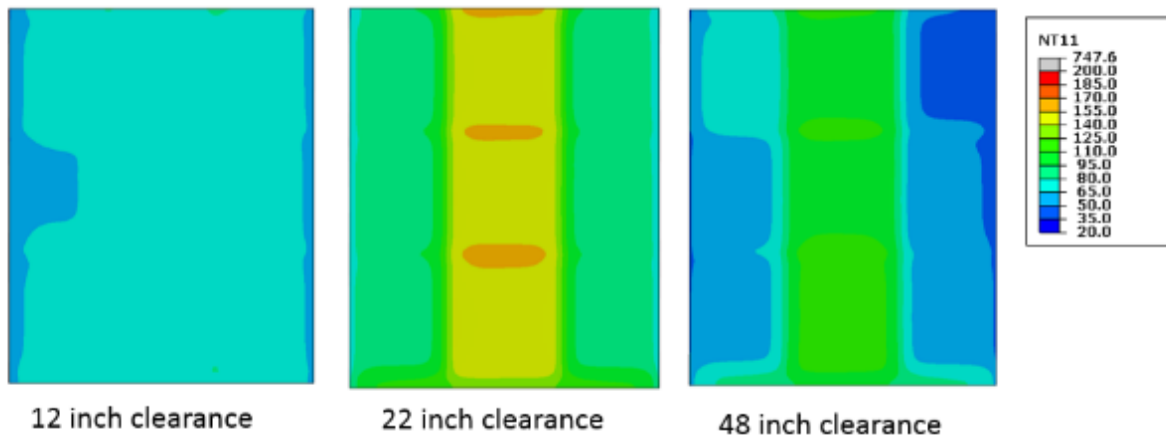
Figure 6-57. Unexposed Surface Temperature for Diesel Fire at 1 Hour for All Three Floor Configurations Representing Distance Between Rail and the Rail Car Floor

The maximum temperature recorded at the exposed surface for all three configurations as a function of time is shown in Figure 6-60. The figure also shows the temperature rise due to the ASTM E119 exposure.
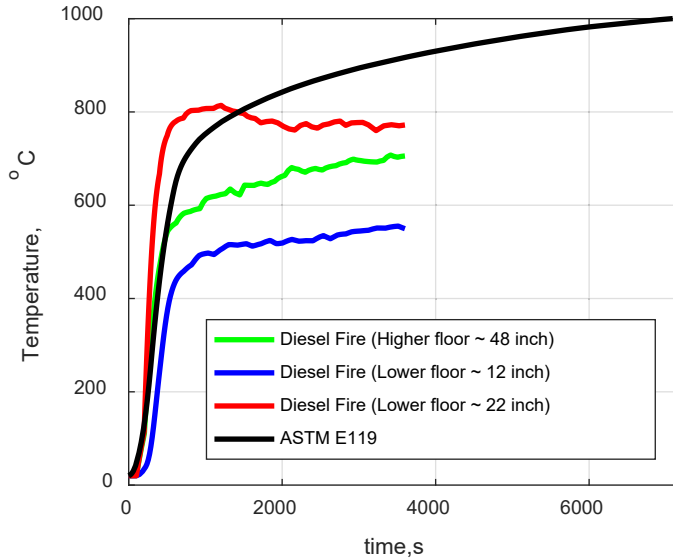
Figure 6-58. Maximum Exposed Surface Temperature with Time for Diesel Fire and Standard ASTM E119 Exposure
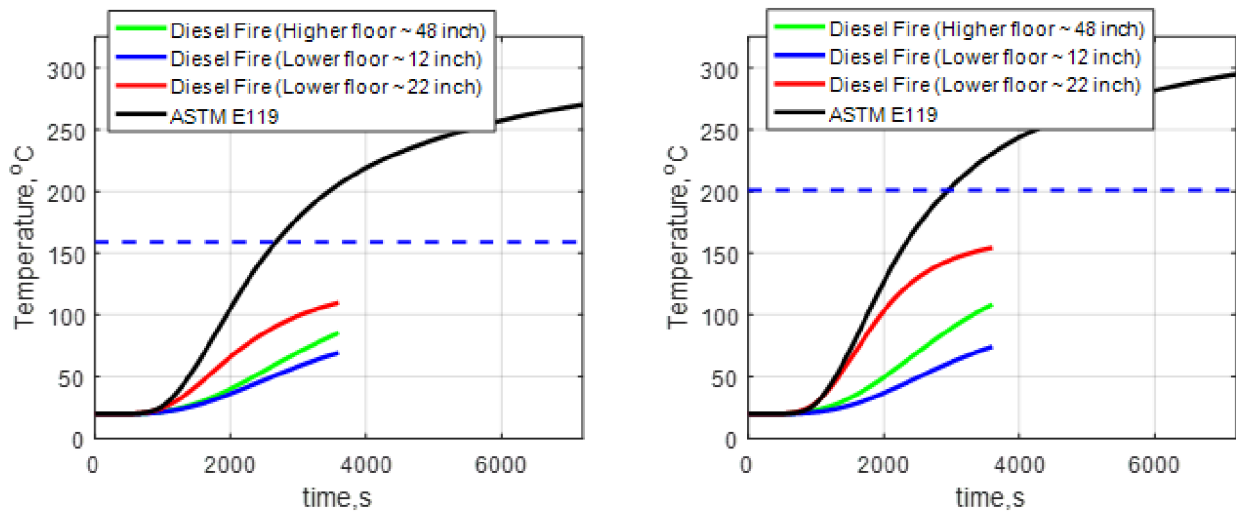
Figure 6-59. Average(Left) and Maximum (Right) Unexposed Surface Temperature for Diesel Fire. The Blue Dashed Line Shows the ASTM Limit for a 30-Minute Exposure

The temperature recorded at the unexposed surface according to ASTM E119 is shown in Figure 6-61. The figure shows both the average and maximum temperatures along with the ASTM limit for a 30-minute exposure. The temperature rise at the unexposed surface for different scenarios is also tabulated in Table 6-5. The table shows that the ASTM E119 exposure is severe compared to the diesel spill fire.

136

Table 6-5. Rating in Minutes for Unexposed Surface Temperature Rise for Diesel Fire and Standard ASTM E119 Exposure

Scenario	Time to Exceed (min).			
	50 °C Rise	75 °C Rise	181 °C Rise (ASTM Condition Maximum)	139 °C Rise (ASTM Condition Average)
ASTM E119	25	30	50	45
Higher Floor ~48 inch	43	56	–	–
Lower Floor ~12 inch	60	–	–	–
Lower Floor ~22 inch	28	34	–	–

6.6.2. Diesel Spill with Pooling

An additional diesel fuel spill scenario with pooling and a higher burning rate was also modeled for different rail car floor configurations. This scenario would represent the diesel spill fire burning on a flat surface exposed to radiation from the heated rail car. This results in a 100 percent burning rate as compared to 20 percent burning rate considered in the previous case and corresponds to Model 2, Model 5 and Model 7. The temperature distribution at the exposed surface for all three models at 1 hour is shown in Figure 6-62. The maximum temperature at the exposed surface is highest for the floor with 48-inch clearance from the rail. The temperature at the unexposed surface for all the models at 3,600 seconds (1 hour) is shown in Figure 6-63.

12 inch clearance   22 inch clearance   48 inch clearance
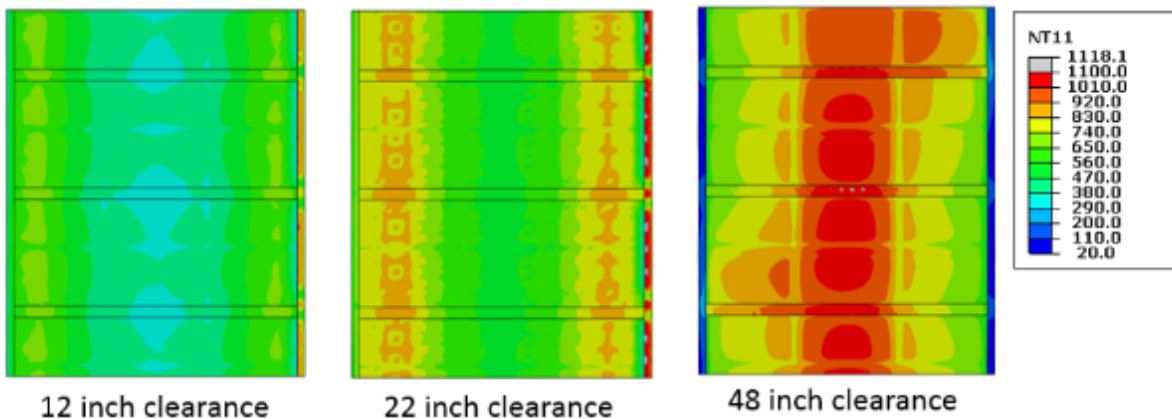
Figure 6-60. Exposed Surface Temperature for Diesel Fire with Pooling at 1 Hour for All Three Floor Configurations Representing Distance Between Rail and the Rail Car Floor

12 inch clearance 22 inch clearance 48 inch clearance
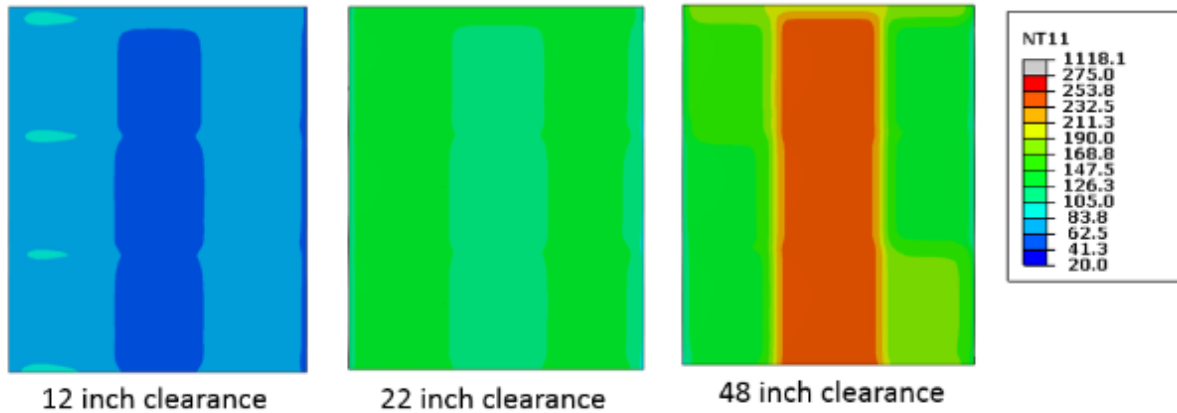
Figure 6-61. Unexposed Surface Temperature for Diesel Fire with Pooling at 1 Hour for All Three Floor Configurations Representing Distance Between Rail and the Rail Car Floor

The maximum temperature recorded at the exposed surface for all three configurations as a function of time is shown in Figure 6-64. The figure also shows the temperature rise due to ASTM E119 exposure. The temperature recorded at the unexposed surface according to ASTM E119 is shown in Figure 6-65. The figure shows both the average and maximum temperatures along with the ASTM limit for a 30-minute exposure. These temperatures at the unexposed surface (48-inch clearance floor) after an hour of exposure are in the range of 200–250 °C (392–486 °F) which are higher than the ASTM E119 recommendation. Also, it should be noted that the maximum temperature at the exposed surface for the 22-inch clearance scenario is higher than the ASTM E119 for approximately the initial 2,000 seconds (22 minutes). However, this happens only at the edge of the rail car floor resulting in lower averaged and maximum temperatures at the unexposed surface as calculated according to the ASTM E119 criterion.

Figure 6-62. Maximum Exposed Surface Temperature with Time for Diesel Fire with Pooling and Standard ASTM E119 Exposure

138
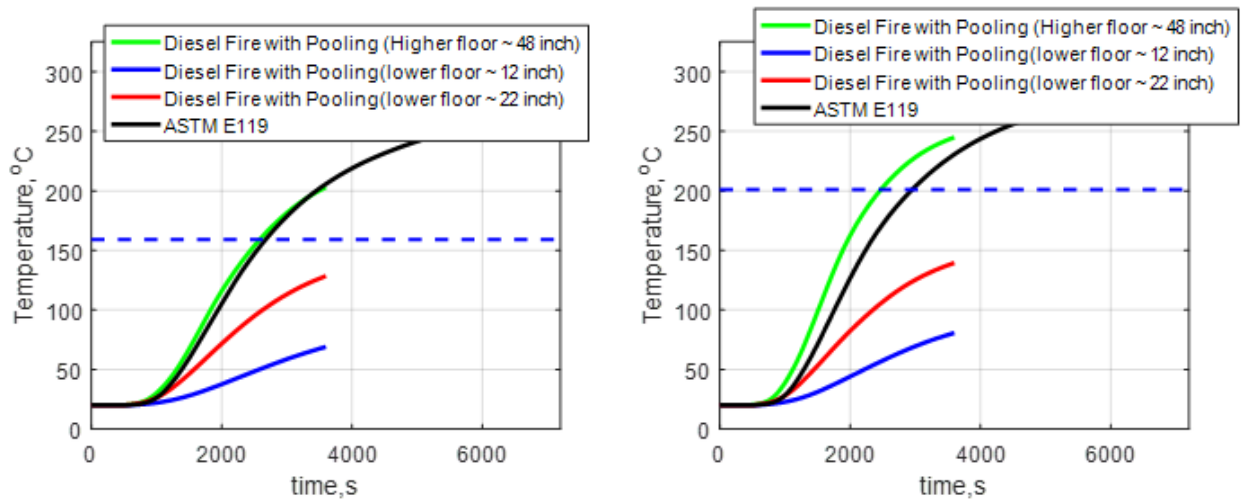
Figure 6-63. Average (Left) and Maximum(Right) Unexposed Surface Temperature for Diesel Fire with Pooling. The Blue Dashed Line Shows the ASTM Limit for a 30-Minute Exposure

The temperature rise at the unexposed surface for different scenarios is also tabulated in Table 6-6. The table shows that the diesel spill fire with pooling exposure for the 48-inch floor clearance is severe compared to ASTM E119. The maximum temperature rise condition of ASTM E119 (181 °C [357 °F]) is reached in 43 minutes for the diesel fire with pooling for the rail car floor with 48-inch clearance. The same condition lags by 7 minutes for ASTM E119. However, the average temperature rise condition only differs by 1 minute for these two scenarios. This happens due to uniform spatial heating of the rail car floor in the case of the standard ASTM E119 exposure as compared to the spatially varying realistic exposure.

Table 6-6. Rating in Minutes for Unexposed Surface Temperature Rise for Diesel Fire with Pooling and Standard ASTM E119 Exposure

Scenario	Time to Exceed (min).			
	50 °C Rise	75 °C Rise	181 °C Rise (ASTM Condition Maximum)	139 °C Rise (ASTM Condition Average)
ASTM E119	25	30	50	45
Higher Floor ~48 inch	22	25	43	44
Lower Floor ~12 inch	58	–	–	–
Lower Floor ~22 inch	28	38	-	–

139

6.6.3. Gasoline Spill

The gasoline fire scenario simulated in this work would be the aftermath of a collision with an automobile at a highway-grade railroad crossing. The FDS models corresponding to these spill cases are Model 3, Model 6, and Model 9. The fire was simulated for 1 hour and spatially and temporally varying ASTs were extracted at the underside of the rail car floor. In addition to ASTs, heat transfer coefficients from FDS were extracted to accurately predict the response a rail car floor assembly to a gasoline fuel fire. The temperature distribution at the exposed surface for all three models at 3 minutes is shown in Figure 6-66. The maximum temperature at the exposed surface is highest for the floor with 48-inch clearance from the rail. The temperature at the unexposed surface for all the models at 3,600 seconds (1 hour) is shown in Figure 6-67.
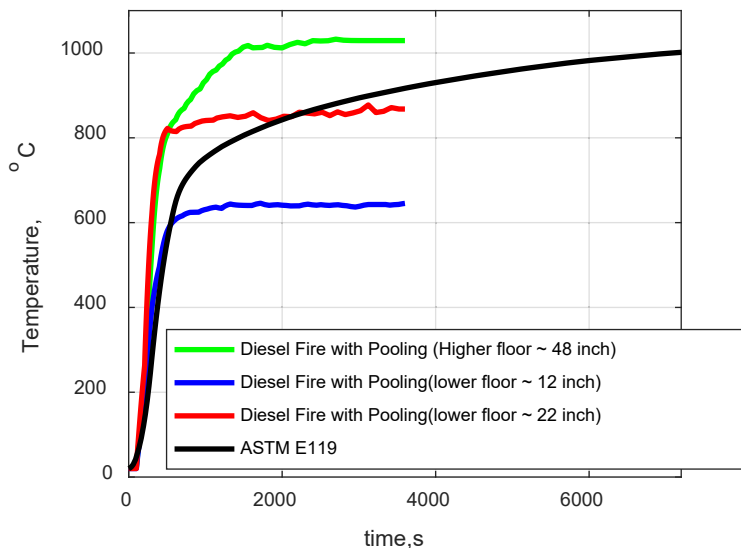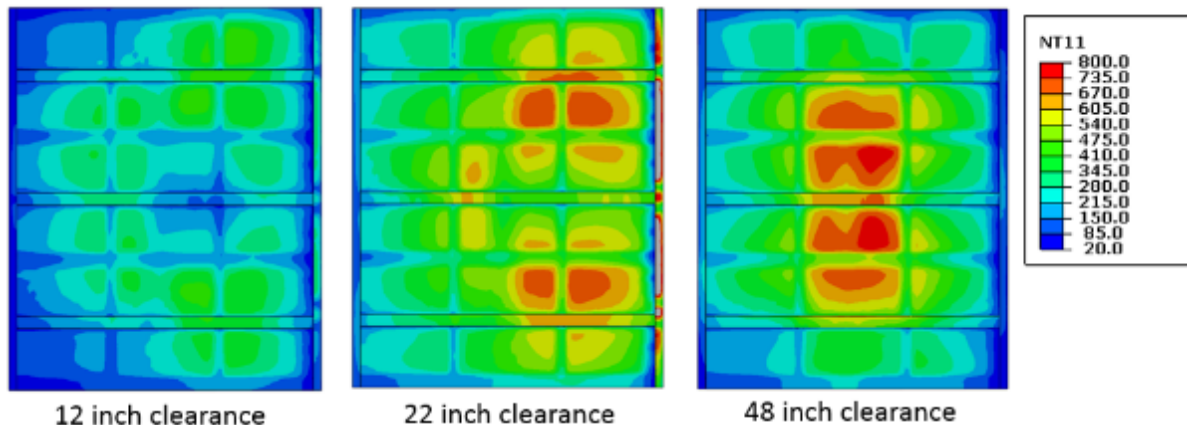

Figure 6-64. Exposed Surface Temperature for Gasoline Fire at 3 Minutes for All Three Floor Configurations Representing Distance Between Rail and the Rail Car Floor
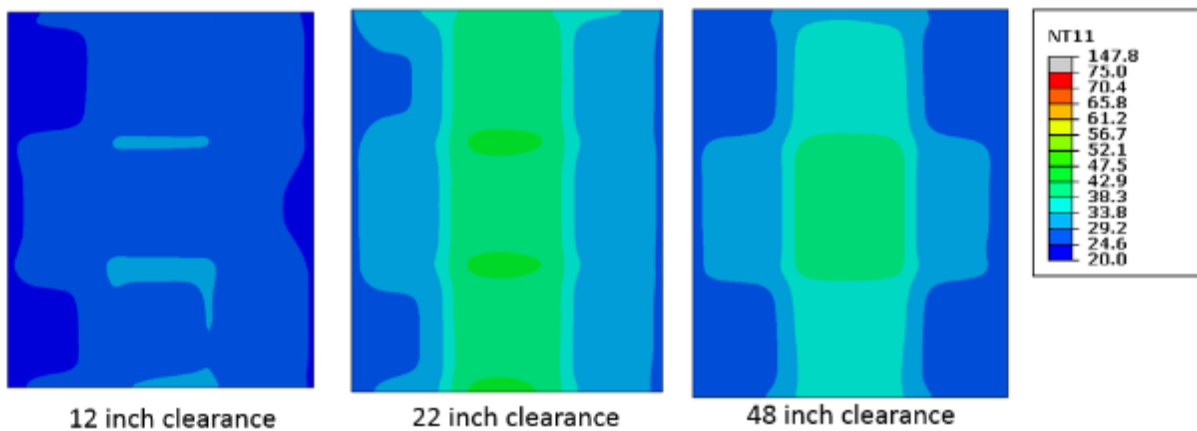
Figure 6-65. Unexposed Surface Temperature for Gasoline Fire at 1 Hour for All Three Floor Configurations Representing Distance Between Rail and the Rail Car Floor

The maximum temperature recorded at the exposed surface for all three configurations as a function of time is shown in Figure 6-68. The figure also shows the temperature rise due to ASTM E119 exposure. The temperature recorded at the unexposed surface

according to ASTM E119 is shown in Figure 6-69. The figure shows both the average and maximum temperature along with the ASTM limit for a 30-minute exposure. The temperature rise at the unexposed surface for different scenarios is also tabulated in Table 6-7. The table shows that the ASTM E119 exposure is severe compared to all gasoline spill fires.
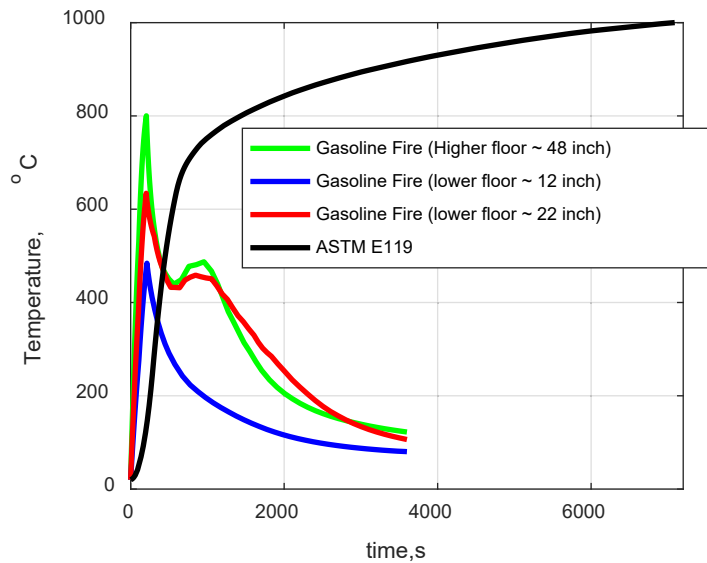
Figure 6-66. Maximum Exposed Surface Temperature with Time for Gasoline Fire and Standard ASTM E119 Exposure
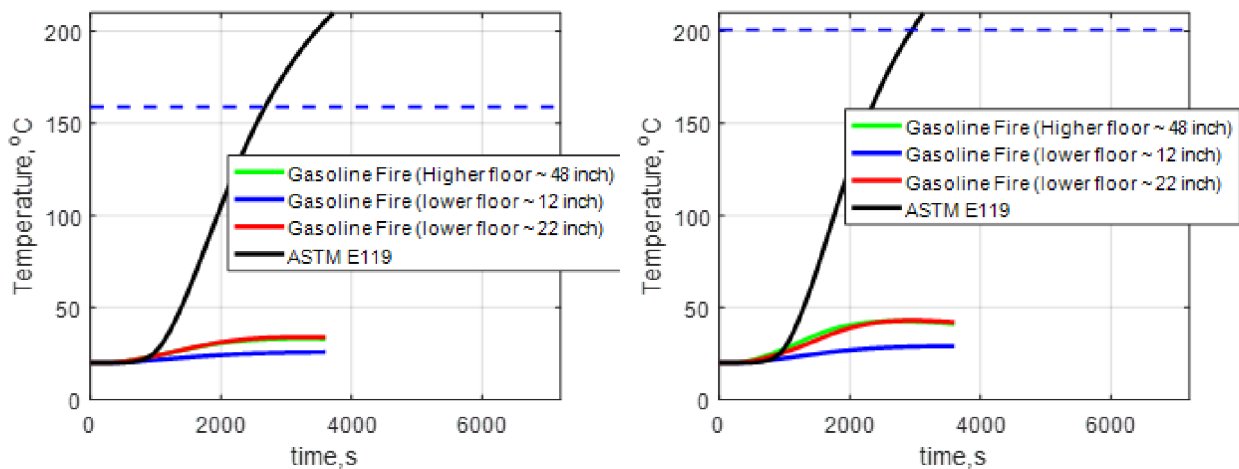
Figure 6-67. Average (Left) and Maximum (Right) Unexposed Surface Temperature for Gasoline Fire. The Blue Dashed Line Shows the ASTM Limit for a 30-Minute Exposure

Table 6-7. Rating in Minutes for Unexposed Surface Temperature Rise for Gasoline Fire and Standard ASTM E119 Exposure

| Scenario	Time to Exceed (min).			
	50 °C Rise	75 °C Rise	181 °C Rise (ASTM Condition Maximum)	139 °C Rise (ASTM Condition Average)
ASTM E119	25	30	50	45
Higher Floor ~48 inch	–	–	–	–
Lower Floor ~12 inch	–	–	–	–
Lower Floor ~22 inch	–	–	–	–

6.7. Section Summary

Six simulations were conducted to model typical fire exposures that occur underneath typical bi-level commuter rail cars that are found on the West Coast. Based on site survey data, the bi-level rail car undercarriages may be 12 in. to 22 in. above the ground. For comparison, results from three simulations for single level rail cars with an undercarriage 48 in. above the ground and undercar components have also been provided.

The six simulations on the bi-level rail cars conducted in this work were intended to predict the thermal conditions of the undercar structural frames and flooring assemblies created by the three most severe potential common fire sources identified in previous work. The fuel sources included a diesel fuel spill, a diesel fuel spill in which pooling occurred, and a gasoline fuel spill. All simulations included cables as a possible fuel source in the undercarriage. The duration of the simulations was 1 hour which was determined to be typically based on a review of rail car fire incidents. Complex reaction chemistry was defined to account for soot and carbon monoxide production and combustion as well as the potential for under-ventilated conditions.

It is evident from these simulations that the diesel fuel fires produce the highest surface temperatures for the undercar frame and floor assemblies. For the two different types of diesel fuel spills, it is clear that the fire involving the diesel fuel spill with pooling is more intense compared with the diesel fuel spill fire scenario. However, these severe diesel fires with relatively high burning rates can create a ventilation-limited situation in the low clearance undercar configurations simulated in this work. This results in lower heat fluxes which decrease as the undercarriage height decreases. The burning rate for the diesel fuel spill with pooling is also representative of a spill fire without pooling with significant radiation feedback from the bottom of the rail car.

In addition, the highest instantaneous heat fluxes to the undercar frames observed in these simulations were produced by the gasoline spill fire and the diesel spill with

pooling for the high clearance undercarriage case with undercar components. In both cases, the maximum local heat fluxes were greater than 150 kW/m^2. Due to the more local and limited fuel, the gasoline fuel spill scenario duration was shorter resulting in a less severe exposure. Based on the duration and exposure, the diesel spill fire with pooling (also representing a spill fire without pooling and significant radiation feedback from the bottom of the rail car) produced the most severe exposure conditions.

The cables ignited in all simulations with the exception of Models 4, 5, and 8. The cables did not ignite in the simulations of these models because the fire source was under-ventilated and did not allow sufficient oxygen in the vicinity of the cables to facilitate ignition. In cases where the cables ignited, their HRR contribution was minor compared with the initiating fire HRRs. As a result, the floor assembly surface temperatures were not significantly affected by the additional HRR from the cables.

The realistic exposure data from the FDS simulations was used as input to detailed three-dimensional thermal simulations of a section of the undercar frame and flooring assembly. The standard exposures were simulated using the ASTM E119 time-temperature curve. An analysis of the temperature at the exposed and the unexposed surfaces was done to identify the appropriate exposure duration in ASTM E119 which would better represent the real fire scenarios. It was observed that the current ASME E119 exposure duration of 30 minutes should be sufficient to provide the fire resistance rating due to most of the realistic fires. However, a diesel pool fire with a higher burning rate would require reevaluating the current exposure duration. In this case, the ASTM E119 temperatures lagged those of the diesel spill fire with the higher burning rate by 300–600 seconds (5–10 minutes).

7.   Comparison of ASTM E119 and ISO 834 Furnace Exposures

Rail car assemblies manufactured in the U.S. are currently required to demonstrate their fire resistance rating which includes structural integrity and limited heat transmission according to ASTM E119 [74] and NFPA 130 [91]. There is a different standard used in the European Union (EU) which requires rail car assemblies to establish their fire resistance requirements according to EN 45545-3 for heat transmission and EN 1365-2 for structural integrity [72] [102]. The U.S. and EU standards use ASTM E119 and ISO 834 thermal exposures, respectively [103]. This work developed a thermal model in Abaqus to identify the thermal transmission performance of a rail car floor assembly exposed to these standard time-temperature curves [1]. The thermal model in Abaqus provided the evolution of temperature in different components of the simulated floor assembly consisting of a structural frame, an insulation layer, and a composite floor. The temperature evolution at various locations in the assembly is compared using both curves and evaluated according to specified test criteria defined in the ASTM E119 and EN 45545-3 standards. In addition, the differences in these standards for assessing the structural integrity are also recognized.

7.1.   Standard Acceptance Conditions

Both ASTM E119 and ISO 834 exposures have acceptance criteria which are stated in NFPA 130 and EN 45545 (which refer to EN 1363 and EN 1365-2 [75] [102]), respectively.

7.1.1. NFPA 130 Requirements (U.S. Standard)

The NFPA 130 requires:

1. Transmission of heat through the assembly shall not be sufficient to raise the temperature on its unexposed surface more than 139 °C (250 °F) on average and 181 °C (325 °F) at a single point.

2. The assembly shall not permit the passage of flame or hot gases sufficient to ignite cotton waste on the unexposed surface of the assembly.

3. The assembly shall support the representative loading. (Structural condition). Though NFPA 130 requirements supersedes ASTM E119, the ASTM E119 conditions for structural integrity acceptance are:

    To obtain an unrestrained beam fire resistance rating the specimen shall have sustained the applied load during the rating period. The specimen shall be deemed as not sustaining the applied load when both of the following conditions are exceeded:

A maximum total deflection of:

$$\delta_{max} = \frac{L_c^2}{400d}$$ (7-1)

and after the maximum total deflection has been exceeded, a maximum deflection rate per minute as determined over 1-minute intervals of

$$\frac{d\delta}{dt} = \frac{L_c^2}{9000d}$$ (7-2)

where:

L_c = the clear span of the beam, and

d = the distance between the extreme fiber of the beam in the compression zone

δ = deflection

The required duration of NFPA 130 is the greater of the following:

- Twice the maximum expected time under normal circumstances for a vehicle to stop completely and safely from its maximum operating speed, plus the time necessary to evacuate a full load of passengers from the vehicle under approved conditions, or

- Fifteen minutes from AGT vehicles, 30 minutes for all other passenger-carrying vehicles

7.1.2. EN 45545 Requirements (EU Standard)

The assembly performance according to the European standard is measured as defined in EN 45545 with further reference to EN 1363-1 and EN 1365-2 as:

1. Loadbearing capacity (R)

This is the time in completed minutes for which the test specimen continues to maintain its ability to support the test load during the test.

2. Integrity (E)

These are the times in completed minutes for which the test specimen continues to maintain its separating function during the test without either:

    a) Causing the ignition of a cotton pad applied against any glowing or flaming visible surface

    b) Resulting in sustained flaming

3. Insulation (I)

This is the time in completed minutes for which the test specimen continues to maintain its separating function during the test without developing temperatures on its unexposed surface which either:

    a) Increase the average temperature above the initial average temperature by more than 140 °C (252 °F)

or

    b) Increase the temperature at any location (including the roving thermocouple) above the initial average temperature by more than 180 °C (322 °F).

In general, a floor assembly with 60 minutes of load bearing capacity, a 45-minute integrity rating and 35 minutes of insulation performance will be classified as R60, RE 45 and REI 35.

7.2. Thermal Comparison

A thermo-structural analysis was performed (Section 5) for a rail car floor assembly known to possess a 30 minute resistance rating (as determined from a test) using the commercially available FE code Abaqus. The modeled section was 3.4 m (11.2 ft.) long with structural repetitions every 1.1 m (3.6 ft.). The modeled section width was 2.7 m (9 ft.) representing the entire rail car width. The section consisted of a stainless steel 304 (SS304) structural frame below a SS304 and plywood (ply-metal) composite floor protected by spun fiberglass blanket insulation as shown in Figure 7-1. The detailed investigation and development of relevant thermal and mechanical material property models, section modeling methods, and analysis was addressed in previous sections. In this work, two standard furnace temperature exposures provided by ASTM E119 and ISO 834 were applied for 2 hours to estimate the thermal response. The time-temperature curves for these standard exposures are shown in Figure 7-2. The rise in temperature for both curves is approximately the same with ASTM E119 showing slightly higher temperature values in between 800 seconds to 1200 seconds and ISO 834 showing higher temperature values after 2,000 seconds. The underside of the assembly was exposed to these furnace exposures with natural convection on the unexposed surfaces.
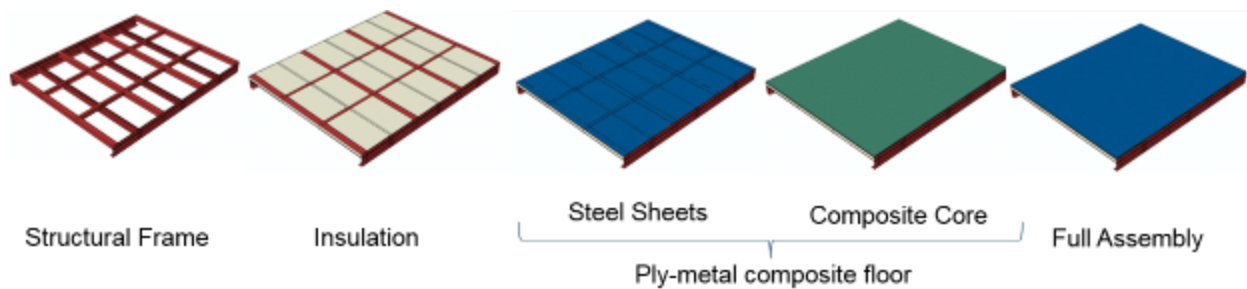
Figure 7-1. Various Components and Abaqus Model Geometry Used for the Standard and the Realistic Exposures
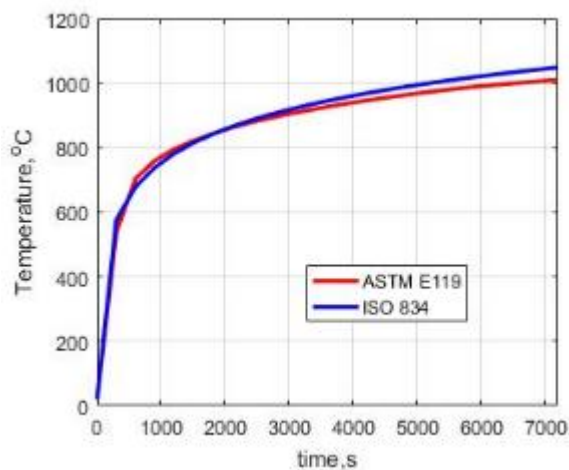
Figure 7-2. Time-Temperature Curves for ASTM E119 and ISO 834

The Abaqus model constructed in Section 5 is used for this work with a modification in the handling of insulation described in Section 6.
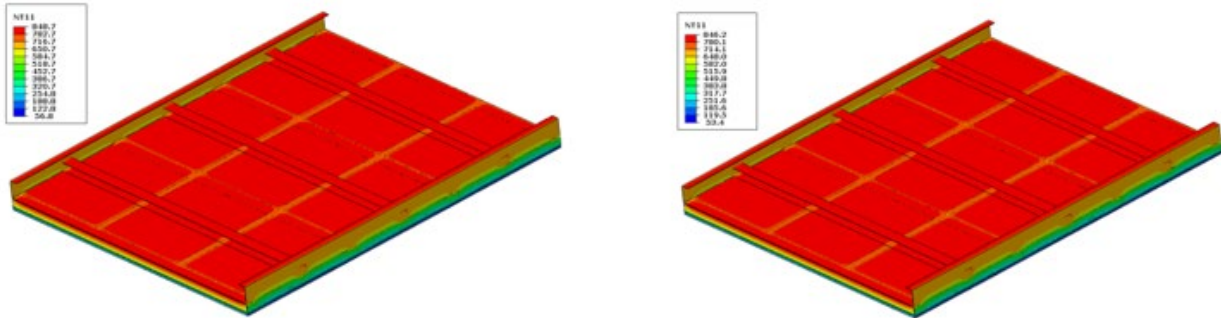
Figure 7-3. Exposed Surface Temperature at 1,800 Seconds: ASTM E119 (Left) and ISO 834 (Right)

The temperature distribution at the exposed and the unexposed surface after an exposure of 30 minutes for both ASTM E119 and ISO 834 is shown in Figure 7-3 and Figure 7-4, respectively.
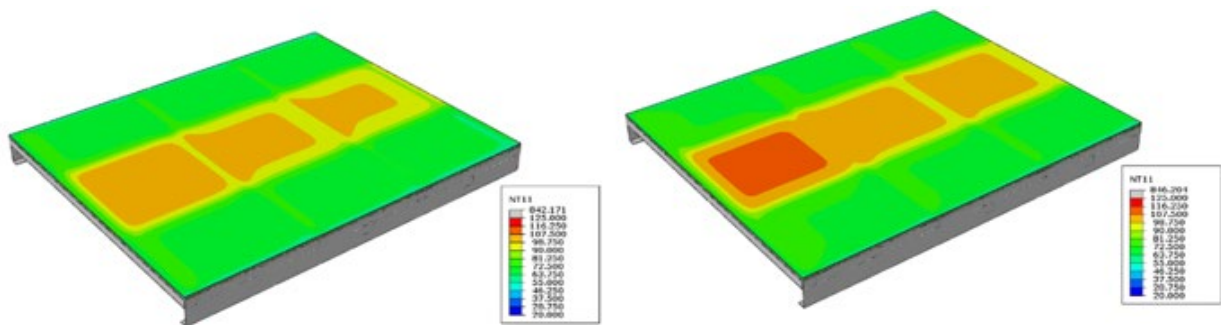
Figure 7-4. Unexposed Surface Temperature at 1,800 Seconds: ASTM E119 (Left) and ISO 834 (Right)

The temperature-time histories recorded at various through-thickness locations are provided in Figure 7-5. The through-thickness temperatures for both simulations follow the time-temperature exposure curves.
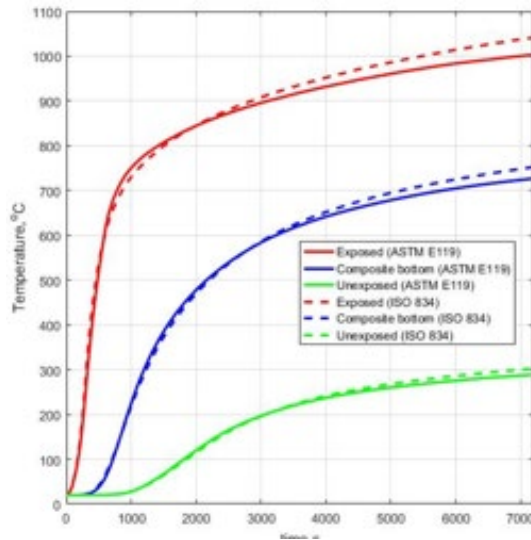
Figure 7-5. Through-Thickness Temperature at Several Locations
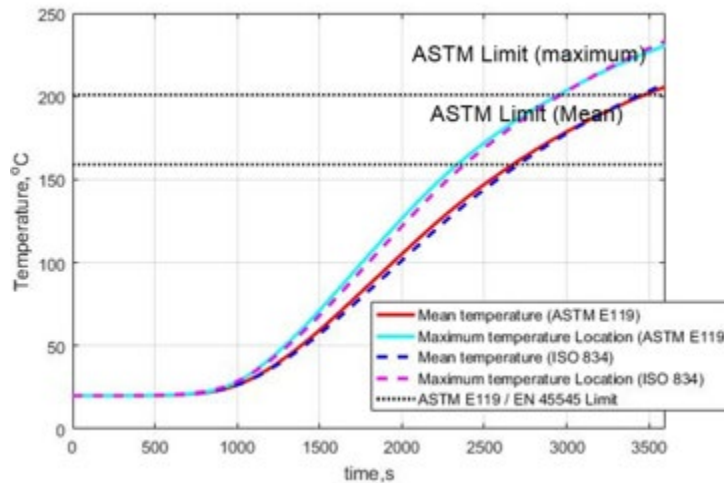
Figure 7-6. Mean and Maximum Unexposed Surface Temperature for ASTM E119 and ISO 834

Figure 7-6 shows the mean and the maximum temperature response for both scenarios. This figure indicates that both mean and the maximum temperature are below the critical limit at 45 minutes (2,700 seconds). The mean temperature goes above its critical limit after 45 minutes (2,700 seconds) while the hottest temperature goes above its critical limit after 50 minutes (3,000 seconds) of exposure. These time intervals indicate that the floor assembly will satisfy the fire resistance requirements of NFPA 130 for 45 minutes and will also have a thermal insulation rating of 45 minutes (I45) according to the EN 45545 criterion described in Section 7.1.2.

148

7.3. Structural Loading and Boundary Conditions

The conditions for structural acceptance for both U.S. and EU standards are given in Section 7.1 and are almost identical. However, the structural loading and boundary conditions are not stated categorically in these standards and require further evaluation.

NFPA 130 states the following requirements regarding the loading:

- The support of the test sample shall be limited to the transverse ends of the test sample only.

- The size of the exposed portion of the floor assembly shall be at least 3.7 m (12 ft.) long by the normal width of the vehicle floor.

- The floor assembly shall be tested with a representative loading consistent with the vehicle design.

EN 45545 states the following requirements regarding the loading:

- The test specimen may be mounted in a supporting construction designed to reproduce the required conditions or the design boundary and support conditions. The type of test frame and the performance required from it will vary according to the element being tested. The document also states to refer to EN 1363 - EN 1365 for specific requirements

EN 1365-2 (Fire resistance tests for the loadbearing elements: floors and roof) describes the general requirements for floors with fire exposures from the underside as:

- The test specimen must be full-size as intended for use in practice. If the test specimen is larger than that which can be accommodated in the furnace, a test specimen with a minimum dimension of 3 m (10 ft.) X 4 m (13 ft.) (exposed width x exposed length) is to be tested.

- The test specimen is installed in a manner representative of its use in practice.

- The test specimen is subjected to loads such that the maximum moments and shear force produced are representative of, or higher than those expected in practice.

The above stated requirements for both U.S. and European standard need further study for a better understanding. Though the sample size and the installation requirements are similar, the loading requirements can be interpreted differently. NFPA 130 states that the assembly should be tested with a representative loading, but it does not mention whether the representative loading be applied to ensure the same uniform load or the same maximum bending moment. Failing to understand this can result in entirely different loading conditions used among U.S. and EU standards as EN 1365-2 clearly states that test specimen should be subject to a load such that maximum moments are representative of, or higher than those expected in practice. JENSEN HUGHES recommends investigating these requirements to ensure that the testing in U.S. is representative of loading experienced in practice.

7.4. Section Summary

Thermal simulations involving the standard fires were done to determine the difference in the temperature rise of a rail car floor assembly. The standard exposures were simulated using the ASTM E119 and the ISO 834 time-temperature curves. The two exposures were compared by evaluating the heat transmission through the rail car floor assembly. The evolution of temperature at the exposed and the unexposed surfaces were calculated to estimate the fire resistance requirements according to NFPA 130 and EN 45545. The rail car floor assembly satisfied the requirement specified by NFPA 130 when exposed to ASTM E119 exposure and did not exceed the critical temperature until 45 minutes. The assembly also had an insulation rating of 45 minutes according to EN 45545 when exposed to the ISO 834 exposure. The thermal performance of the assembly exposed to both ASTM E119 and ISO 834 was similar with no significant difference in the unexposed surface temperatures. However, the rail car floor is a loadbearing member and should be tested for structural integrity according to both standards. It was noted that the representative loading requirements specified in NFPA 130 can be subject to different interpretation by the test laboratories. Test loading can be representative of loading in practice by either creating the same uniform load or by creating the same maximum bending moment. These different interpretations can lead to substantially different results in overall structural integrity of the assembly.

8. Preliminary Modeling and Analysis of Reduced-Scale Rail Floor Assemblies to Determine the Minimum Size

This aspect of the research used computational modeling and analysis to understand the role of various structural members used in a rail car floor assembly and their performance in a typical full-scale floor assembly fire resistance test and the potential for reducing the scale of the test article.

The research focused on reducing the fire resistance test article size currently described in NFPA 130 and 49 CFR Part 238. The current test requirement is to use a floor assembly test article that is 3.6 m (12 ft.) long and has the width of a rail car (approximately 3 m [10 ft.]). The test article is simply supported along the transverse ends and has an applied total distributed load comprising live loads (passenger crush load), dead loads (equipment, other articles), and other relevant design loads. The goal of this effort was to determine whether the size of the test article could be reduced while still capturing similar overall response of the current full-scale fire resistance test.

The simulations were performed using a FEA with the commercial software Abaqus [1]. The FEA included heat transfer through the floor assembly, the reduction in mechanical properties with temperature [Appendix F.1], and the overall structural response. Initially, FEA was conducted on an exemplar full-scale floor assembly to quantify the thermal and structural response expected in a fire resistance test (Section 5). This was used as the baseline response for comparison with that of the reduced scale assemblies. Reduced scale assemblies were then constructed based on the full-scale design and applied loads were developed to create similar overall structural response and potential failure modes (i.e., similar bending moment and shear forces). The response of the reduced scale assemblies was then compared with the full-scale assembly to determine the minimum size test article that would represent the current fire resistance test conditions. These simulation results were further compared with the performance of a full-scale rail car floor assembly, and recommendations were developed on boundary conditions needed in the fire resistance test to replicate the response of an actual rail car floor assembly.

8.1. Baseline Floor Assembly

A thermo-structural analysis (Section 5) was previously performed for a rail car floor assembly known to hold a 30-minute resistance rating using the commercially available FE software Abaqus. Abaqus is a software suite for Computer Aided Engineering (CAE) applications, originally released in 1978. It is used in the automotive, aerospace and many other industries. Modeling furnace exposure experiments of structural assemblies has become common using FEA software packages such as Abaqus [76], [89], [104]–[106]. The modeled section used in this work was 3.4 m (11.2 ft.) long with structural repetitions every 1.1 m (3.6 ft.). The modeled section was 2.7 m (9 ft.) wide representing the entire rail car width. The section consisted of a stainless steel 304 (SS304) structural frame below a SS304 and plywood (ply-metal) composite floor protected by spun fiberglass blanket insulation. A detailed investigation to develop relevant thermal and mechanical material property models, section modeling methods, and analysis was performed.

The underside of the assembly was exposed to an ASTM E119 furnace exposure with natural convection on the unexposed surfaces [74]. A crush load of 3.6 kN/m^2 (75 lb/ft^2) representing the passenger density and the dead weight of items on the floor was applied to the top surface using a uniformly distributed load. Additionally, the weight of the structural frame and composite floor were included in the analysis. The assembly was supported at the transverse ends and allowed to expand according to NFPA 130 (Section 8.5.1.3.1.2) [91]. The model predicted a 30-minute resistance rating with reasonable thermal and mechanical behavior predictions. A section view of the final deformed shape with vertical deflection distribution is shown in Figure 8-1 which indicates the deflection is maximum at the center (represented by the blue color) and almost negligible at the transverse edges (represented by the red color). This model was developed as a full-scale prediction baseline and has shown that the methodology can reasonably capture floor assembly response to furnace exposure making it sufficient for a numerical investigation into the feasibility of reducing the physical scale of assembly in this work.

Current work used the same material properties and material models as used in Section 5. A two-part sequential analysis consisting of a thermal model to predict the temperature response and a structural model to predict the displacement response was conducted. These two models were sequentially coupled together such that any effect of the displacement response on the thermal exposure was neglected. Since it is generally true (for furnace tests) that the exposures are nearly uniform so the effect of displacement on thermal response can be considered negligible.
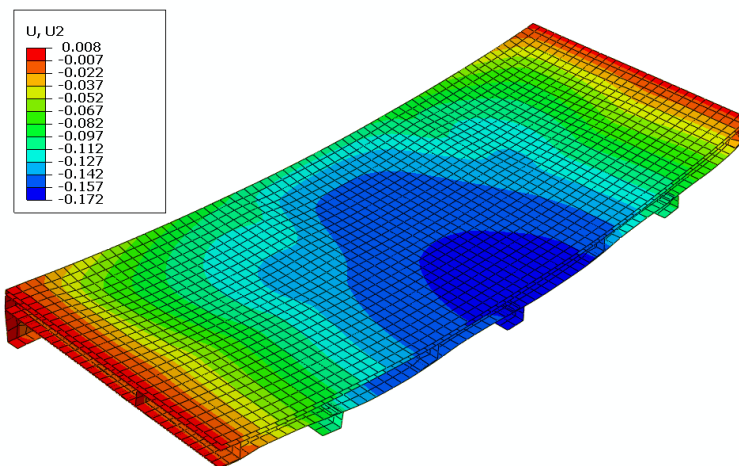
Figure 8-1. Deflection Distribution on Deformed Geometry Following 1,800 Second (30 Minutes) of ASTM E119 Furnace Exposure

8.2.   Scaling Dimensions and Loads

The scaling of structure under similar loading conditions can be challenging due to the presence of a number of variables. The rail car assembly in this work can be simplified as a simply-supported beam to understand the role of these variables [107]. This understanding will help to ensure that the reduced model is subjected to comparable loading conditions and has a similar response when compared to the full-scale one. A simply-supported beam of length l with uniform loading is shown in Figure 8-2.

152
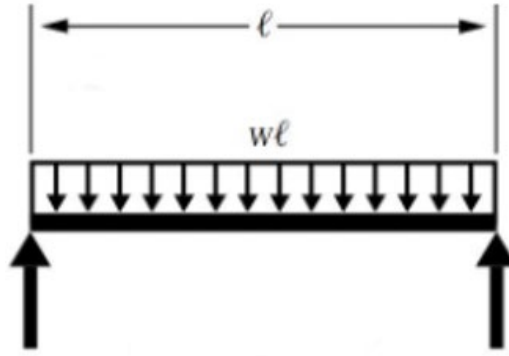
Figure 8-2. A Simply Supported Beam with Uniform Loading as a Representation of a Rail-Car Assembly Supported at the Transverse End

The maximum bending moment *M* experienced by this beam will be at the center and is calculated as [107]

$$M = \frac{wl^2}{8}$$ (8-1)

where *w* is the load per unit length. The above equation can be used to scale the loads for a reduced model, while keeping the same maximum bending moment, such as

$$\frac{w_r}{w_f} = \left(\frac{l_f}{l_r}\right)^2$$ (8-2)

where *f* and *r* are subscripts to represent full-scale and reduced scale assemblies respectively. Note that reducing the beam length by half requires a fourfold increase in uniform load to keep the same maximum bending moment. A similar analysis can be done for the maximum shear force *V*, which is given as

$$V = \frac{wl}{2}$$ (8-3)

The above equation indicates that increasing the uniform load to keep the maximum bending moment the same will result in the maximum shear force being inversely proportional to length of beam such as

$$\frac{V_r}{V_f} = \frac{l_f}{l_r}$$ (8-4)

Continuing with the example above where the length of beam is reduced to one half, keeping the same maximum bending moment will result in twice the maximum shear force. This analysis is only applicable in the elastic regime. Nonetheless it will help to estimate the initial loading condition while adjusting the size of the full-scale assembly.

8.3. Different Reduced Scale Assemblies

This section explains the techniques and modeling efforts to establish guidelines which can be used while designing a reduced scale rail car model. The temperature response of the floor assembly computed from the Abaqus thermal model was sequentially input into a corresponding structural model to predict the deformation behavior during the ASTM E119 furnace exposure. The structural model consisted of an identical geometry as the thermal model except that the fiberglass insulation was not included since it does not contribute to the structural integrity. The main components for structural analysis are

153

stainless-steel frame, stainless-steel sheets, and the composite floor. The stainless-steel frame consists of other structural components such as side sills, transverse and longitudinal channels as shown in Figure 8-3. The cross-network of C channels is attached to stainless-steel sheets which provide a strong though slightly flexible support. The side sills are the main load bearing members and are usually built to bear heavy loads indefinitely. The study done in this work considered reducing the scale of the rail car floor as well as the role of structural members, seen in Figure 8-3, and how those could contribute towards the overall behavior of the assembly. The analysis of these examples led to insights which were used to finalize the minimum size of a reduced rail car, which can depict the same behavior as a full-scale rail car.
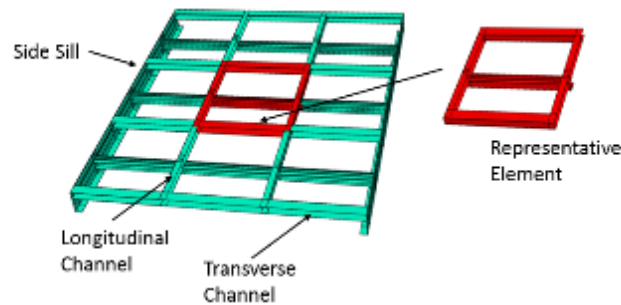
Figure 8-3. Full Scale Representation of Rail Car Stainless Steel Floor with a Representative Element

The base analysis of the full-scale assembly was done using a uniformly distributed load of 3.6 kN/m^2 (75 lb/ft^2) in addition to the weight of the assembly. The assembly was simulated using a plane of symmetry while being supported on the transverse ends. These loading and boundary conditions are depicted in Figure 8-4 where U and R represent displacement and rotation, respectively.
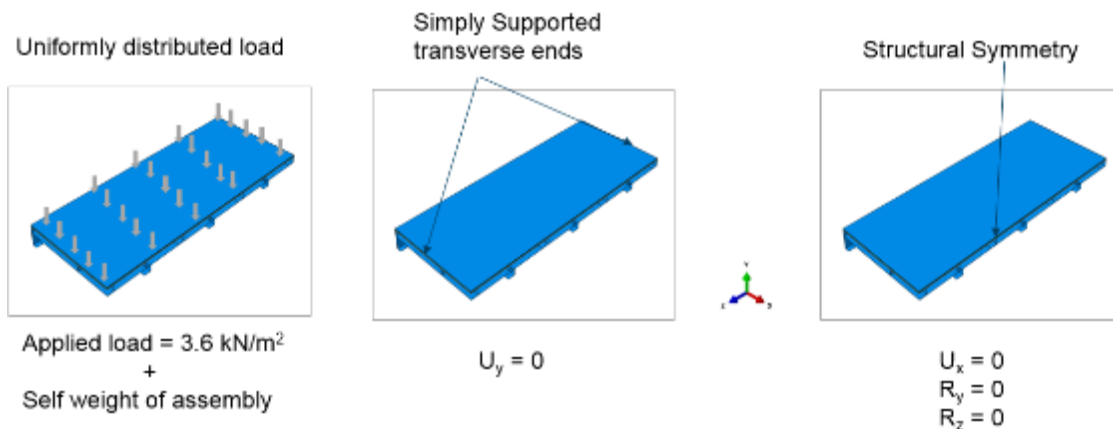

Figure 8-4. Loading and Boundary Conditions for Full-Scale Assembly

The loading condition shown in Figure 8-4 was modified accordingly for the reduced-scale analysis, as discussed in Section 3.

8.3.1. Representative Element Analysis

It can be observed from Figure 8-3 that the smallest possible size for a reduced-scale assembly could be a representative structural element. This representative element has two longitudinal channels and three transverse channels and is repeated three times in both directions to create a full-scale assembly. Therefore, an analysis was conducted on this representative element with a length of 1.17 m (3.8 ft.) and a width of 1 m (3.3 ft.) to evaluate how this test article would compare with the full-scale. The thermal loading on the reduced-scale assemblies is the same as that considered in the full-scale assembly. However, the uniform loading experienced by these members will be 32.4 kN/m^2 (675 lb/ft^2) to keep the same maximum bending moment as the full-scale model. The vertical displacement contours are shown in Figure 8-5.
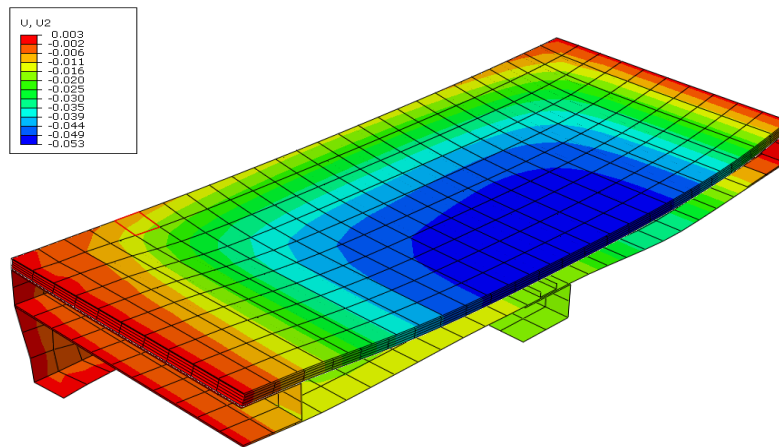
Figure 8-5. Vertical Displacement Contours on Deformed Geometry of Representative Element Following 1,800 Seconds of ASTM E119 Furnace Exposure
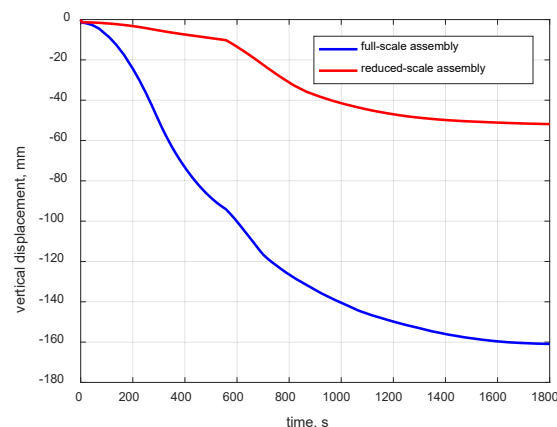
Figure 8-6. Comparison of Vertical Displacement at the Center for Reduced-Scale and Full-Scale Assemblies

The comparison of vertical displacement at the center for reduced-scale and full-scale assemblies is shown in Figure 8-6. It can be seen that apart from the expected different

155

magnitudes of vertical displacement, the rate of change in the vertical displacement of the reduced scale assembly is different from that of the full-scale. The continuous change in the vertical displacement observed in the full-scale assembly is not seen in the reduced-scale assembly. This is due to the change in the moment of inertia as the full width of the assembly is not considered. Therefore, a single representative element cannot depict the behavior of a full-scale assembly. Figure 8-6 also shows that the reduction in size resulted in a decrease in vertical displacement (~50 mm [1.97 in]) as compared to that of the full-scale assembly (~155 mm [6.10 in]) even though the distributed load was increased. This is expected as the maximum deflection for elastic loading (which is at center for a uniformly loaded simply-supported beam) is given by

$$\Delta = \frac{5wl^4}{384EI} \tag{8-5}$$

where E is the modulus of elasticity and I is the moment of inertia. Equation (8-5) clearly shows that changing the length has a major effect on maximum deflection compared to other variables. Note that although the FE model considers both temperature and plasticity effects, this equation simply describes qualitative behaviors, is only valid in the elastic regime and does not consider the change in material properties due to thermal softening as well as plasticity effects which are important in this analysis.

8.3.2. Scaling Along Longitudinal Direction

In this setup, the scaling was done only along the longitudinal direction and the width of the reduced assembly was kept same as the full-scale assembly. This simulated test article had a length of 1.17 m (3.84 ft.) and the entire width of a rail car (2.7 m [9 ft.]) created by three representative elements. Two cases were considered to reflect the importance of the scaling of the load. In the first scenario, the maximum bending moment was kept the same as the full-scale assembly by loading the reduced-scale assembly to a crush load of 32.4 kN/m^2 (675 lb/ft^2) and in the second scenario the uniform load of 3.6 kN/m^2 (75 lb/ft^2) was kept the same as of the full-scale assembly. The vertical displacement contours for the case in which the maximum bending moment was preserved are shown in Figure 8-7.
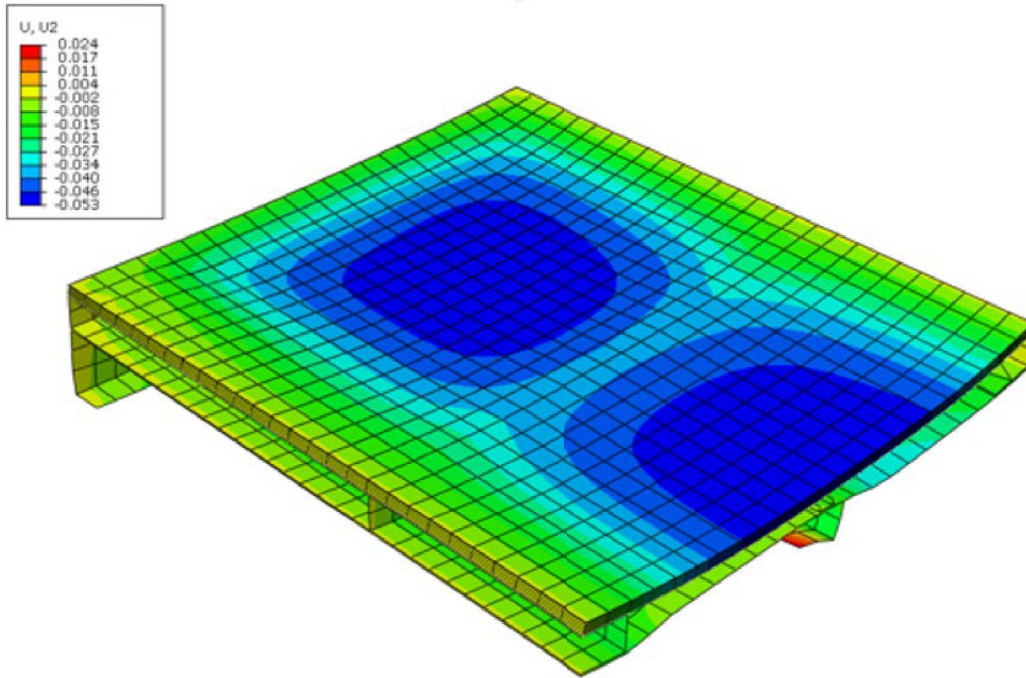
Figure 8-7. Vertical Displacement Contours on the Deformed Reduced-Scale Geometry (the Maximum Bending Moment was Kept Same) Following 1,800 Seconds of ASTM E119 Furnace Exposure

The vertical displacements at the center of the reduced-scale assembly for the same uniform load and the same maximum bending moment as that of the full-scale assembly are shown in Figure 8-8. It also shows the vertical displacement at the center of a full-scale assembly.
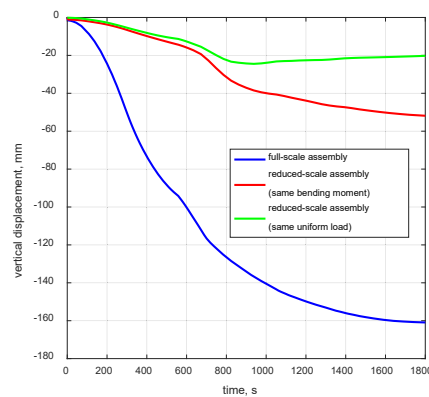
Figure 8-8. Vertical Displacement Response at the Center of the Various Configurations

It can be seen from Figure 8-8 that reducing the longitudinal dimension makes it very difficult to bend the reduced-scale assembly under the same uniform load. This happens as the beam with a reduced length is less prone to deflection under the same uniform load [Equation 6]. The slope of the displacement curve corresponding to uniform load also changes sign between 800–1,200 seconds which is not seen when

157

the maximum bending moment is kept the same or for the full-scale assembly. Though the behaviors of the reduced-size and full-scale assemblies in this study is very similar, it is important to note that substantial reduction in specimen length should be avoided as it will lead to major disparity in shear force. For instance, to keep the same maximum bending moment, the maximum shear force experienced by the reduced scale model can be calculated using Equation 4. In this case, the maximum shear force is three times that experienced by the full-scale model. Also, the vertical shear observed in the composite core for this case is around 0.05 MPa, which is higher than the threshold value of 0.041 MPa for plywood (Appendix F.2) [5].

8.3.3. Scaling Along Both Longitudinal and Transverse Directions

In this setup, the assembly was scaled such that it had two representative structural elements in the transverse and longitudinal directions. The overall dimensions of the assembly were of 2.24 m (7.35 ft.) long and 1.84 m wide (6 ft.). This resulted in a reduced assembly illustrated by four representative elements which does not have a plane of symmetry resulting in one of the longitudinal edges without the side sill as shown in Figure 8-9. The assembly was supported on the transverse ends.
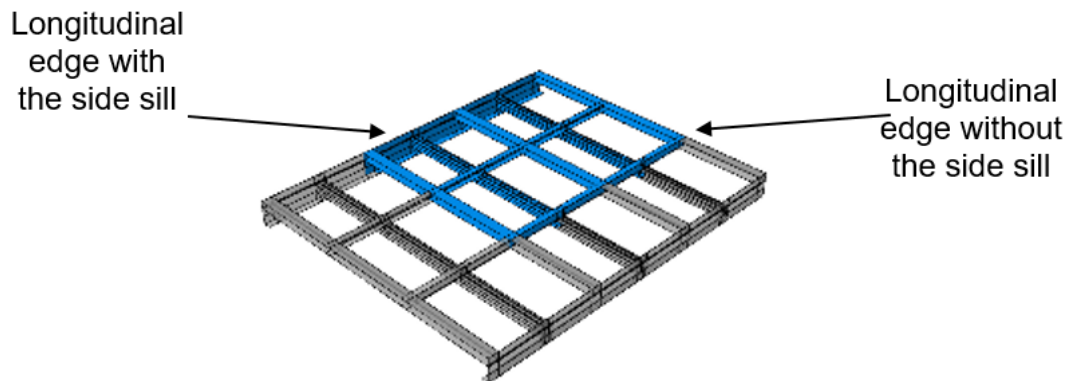
Figure 8-9. Selected Reduced-Scale Assembly (in Blue) as a Subset of Full-Scale Assembly

The vertical displacement for this setup compared with the full-scale assembly is shown in Figure 8-10.
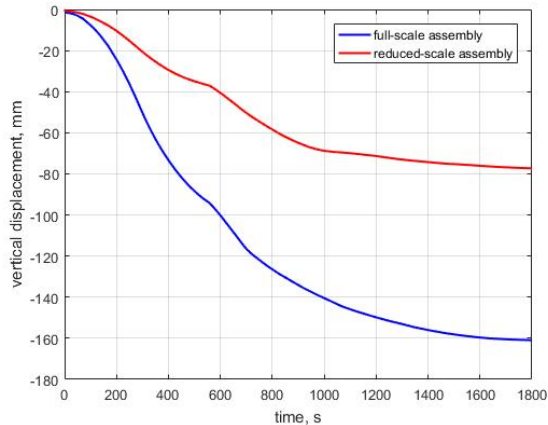
Figure 8-10. Comparison of Vertical Displacement at the Center for Reduced-Scale and Full-Scale Assemblies

The vertical displacement contours for this scenario are shown in Figure 8-11. The figure also shows the interface separation between the sheet and the frame along the free longitudinal edge which does not have a side sill. This sheet was attached to the frame using a tie-constraint and resulted in separation in the absence of a side sill. This separation happened as the local buckling of the lower sheet was not constrained by the side sill support. Though the displacement profiles are similar among the reduced and the full scales (Figure 8-10), the separation of the interface between the C-channel and the metal sheet indicates that it will not be desirable to reduce the width of rail car.
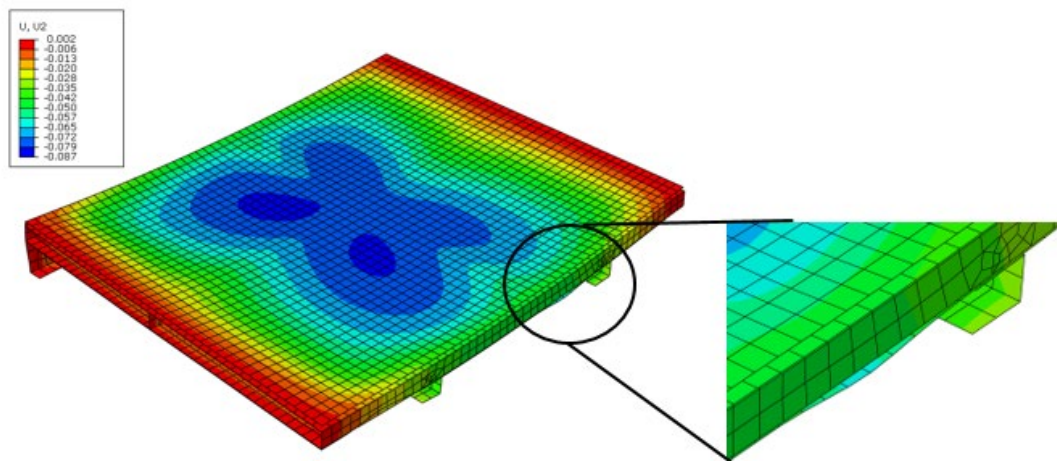
Figure 8-11. Vertical Displacement Contours on Deformed Geometry Indicating Interface Failure Following 1,800 Seconds of ASTM E119 Furnace Exposure

8.3.4. Role of Side Sill

The side sills are the main load bearing members and are usually built to bear heavy loads indefinitely. The role of a side sill was numerically investigated by loading the full-scale assembly for a longer duration than the suggested 30-minutes duration. It should

159

be noted that although the passenger load remains constant with time during these simulations the material undergoes thermal softening leading to further decrease in strength as the test duration increases. Moreover, the furnace temperature also increased with time resulting in exposure to higher temperatures as the testing time was increased. The reason to test the side sill is to investigate whether it is strong enough and is less likely to fail in an actual test. Thus, a modified rail car assembly could be created by removing the side sills (which are the major load bearing members) and replacing them with simple supports, resulting in a reduced cost of manufacturing. Both configurations with (same as shown in Figure 8-1) and without side sills were exposed to a crush load of 3.6 kN/m² (75 lb/ft²) in addition to their individual weight.
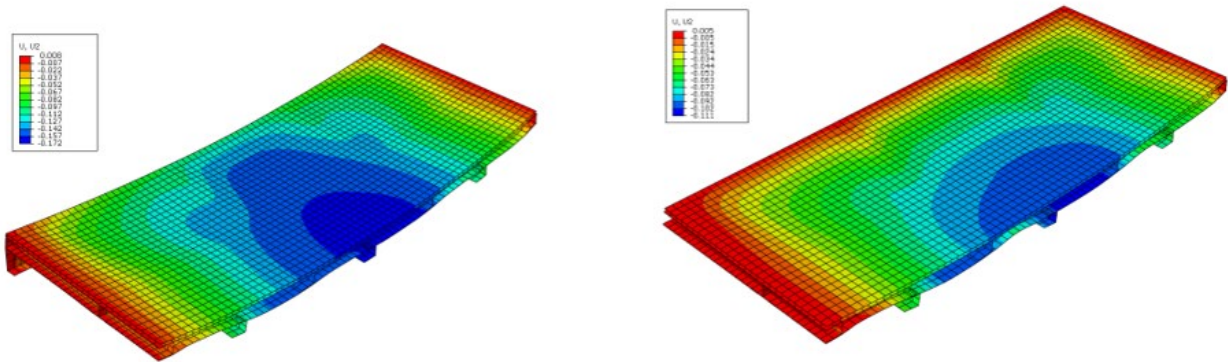
Figure 8-12. Vertical Displacement Contours on Deformed Geometry with Side Sill (Left) and Without Side Sill (Right) Following 2,000 Seconds of ASTM E119 Furnace Exposure

Vertical (out-of-plane) displacement contours representing the deflection for both scenarios at 2,000 seconds are shown in Figure 8-12. The figure indicates that supporting the assembly (without side sills) on all four sides resulted in reduced displacement at the center compared to supporting it (with side sills) only on transverse ends. Even though the displacements were larger in the model with side sills, the model was still able to support the loads even after exposure to a longer duration than suggested in NFPA 130. Additionally, the displacement at 2,000 seconds (~160 mm [6.3 in]) is less than the deflection acceptance criterion at 1,800 seconds in ASTM E119 Section 8.8.5.1 [74]:

$$\delta_{max} = \frac{L_c^2}{400d} = \frac{(3400 \text{ mm})^2}{400 * 177.8 \text{ mm}} = 163 \text{ mm [6.4 in]} \qquad (8\text{-}6)$$

where L_c is the longitudinal span of the full-scale assembly and d is the total depth. This shows that the side sill is designed to withstand harsher loading conditions than the test conditions described in ASTM E119.

The vertical displacement response at the center of the assembly for both configurations is shown in Figure 8-13. Due to the thermo-structural loading, the vertical displacements at the center of assembly were different with the assembly supported on all four sides exhibiting more resistance to deformation. This happened due to membrane behavior when the assembly was supported on all sides compared to a beam behavior when supported only on transverse sides. In addition to vertical displacement response, the figure also indicates that there is no significant change in

160

displacement after 1,500 seconds for either configuration. The cutoff displacement criterion at 1,800 seconds is also shown in Figure 8-13. This study suggests that the side sill can support the assembly for more than 1,800 seconds, which is the requirement in NFPA 130. It will not fail under the specified load and might be replaced by simply supporting the assembly. However, removal of the side support and replacing it with a simple support along the longitudinal edges is non-conservative compared to the boundary conditions specified in NFPA 130.
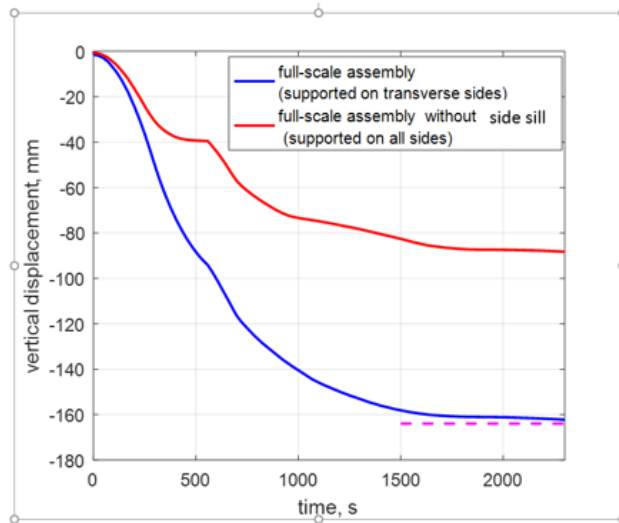
Figure 8-13. Vertical Displacement Response at the Center of Assemblies with Temperature at the Exposed Surface. The Dashed Line (Purple) Indicates Cutoff Displacement at 1,800 Seconds as per ASTM E119

8.3.5. Summary of Reduced Scale Modeling

The example studies described above have resulted in the following findings which should be considered to determine the minimum size:

1. A single representative element cannot depict the characteristic behavior of full-scale assembly. The rate of change of vertical displacement response for the reduced scale assembly is different from the full-scale.

2. The loading should be increased for a reduced-size assembly to keep the same maximum bending moment.

3. The size should not be too small so as not to lead to a large difference in shear stress between the full and reduced scale models.

4. Reducing the assembly width exposes a free longitudinal edge which neither has a side sill nor it is simply supported leading to separation of the interface between the channels and the metallic sheet.

8.4. Minimum Size of The Reduced Scale Assembly

After evaluating the different studies in Section 8.3, it was concluded that the minimum size of the reduced scale assembly should have the width of the full-scale assembly to avoid interface separation and should also have at least two representative elements

161

along the longitudinal direction to avoid high shear stresses. The various reduced scale rail car floor assemblies are summarized in Table 8-1, along with the full-scale results to indicate number of representative elements, applied uniform load, maximum bending moment and maximum shear stress. The reduced scale assembly in the second case shown in Table 8-1 with a length of 2.24 m (7.35 ft.) and the full rail car width (27 m [9 ft.]), can reproduce the full-scale behavior. For the suggested reduced-size assembly, the thermo-structural analysis was conducted with same maximum bending moment and 1.5 times the shear stress compared to the full-scale assembly.

Table 8-1. Summary of Reduced Scale Rail Car Floor Assemblies Considered

Case	Representation		Uniform Load, Maximum Bending Moment, Maximum Shear Force	Remarks
Full Scale Assembly			w,M,V	None
Reduced Scale Assembly			9w/4,M,1.5V	Depicts full-scale behavior
Representative Element			9w,M,3V	Too short to depict full-scale behavior
Scaling Along Longitudinal Direction			9w,M,3V	High vertical shear in composite core
Scaling Along Both Directions			9w/4,M,1.5V	Interface Separation

The vertical displacement contours for the two scenarios, one with side sill and one without side sill, are shown in Figure 8-14. The results are similar to those observed in Figure 8-12, where full-scale analysis was done with and without side sill. The vertical displacement at the center of reduced assemblies along with the full assemblies with and without side sill is shown in Figure 8-15.
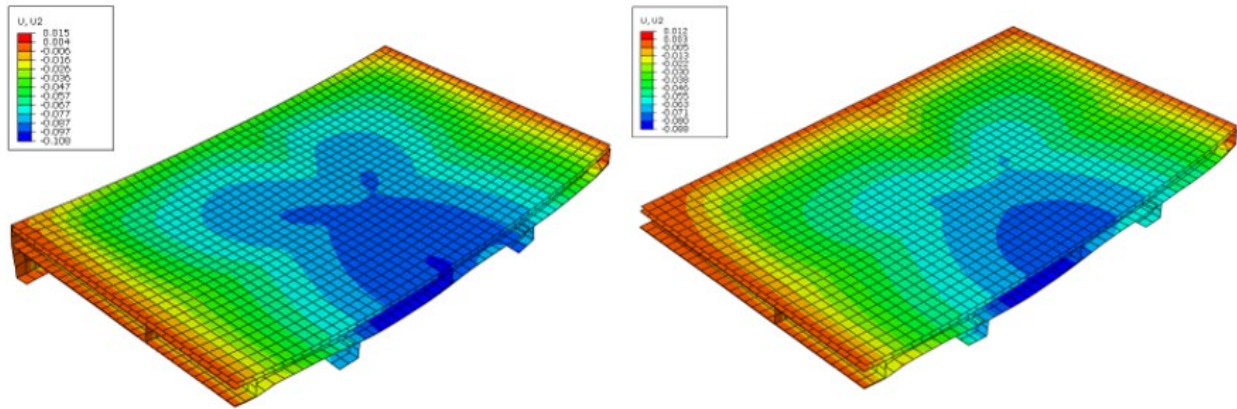
Figure 8-14. Vertical Displacement Contours on Deformed Reduced-Scale Assembly Following 1,800 Seconds of ASTM E119 Furnace Exposure
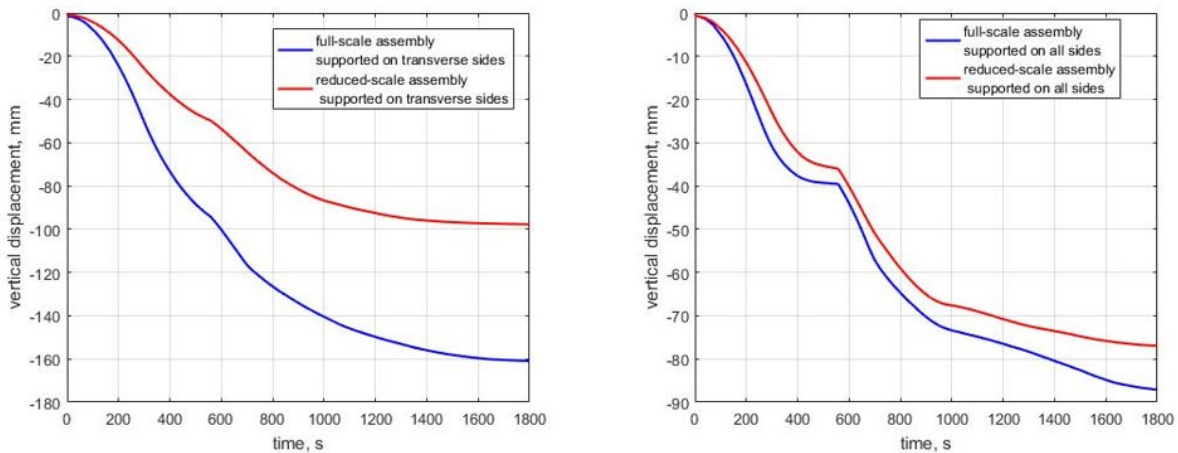
Figure 8-15. Vertical Displacement Response at the Center of the Various Configurations: Supported on Transverse Sides (Left) and Supported on All Sides (Right)

Figure 8-15 shows that the deflection profile of the final reduced assembly is consistent with the full-scale assembly for both the with and without side sill scenarios. This reduced assembly depicts the behavior of the full-scale assembly while addressing all the concerns (Section 4.5) identified for other reduced models. Also, the maximum shear stress observed in the composite core of this model is 0.04 MPa which is less than the threshold value for plywood (Appendix F.2) [5].

8.5.   Alternative Boundary Conditions to Represent Actual Rail Car Floor

Analyses were also conducted as part of this effort to compare the structural response of a test assembly during a fire resistance test and the expected response of such an assembly in a full rail car. These differences have been preliminarily explored using the exemplar floor assembly from this investigation with all simulations performed at room temperature.

A representative full rail-car structure was constructed by patterning the test article to generate an 18.3 m (60 ft.) span which is a typical distance between trucks. A simple shell was placed above the floor to represent the remainder of the rail car structure. The displacement response of the representative full-car was modeled under the passenger crush load of 3.6 kN/m² (75 lb/ft²). The displacement profile of the floor for the full-car analysis is provided in Figure 8-16.
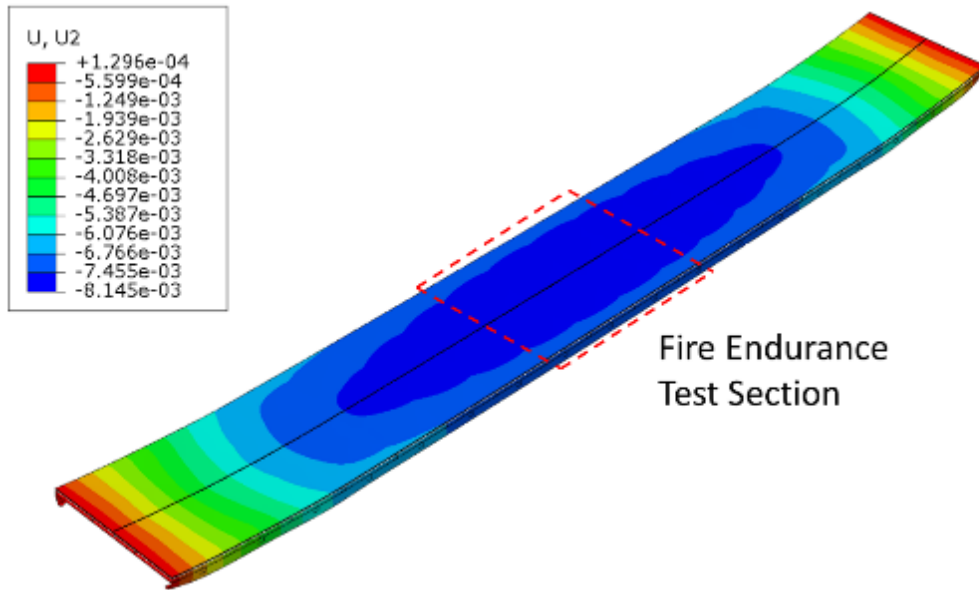

Figure 8-16. Vertical Displacement of Representative Full-Car Constructed from Exemplar Geometry Under Passenger Crush Load (Displayed Deflection Magnified 50x)

A typical fire resistance test section can be taken from the center of the rail car where stresses are highest according to classical beam theory. The localized displacement response of this section of the full-car model at room temperature was compared to the test article models with the same distributed loading at room temperature. The test articles were modeled with two possible boundary conditions: first, the boundary conditions as specified in NFPA 130 where the specimen is simply supported at the transverse ends and, second, with the specimen simply supported on the longitudinal ends at the side sills.

The vertical displacement profiles for each of the three models are shown in Figure 8-17. The displacement profile of the test assembly supported on the longitudinal edges at the side sills is representative of the profile of the full-car analysis while the test assembly supported at the transverse ends results in a different profile. This difference is further seen in the vertical displacement profiles along the transverse and longitudinal centerlines of the assembly provided in Figure 8-18. When supporting a test assembly from the side sills, the local vertical displacement is within 0.2 mm (0.0079 in.) of the results predicted from the full-car model along both the transverse and longitudinal directions. Conversely, the displacement profile in the transverse direction is only 30 percent as large when supporting from the transverse ends. This is because of the additional membrane action generated from the supports at the transverse ends. These

supports also create longitudinal displacement profiles that are not representative of the full rail car analysis results.
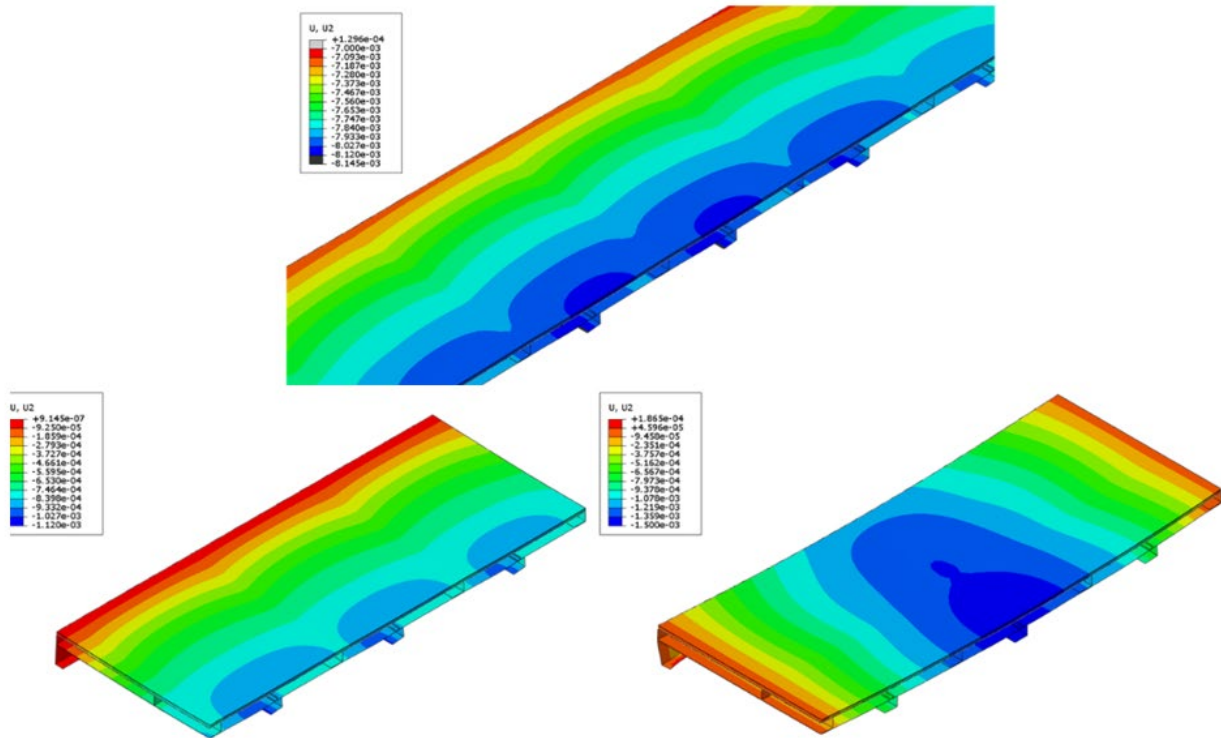
Figure 8-17. Displacement Profiles for (Top) Center Section of Full-Car Model (Left) Side Sill Supported Test Assembly and (Right) Transverse End Supported Test Assembly
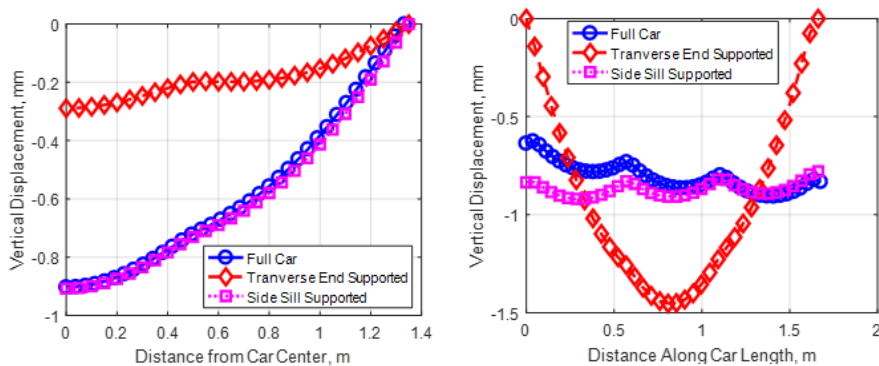
Figure 8-18. Localized Vertical Displacement Profile in (Left) the Transverse Direction (Across Car Width) and (Right) the Longitudinal Direction (Along Car Length) Under Different Boundary Conditions Compared to Full-Car Analysis

8.6. Section Summary

This study was conducted to determine the minimum size of a reduced-scale assembly such that it represents the behavior of a full-scale assembly and can be used for standard fire resistance experiments. A nomenclature was created to define a

representative element which can be used as a building block to construct both full-scale and reduced-scale test articles. A modeling and analysis approach was adopted to ensure loading similarity among different scales by adjusting the uniform load applied to the assembly. The loading conditions were finalized by simplifying the rail car assembly as a simply supported beam under uniform loading. Two major loads on a simply supported beam under uniform loading come from bending moment and shear force. The analysis was done to ensure the final reduced-assembly undergoes similar bending moment and shear force as a full-scale assembly. Several models were considered to finalize the minimum size by eliminating scenarios such as the assembly being too small to depict the full-scale behavior, high shear force compared to full-scale assembly and interface failure. Finally, a reduced model was suggested with the dimensions equal to full rail car width (2.7 m [9 ft.]) and a length comprising of two-thirds of the full-scale model length (2.24 m [7.35 ft.]). An analysis to understand the role of the side sill as the main load bearing member was conducted. The side sill was found to be strong enough to last beyond the test duration and can be replaced by simply supporting the assembly on its longitudinal edges. However, replacing the side sill with a simple support results in a non-conservative design and should only be exercised after a detailed analysis of the rail car assembly.

A preliminary modeling effort comparing the actual rail car floor with test articles with different end support conditions has shown that supporting the fire resistance test article on the longitudinal ends instead of the transverse ends better represents the displacement profiles present in an actual rail car model for the exemplar geometry. It is recommended that these alternative boundary conditions are further investigated to evaluate the differences in the actual rail car response with a fire exposure compared to the test article response with different support conditions. In addition, the configuration with support on its longitudinal edges may provide a configuration that is more amenable to scaling. As a result, the potential for scaling with different support conditions should also be further evaluated.

9. Modeling and Analysis of Rail Floor Assemblies at Different Scales to Determine the Minimum Size to Maintain Fire Safety Resistance

This section is focused on the use of computer modeling to understand the behavior of a full rail car (60 ft. long, 9 ft. wide) subjected to thermal and structural loading conditions according to NFPA 130 compared with furnace size test articles. The full rail car's response to these loading conditions was used to better understand and identify novel boundary conditions relevant at a test scale (12 ft. long, 9 ft. wide) required for a furnace test. This effort further aligned with the interest of rail car manufacturers in reducing the physical size of the test article used to qualify the fire resistance of a rail car floor assembly to decrease the cost of the compliance process. The new boundary conditions were used to determine whether the size of the test article could be reduced while still capturing a similar overall response of the test scale fire resistance test.

The simulations were performed using the FEA with the commercial software Abaqus [1]. The FEA included heat transfer through the floor assembly, the reduction in mechanical properties with temperature (Appendix F.1), and the overall structural response. The response of these assemblies at different scales in terms of deflection, plastic strain accumulation and maximum shear stress distribution was compared to determine the minimum size article that would best reproduce the test scale fire resistance test response.

9.1. Nomenclature

The terminology used to represent the different scales of the rail car floor is as follows:

Full rail car: A representative full rail car structure between the trucks with a length of 18.3 m (60 ft.) and a width of 2.7 m (9 ft.) representing the full width of the rail car. This structure also includes a shell to represent the rail car walls and roof as shown in Figure 9-1.

Test scale rail car floor: A floor assembly according to NFPA 130 with a length of 3.4 m (11.22 ft.) and a width of 2.7 m (9 ft.) representing the full width of the rail car.

Reduced scale rail car floor: A floor assembly proposed in this work with overall dimensions less than the test scale rail car floor.
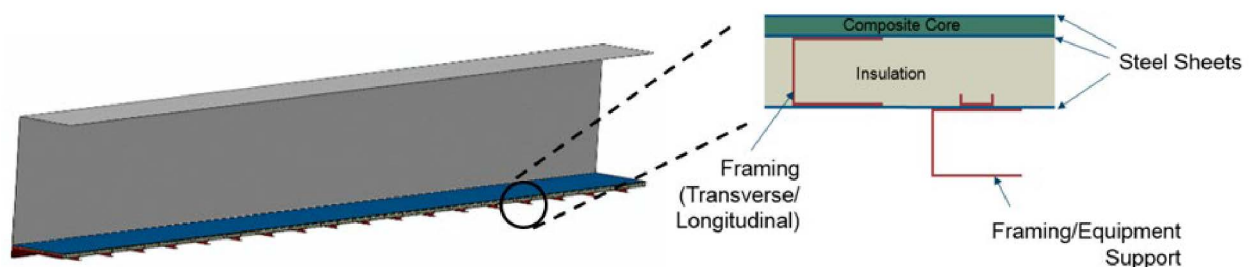

Figure 9-1. Cross-Section of the Full Rail Car with Floor, Wall and Roof

9.2.   Full Rail Car Analysis

A thermo-structural analysis was performed for a full rail car floor assembly using the commercially available FE software, Abaqus. The modeled section used in this work was 18.3 m (60 ft.) long with structural repetitions every 1.1 m (3.6 ft.). The modeled full rail car was 2.7 m (9 ft.) wide representing the entire rail car width. The section consisted of a stainless steel 304 (SS304) structural frame below an SS304 and plywood (ply-metal) composite floor protected by a spun fiberglass blanket insulation of thickness 76 mm (3 inch). The model also included a shell attached to the rail car floor using a standard tie constraint to represent the ceiling and walls of the full rail car. The full rail car specimen was selected for this analysis to understand how a test scale specimen can capture the full rail car behavior as a reference to compare with furnace test articles.

The underside of the rail car floor was exposed to an ASTM E119 furnace exposure with convective and radiative boundary conditions using a convection heat transfer coefficient of 25 W/m^{2}K and an emissivity of 0.7 [74] [108]. An ambient temperature of 25 °C was applied to the unexposed side boundary conditions with a convection heat transfer coefficient of 9 W/m^{2}K and an emissivity of 0.7 [108]. A crush load of 3.6 kN/m^2 (75 lb/ft^2) representing the passenger density and the dead weight of items on the floor was applied to the top surface using a uniformly distributed load [90]. Additionally, the weight of the structural frame and composite floor were included in the analysis. The assembly was supported at the transverse ends which represented the rail car trucks as shown in Figure 9-2.
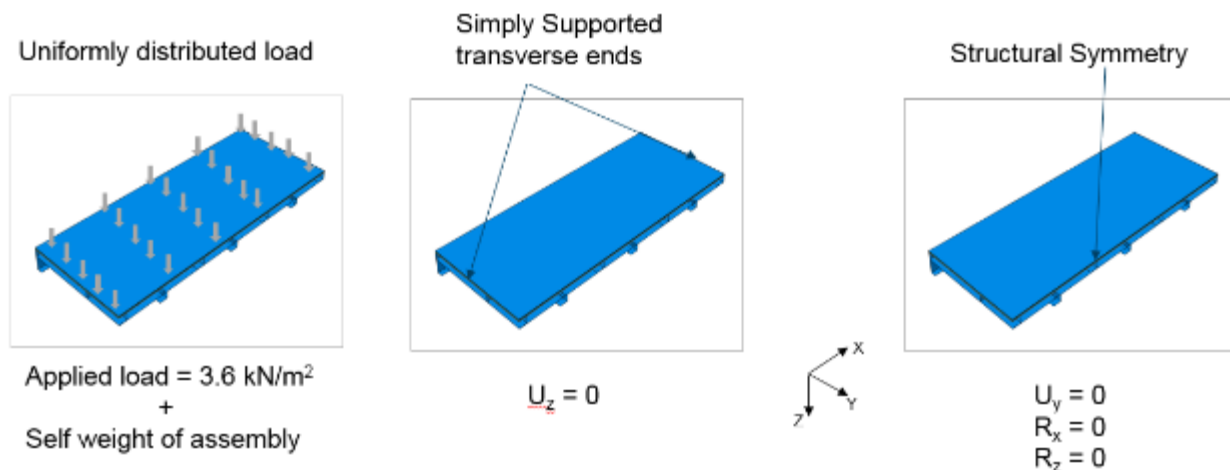
Figure 9-2. Loading and Boundary Conditions for Full-Scale Rail Car

The temperature distribution in the model after 30 minutes of exposure is shown in Figure 9-3. The time/ temperature distribution from the thermal analysis was used in a structural model to predict the displacement response and stress distribution in the different components of the rail car. The vertical displacement in the Z-direction of the full rail car floor is shown in Figure 9-4. The figure also shows a representative fire resistance test section (dashed black lines) which can be taken from the center of the rail car where it experiences maximum bending moment according to classical theory of simply supported beams under the uniform load [107]. The reason to capture the

response of this section of the full rail car is to find the optimum boundary conditions which could be used for a test scale floor to better represent a full rail car floor behavior.
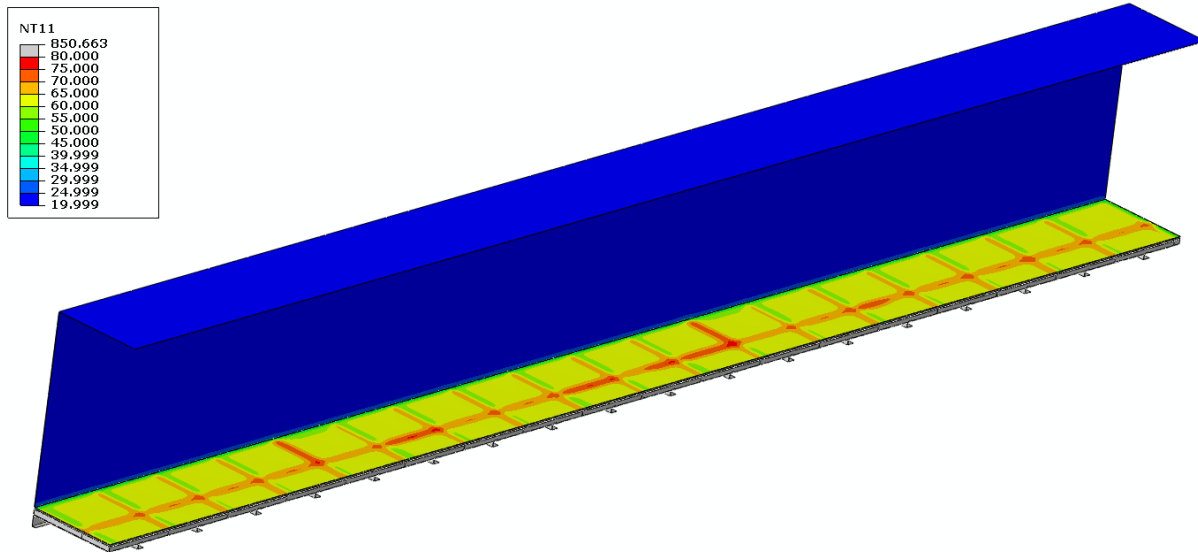
**Figure 9-3. Distribution of Temperature (°C) on the Full Rail Car Assembly at 30 Minutes**
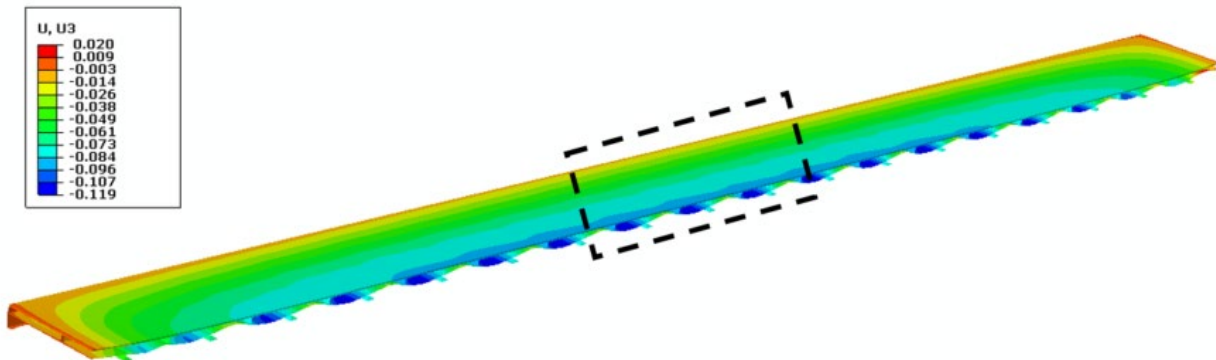
Figure 9-4. Vertical Displacement Contours (in Meters) on the Full-Scale Rail Car Floor

Two boundary condition options are available for evaluating the performance of the test scale floor: supporting the specimen on the transverse ends as specified in NFPA 130, or supporting the specimen on the longitudinal edges. These two boundary conditions were applied to a test scale rail car floor, and the deflection is compared to the deflection of the full-scale rail car floor. The deflection of the top sheet for the full rail car floor is captured and is shown in Figure 9-5. The figure also shows the transverse edges which are simply supported with zero deflection and the longitudinal edges with small values of deflection due to the presence of the side sill and upper frame adding resistance to bending. This results in a global deflection profile of the top sheet exhibiting a membrane effect where the deflection values are smaller at the edges and increase as one moves towards the middle of the floor. However, a representative section with the same dimensions as the test section taken from the center of the full rail

car, shown in Figure 9-6, indicates a local behavior where the deflection is larger on the transverse ends compared to the deflection at the longitudinal ends. In addition, the figure also indicates a gap between the original floor location and the deformed floor location as the supports are applied only at the far transverse ends.
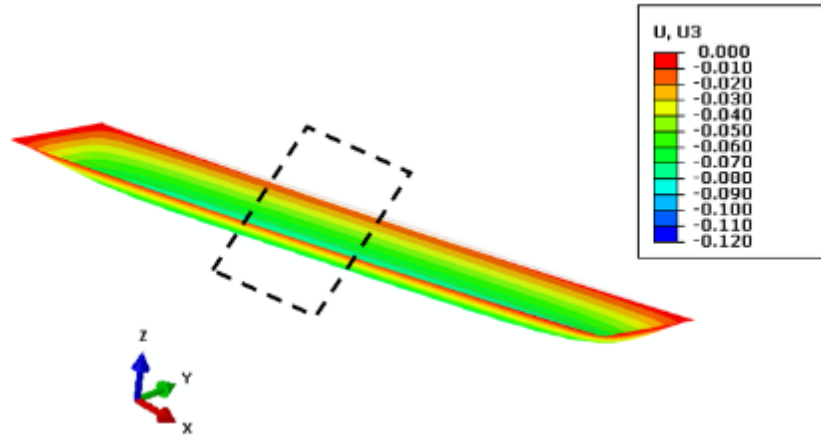
Figure 9-5. Vertical Displacement Contours (in m) of the Top Sheet of Full Rail Car Floor (Displayed Deflection Magnified 5X)

The local deflection behavior for the full rail car floor is compared with the test rail car floor were subjected to the two different boundary conditions described above. The deformation of the floor for both these scenarios is compared with the full-scale floor deflection at the same time and is shown in Figure 9-6. The figure shows that the test section subjected to support at longitudinal ends captures the behavior of full rail car with higher deflection value at the transverse ends and zero deflection at the longitudinal ends. However, the test section subjected to support at the transverse ends as suggested by NFPA 130 does not capture the full rail car floor behavior.
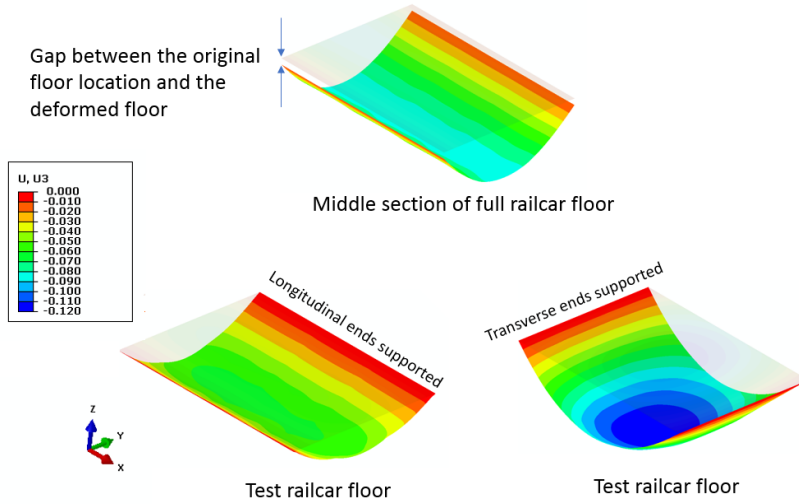
Figure 9-6. Vertical Displacement Contours (in m) of the Top Sheet of Full Rail Car Floor (Top), Test Rail Car Floor Supported on Longitudinal Ends (Left) and Test Rail Car Floor Supported on Transverse Ends Prescribed in NFPA 130 (Right) (Displayed Deflection Magnified 5X)

The deflection values were also quantified and plotted along the transverse and longitudinal centerlines bisecting the rail car floor and are shown in Figure 9-7.
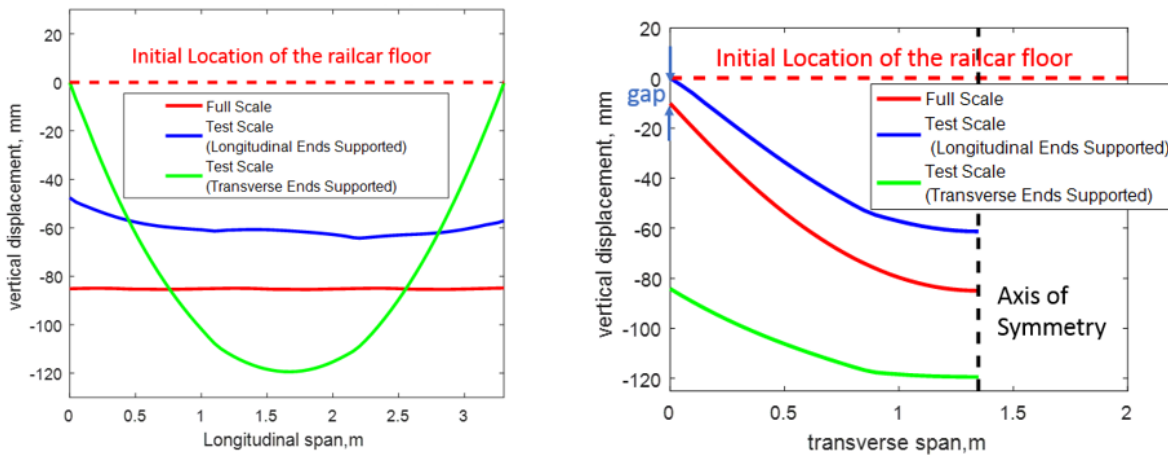
Figure 9-7. Vertical Displacement Profiles for Full Scale and Test Scale Rail Car Floors Along the Longitudinal (Left) and Transverse (Right) Span

The deflection along the longitudinal span indicates that the deflection values for the full rail car floor are approximately the same along the whole span. This behavior is better represented by the test article which is supported along the longitudinal ends, as compared to the test article supported on the transverse ends. A similar conclusion can be made regarding the deflections along the transverse span shown in Figure 9-7, where the deflection profile of the full rail car is closely represented by the deflection

171

profile generated by supporting the test article on longitudinal ends. The figure also shows the gap between the original floor location and the deformed floor location, indicating less displacement at the longitudinal end. This analysis demonstrates that the test article better represents the real car behavior when supported along the longitudinal ends as compared to when it is supported along the transverse ends as recommended in NFPA 130.

9.3. Reduced Scale Assemblies

After evaluating the boundary conditions and ensuring the test article supported on the longitudinal ends better represents a full rail car behavior, this study investigated the reduced scale models using the same loading and boundary conditions. The study considered two reduced scale models shown in Figure 9-8 along with the test article. These models were selected on the basis of an analysis completed in the previous section.
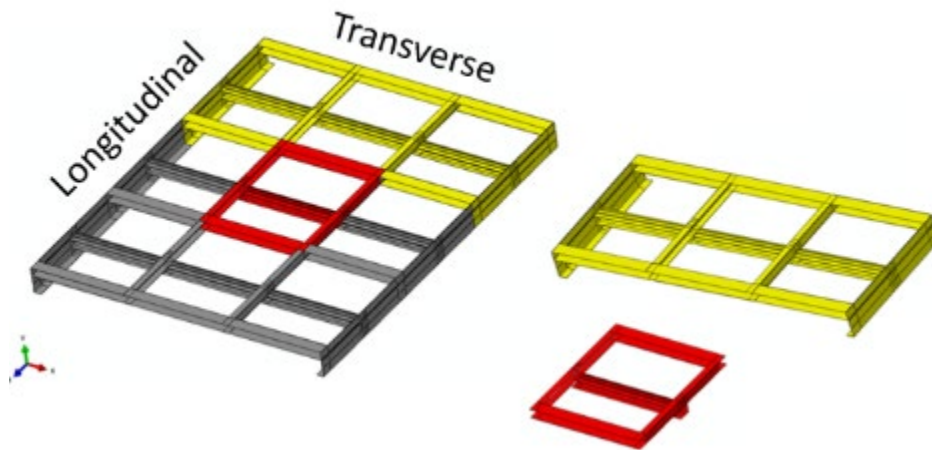

Figure 9-8. Selected Reduced-Scale Assembly (in Red and Yellow) as a Subset of Full-Scale Assembly

It can be observed from Figure 9-8 that the smallest possible size for a reduced-scale assembly could be a representative element (a bay). This representative element has two longitudinal channels and three transverse channels and is repeated three times in both directions to create a full-scale assembly. Therefore, the analysis was conducted on this representative element with a length of 1.17 m (3.8 ft.) and a width of 1 m (3.3 ft.) to evaluate how this test article would compare with the full scale. Two scenarios were considered for this reduced model. In the first case, the thermal exposure represented by ASTM E119 and the structural loading represented by a uniform load of 3.6 kN/m^2 (75 lb/ft^2) were applied on the reduced-scale assembly. These exposures and loading conditions were the same as that considered in the test-scale assembly. However, in the second case the uniform loading experienced by the reduced model was increased to 32.4 kN/m^2 (675 lb/ft^2) to achieve the same maximum bending moment as the test-scale model. The other reduced model considered consisted of three representative elements and had a width of the full rail car model and a length of 1.17m (3.8 ft.). This model was exposed to the same thermal and structural loading as the test scale specimen.

172

9.3.1. Deflection Analysis

The reduced scale models exposed to the same thermal and structural loading as the test scale article were compared for deflection. The deformation of these reduced models along with the test scale model at 30 minutes is shown in Figure 9-9. The figure shows that the reduced scale model represented by three representative elements captures the overall deflection behavior.
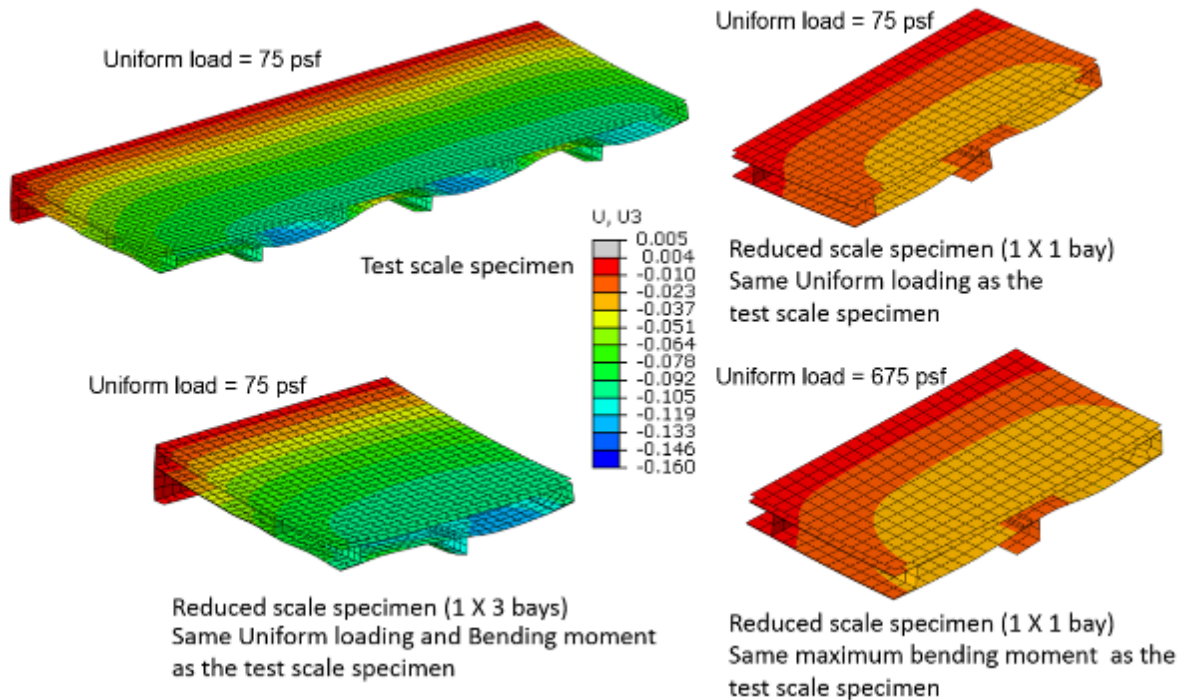
Figure 9-9. Vertical Displacement Contours of the Test Scale Specimen and Reduced Scale Specimens

The deflection values were plotted along the transverse and longitudinal centerlines bisecting the rail car floors and are shown in Figure 9-10. The deflections along the longitudinal and transverse spans show a similar profile for all the cases. The magnitude of deflection for the reduced model with full width of the rail car is higher as it has a lower moment of inertia when compared to the test scale model. Also, the magnitude of deflection for the reduced model represented by uniform loading is lower compared to the test model, as it is one-third the length, even though the moment of inertia is decreased in this case as well. This is expected as the maximum deflection for elastic loading (which is at center for a uniformly loaded simply-supported beam) is given by

$$\Delta = \frac{5wl^4}{384EI} \qquad\qquad (9\text{-}1)$$

where E is the modulus of elasticity, l is the beam length, w is the uniform load, and I is the moment of inertia. The equation clearly shows that changing the length has a major effect on maximum deflection compared to the other variables. In addition, increasing the uniform load to match the maximum bending moment as experienced by the test scale article results in an increase in deflection magnitude. Note that although the FE

model considers both temperature and plasticity effects, this equation simply describes qualitative behaviors, is only valid in the elastic regime and does not consider the change in material properties due to thermal softening as well as plasticity effects which are important in this analysis.

Though the deflection profiles for models represented by one bay are similar in shape, the magnitude of deflection is considerably lower compared to that of the test scale specimen. Also, the increase in uniform load to match the maximum bending moment can result in additional furnace test cost or a new furnace design to support the reduced model under a higher load.
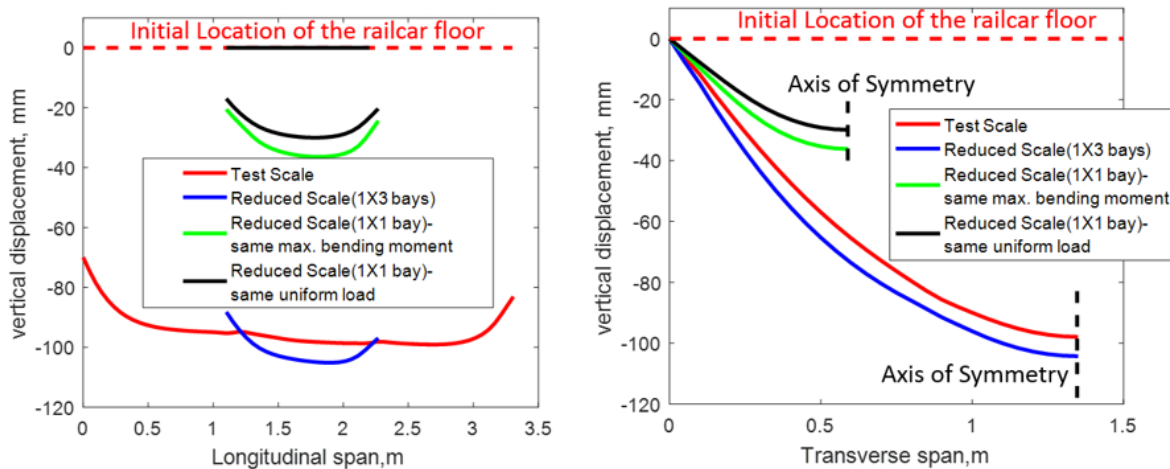

Figure 9-10. Vertical Displacement Profiles for Test Scale and Reduced Scale Rail Car Floors Along the Longitudinal (Left) and Transverse (Right) Span

9.3.2. Plastic Deformation

Most engineering materials show a linear stress-strain behavior up to their proportional limit. Beyond this point, the stress-strain relationship can become non-linear but not necessarily become inelastic. Plastic behavior is accompanied by an irreversible behavior of a material and begins when the applied stress exceeds the yield strength of the material. There are different material models which can be used to represent this elastic-plastic material behavior such as a bilinear elastoplastic material, elastoplastic material and elastic perfectly plastic material. In this work, an elastic perfectly plastic material model is used which accumulated plastic strain as the material yielded. The plastic strain accumulation is a measure of amount of permanent strain (deformation) in a material. Since these models do not include any failure or damage criterion, the accumulated plastic strain gives a good indication of sites where material may fail in the future. The stress-strain (σ-ϵ) behavior of the elastic perfectly plastic model in a one-dimensional setting is shown in Figure 9-11. The figure shows that if the modeled material experiences a stress state (represented by symbol x) which is greater than the yield strength (σ_y) of the material, the state of the stress is modified by bringing the stress back to the yield strength of the material. The process of returning the stress back to the yield strength results in a permanent deformation at that material location which is addressed by assigning the plastic strain (ϵ_p) to that material location.

174

Therefore, equivalent plastic strain which is a combination of all the plastic strain components at a material location is a monotonically increasing scalar and can give a good indication of potential failure sites.
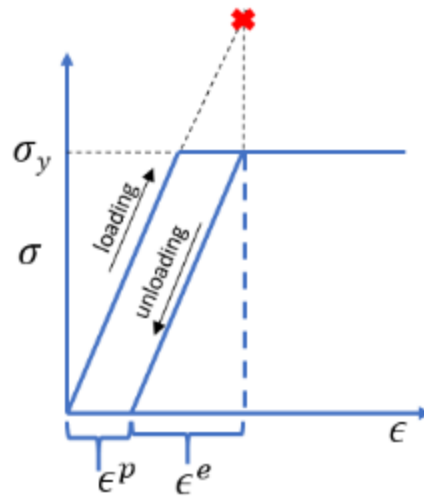
Figure 9-11. Stress Strain Curve Showing Loading and Unloading of an Elastic Perfect Plastic Material with Accumulation of Plastic Strain

The distribution of plastic strain for the full rail car is shown in Figure 9-12 at 10 minutes and is maximum at the exposed surface. This is due to a decrease in the yield strength of the material with temperature as described in Appendix F.1. This decrease in the strength of the material with increase in temperature results in yielding at locations with higher temperature such as the exposed surface compared to locations at lower temperature such as the unexposed surface. The figure also shows that the maximum plastic strain is located off-center along the longitudinal channel. This happened due to local plastic buckling of the underside surface. Note that Figure 9-12 shows a representative region of the full-scale rail car floor under maximum bending moment.
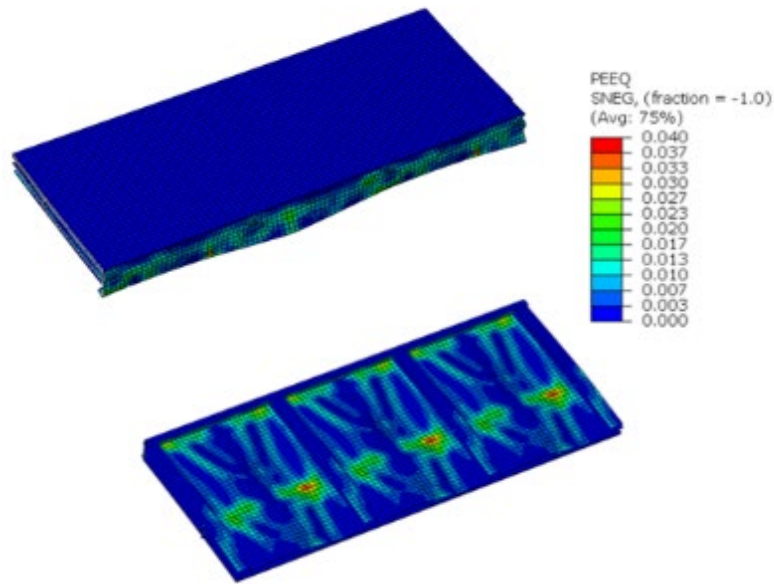
Figure 9-12. Equivalent Plastic Strain Distribution at the Unexposed and the Exposed Side of Full Rail Car Floor Assembly

The accumulated plastic strain is also calculated for the test scale and the reduced scale models and is shown in Figure 9-13. The figure shows that the maximum plastic strain seen in the test scale specimen matches well with the full-scale specimen's plastic strain (Figure 9-12). Figure 9-13 also shows the plastic strain accumulation for the reduced scale models. It is evident from the figure that the reduced models capture the magnitude and location of plastic strain consistent with the test scale specimen.
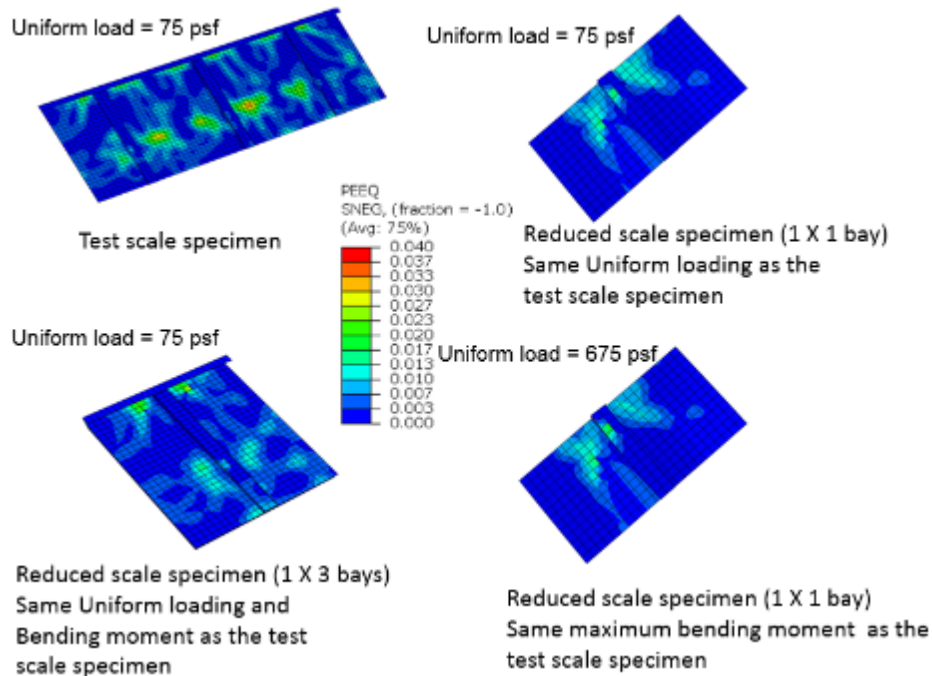
Figure 9-13. Equivalent Plastic Strain Distribution at the Underside of Rail Car Floor Assemblies

9.3.3. Shear Stress Distribution

In addition to deflection and plastic strain accumulation, the maximum shear stress distribution can provide insights to potential sites prone to shear failure. A uniformly-loaded simply supported beam experiences maximum shear force at its edges and is most likely to fail at the supports due to shear as shown in Figure 9-14.
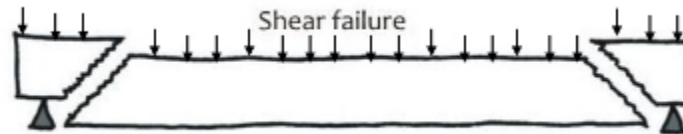

Figure 9-14. Representation of Shear Failure for a Simply Supported Beam Under Uniform Load

Shear force along with the bending of the beam results in a shear failure in a plane which is at an angle to the applied load rather than in line with the applied load. In a three-dimensional loading scenario, the maximum shear can be calculated using the Tresca criterion of failure which calculates the maximum shear, which is given as

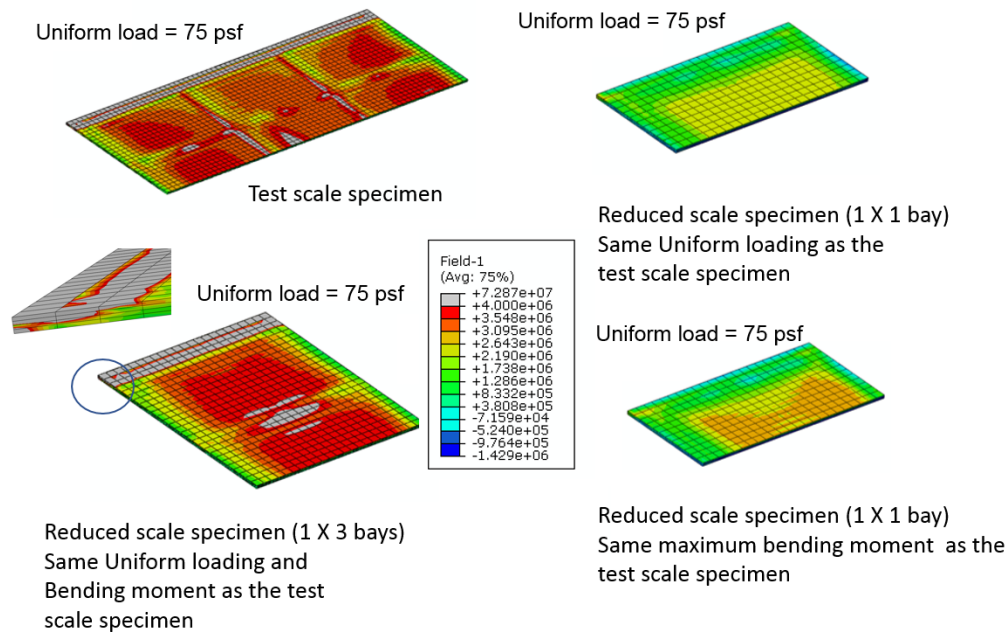$$\tau_{max} = \frac{\sigma_1 - \sigma_3}{2} \tag{9-2}$$

where σ_1 and σ_3 are maximum and minimum principal stresses, respectively. The maximum shear stress is calculated in the plywood core of the rail car floor assembly and its distribution for the full rail car floor is shown in Figure 9-15.

177
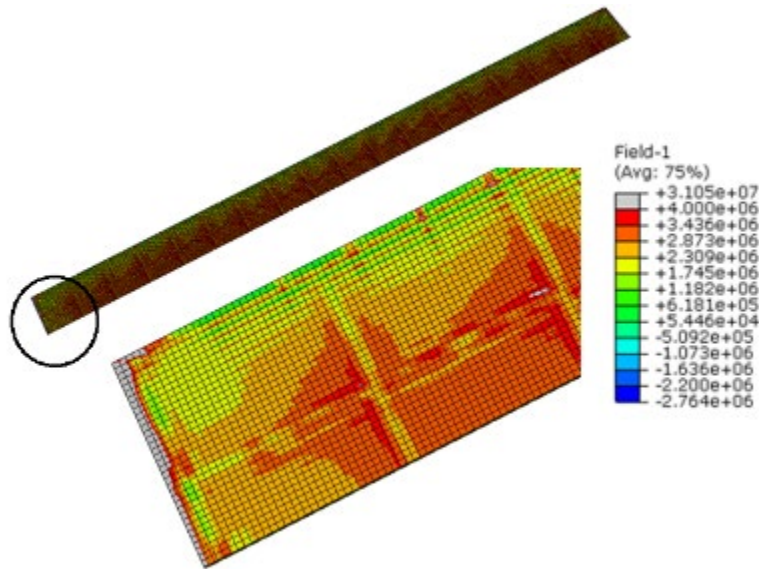
Figure 9-15. Maximum Shear Stress Distribution on the Full Rail Car Core with the Highest Values at the Supported Transverse End

The maximum shear stress distribution for the test floor as well as reduced scale floors supported on the longitudinal ends is also calculated (Figure 9-16). Figure 9-16 also shows that the distribution of shear stress is maximum at the longitudinal edges for the test scale specimen as well as the reduced scale specimen with three bays. However, the reduced scale model with one representative bay does not show the same distribution as the test scale specimen. This is because the model is too small to undergo any deflection even when the load is increased to match the maximum bending moment and may fail suddenly under shear at a higher load. The shear stress distribution indicates that the reduced model with the full width of rail car floor better represents the test rail car and the full rail car behavior. A further reduction in the model size depicted by a single representative element will not capture the shear failure.

Field-1
(Avg: 75%)
+7.287e+07
+4.000e+06
+3.548e+06
+3.095e+06
+2.643e+06
+2.190e+06
+1.738e+06
+1.286e+06
+8.332e+05
+3.808e+05
-7.159e+04
-5.240e+05
-9.764e+05
-1.429e+06

Figure 9-16. Maximum Shear Stress Distribution on the Test Scale and Reduced Scale Rail Car Floors

9.4.   Section Summary

This study was conducted to understand the behavior of a full rail car exposed to thermal and structural loading conditions as suggested in NFPA 130. It was found that the full rail car behavior is better represented by the NFPA 130 rail car floor test article when it is supported on the longitudinal ends rather than the transverse ends. In addition, new boundary conditions were used to reduce the size of the current test article while still capturing the essential deflection and failure behavior.

Two reduced scale models were considered to determine the minimum size and were compared with the current test article in terms of deflection profile, plastic strain accumulation and shear stress distribution with similar boundary conditions. It was found that the reduced scale model with the dimensions equal to current test article width (2.7 m [9 ft.]) and a length of one-third of the current test article (1.17 m [3.8 ft.]) can adequately capture the behavior. This reduced model exhibited similar deflection, plastic strain distribution and maximum shear stress distribution as observed in the current test article with similar boundary conditions. The other reduced scale model, with a length of 1.17 m (3.8 ft.) and a width of 1.0 m (3.3 ft.) did not compare well in terms of shear stress distribution. Moreover, this model had to be exposed to nine times the uniform load experienced by the current test article to keep the same maximum bending moment as experienced by the test scale model.

These simulation results demonstrate that a test article that is one-third the length and equal in width to the current test article provides a similar response during a fire resistance test when supported on the longitudinal ends with the same load. Therefore, a manufacturer should be able to construct a much smaller test article to evaluate the

179

fire resistance of the floor assembly. If needed, more than one test article with different characteristics could be tested as well in the same fire resistance test.

10.   Conclusion

The research effort in this work considered important requirements focused on fire exposure duration and severity according to NFPA 130 as well as the potential of reducing the size of the test article to make the compliance process more cost effective. The fire exposure duration and severity requirement were investigated by identifying incidents involving fire exposures to rail cars with an emphasis on incidents that involved exposure of passenger cars to an external fire in North America and internationally over the past 50 years. A combined effort involving fire testing and fire modeling was done to validate the fire models in FDS used for modeling fire exposures for larger fires found in accident history. A separate study was conducted to develop modeling methods using the finite element software Abaqus for predicting the response of rail car floor assemblies to standard fire resistance experiments. This separate study included the investigation and development of relevant thermal and mechanical material property models, section modeling methods, and the analysis of an exemplar assembly. This exemplar model was used as a full-scale prediction baseline and showed that the methodology can reasonably capture floor assembly response to furnace exposure making it sufficient for a numerical investigation for further studies in this work.

FDS and Abaqus were then used in conjunction to conduct a series of simulations to predict the results of exterior realistic fire scenario incidents identified in the review of fire incidents. The realistic thermal exposures from FDS were applied to a representative floor assembly section in Abaqus to analyze the heat transmission across the various components of the rail car floor. The performance of rail car floors exposed to real exposure was compared with the ASTM E119 exposure to re-evaluate the standard exposure duration of 30 minutes. It was observed that the current ASTM E119 exposure duration of 30 minutes should be sufficient to provide a fire resistance rating for most of the realistic fires. However, a diesel pool fire with a higher burning rate would require closer consideration of the current exposure duration. In this case, the ASTM E119 temperatures lagged those of the diesel spill fire with the higher burning rate by 300–600 seconds (5–10 minutes). The standard thermal exposures such as ASTM E119 were also compared with ISO 834 to determine the difference in the temperature rise of a rail car floor assembly. This computational study also resulted in development of an insulation model allowing for shrinking of fiberglass insulation to better represent the experimental observations.

The reduction of size of the test article was investigated by developing a methodology to simulate the fire resistance test using Abaqus. The thermal and mechanical material models developed in Abaqus were used for thermo-structural analysis to understand the response of a full-scale rail car floor supported at the transverse ends and subjected to ASTM E119 exposure and passenger load. The response of the full-scale rail car floor was compared with the response of the test-scale article (as defined by NFPA 130) subjected to the same conditions. The test-scale response was also evaluated using the new boundary conditions. In order to get the same structural response between the full-scale and test-scale, these boundary conditions required supporting the test-scale rail car floor on its longitudinal ends rather than the transverse ends as suggested by NFPA 130. It was demonstrated that the overall behavior of the full-scale rail car floor is better represented by test-scale rail car floor when supported at the longitudinal ends. The

new boundary conditions were used to further reduce the size of the rail car floor test specimen by evaluating and comparing the response at different scales using the deflection of the assembly, plastic deformation, and shear stress distribution. It was demonstrated that for the exemplar assembly a reduced-scale specimen with a length of approximately one-third (4 ft.) the current requirement, and comprising of the full-width of the rail car floor can adequately represent the behavior of a test-scale specimen.

10.1. Recommendations for Future Work

The evaluation of the standard exposure compared with realistic fires indicates that ASTM E119 exposure durations should be revisited for cases where large spill fires may occur. The ASTM E119 temperatures lagged those of the diesel spill fire with the higher burning rate by 300–600 seconds (5–10 minutes). In these cases, a fire hazard assessment may be a tool that could be used to assess the severity of these fires and to determine if the additional exposure duration is warranted. The shrinking insulation model developed to predict fiberglass melting to better represent the experimental observations should also be validated by performing small-scale thermal experiments.

It is also recommended to understand the representative loading requirements in NFPA 130 to ensure the rail car floor assembly is going through the same loading conditions as experienced by a rail car floor in practice. Specifically, the loading detail needs to include whether this should be consistent with the bending load or the shearing load that is expected in the end-use condition. A recommendation should be made to NFPA 130 committee to ensure the representative loading does not lead to any ambiguity related to the loading procedure.

A series of simulations are recommended to demonstrate that the methodology for reducing the size of the test article can be generally applied to the different floor assembly designs in rail cars. This should include the effect of different structural element layouts and floor surface types.

Fire resistance tests should:

- Conduct fire resistance tests to validate the simulation results showing that the scaling of the floor assembly is feasible
  - Include large test articles having a size currently recommended as well as a smaller size reduced-scale test articles
  - Include different test article support boundary conditions as well as structural construction details
  - Compare data to demonstrate the feasibility of reducing the test article size
  - Include representative penetrations to demonstrate equivalent performance in the large and reduced scale test articles
  - Compare measured responses with simulation results to validate the use of the modeling methodology for use in future design

11. References

[1]   "Abaqus - Dassault Systèmes®."

[2]   National Transportation Safety Board, "Preliminary Report Railroad DCA15MR006," Valhalla, NY, 2015. Available at: https://www.ntsb.gov/investigations/AccidentReports/Reports/DCA15MR006_preliminary.pdf.

[3]   National Transportation Safety Board, "Highway Accident Report NTSB/HAR-12/03," Miriam, NV, 2012.

[4]   National Transportation Safety Board, "Accident Report NTSB/RAR-10/01," Chatsworth, CA, 2008.

[5]   National Transportation Safety Board, "Railroad Accident Brief NTSB/RAB-05/01," Queens, NY, 2004.

[6]   National Transportation Safety Board, "Railroad Accident Report NTSB/RAR-02/01," Bourbonnais, IL, 1999.

[7]   National Transportation Safety Board, "Railroad Accident Brief RAB/98-03," Branson, MO, 1997.

[8]   National Transportation Safety Board, "Accident Report NTSB/RAR-97/02," Silver Spring, MD, 1996.

[9]   National Transportation Safety Board, "Railroad-Marine Accident Report NTSB/RAR-94/01," Mobile, AL, 1993.

[10]   United States Fire Administration, "The Derailment of the Sunset Limited," Report No. FA-163B, Big Bayou Canot, AL, 1993.

[11]   United States Fire Administration, "Rail Emergencies," Report No. TR-094, Emmitsburg, MD, 2003.

[12]   National Transportation Safety Board, "Railroad Accident Report NTSB/RAR-92/01," Boston, MA.

[13]   National Transportation Safety Board, "Safety Recommendation R-90-45," Stockton, CA, 1989.

[14]   National Transportation Safety Board, "Safety Recommendation H-82-14," Mineola, NY, 1982.

[15]   National Transportation Safety Board, "Safety Recommendation NTSB/RHR-82/03," Southampton, PA, 1982.

[16]   National Transportation Safety Board, "Railroad Accident Report NTSB/RAR-79/5," San Francisco, CA.

[17]   National Transportation Safety Board, "Accident Report NTSB/RAR-12/02," Red Oak, IA, 2011.

[18]   National Transportation Safety Board, "Railroad Accident Brief NTSB/RAB-08/05," Oneida, NY, 2007.

[19]   National Transportation Safety Board, "Railroad Accident Brief NTSB/RAB-12/03," Shepherdsville, Kentucky, 2007.

[20]   National Transportation Safety Board, "Accident Report NTSB/RAR-08/02," New Brighton, PA, 2006.

[21]   National Transportation Safety Board, "Accident Report NTSB/RAR-07/01," Anding, MS, 2005.

[22]   National Transportation Safety Board, "Railroad Accident Report NTSB/RAR-06/02," Gunter, TX, 2004.

[23]   National Transportation Safety Board, "Railroad Accident Brief NTSB/RAB-05/03," Kelso, WA, 2003.

[24]   Transportation Safety Board of Canada, "Railway Investigation Report R09H0010," Richmond, ON, 2009.

[25]   Transportation Safety Board of Canada, "Report Number R94T0357," Brighton, ON, 1994.

[26]   Republic of Bulgaria Ministry of Transport Information Technologies and Communications Railway Accident Investigation Unit, "Final Report from Technical investigation of railway accident - fire occurence during movement in electrical locomotive No 44096.6, which serviced fast train No 80290 in Chernograd - Karnobat interstation on 14.09.2016," 2016.

[27]   Republic of Bulgaria Ministry of Transport Information Technologies and Communications Railway Accident Investigation Unit, "Final Report from technical investigation of railway accident - fire occurred during movement in electrical locomotive No 44141.0, which serviced fast train No 4681 in Mihaylovo - Svoboda interstation on 08.07.2016," 2016.

[28]   Republic of Bulgaria Ministry of Transport Information Technologies and Communications Railway Accident Investigation Unit, "Final Report from Technical investigation of railway accident - fire occurred during movement of electrical locomotive No 44085.9, which serviced fast train No 3622 in Sahrane railway station on 16.06.2016," 2016.

[29]   Republic of Bulgaria Ministry of Transport Information Technologies and Communications Railway Accident Investigation Unit, "Final Report on Technical Investigation of Railway Transport Accident - fire outburst in electric locomotive No 44081.8 servicing fast train No 8626 at a time of movement between Aytos - Chernograd station on railroad No 2 on April 13th, 2016." 2016.

[30]   Republic of Bulgaria Ministry of Transport Information Technologies and Communications Railway Accident Investigation Unit, "Final Report from Technical investigation of railway accident - fire occurred in el. locomotive No 44169.1, which serviced fast train No 1621 in Elin Pelin - Vakarel interstation on 13.10.2015," 2015.

[31]   Rail Accident Investigation Branch, "Rail Accident Report: Electrical arcing and fire under a train near Windsor & Eton Riverside," London, UK, 2015. Available at: https://www.gov.uk/raib-reports/arcing-and-fire-at-windsor-eaton-riverside.

[32] Railway Accident Investigation Unit, "Investigation Report Tram fire on approach to Busaras Luas Stop," Busaras Luas, Ireland, 2014.

[33] Rail Accident Investigation Branch, "Train fire at South Gosforth," London, UK, 2013.

[34] Republic of Bulgaria Ministry of Transport Information Technologies and Communications Railway Accident Investigation Unit, "Final Report from Technical Investigation of Railway Accident that Took Place on 19.12.2012 around 11:38 hour at Shumen railway station - fire of electric locomotive No 42081.0 of passenger train No 90101," 2012.

[35] Romanian Railway Authority Ministry of Transports and Infrastructure, "Investigating Report on the fire occurred on the 2nd of August 2012," 2012.

[36] Republic of Bulgaria Ministry of Transport Information Technologies and Communications Railway Accident Investigation Unit, "Final Report from technical investigation of railway incident, which took place on 20.07.2011 around 17:20 hrs. with train No 2615, served by electrical locomotive No 44.089.1 in the stage Shunting Post (SP) Lesichery - Resen,," 2011.

[37] Romanian Railway Authority Ministry of Transports and Infrastructure, "Investigating Report on the fire that occurred on 11th of May 2011," Bucharest, Romania, 2011.

[38] Romanian Railway Authority Ministry of Transports and Infrastructure, "Investigating Report On the fire occurred on the 2nd of November 2010 at the locomotive DA 60-0965-8, hauling the passenger train no.1555-2, in the Branch of the Railway County Iasi, between the railway stations Bucecea - Veresti, at the km 13+500," 2010.

[39] Romanian Railway Authority Ministry of Transports and Infrastructure, "Investigating Report on the fire occurred at the locomotive DA 60-0945-0 owned by SNTFM 'CFR Marfa' SA, in the running of the train no. 83972, on the current line targusor Dobrogea-Nicolae Balcescu (km 31+000) on the 23th of August 2010," 2010.

[40] Romanian Railway Authority Ministry of Transports and Infrastructure, "Investigating Report on the railway accident occurred between Ciocanesti railway station and Baldana railway station at km 26+700, on February 7, 2010," 2010.

[41] Bureau d'enquetes sur les Accidents de transport terrestre, "Technical Report BEATT-2010-001," 2011.

[42] Republic of Bulgaria Ministry of Transport Information Technologies and Communications Railway Accident Investigation Unit, "Final Report on completed technical investigation of a railway accident - fire in electric locomotive No. 45-167.4 of train composition No. 3601 Sofia - Burgas at 145+580 km, in the Stamboliiski-Kableshkov inter0station section, on road No. 1, which occur." 2009.

[43] Czech Republic Rail Safety Inspection Office, "Investigation Report of Railway Accident - Fire on the traction unit of train R 766 while underway between Pnovany railway station and Vranov u Stribra railway station on the Pilsen hl. n.

Cheb open railway line," 2008.

[44]   Bureau d'enquetes sur les Accidents de transport terrestre, "Technical Report BEATT-2008-012," 2009.

[45]   Bureau d'enquetes sur les Accidents de transport terrestre, "Technical Report BEATT-2005-008," 2006.

[46]   Health and Safety Commision, "The Ladbroke Grove Rail Inquiry, Part 1 Report," UK, 1999.

[47]   Health and Safety Executive, "Internal Report on A Fire on the 18:30 Paddington to Swansea Train Near Maidenhead on Friday 8 Sept. 1995," London, UK, 1995.

[48]   W. K. Chow, "Study on passenger train vehicle fires," *Proceedings of the Institution of Mechanical Engineers, Part F: Journal of Rail and Rapid Transit*, vol. 211, no. 2, pp. 87–94, March 1997.

[49]   S. -K. Roh, J. -H. Hur, J. H. Kim, W. H. Kim, and K. S. Lee, "Early Response System and Improvement of Fire Safety Performance In Dae-gu Subway Disaster," in *International Association for Fire Safety Science*.

[50]   Y. Hasemi *et al.*, "Research Needs on the Fire Safety of Subway Stations - Fire disasters, regulations, research efforts and recent smoke movement tests in subway stations in Japan," in *Proceedings of the Asia-Oceania Symposium on Fire Science & Technology*, 2004.

[51]   M. J. Hurley *et al.*, Eds., *SFPE Handbook of Fire Protection Engineering*, 5th ed. Bethesda, MD, 2016.

[52]   U.S. Nuclear Regulatory Commission, "Fire Dynamics Tools (FDTS) - Quantitative Fire Hazard Analysis Methods for the U.S. Nuclear Regulatory Commission Fire Protection Inspection Program," 2004.

[53]   K. B. McGrattan, H. R. Baum, and A. Hamins, "Thermal Radiation from Large Pool Fires," Gaithersburg, MD, 2000.

[54]   Federal Railroad Administration, "Passenger Rail Car Egress Time Prediction," Research Results, RR06-04, Washington, DC, 2006. Available at: https://www.fra.dot.gov/eLib/details/L03527#p1_z5_gD_kPassenger%20Rail%20Car%20Egress%20Time%20Prediction.

[55]   Electro-Motive Diesel, "Electro-Motive Diesel F125 Passenger Locomotive Specifications."

[56]   Amtrak, "Amtrak Fleet Strategy," 2012.

[57]   National Fire Protection Association, "NFPA 70E Standard for Electrical Safety in the Workplace," Quincy, MA, 2012.

[58]   P. A. Hansen, "Fire in tyres. Heat release rate and response of vehicles," Trondheim, Norway.

[59]   C. M. Rippe and B. Y. Lattimer, "Full-field surface heat flux measurement using non-intrusive infrared thermography," *Fire Safety Journal*, vol. 78, pp. 238–250, 2015.

[60] "SBG01 heat flux meter | Hukseflux." [Online]. Available: https://www.hukseflux.com/products/heat-flux-sensors/heat-flux-meters/sbg01-heat-flux-meter. [Accessed: 29-Aug-2018].

[61] V. Babrauskas, "Heat Release Rates," in *SFPE Handbook of Fire Protection Engineering*, 5th ed., Springer, 2015, pp. 799–904.

[62] N. Nagy, P. Mulherin, M. J. DiDomizio, and E. J. Weckman, "Investigation of the fire hazard of mixed material piles in recycling facilities," in *Fire and Materials 2015 - 14th International Conference and Exhibition, Proceedings*, 2015.

[63] D. Drysdale, *An Introduction to Fire Dynamics*, 3rd ed. West Sussex, UK: John Wiley & Sons, 2011.

[64] R. N. Walters, S. M. Hackett, and R. E. Lyon, "Heats of combustion of high temperature polymers," Fam *Fire and Materials*, vol. 24, no. 5, pp. 245–252, 2000.

[65] Y. Z. Li, H. Ingason, and A. Lönnermark, "Fire development in different scales of train carriages," in *Fire Safety Science – Proceedings of the Eleventh International Symposium*, 2014, pp. 302–315.

[66] G. Heskestad, "Fire Plumes, Flame Height, and Air Entrainment," in *SFPE Handbook of Fire Protection Engineering*, 5th ed., Springer, 2015, pp. 396–428.

[67] "FLIR T440 Infrared Camera." [Online]. Available: https://www.flir-direct.com/product/flir-t440-infrared-camera. [Accessed: 29-Aug-2018].

[68] "Type k thermocouples | OMEGA Engineering." [Online]. Available: https://www.omega.com/kwbld/typekthermocouples.html. [Accessed: 29-Aug-2018].

[69] "Comparison of Time Constant vs. Overall Outside Diameter of Bare Thermocouple Wires or Grounded Junction Thermocouples In Air," Omega Engineering, Norwalk, CT, 2005.

[70] "Data Acquisition (DAQ) - National Instruments." [Online]. Available: http://www.ni.com/data-acquisition/. [Accessed: 05-Sep-2018].

[71] K. McGrattan, S. Hostikka, R. McDermott, J. Floyd, C. Weinschenk, and K. Overholt, "Fire Dynamics Simulator User' s Guide," Gaithersburg, MD, 2016.

[72] "BS EN 45545-3:2013 - Railway applications. Fire protection on railway vehicles. Fire resistance requirements for fire barriers."

[73] "NFPA 130 Standard for Fixed Guideway Transit and Passenger Rail Systems," National Fire Protection Association, Quincy, MA, 2017.

[74] "ASTM E119-16a: Standard Test Methods for Fire Tests of Building Construction and Materials," 2016.

[75] "EN 1363-1: Fire resistance tests Part 1: General requirements," 1999.

[76] C. Borsellino, L. Calabrese, and A. Valenza, "Experimental and numerical evaluation of sandwich composite structures," *Composites Science Technology*, 2004.

[77]   L. Gardner, A. Insausti, K. T. Ng, and M. Ashraf, "Elevated temperature material properties of stainless steel alloys," *Journal of Constructional Steel Research*, vol. 66, pp. 634–647, 2010.

[78]   L. Gardner, Y. Bu, P. Francis, N. R. Baddoo, K. A. Cashell, and F. Mccann, "Elevated temperature material properties of stainless steel reinforcing bar," *Construction and Building Materials*, vol. 114, pp. 977–997, 2016.

[79]   P. T. Summers *et al.*, "Overview of aluminum alloy mechanical properties during and after fires," *Fire Science Reviews*, vol. 4, no. 1, p. 3, Dec. 2015.

[80]   T. W. Goodrich and B. Y. Lattimer, "Fire decomposition effects on sandwich composite materials," *Composits Part A: Applied Science and Manufacturing*, 2012.

[81]   D. J. Hall and B. L. Robson, "A review of the design and materials evaluation programme for the GRP/foam sandwich composite hull of the RAN minehunter," *Composites*, vol. 15, no. 4, pp. 266–276, 1984.

[82]   M. L. Hobbs, K. L. Erickson, and T. Y. Chu, "Modeling Decomposition of Unconfined Rigid Polyurethane Foam," Albuquerue, NM, 1999.

[83]   T. Fateh, T. Rogaume, and F. Richard, "Multi-scale modeling of the thermal decomposition of fire retardant plywood," *Fire Safety Journal*, vol. 64, pp. 36–47, 2014.

[84]   "Wood Handbook: Wood as an Engineering Material," Madison, WI, USA, 1999.

[85]   A. Zinno, E. Fusco, A. Prota, and G. Manfredi, "Multiscale approach for the design of composite sandwich structures for train application," *Composite Structures*, vol. 92, no. 9, pp. 2208–2219, Aug. 2010.

[86]   A. C. Manalo, T. Aravinthan, W. Karunasena, and M. M. Islam, "Flexural behaviour of structural fibre composite sandwich beams in flatwise and edgewise positions," *Composites Structures*, 2010.

[87]   L. Couchman and A. Mouritz, *Modeling of Naval Composite Structures in Fire*. United States Office of Naval Research, 2005.

[88]   "MSDS: HTB 26 EW Spin-Glas by Johns Manville," 2016.

[89]   M. Nahid and B. Y. Lattimer, "Modeling thermal response of steel-concrete floor systems in a furnace," *Fire Safety Journal*, 2014.

[90]   P. Brinckerhoff, *Transit Capacity and Quality of Service Manual, Third Edition,* Transportation Research Board, Washington, DC, 2013.

[91]   "NFPA 130-14 Standard for Fixed Guideway Transit and Passenger Rail Systems 2014 Edition," 2014.

[92]   K. McGrattan, S. Hostikka, R. McDermott, J. Floyd, C. Weinschenk, and K. Overholt, "Fire Dynamics Simulator Technical Reference Guide Volume 1 : Mathematical Model," Gaithersburg, MD, 2016.

[93]   K. McGrattan *et al.*, "Fire Dynamics Simulator Technical Reference Guide Volume 3 : Validation," Gaithersburg, MD.

[94] N. P. Bansal and R. H. Doremus, *Handbook of glass properties*. Academic Press, 1986.

[95] *UL1709 : Standard for Rapid Rise Fire Tests of Protection Materials for Structural Steel*. .

[96] "N-Class Fire Resistant Divisions in U.S. Naval Ships."

[97] R. Mcdermott, "Sixth Edition Fire Dynamics Simulator Technical Reference Guide Volume 3 : Validation," vol. 3.

[98] S. (LTK E. Roman, "Personal Communcation." .

[99] K. B. McGrattan, S. Bareham, and D. W. Stroup, "Cable Heat Release, Ignition, and Spread in Tray Installations During Fire (CHRISTIFIRE), Phase 2: Vertical Shafts and Corridors," Rockville, MD, 2012.

[100] V. Kodur, M. Dwaikat, and R. Fike, "High temperature properties of steel for fire resistance modeling of structures," *Journal of Materials in Civil Engineering*, vol. 22, no. May, pp. 423–434, 2010.

[101] J. G. Quintiere, *Fundamentals of Fire Phenomena*, 1st ed. Hoboken, NJ: John Wiley & Sons, Ltd., 2009.

[102] "EN 1365-2 EN 1365-2 Fire resistance tests for loadbearing elements – Part 2: Floors and roofs General principles."

[103] "Fire-resistance tests — Elements of building construction — Part 1: General requirements," *ISO 834*, 1999.

[104] M. Dawood, W. Ballew, and J. Seiter, "Enhancing the resistance of composite sandwich panels to localized forces for civil infrastructure and transportation applications," *Composite Structures*, vol. 93, no. 11, pp. 2983–2991, 2011.

[105] S. Guo, "Experimental and numerical study on restrained composite slab during heating and cooling," *Journal of Constructional Steel Research*, vol. 69, no. 1, pp. 95–105, 2012.

[106] T. T. Nguyen, K. H. Tan, and I. W. Burgess, "Behaviour of composite slab-beam systems at elevated temperatures: Experimental and numerical investigation," *Engineering Structures*, vol. 82, pp. 199–213, 2015.

[107] S. P. Timoshenko and J. M. Gere, *Theory of Elastic Stability*. 1961.

[108] "EN 1991-1-2: 2002 Eurocode 1. Actions on Structures. Actions on Structures Exposed to Fire." 2002.

[109] T. Fateh, T. Rogaume, and F. Richard, "Multi-scale modeling of the thermal decomposition of fire retardant plywood," *Fire Safety Journal*, vol. 64, pp. 36–47, 2014.

[110] R. Jansson, "Measurement of thermal properties at elevated temperatures – Brandforsk project 328-031," Boras, Sweden, 2004.

Appendix A.
Instrumentation Details

This appendix details the position of each sensor used in the test series. All sensor positions are referenced relative to the global coordinate system depicted in Figure A-1.
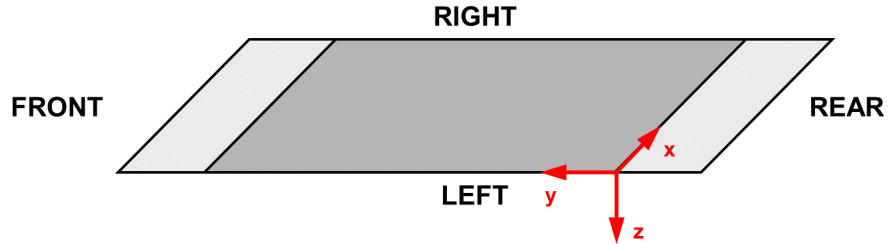
Figure A-1: Global coordinate system used for sensor position references.

A graphical overview of each sensor location is provided in Figure A-2 (cement board test series) and Figure A-3 (steel test series), below. For each sensor, the spatial coordinates are listed in Table A-1 (cement board test series) and Table A-2 (steel test series).

Table A-1: Sensor locations relative to the global coordinate system for the cement board tests.

Label	X (in)	Y (in)	Z (in)
T_C1	36	60	1
T_C2	36	12	1
T_C3	12	60	1
T_C4	12	12	1
T_C5	24	36	5
T_C6	24	36	7.5
T_C7	24	36	10
HF_C1	24	60	0
HF_C2	24	36	0
HF_C3	24	12	0

Table A-2: Sensor locations relative to the global coordinate system for the steel tests.

Label	X (in)	Y (in)	Z (in)
T_S1	36	72	1
T_S2	36	54	1
T_S3	36	36	1
T_S4	36	18	1
T_S5	36	0	1
T_S6	12	72	1
T_S7	12	54	1
T_S8	12	36	1
T_S9	12	18	1
T_S10	12	0	1
T_S11	24	36	5
T_S12	24	36	7.5
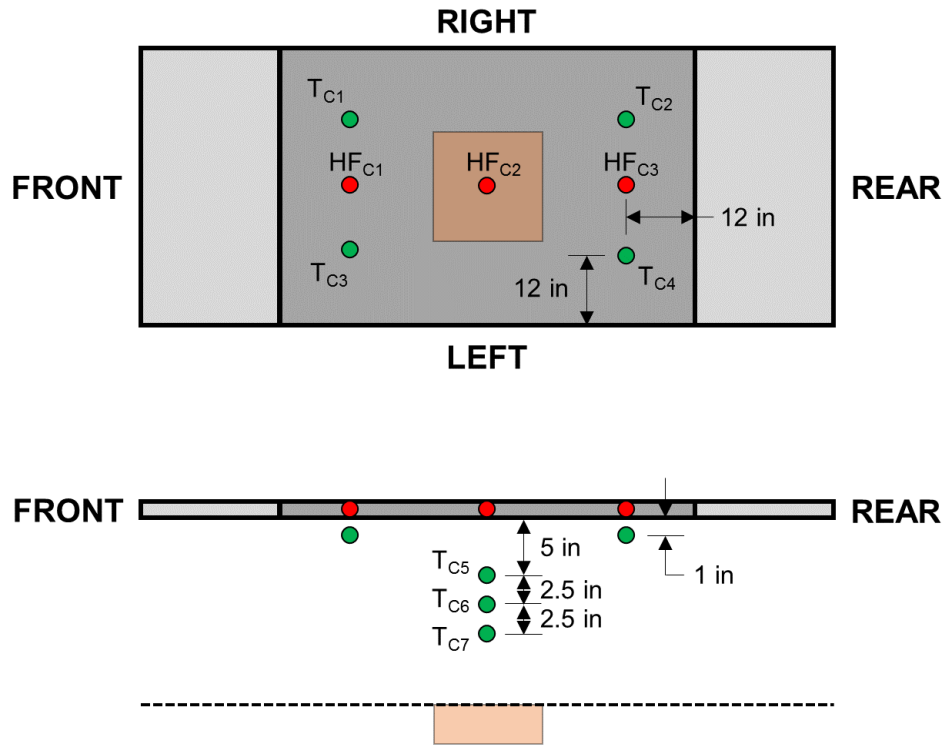
Figure A-2: Sensor locations for the cement board tests (overhead view and side view).
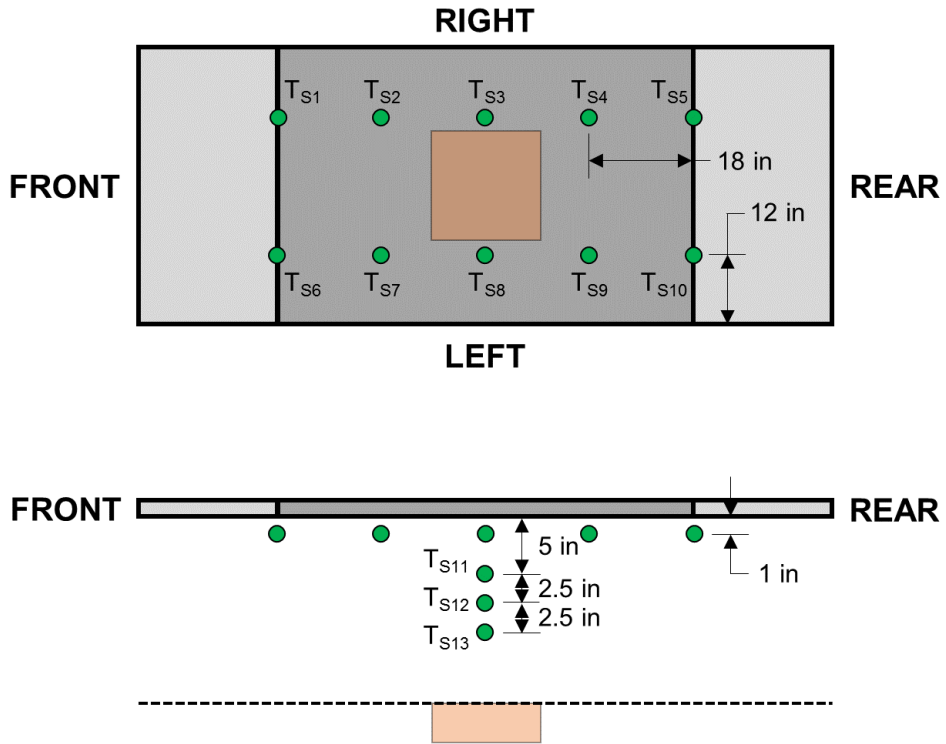
Figure A-3: Sensor locations for the steel tests (overhead view and side view).

Appendix B.
Test Results: Flat Configuration / Diesel Fire

a. Steel Panel Tests – IR Camera

The following figures show temperature and gauge heat flux contour plots 8 min after ignition. In the figures, the bottom of the contour corresponds to the "back" of the mockup (where the IR camera was located). Note that the steel panel measured 48 in. wide and 72 in. long; 1.5 in. has been clipped on each side in the figures below to account for the presence of the steel supporting frame.
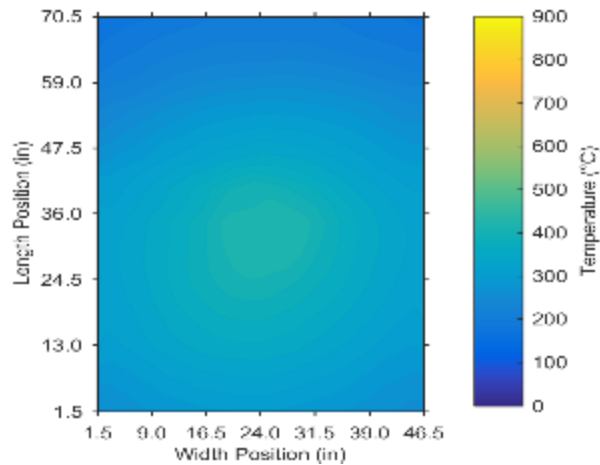
Figure B-1: Temperature gradient of the steel panel after 8 min (flat/diesel configuration).
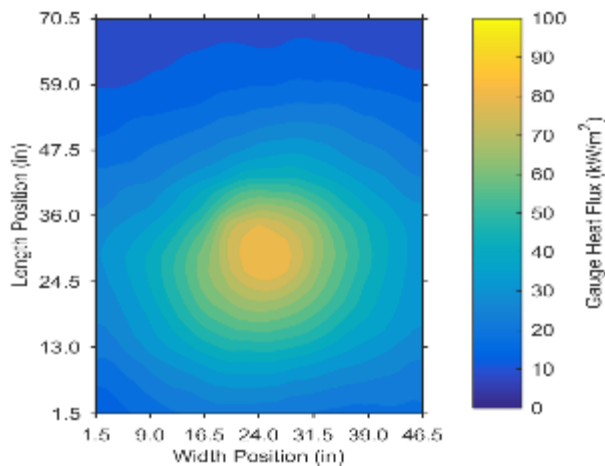
Figure B-2: Gauge heat flux gradient to the steel panel after 8 min (flat/diesel configuration).

The following figures show temperature and gauge heat flux over time at the center of the panel, 2 ft from the center in the length direction (averaged on both sides), and the maximum in-plane.
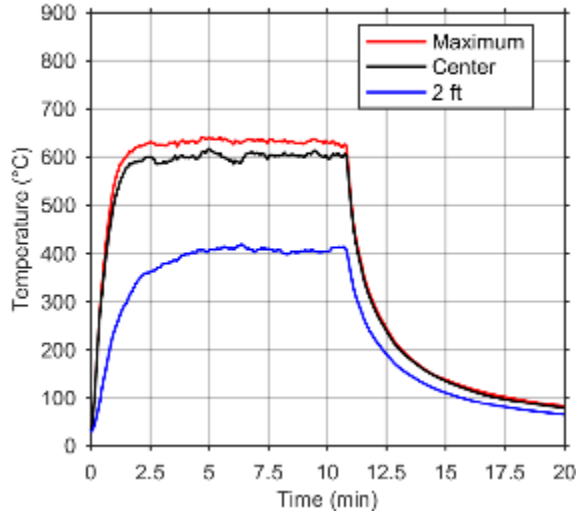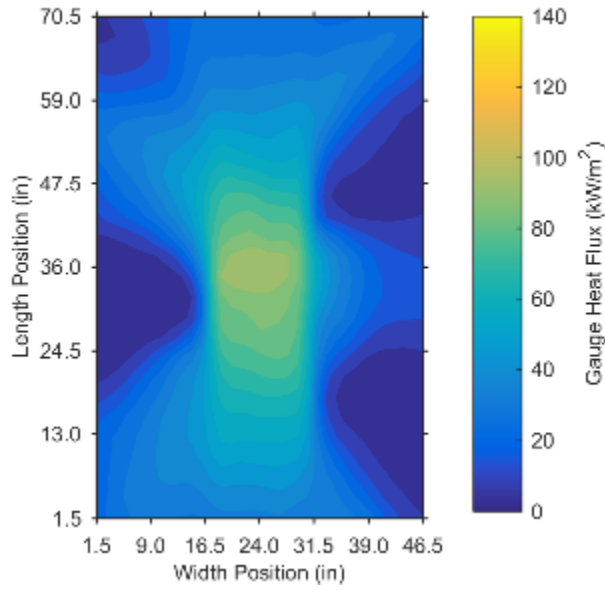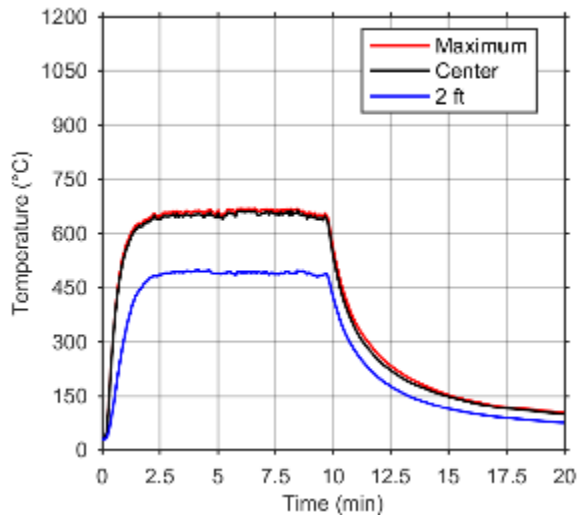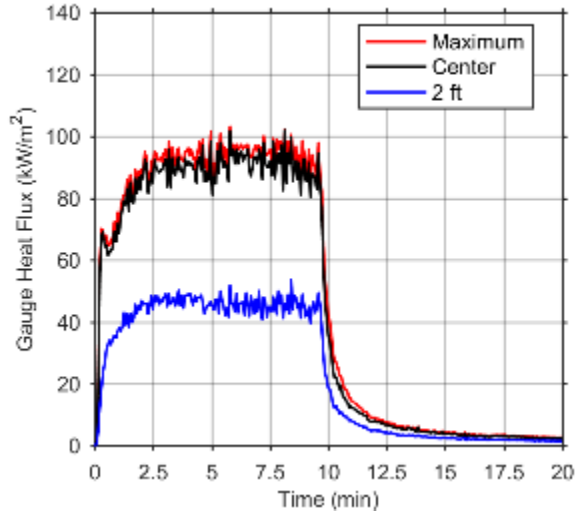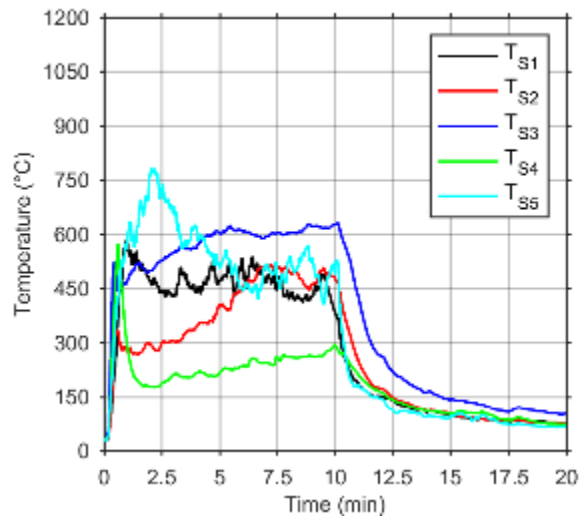
Figure B-3: Temperature of the steel panel, over time (flat/diesel configuration).
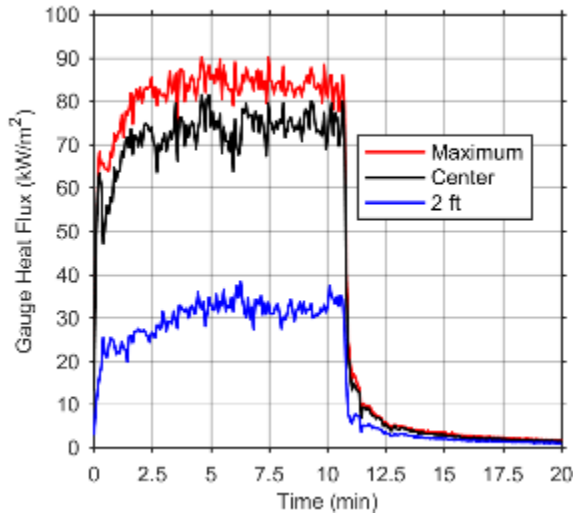
Figure B-1: Gauge heat flux to the steel panel, over time (flat/diesel configuration).

b. Steel Panel Tests

The following figures show temperature of the gases 1 in. below the mockup, over time (steel panel tests). Refer to Appendix A for details on the sensor locations. Note that, due to the proximity of these sensors to the steel panel and the tendency of the steel panel to warp as a result of the non-uniform heating, there are some discontinuities in these temperature traces, which may be attributed to the thermocouple making contact either with the steel panel or with the channel obstruction below.
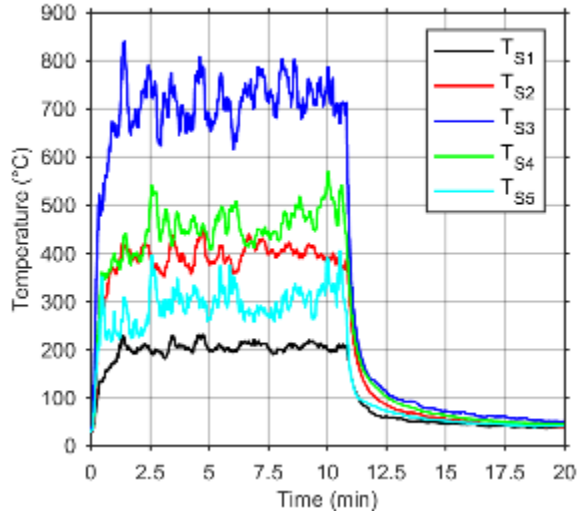
Figure B-2: Temperature of gases below the steel panel, on the right side, over time (flat/diesel configuration).
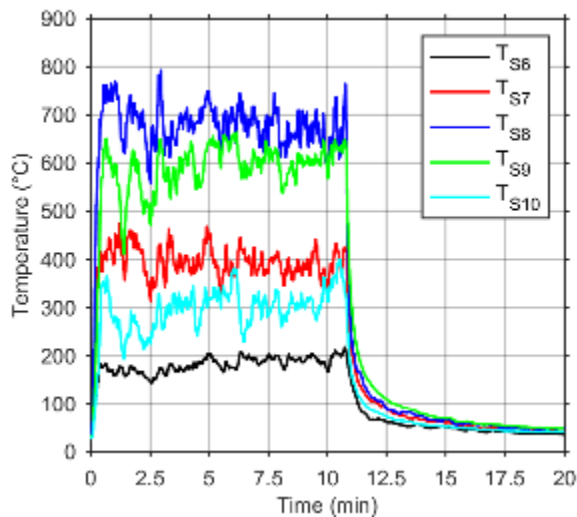
Figure B-3: Temperature of gases below the steel panel, on the left side, over time (flat/diesel configuration).

The figure below shows temperature of the gases directly above the burner at three heights, over time (steel panel tests). Refer to Appendix A for details on the sensor locations.
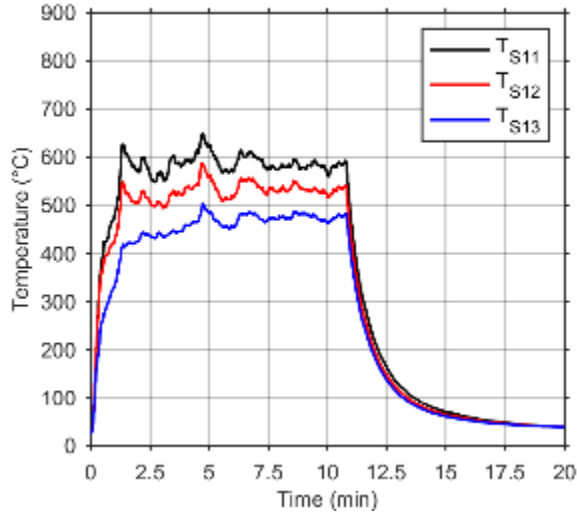
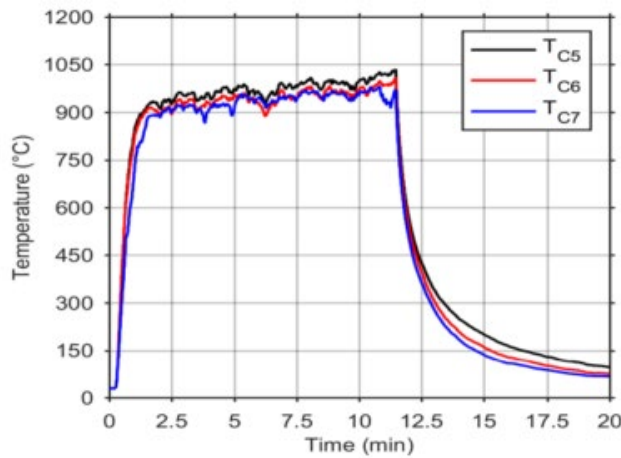**Figure B-4: Temperature of gases below the steel panel, directly above the burner, over time (flat/diesel configuration).**

c. Cement Board Panel Tests

The following figures show temperature of the gases 1 in. below the mockup, as well as temperature of the gases directly above the burner at three heights over time (cement board tests). Refer to Appendix A for details on the sensor locations.
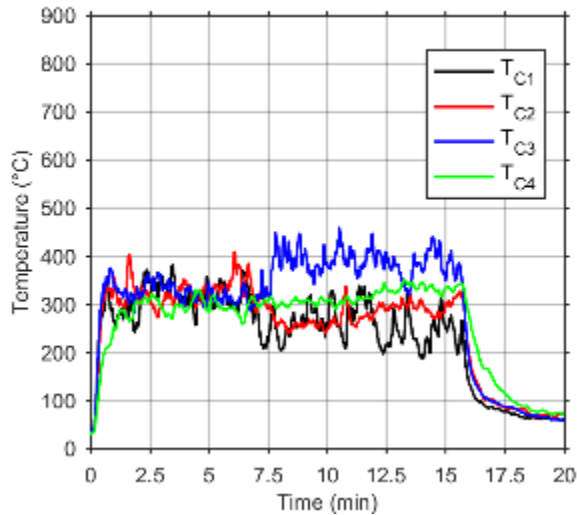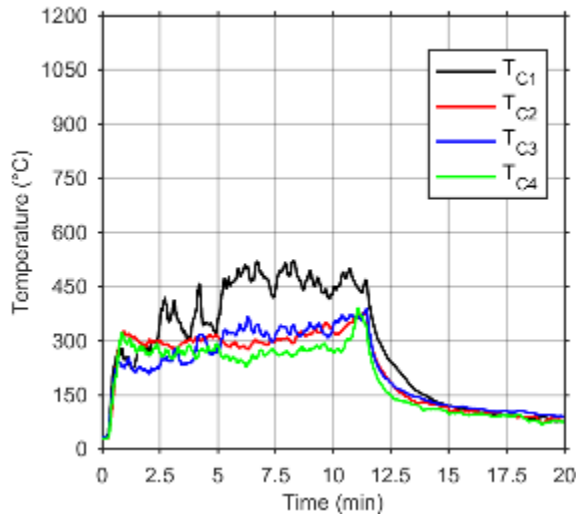

Figure B-5: Temperature of gases below the cement board panel, over time (flat/diesel configuration).
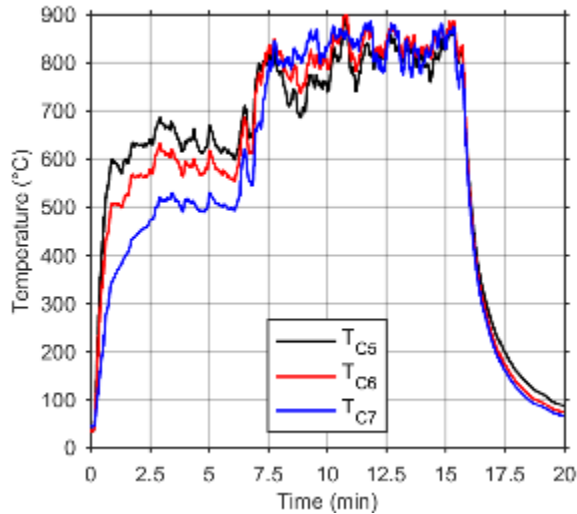
Figure B-6: Temperature of gases below the cement board panel, directly above the burner, over time (flat/diesel configuration).

The figure below shows heat flux to the mockup at three locations, measured by Schmidt-Boelter heat flux gauges. Refer to Appendix A for details on the sensor locations.
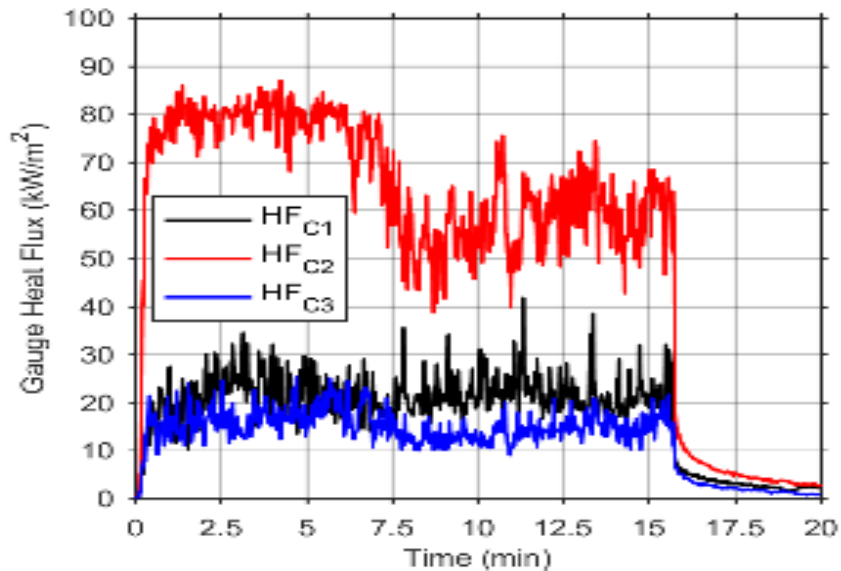
Figure B-7: Gauge heat flux to the cement board panel over time (flat/diesel configuration).

d. Steel Panel Tests – IR Camera

The following figures show temperature and gauge heat flux contour plots 8 min. after ignition. In the figures, the bottom of the contour corresponds to the "back" of the mockup (where the IR camera was located). Note that the steel panel measured 48 in. wide and 72 in. long; 1.5 in. has been clipped on each side in the figures below to account for the presence of the steel supporting frame.
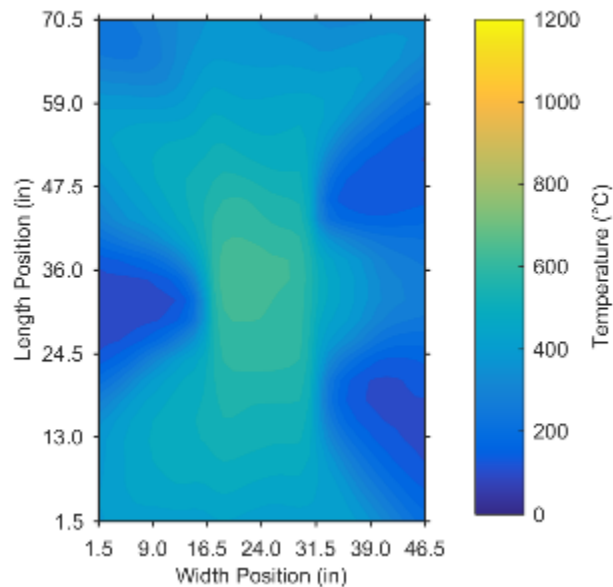
Figure C-1: Temperature gradient of the steel panel after 8 min (channel/diesel configuration).

Figure C-2: Gauge heat flux gradient to the steel panel after 8 min (channel/diesel configuration).

The following figures show temperature and gauge heat flux over time at the center of the panel, 2 ft from the center in the length direction (averaged on both sides), and the maximum in-plane.

Figure C-3: Temperature of the steel panel, over time (channel/diesel configuration).

Figure C-4: Gauge heat flux to the steel panel, over time (channel/diesel configuration).

e. Steel Panel Tests

The following figures show temperature of the gases 1 in. below the mockup, over time (steel panel tests). Refer to Appendix A for details on the sensor locations. Note that, due to the proximity of these sensors to the steel panel and the tendency of the steel panel to warp as a result of the non-uniform heating, there are some discontinuities in these temperature traces, which may be attributed to the thermocouple making contact either with the steel panel or with the channel obstruction below.

Figure C-5: Temperature of gases below the steel panel, on the right side, over time (channel/diesel configuration).
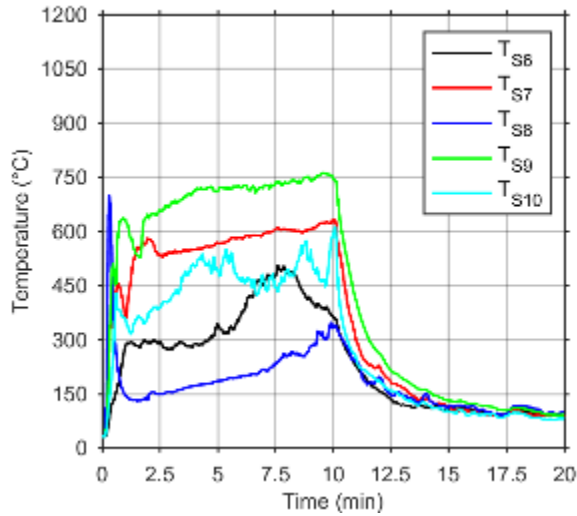
Figure C-6: Temperature of gases below the steel panel, on the left side, over time (channel/diesel configuration).

The figure below shows temperature of the gases directly above the burner at three heights, over time (steel panel tests). Refer to Appendix A for details on the sensor locations.

Figure C-7: Temperature of gases below the steel panel, directly above the burner, over time (channel/diesel configuration).

Cement Board Panel Tests

The following figures show temperature of the gases 1 in below the mockup, as well as temperature of the gases directly above the burner at three heights, over time (cement board tests). Refer to <u>Appendix A</u> for details on the sensor locations.

Figure C-8: Temperature of gases below the cement board panel, over time (channel/diesel configuration).
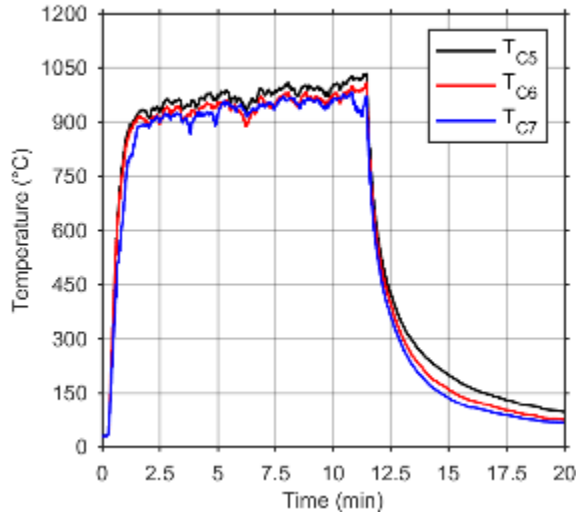
Figure C-9: Temperature of gases below the cement board panel, directly above the burner, over time (channel/diesel configuration).

The figure below shows heat flux to the mockup at three locations, measured by Schmidt-Boelter heat flux gauges. Refer to <u>Appendix A</u> for details on the sensor locations.
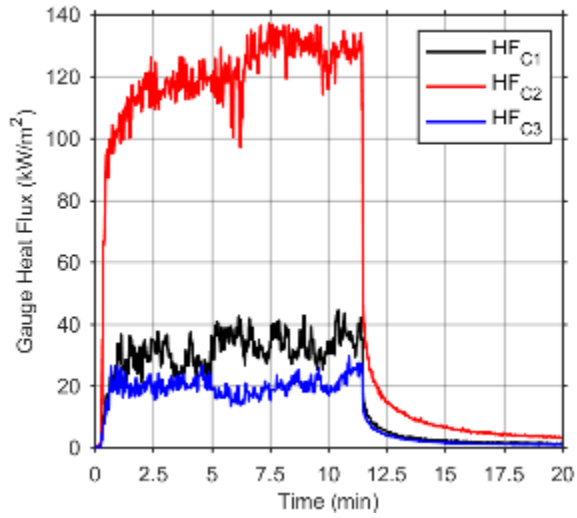
Figure C-10: Gauge heat flux to the cement board panel over time (channel/diesel configuration).

Appendix D.
Test Results: Flat Configuration / Trash Fire

f.   Steel Panel Tests – IR Camera

The following figures show temperature and gauge heat flux contour plots 8 min. after ignition. In the figures, the bottom of the contour corresponds to the "back" of the mockup (where the IR camera was located). Note that the steel panel measured 48 in. wide and 72 in. long; 1.5 in. has been clipped on each side in the figures below to account for the presence of the steel supporting frame.
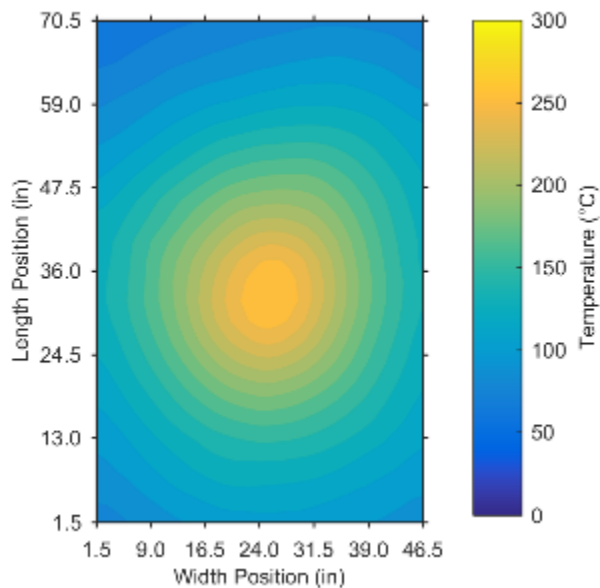
Figure D-1: Temperature gradient of the steel panel after 8 min (flat/trash configuration).
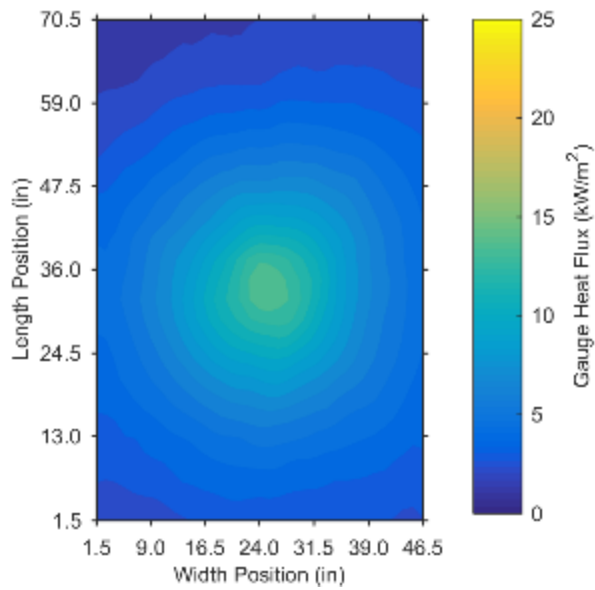
Figure D-2: Gauge heat flux gradient to the steel panel after 8 min (flat/trash configuration).

The following figures show temperature and gauge heat flux over time at the center of the panel, 2 ft from the center in the length direction (averaged on both sides), and the maximum in-plane.
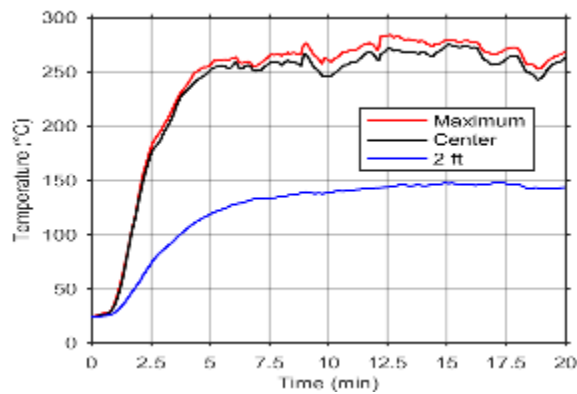
Figure D-3: Temperature of the steel panel, over time (flat/trash configuration).
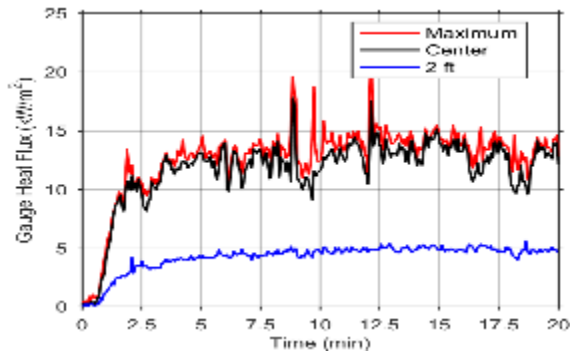
Figure D-4: Gauge heat flux to the steel panel, over time (flat/trash configuration).

g. Steel Panel Tests

The following figures show temperature of the gases 1 in. below the mockup, over time (steel panel tests). Refer to Appendix A for details on the sensor locations. Note that, due to the proximity of these sensors to the steel panel and the tendency of the steel panel to warp as a result of the non-uniform heating, there are some discontinuities in these temperature traces, which may be attributed to the thermocouple making contact either with the steel panel or with the channel obstruction below.
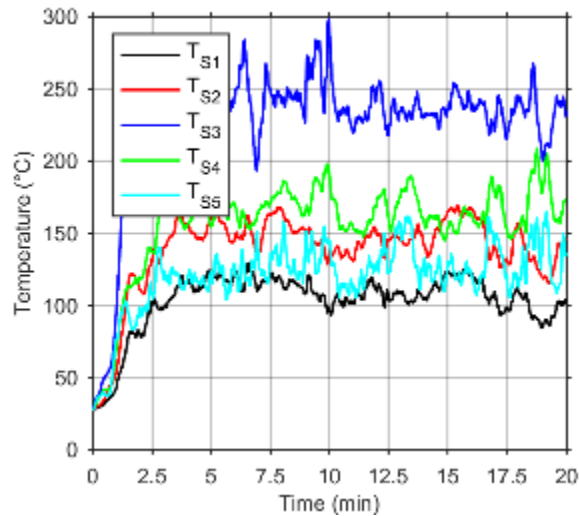
Figure D-5: Temperature of gases below the steel panel, on the right side, over time (flat/trash configuration).
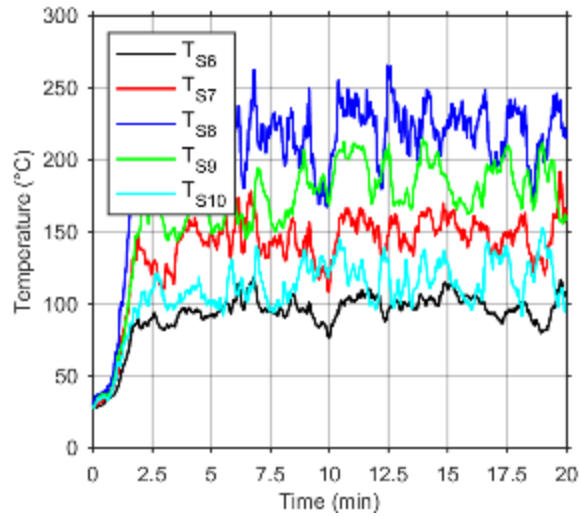
Figure D-6: Temperature of gases below the steel panel, on the left side, over time (flat/trash configuration).

The figure below shows temperature of the gases directly above the burner at three heights, over time (steel panel tests). Refer to Appendix A for details on the sensor locations.
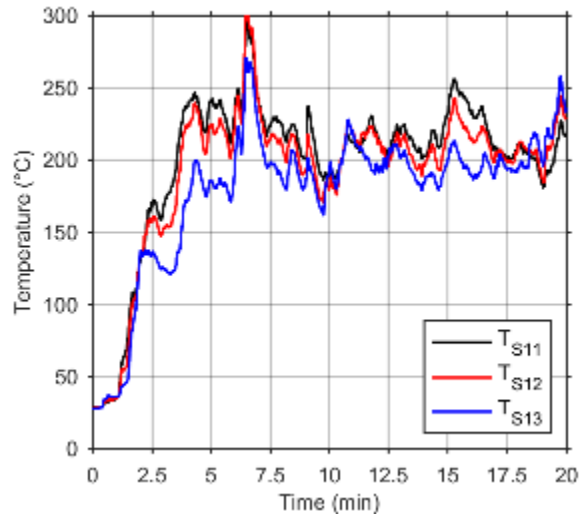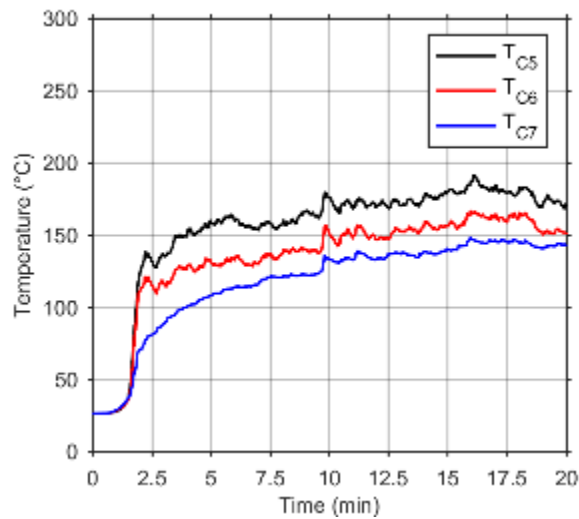

Figure D-7: Temperature of gases below the steel panel, directly above the burner, over time (flat/trash configuration).

h. Cement Board Panel Tests

The following figures show temperature of the gases 1 in. below the mockup, as well as temperature of the gases directly above the burner at three heights, over time (cement board tests). Refer to Appendix A for details on the sensor locations.
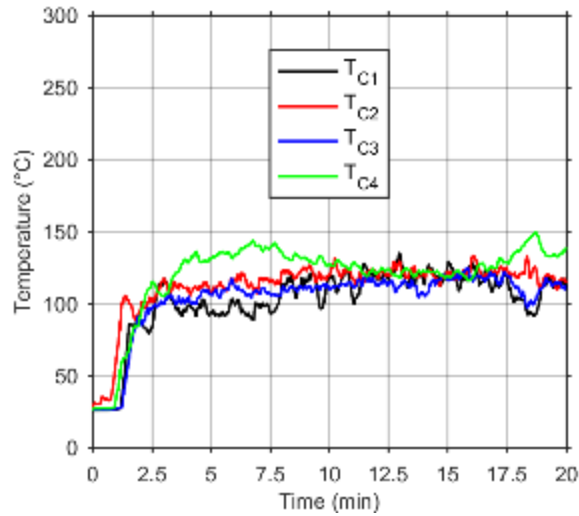
Figure D-8: Temperature of gases below the cement board panel, over time (flat/trash configuration).


Figure D-9: Temperature of gases below the cement board panel, directly above the burner, over time (flat/trash configuration).

The figure below shows heat flux to the mockup at three locations, measured by Schmidt-Boelter heat flux gauges. Refer to Appendix A for details on the sensor locations.
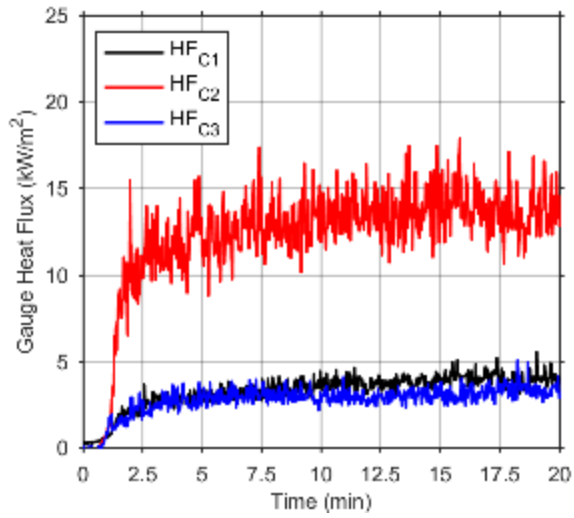
Figure D-10: Gauge heat flux to the cement board panel over time (flat/trash configuration).

# Appendix E.
Test Results: Channel Configuration / Trash Fire

i.   Steel Panel Tests – IR Camera

The following figures show temperature and gauge heat flux contour plots 8 min after ignition. In the figures, the bottom of the contour corresponds to the "back" of the mockup (where the IR camera was located). Note that the steel panel measured 48 in wide and 72 in long; 1.5 in has been clipped on each side in the figures below to account for the presence of the steel supporting frame.
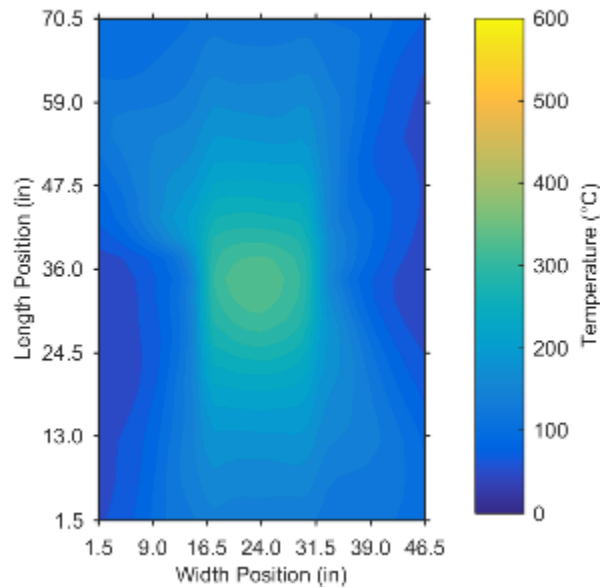

Figure E-1: Temperature gradient of the steel panel after 8 min (channel/trash configuration).
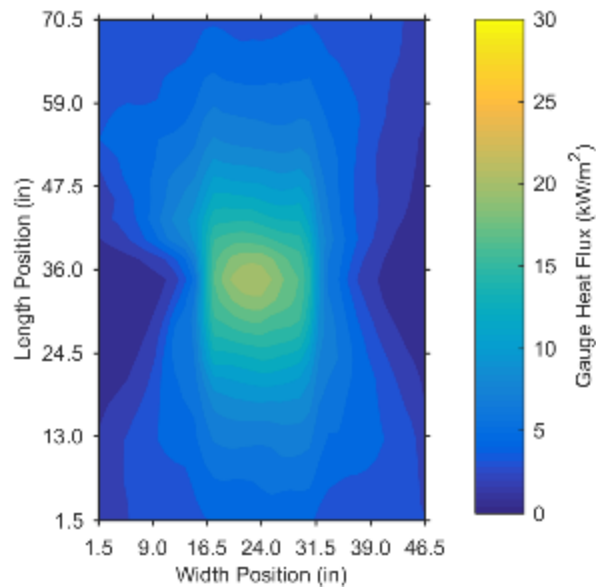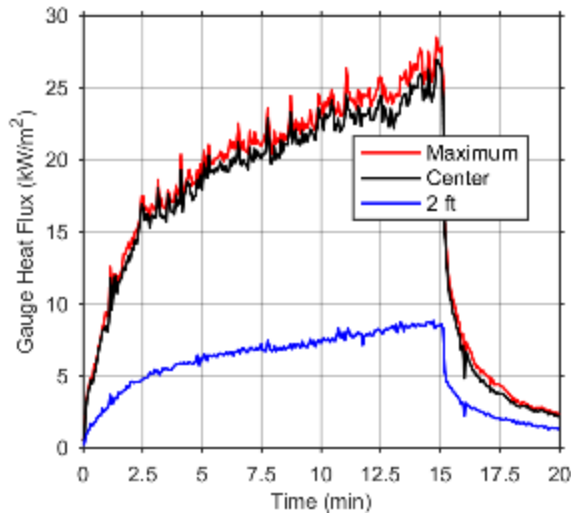
Figure E-2: Gauge heat flux gradient to the steel panel after 8 min (channel/trash configuration).

The following figures show temperature and gauge heat flux over time at the center of the panel, 2 ft from the center in the length direction (averaged on both sides), and the maximum in-plane.
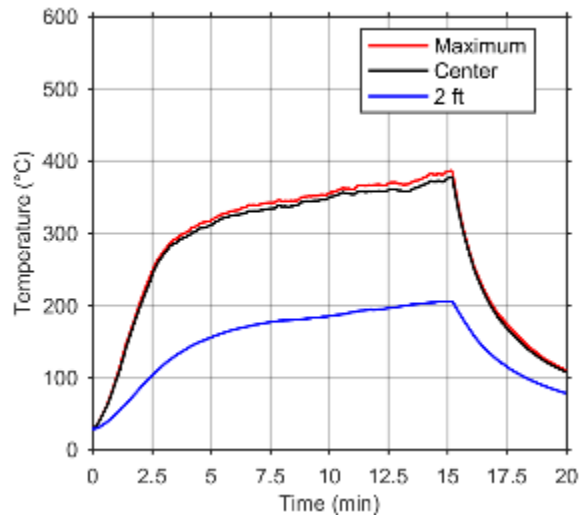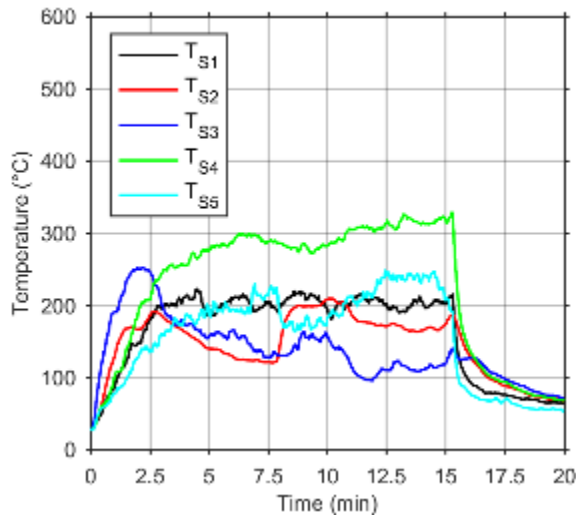

Figure E-3: Temperature of the steel panel, over time (channel/trash configuration).
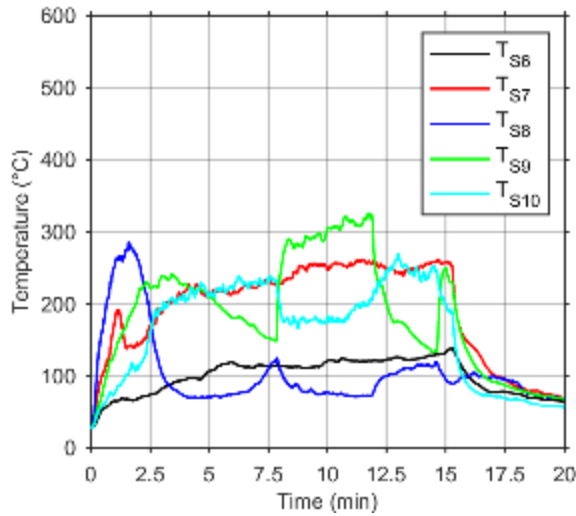
Figure E-4: Gauge heat flux to the steel panel, over time (channel/trash configuration).

j. Steel Panel Tests

The following figures show temperature of the gases 1 in. below the mockup over time (steel panel tests). Refer to Appendix A for details on the sensor locations. Note that, due to the proximity of these sensors to the steel panel and the tendency of the steel panel to warp as a result of the non-uniform heating, there are some discontinuities in these temperature traces, which may be attributed to the thermocouple making contact either with the steel panel or with the channel obstruction below.
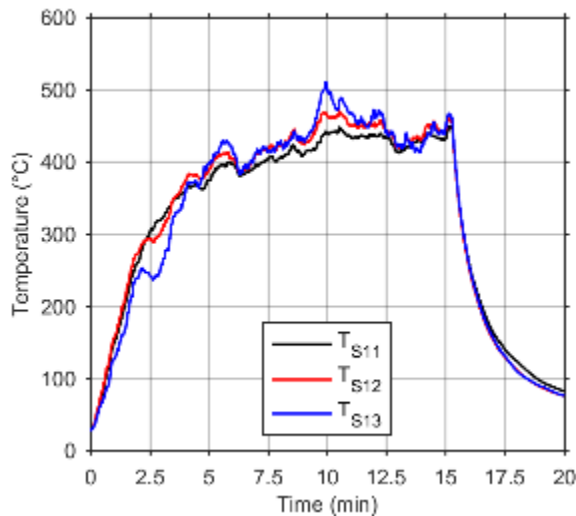

Figure E-5: Temperature of gases below the steel panel, on the right side, over time (channel/trash configuration).

Figure E-6: Temperature of gases below the steel panel, on the left side, over time (channel/trash configuration).
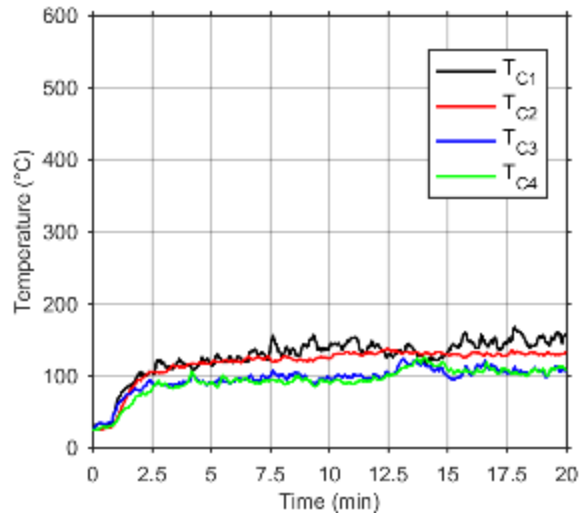
The figure below shows temperature of the gases directly above the burner at three heights, over time (steel panel tests). Refer to Appendix A for details on the sensor locations.
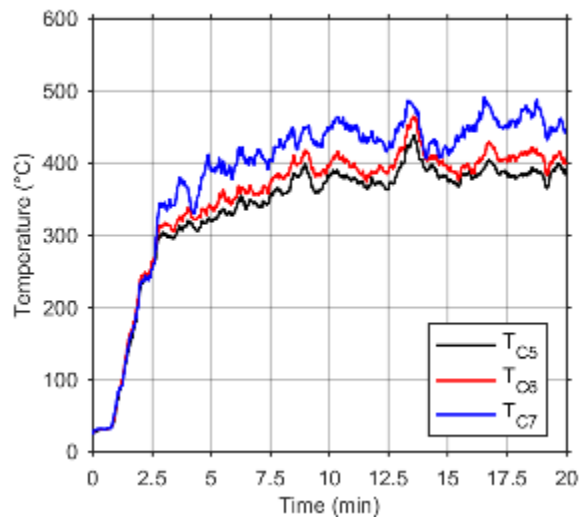

Figure E-7: Temperature of gases below the steel panel, directly above the burner, over time (channel/trash configuration).

k. Cement Board Panel Tests

The following figures show temperature of the gases 1 in. below the mockup, as well as temperature of the gases directly above the burner at three heights over time (cement board tests). Refer to Appendix A for details on the sensor locations.

Figure E-8: Temperature of gases below the cement board panel, over time (channel/trash configuration).

Figure E-9: Temperature of gases below the cement board panel, directly above the burner, over time (channel/trash configuration).

The figure below shows heat flux to the mockup at three locations, measured by Schmidt-Boelter heat flux gauges. Refer to Appendix A for details on the sensor locations.
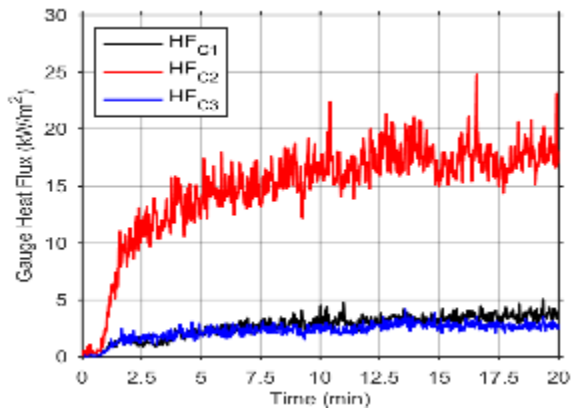
Figure E-10. Gauge heat flux to the cement board panel over time (channel/trash configuration).

Appendix F.
Material Models for Example Analysis

F.1 Stainless Steel (SS304)

Source: Eurocode EN 1991-1-2

Density
$$\rho = 7850 \text{ kg/m}^3$$

Thermal Elongation
$$\alpha \ (/°C) = (15.9042 + 9.63 * 10^{-3}T - 3.729 * 10^{-6}T^2) * 10^{-6}$$

Specific Heat Capacity
$$c_p(^J/_{\text{kg} - \text{K}}) = 450 + 0.28T + 2.91 * 10^{-4}T^2 + 1.34 * 10^{-7}T^3$$

Thermal Conductivity
$$k \ (^W/_{m - K}) = 14.6 + 1.27 * 10^{-2}T$$
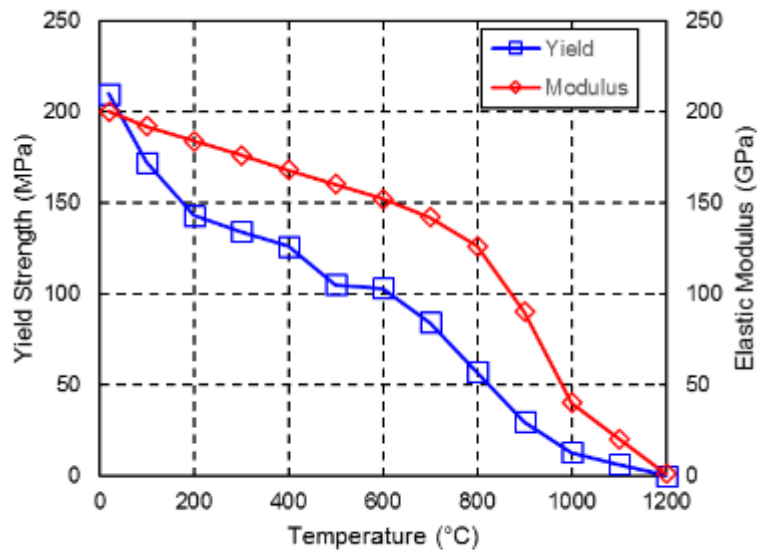
Elastic Modulus and Yield Strength

Figure F-1. Mechanical properties of SS304 at elevated temperature.

F.2 Plywood

Sources: Fateh et. al [109], Couchman and Mouritz [87], Wood Handbook [84]

Density
$$\rho = 36 \text{ kg/m}^3$$

Thermal Elongation
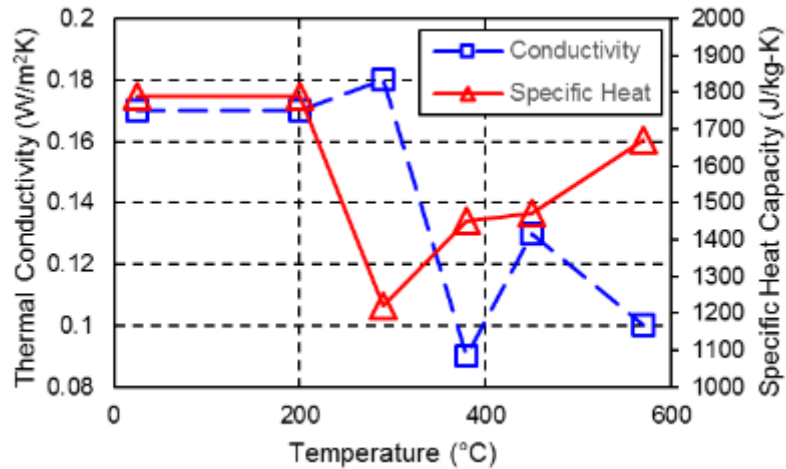$$\alpha \ (/°C) = 6.1 * 10^{-6}$$

Figure F-2. Temperature dependent thermal property model of 480 kg/m³ plywood.

Table F-1. Material elasticity constants for plywood material model

T (°C)	E_1 (GPa)	E_2 (GPa)	E_3 (GPa)	G_{12} (GPa)	G_{13} (GPa)	G_{23} (GPa)
25	6.89	6.89	2.05	0.14	0.47	0.47
100	3.45	3.45	1.03	0.056	0.19	0.19
300	0.69	0.69	0.21	0.14	0.047	0.047

Table F-2. Shear stress thresholds for core shear failure of plywood

T (°C)	T_{12} (MPa)	T_{13} (MPa)	T_{23} (MPa)
25	1.7	4.1	4.1
100	0.68	1.64	1.64
300	0.017	0.041	0.041

F.3   Spun Fiberglass
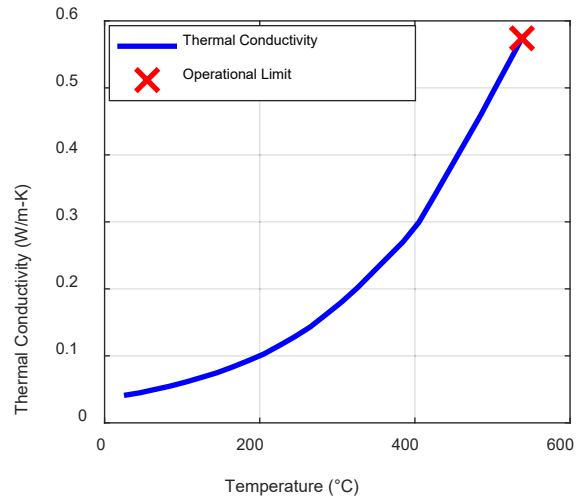
Sources: Jansson [110], Commercial MSDS [88]

Density
$\rho = 16 \text{ kg/m}^3$

Specific Heat
$c_p = 670 \text{ J}/\text{kg} - \text{K}$

Figure F-3. Thermal conductivity of spun fiberglass insulation blanket.

Abbreviations and Acronyms

Abbreviations	Acronyms
AGT	Automated Guideway Transit
AST	Adiabatic Surface Temperature
BART	Bay Area Rapid Transit Authority
BEATT	Bureau d'Enquêtes sur les Accidents de Transport Terrestre
CO	Carbon Monoxide
CFR	Code of Federal Regulations
CAE	Computer Aided Engineering
CFD	Computational Fluid Dynamics
ERAIL	European Railway Accident Information Links
FEA	Finite Element Analysis
FE	Finite Element
FDS	Fire Dynamics Simulator
FRA	Federal Railroad Administration
ga	Gauge
HRR	Heat Release Rate
HRRPUA	Heat Release Rate Per Unit Area
HRRUV	Heat Release Rate Per Unit Volume
IR	Infrared
ISO	International Organization for Standardization
LES	Large Eddy Simulation
LUL	London Underground
MARC	Maryland Area Regional Commuter
MBTA	Massachusetts Bay Transportation Authority
STM	Montreal Transit Corporation (Société de transport de Montréal)
NFPA	National Fire Protection Association
NIST	National Institute of Standards and Technology
NTSB	National Transportation Safety Board
NYCTA	New York City Transit Authority
PPM	People Per Minute

Abbreviations	Acronyms
PATH	Port Authority Trans-Hudson
RAIU	Railway Accident Investigation
SEPTA	Southeast Pennsylvania Transit Authority
TTC	Toronto Transit Commission
HSE	UK Health and Safety Executive
USFA	U.S. Fire Administration
WMATA	Washington Metropolitan Area Transit Authority